# MODELLING STUDIES OF EXOPLANETARY OCEANS

A thesis submitted to the School of Mathematics at the University of East Anglia in partial fulfilment of the requirements for the degree of Doctor of Philosophy

Jodie Cullum

May 2018

# Abstract

The ocean plays a key role in the climate of Earth, and it is therefore expected that any oceans present on an exoplanet would also be a crucial component of the climate system and hence have implications for the habitability of the planet. However, many planetary and oceanic properties cannot be assumed to be the same on an exoplanet as on Earth, and therefore the behaviour of the ocean cannot be assumed.

Here, basic land configurations are explored and a single meridional barrier is used throughout the other experiments, as this is the simplest configuration of any substantial land mass. The effect of ocean salinity, at a level both higher and lower than on Earth, is explored for the first time and reversal of the Earth-like meridional overturning circulation is found. The proportionality between mean salinity and salinity gradients in the ocean is established. The impact of planetary rotation period is also investigated, and it is concluded that a longer rotation period results in a greater poleward ocean heat transport, with the additional novel conclusions of a shallower thermocline depth, increased horizontal ocean velocities, and stronger overturning circulation. Finally, existing ocean modelling of a tidally locked configuration is furthered by the addition of different land masses, the extent of the zonal circulation and magnitude of the zonal heat transport is found to have significant dependence on the location of a meridional barrier in the ocean, with resulting dark side mean temperatures varying by over 7°C.

The modelling presented here highlights the importance of the consideration of the ocean in exoplanetary climate studies, and its role in planetary habitability.

# Acknowledgements

I am very grateful to my supervisors, David Stevens and Manoj Joshi, for their support and guidance throughout, without the encouragement and understanding they offered this would not have been possible. I'd also like to thank my family and friends who have consistently been there for me, through both the highs and the lows.

# Contents

# Chapter 1

# Introduction

The habitability of the growing number of discovered exoplanets, 3,506 confirmed planets at the time of writing (NASA 2017*b*), is a fundamental question of great scientific and social interest. However, it is not a simple question to answer, and is severely limited by constraints on observational capabilities. Hence, modelling possible climates of these alien worlds gives a crucial insight into their potential habitability.

## 1.1 Motivation

On Earth the ocean is a core component of the climate system; it is responsible for transporting a significant amount of heat from regions that receive the greatest solar insolation to those that receive the least (Trenberth & Caron 2001), it provides a large amount of heat storage, and is the source of water vapour for the hydrological cycle and greenhouse effect. Hence, when considering the climate of terrestrial exoplanets any oceans present on their surface are expected to play a key role in redistributing heat, and consequently have important implications for the habitability of any such planets.

There are many properties of an exoplanet, both of the planetary system and of the ocean, which may be expected to vary from their Earth like values, for example, orbital configuration, planetary size and mass, composition and volume of any oceans, and properties of the host star. Modelling different configurations of these is needed to identify the influence that varying these properties has on the circulation and heat transport of the ocean, and the consequent impact on the climate of the planet.

## 1.2 Exoplanet exploration

### 1.2.1 Discoveries

At the time of writing 3,506 exoplanet discoveries have been confirmed, with a further 2,248 unconfirmed candidates (NASA 2017*b*). The first discovery of an exoplanet was in 1992, when two planets were found orbiting the pulsar PSR1257+12 (Wolszczan & Frail 1992). The first found orbiting a main sequence star was in 1995; a gas giant with a small orbital radius, a *hot Jupiter*, around the Sun-like star 51 Pegasi (Mayor & Queloz 1995).

Further notable discoveries include Gliese-876d, which at 7.5 Earth-mass was the first super-Earth, a planet with mass greater than Earth but smaller than Neptune, found orbiting a main sequence star in 2005 (Rivera et al. 2005).

In 2013 the first Earth-sized exoplanet was discovered; Kepler-78b with a size of $1.16 \pm 0.19$ Earth-radius (Sanchis-Ojeda et al. 2013), and the first Earth-sized exoplanet discovered to be orbiting in the habitable zone was found in 2014, named Kepler-186f (Quintana et al. 2014).

### 1.2.2 Detection

The vast majority of the confirmed exoplanets have been discovered by either the transit method or the radial velocity method, responsible for detecting 2,734 and 643 exoplanets at the time of writing, respectively (NASA 2017*b*). The transit method involves observing a regular dip in the brightness of a star as an orbiting planet passes between the star and observer (figure 1.1(a)). The gravitational force on a star from an orbiting planet causes a small movement of the star, the radial velocity method involves detecting the red shift in light from the star which results from this movement (figure 1.1(b)).

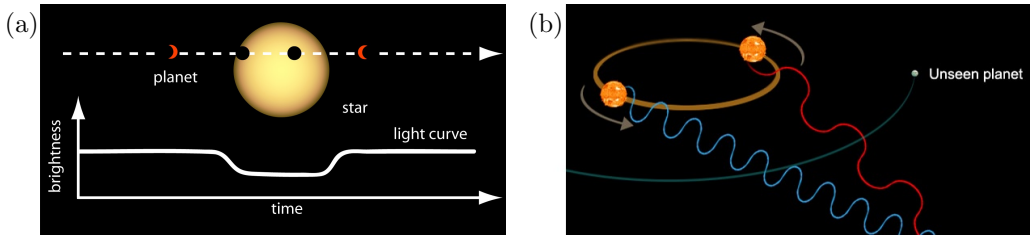


Figure 1.1: Schematics showing the way exoplanets are detected using (a) the transit method, and (b) the radial velocity method. Figures adapted from NASA (2017*a*).

The most notable mission finding exoplanets is the *Kepler Space Observatory* launched by NASA in 2009, responsible for discovering 2,337 confirmed exoplanets at the time of writing, using the transit method, and with many more unconfirmed candidates identified (NASA 2017*b*). At the time of launching the catalogue of discovered exoplanets was dominated by giant planets, and hence the Kepler mission was designed with the aim of finding Earth-sized planets. At the time of writing it has enabled the discovery of 295 confirmed exoplanets with a size up to 1.25 Earth-radius (NASA 2017*b*).

### 1.2.3 Characterisation

Depending on the method used to detect an exoplanet some planetary properties can also be identified. The transit method gives the radius of the planet, from the amount of light which is blocked, as well as the orbital period from the transit frequency. The radial velocity method gives information about the mass of the planet, and therefore, if a planet can be detected using both the transit and radial velocity method the density may be calculated. Knowledge of the density allows conclusions about the composition of the planet; for example whether it is rocky or gaseous.

The transit method has an additional benefit of being able to make conclusions about the compositions of any atmosphere surrounding the planet, an important factor in the search for life. This is achieved by analysing the spectrum of light which either passes straight through the atmosphere or is emitted by the planet, termed *transmission spectroscopy* and *emission spectroscopy*, respectively.

## 1.3 Habitability

### 1.3.1 Definition

The most widely accepted definition of the *habitable zone* is the range of orbital radii where liquid water may be present on the the surface of a planet (Kasting et al. 1993) (figure 1.2(a)). This definition is heavily influenced by the existence of life on Earth which universally requires liquid water to survive, and is therefore the most suitable definition within current knowledge. An earlier definition of habitability focused on the requirements for humans, highlighting the importance of temperature, and suggesting that at least 10% of the surface should have a mean annual temperature between 0°C and 30°C, and seasonal mean daily temperatures not to exceed -10°C or 40°C (Dole 1964).

The habitable zone of a planet is not constant in time because the luminosity

of a star changes during its lifetime; an increase in the luminosity with time increases the radius of the habitable zone. This gives rise to the concept of the *continuously habitable zone* which takes account of this process (Hart 1979, Kasting et al. 1993, Rushby et al. 2013) (figure 1.2(b)). The smaller stars have the longest lived continuously habitable zones due to their slow evolution.

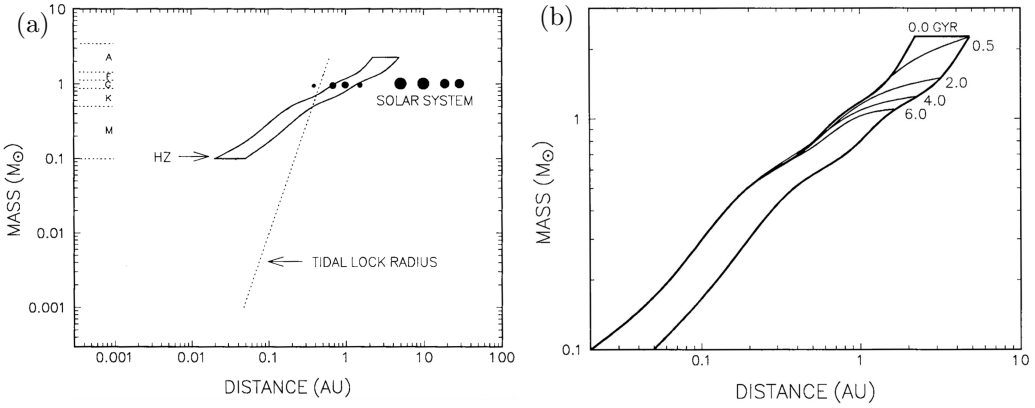


Figure 1.2: (a) The habitable zone width as a function of stellar mass, shown with solid line. The tidal locking radius is shown with dotted line, all planets in the habitable zone of M stars are expected to be tidally locked. The different stellar categories and planets of our solar system are shown. (b) The continuously habitable zone as a function of stellar mass, with varying lifetimes up to $6 \times 10^9$ years. Figures adapted from Kasting et al. (1993).

### 1.3.2 Boundaries

A limit for the inner edge of the habitable zone is the state of *runaway greenhouse*; the complete evaporation of the oceans. A more conservative limit, which is argued to be more relevant to habitability, is that of a *moist greenhouse*; the stratosphere becomes saturated with water vapour and photolysis results in a rapid escape of hydrogen to space (Kasting et al. 1993). The consideration of the effect of $H_2O$ clouds, which increase the albedo of the planet, provides a negative feedback and extends the inner limit of the habitable zone (Kasting 1988).

At the colder, outer edge of the habitable zone the most conservative limit is where $CO_2$ condenses to form clouds. A more generous limit is given by the *maximum greenhouse*; the radius at which a cloud free $CO_2$ atmosphere can sustain a surface temperature above 0°C (Kasting et al. 1993). Beyond these

limits, which are determined by $CO_2$, hydrogen could provide a greenhouse effect which is sufficient to maintain surface liquid water, which could significantly extend the outer limit of the habitable zone (Pierrehumbert & Gaidos 2011).

## 1.4 Climate modelling

### 1.4.1 Energy balance modelling

The simplest way to obtain an estimate for global mean surface temperature is to balance the radiation a planet receives and emits as a black body, however, this underestimates the global temperature, by approximately 30°C in the case of Earth, as it does not account for the greenhouse effect. This zero dimensional energy balance model can be modified to include a greenhouse factor, which depends on the radiative properties of the atmosphere, resulting in a warmer global mean temperature (Fowler 2011). Such models may be developed by introducing one dimension of variation; either vertical or horizontal.

A one dimensional model with variation in the vertical involves modelling the global atmosphere as a single column in which temperature is determined with dependence on height. Convective adjustment is included in the model to prevent exceeding the critical lapse rate, which is a balance between destabilising radiative transfer and stabilising convective transfer (Manabe & Strickler 1964). Such models are used to determine the limits of the habitable zone detailed above (Kasting et al. 1993).

Alternatively, variation with latitude allows for the inclusion of the large variation in received radiation between low and high latitudes, and allows for temperature to be determined with horizontal dependence. The poleward transport of energy resulting from large scale motions may be represented in the model, and the variation in albedo with latitude may also be included (Fowler 2011). Such models are useful in modelling planetary climate over particularly long time scales, for example variations in obliquity (Williams & Kasting 1997, Armstrong et al. 2014), where a more complex model would

be computationally infeasible.

An important factor to include, particularly at the outer edge of the habitable zone, is the carbonate-silicate cycle, which controls concentrations of atmospheric $CO_2$. It is a key consideration due to its dependence on temperature and implications for the greenhouse effect. Carbon is released into the atmosphere via volcanic activity, and removed via weathering processes and precipitation of carbonate materials to the sea floor. At higher (lower) temperatures weathering is increased (decreased) and more (less) $CO_2$ is removed from the atmosphere, this has the impact of cooling (warming) the climate and hence provides a negative feedback on the system. This effect may be parameterised in energy balance models through calculation of the change in weathering rate, and hence atmospheric $CO_2$ levels, with temperature (Williams & Kasting 1997).

### 1.4.2 General circulation modelling

More complex modelling is carried out using three dimensional general circulation models, which provide simulations of the atmosphere or ocean in isolation, or the coupled system. The focus of existing modelling studies of exoplanetary climates has been on the atmospheric component of the climate system. Simulations with different rotation periods found a change in dynamics at longer rotation periods due to the response of the Rossby radius of deformation (Del Genio & Suozzo 1987). The potential habitability of tidally locked planets was concluded from modelling the atmospheric circulation (Joshi et al. 1997), which was furthered to include variability in rotation period (Merlis & Schneider 2010) and the effect of an ocean, which was shown to warm the planet due to the increased greenhouse effect from water vapour (Edson et al. 2011). Further details of existing atmospheric studies will be given in the relevant chapters.

Some exoplanet studies using a coupled atmosphere-ocean general circulation model, with a dynamic sea ice model, provide analysis of the ocean component, concluding the importance of the ocean in limiting the thickness of sea ice on the dark side of a tidally locked planet (Hu & Yang 2014, Yang et al. 2014b). Modelling is developing toward the use of Earth

system models, which aim to include interactive physical, chemical and biological components, for example including an ice sheet model for the ice over continents to investigate the effect of different configurations of land mass on water storage as ice (Yang et al. 2014b). Here, modelling the response of the ocean to the different conditions of some possible exoplanet configurations will be the focus. The models used in this investigation range from a simple conceptual box model to a global coupled atmosphere-ocean general circulation model.

## 1.5 Ocean circulation and habitability

The habitable zone limits are introduced through one-dimensional arguments about planetary climate (§1.3.2), however, when considering the habitability of a planet the important factor is the regions of extremes in temperature where these limiting processes can occur. It is therefore important to consider how the climate system transports heat from the warmest to the coolest regions of a planet to make conclusions about the habitability of the planet. The large scale ocean circulation, alongside the atmosphere, is responsible for a significant proportion of this heat transport, and it is therefore an important consideration in the habitability of exoplanets. For example, a weaker overturning circulation in the ocean would transport less heat away from the warmest regions toward the coldest regions, increasing (decreasing) the temperature of the warmest (coolest) regions and reducing the size of the habitable zone.

## 1.6 Research aims

The importance of the ocean for global heat transport on Earth is well established (Trenberth & Caron 2001), which gives rise to the hypothesis that it is an important climatic feature on other terrestrial planets. With the focus of the majority of existing studies being on the influence of the atmosphere on the climate of exoplanets with many not including a dynamic ocean (Joshi et al. 1997, Merlis & Schneider 2010, Edson et al. 2011), here,

the question of the influence of the response of the ocean component of the climate system to changing conditions on the temperature distribution, and hence habitability, is investigated. In particular, it is hypothesised that the ocean can not be appropriately assumed to behave in an Earth-like manner, and that varying planetary and oceanic properties can have a significant impact on the global ocean heat transport on an exoplanet.

## 1.7 Thesis outline

Chapters 2 and 3 give the details of the box model and general circulation model used, respectively, including the results for an Earth-like configuration in each case. Chapter 4 investigates the impact of idealised land configurations on ocean circulation, and the key influencing features. Chapter 5 investigates the impact of changing ocean salinity, both increasing and decreasing levels from the Earth-like value, using both the box model and ocean general circulation model. Chapter 6 investigates the impact of changing the planetary rotation period, using scaling arguments and the ocean general circulation model. Chapter 7 investigates a tidally locked configuration with different land positions, using the coupled atmosphere-ocean general circulation model. The conclusions are presented in chapter 8.

# Chapter 2

# Box Model

A simple box model can be used to make predictions about the direction and magnitude of the buoyancy-driven component of the oceanic overturning circulation (Stommel 1961). The degree of simplification in the model allows for analytic solutions to be sought when appropriate approximations are made. The understanding of the solutions is furthered through a stability analysis of the model equations.

## 2.1 Model description

The model consists of two connected boxes, each containing a well-mixed water mass of spatially constant temperature, $T$, and salinity, $S$, which allow water to flow between them. The water in the boxes exchanges heat and salt with a surrounding reservoir, which represents the atmosphere where salt transfer is determined by freshwater exchange through evaporation and precipitation. These reservoirs are assumed to be large enough to maintain constant temperature, $T^*$, and effective salinity, $S^*$. The variables $T_1$, $S_1$, $T_2$, $S_2$ are the temperature and salinity values in boxes 1 and 2 respectively, with the associated reservoir values being denoted with an asterisk (figure 2.1). This is the original configuration (Stommel 1961) without the restriction of $T_1^* = -T_2^*$ and $S_1^* = -S_2^*$.

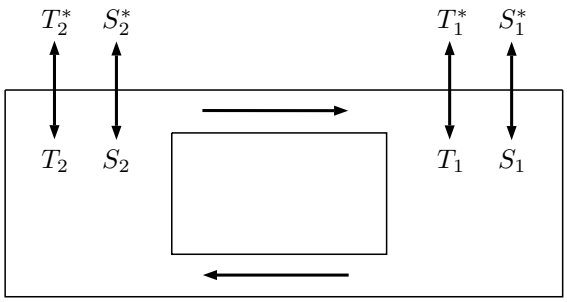


Figure 2.1: The Stommel box model with two boxes. Box 1 (2) represents the high (low) latitudes.

Water circulates around the system due to, and with strength proportional to, the difference between the density of water in each box, which results from differences in temperature and salinity. Warm and saline water fills one box, representative of the region of greatest evaporation and stellar radiation, with the opposite conditions in the other box. Since higher temperatures decrease density and greater salinities increase density, the differences in temperature and salinity force the circulation in opposing directions, hence, the buoyancy-driven circulation is a balance between these two differences. Note the difference in the driving mechanism of this model compared to what is found on Earth; on Earth the formation of deep water in isolated regions drives the overturning circulation, whereas the box model has no vertical stratification and instead the circulation is driven by a horizontal difference in density which is correlated to the strength of the meridional

overturning circulation (Thorpe et al. 2001).

When considering the application of this model to the North Atlantic, box 1 is taken to be the high latitudes and box 2 the equatorial regions. The low latitudes are warm and saline and the high latitudes are colder and fresher; $T_1 < T_2$ and $S_1 < S_2$. In this scenario, the forcing from the temperature difference dominates that of salinity, and so drives the circulation, with the salinity difference reducing the strength but not being sufficiently significant enough to dominate (Huang et al. 1992, Marotzke & Stone 1995, Rahmstorf 1996). This scenario results in sinking in the high latitudes and upwelling in the low latitudes, consistent with the observed overturning in the North Atlantic (figure 2.1). With sufficiently different conditions, the salinity forcing could be more influential and cause a circulation of opposite direction; sinking in the warmer regions and upwelling in the coldest.

## 2.2 Model equations

First considering just one box, the change with time of temperature, $T$, and salinity, $S$, is determined by the transfer of heat and salt between the box and the adjoining reservoir of constant temperature and salinity, $T^*$ and $S^*$, respectively. In the absence of inflow or outflow, this process is modelled by the equations

$$\frac{\mathrm{d}T}{\mathrm{d}t} = c(T^* - T), \tag{2.1}$$

$$\frac{\mathrm{d}S}{\mathrm{d}t} = d(S^* - S), \tag{2.2}$$

where the parameters $c$ and $d$ are inverse timescales for temperature and salinity forcing respectively (Stommel 1961).

Extending the model to contain two boxes requires the addition of an advection term, proportional to the differences between the boxes, in (2.1) and (2.2) to account for the flow between the boxes. The introduction of an equivalent pair of equations for the additional box is also required. This

gives the equation set

$$\frac{\mathrm{d}T_1}{\mathrm{d}t} = c(T_1^* - T_1) - \frac{2}{V}|\Psi|(T_1 - T_2), \tag{2.3}$$
$$\frac{\mathrm{d}T_2}{\mathrm{d}t} = c(T_2^* - T_2) - \frac{2}{V}|\Psi|(T_2 - T_1), \tag{2.4}$$
$$\frac{\mathrm{d}S_1}{\mathrm{d}t} = d(S_1^* - S_1) - \frac{2}{V}|\Psi|(S_1 - S_2), \tag{2.5}$$
$$\frac{\mathrm{d}S_2}{\mathrm{d}t} = d(S_2^* - S_2) - \frac{2}{V}|\Psi|(S_2 - S_1), \tag{2.6}$$

where $V$ is the volume of each box, $\Psi$ is the overturning streamfunction, and the factor of 2 arises from the presence of inflow and outflow due to the circulation.

The circulation is proportional to the density difference between the two boxes;

$$\Psi = A(\rho_1 - \rho_2), \tag{2.7}$$

where $\rho_1(T_1, S_1)$ and $\rho_2(T_2, S_2)$ are the densities of the water in boxes 1 and 2, respectively, and $A$ is a constant of proportionality representing the ease at which the water can circulate around the system. With the assumptions $T_1 < T_2$ and $S_1 < S_2$, a positive (negative) value of $\Psi$ is indicative of a temperature- (salinity-) driven circulation.

The steady state is found by solving equations (2.3)-(2.7) with $\mathrm{d}/\mathrm{d}t \equiv 0$;

$$c(T_1^* - T_1) - \frac{2}{V}|\Psi|(T_1 - T_2) = 0, \tag{2.8}$$
$$c(T_2^* - T_2) - \frac{2}{V}|\Psi|(T_2 - T_1) = 0, \tag{2.9}$$
$$d(S_1^* - S_1) - \frac{2}{V}|\Psi|(S_1 - S_2) = 0, \tag{2.10}$$
$$d(S_2^* - S_2) - \frac{2}{V}|\Psi|(S_2 - S_1) = 0, \tag{2.11}$$
$$\Psi = A(\rho_1 - \rho_2), \tag{2.12}$$
$$\rho = \rho(T, S). \tag{2.13}$$

When the density is a nonlinear function of temperature and salinity, equations (2.8)-(2.13) are solved to find the steady state solutions. The system (2.8)-(2.13) can be manipulated to obtain an equivalent system of just three equations if $\rho(T, S)$ can be approximated by a linear relation of

the form

$$\rho(T, S) = \rho_0(1 - \alpha T + \beta S), \tag{2.14}$$

where $\rho_0$ is a reference density, $\alpha$ is the coefficient of thermal expansion, and $\beta$ is the coefficient of haline contraction. This approximation is used in the original analysis of the box model for Earth (Stommel 1961), and has been shown to give qualitatively representative results of the Atlantic overturning circulation in more complex modelling (Roquet et al. 2015). The reduction of the system to three equations is possible because the linearisation allows the problem to be solved with the consideration of just the differences in temperature and salinity, defined as $\Delta T = T_2 - T_1$ and $\Delta S = S_2 - S_1$, respectively, rather than their absolute values. Similarly, it is only necessary to consider the differences in the temperature and salinity forcing, defined as $\Delta T^* = T_2^* - T_1^*$, and $\Delta S^* = S_2^* - S_1^*$.

With this approximation it is possible to obtain an expression for the overturning streamfunction in terms of the differences in forcing; $\Psi(\Delta T^*, \Delta S^*)$, which may then be used to find $\Delta T$ and $\Delta S$. The first step is to express $\Psi$ in terms of the differences in the temperature and salinity in the boxes;

$$\begin{aligned} \Psi &= A(\rho_1 - \rho_2) \\ &= A\rho_0(\alpha(T_2 - T_1) - \beta(S_2 - S_1)) \\ &= \gamma(\alpha\Delta T - \beta\Delta S), \end{aligned} \tag{2.15}$$

where $\gamma = A\rho_0$. Subtracting (2.3) from (2.4) gives

$$\begin{aligned} \frac{\mathrm{d}(T_2 - T_1)}{\mathrm{d}t} &= c(T_2^* - T_1^* - T_2 + T_1) - \frac{4}{V}|\Psi|(T_2 - T_1) \\ \Rightarrow \quad \frac{\mathrm{d}\Delta T}{\mathrm{d}t} &= c(\Delta T^* - \Delta T) - \frac{4}{V}|\Psi|\Delta T, \end{aligned} \tag{2.16}$$

and, similarly for salinity, subtracting (2.5) from (2.6) gives

$$\frac{\mathrm{d}\Delta S}{\mathrm{d}t} = d(\Delta S^* - \Delta S) - \frac{4}{V}|\Psi|\Delta S. \tag{2.17}$$

Setting $\mathrm{d}/\mathrm{d}t \equiv 0$ in (2.16) and (2.17) gives the equations for the steady state

system;

$$c(\Delta T^* - \Delta T) - \frac{4}{V}|\Psi|\Delta T = 0, \tag{2.18}$$

$$d(\Delta S^* - \Delta S) - \frac{4}{V}|\Psi|\Delta S = 0, \tag{2.19}$$

$$\Psi = \gamma(\alpha\Delta T - \beta\Delta S). \tag{2.20}$$

This system is equivalent to the steady state of that found in nondimensional form in the original analysis of the model (Stommel 1961).

A single equation for $\Psi$ is obtained by manipulating (2.18)-(2.20), as follows. Rearranging (2.18) gives

$$\begin{aligned} c\Delta T^* &= \Delta T\left(c + \frac{4|\Psi|}{V}\right) \\ \Rightarrow \quad \Delta T &= \frac{\Delta T^*}{1 + \frac{4|\Psi|}{cV}} \end{aligned} \tag{2.21}$$

and, similarly, rearranging (2.19) gives

$$\Delta S = \frac{\Delta S^*}{1 + \frac{4|\Psi|}{dV}}. \tag{2.22}$$

Substituting (2.21) and (2.22) into (2.20) gives

$$\Psi = \frac{\gamma\alpha\Delta T^*}{1 + \frac{4|\Psi|}{cV}} - \frac{\gamma\beta\Delta S^*}{1 + \frac{4|\Psi|}{dV}}. \tag{2.23}$$

By defining the parameters

$$A_1 = \gamma\alpha\Delta T^*, \tag{2.24}$$

$$A_2 = \gamma\beta\Delta S^*, \tag{2.25}$$

$$A_3 = \frac{4}{cV}, \tag{2.26}$$

$$A_4 = \frac{4}{dV}, \tag{2.27}$$

(2.23) is written more neatly as

$$\Psi = \frac{A_1}{1 + A_3|\Psi|} - \frac{A_2}{1 + A_4|\Psi|}. \tag{2.28}$$

Further rearrangement of (2.28) shows the cubic nature of the system;

$$\Psi(1 + A_3|\Psi|)(1 + A_4|\Psi|) = A_1(1 + A_4|\Psi|) - A_2(1 + A_3|\Psi|) \tag{2.29}$$

$$\Rightarrow \quad \Psi + A_3\Psi|\Psi| + A_4\Psi|\Psi| + A_3A_4\Psi^3 = A_1 + A_1A_4|\Psi| - A_2 - A_2A_3|\Psi|, \tag{2.30}$$

$$\Rightarrow \quad \Psi^3 + \left(\frac{1}{A_3} + \frac{1}{A_4}\right)\Psi|\Psi| + \left(\frac{A_2}{A_4} - \frac{A_1}{A_3}\right)|\Psi| + \frac{1}{A_3A_4}\Psi + \frac{A_2 - A_1}{A_3A_4} = 0. \tag{2.31}$$

Expressions for the temperature and salinity differences, (2.21) and (2.22), in terms of the parameters (2.24)-(2.27), are

$$\Delta T = \frac{A_1}{\gamma\alpha(1 + A_3|\Psi|)} \quad \text{and} \quad \Delta S = \frac{A_2}{\gamma\beta(1 + A_4|\Psi|)}, \tag{2.32}$$

respectively, which are used to find the corresponding temperature and salinity differences after obtaining a solution for $\Psi$ using (2.28).

There are two possible directions of circulation, which are most easily seen by separately setting either the value of salinity (figure 2.2(a)), or temperature (figure 2.2(b)), forcing of each box to be equal; $\Delta S^* = 0$ and $\Delta T^* = 0$, resulting in $\Delta S = 0$ and $\Delta T = 0$, respectively. When salinity (temperature) is constant the second (first) term of (2.28) is zero, giving $\Psi > 0$ ($\Psi < 0$) which is indicative of a temperature- (salinity-) driven circulation.

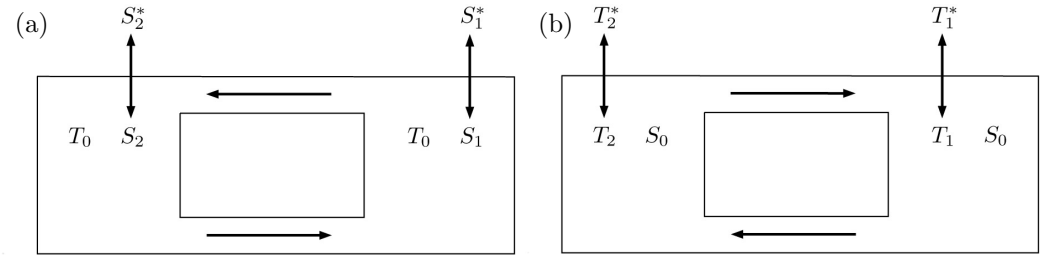


Figure 2.2: (a) Positive ($\Psi > 0$) and (b) negative ($\Psi < 0$) circulation regimes, where $T_0$ and $S_0$ are constants.

Earth-like values are used as the default for the different parameters in the box model (table 2.1), and are henceforth used throughout the model analysis both here and in following chapters unless otherwise stated.

| Description | Parameter | Value | Unit |
|---|---|---|---|
| Reference density | $\rho_0$ | $1 \times 10^3$ | $\mathrm{kg\,m^{-3}}$ |
| Coefficient of thermal expansion | $\alpha$ | $1.7 \times 10^{-4}$ | $^\circ\mathrm{C}^{-1}$ |
| Coefficient of haline contraction | $\beta$ | $7.8 \times 10^{-4}$ | $\mathrm{kg\,g^{-1}}$ |
| Constant of proportionality ($\Psi \propto \Delta\rho$) | $A$ | $1 \times 10^7$ | $\mathrm{m^6\,kg^{-1}\,s^{-1}}$ |
| $A\rho_0$ | $\gamma$ | $1 \times 10^{10}$ | $\mathrm{m^3\,s^{-1}}$ |
| Volume of a box | $V$ | $1 \times 10^{15}$ | $\mathrm{m^3}$ |
| Inverse temperature forcing timescale | $c$ | $6.4 \times 10^{-8}$ | $\mathrm{s^{-1}}$ |
| Inverse salinity forcing timescale | $d$ | $2.1 \times 10^{-8}$ | $\mathrm{s^{-1}}$ |
| Temperature forcing difference | $\Delta T^*$ | 15 | $^\circ\mathrm{C}$ |
| Salinity forcing difference | $\Delta S^*$ | 1 | $\mathrm{g\,kg^{-1}}$ |
| $\gamma\alpha\Delta T^*$ | $A_1$ | $2.55 \times 10^7$ | $\mathrm{m^3\,s^{-1}}$ |
| $\gamma\beta\Delta S^*$ | $A_2$ | $7.8 \times 10^6$ | $\mathrm{m^3\,s^{-1}}$ |
| $4/cV$ | $A_3$ | $6.2 \times 10^{-8}$ | $\mathrm{s\,m^{-3}}$ |
| $4/dV$ | $A_4$ | $1.9 \times 10^{-7}$ | $\mathrm{s\,m^{-3}}$ |

Table 2.1: Parameters in the box model and their default values.

## 2.3 Earth-like solutions

The density of water is determined by an appropriate equation of state $\rho(S,T)$, which is an empirical relationship depending on temperature and salinity. In the case of the oceans on Earth, one example is

$$\begin{aligned}\rho(S,T) = \rho_w(T) &+ S(0.824493 - 4.0899 \times 10^{-3}T + 7.6438 \times 10^{-5}T^2 \\ &- 8.2467 \times 10^{-7}T^3 + 5.3875 \times 10^{-9}T^4) \\ &+ S^{3/2}(-5.72466 \times 10^{-3} + 1.0227 \times 10^{-4}T \\ &- 1.6546 \times 10^{-6}T^2) + 4.8314 \times 10^{-4}S^2, \end{aligned} \tag{2.33}$$

where temperature is in $^\circ$C and salinity is on the Practical Salinity Scale, and

$$\begin{aligned}\rho_w(T) = 999.842594 &+ 6.793952 \times 10^{-2}T - 9.095290 \times 10^{-3}T^2 \\ &+ 1.001685 \times 10^{-4}T^3 - 1.120083 \times 10^{-6}T^4 + 6.536332 \times 10^{-9}T^5 \end{aligned} \tag{2.34}$$

is the density of pure water (Gill 1982, p.599).

A linear approximation is found by using a Taylor expansion of (2.33) about

$T = 10°\mathrm{C}$ and $S = 35$, which are average values of temperature and salinity in the oceans on Earth, to find appropriate values for the parameters $\rho_0$, $\alpha$ and $\beta$ in the linearised form (2.14);

$$\begin{aligned} \rho_0 &= 1000\,\mathrm{kg\,m^{-3}}, \\ \alpha &= 1.7 \times 10^{-4}\,{}^{\circ}\mathrm{C}^{-1}, \\ \beta &= 7.8 \times 10^{-4}\,\mathrm{kg\,g^{-1}}, \end{aligned}$$

to 2 significant figures accuracy. On simultaneously plotting contours of the full equation of state (2.33) and linearised form (2.14) with these values of $\rho_0$, $\alpha$ and $\beta$, it is seen graphically that this is a reasonable approximation to make in the Earth-like case (figure 2.3). The maximum error of this

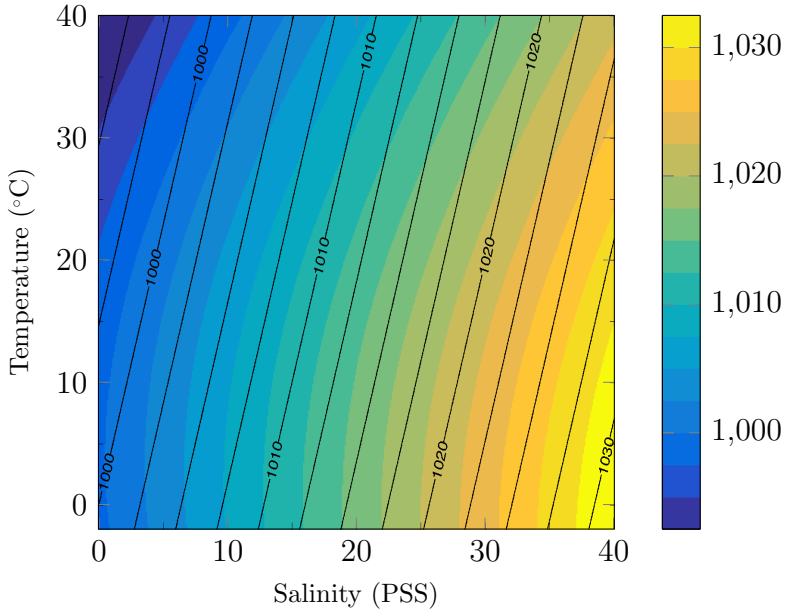


Figure 2.3: Contour plot of the density of seawater ($\mathrm{kg\,m^{-3}}$) as a function of temperature (°C) and salinity (PSS). Coloured contours are of the full equation of state (2.33), and the overlaid black contours are the linearised approximation.

approximation in the domain shown is 0.27%, which occurs at the maximum value of temperature and salinity; $T = 40°\mathrm{C}$, $S = 40$ (figure 2.4). Note that the error is not minimised at the point of linearisation due to rounding of $\rho_0$, $\alpha$ and $\beta$.

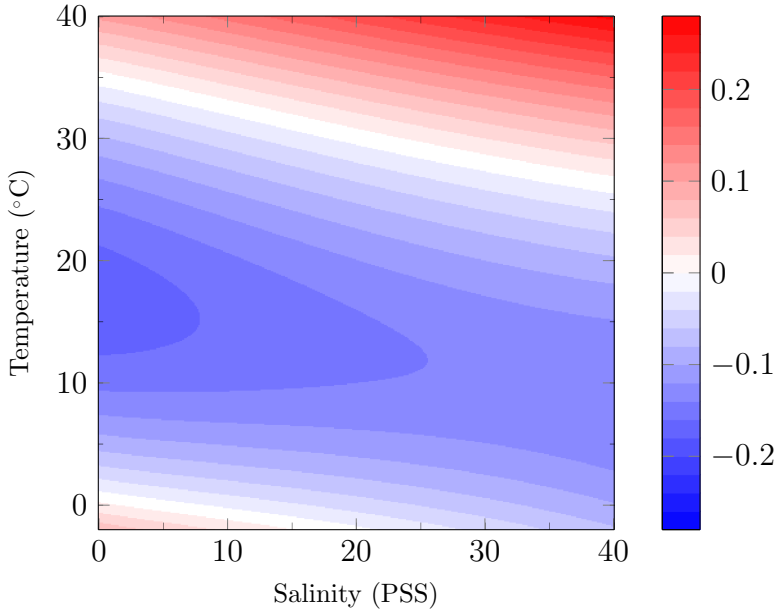


Figure 2.4: Contour plot of the percentage error of the linearisation of the equation of state for seawater, as a function of temperature (°C) and salinity (PSS).

When employing a linearised equation of state, solutions are sought to (2.28);

$$\Psi = \frac{A_1}{1 + A_3|\Psi|} - \frac{A_2}{1 + A_4|\Psi|}.$$

The solutions to this equation, found using the computer algebra system *Maple*, are investigated by varying one of the parameters $A_1$-$A_4$ in turn whilst holding the remaining three constant. In analysing the following results it is important to recall that a positive (negative) value for $\Psi$ is indicative of a temperature (salinity) driven circulation (figure 2.2).

First consider varying the parameters $A_3$ and $A_4$, related to the timescales of heat and salinity transfer, respectively, between the box and adjacent reservoir. As $A_3$ increases, equivalent to lengthening the time scale for heat transfer and weakening the temperature forcing, when in a temperature-driven regime there is a decrease in the magnitude of $\Psi$, whilst remaining in a positively circulating regime (figure 2.5(a,b)). For a smaller value of $A_3$ the temperature in each box is forced more strongly to the reservoir temperature values; $\Delta T \to \Delta T^*$. This results in a larger temperature difference between the boxes; an increase in $\Delta T$, and hence the overturning circulation $\Psi$ is more strongly driven by the temperature difference. By the reverse of this argument, at longer time scales of

heat transfer, $\Delta T$ is smaller and $\Psi$ decreases. By an equivalent physical justification as for $A_3$, an increase in $A_4$ results in a more salinity driven circulation and a decrease in $\Psi$, again remaining in a temperature driven regime for the realistic range of values considered (figure 2.6(a,b)).

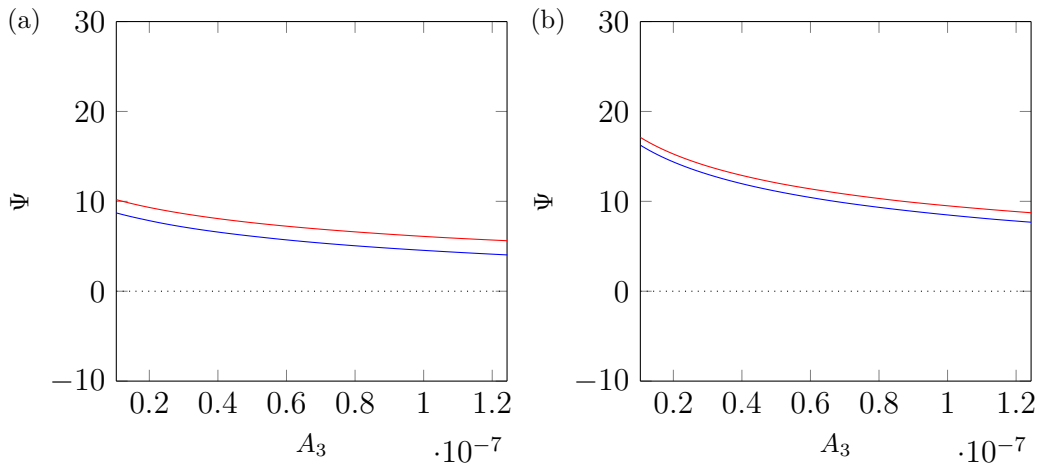


Figure 2.5: Plots showing the effect of varying $A_3$ ($\mathrm{s\,m^{-3}}$) on the overturning circulation $\Psi$ (Sv) for Earth range salinity, at different values of the reservoir temperatures and salinities; (a) $\Delta T^* = 15°\mathrm{C}$, (b) $\Delta T^* = 25°\mathrm{C}$, $\Delta S^* = 1$ (red), $\Delta S^* = 2$ (blue).

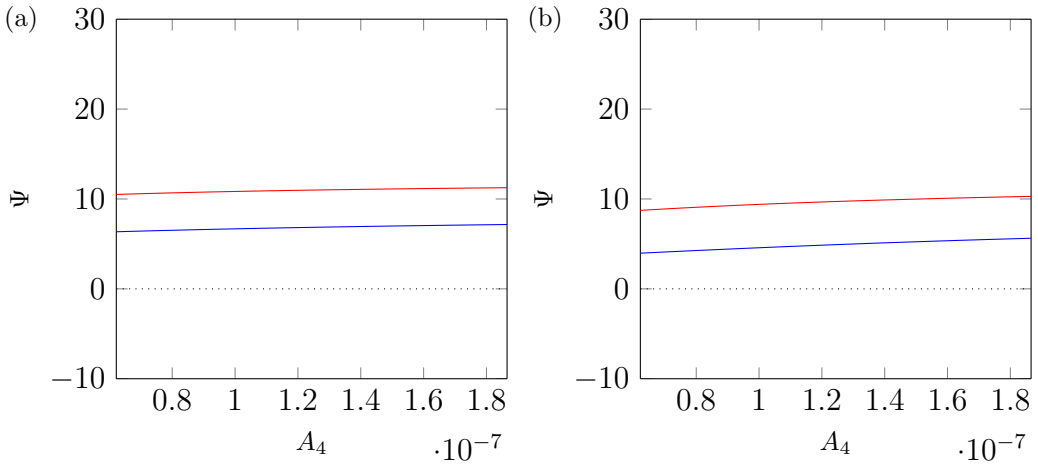


Figure 2.6: Plots showing the effect of varying $A_4$ ($\mathrm{s\,m^{-3}}$) on the overturning circulation $\Psi$ (Sv) for Earth range salinity, at different values of the reservoir temperatures and salinities; (a) $\Delta S^* = 1$, (b) $\Delta S^* = 2$, $\Delta T^* = 15°\mathrm{C}$ (blue), $\Delta T^* = 25°\mathrm{C}$ (red).

Varying the parameters $A_1$ and $A_2$ is equivalent to varying the forcing by the difference in temperature, $\Delta T^*$, and salinity, $\Delta S^*$, respectively. These variables are not entirely independent, the important factor is the ratio of

the values of $\alpha\Delta T$ and $\beta\Delta S$, which are in large part determined by $\Delta T^*$ and $\Delta S^*$, respectively. For example, increasing the temperature difference has the same effect on the behaviour of the solution as decreasing the salinity difference. This may be seen on inspection of (2.28), and can also be concluded by observing the symmetrical behaviour between the solutions when $A_1$ (figure 2.7) and $A_2$ (figure 2.8) are varied. Hence, the following investigation will focus on the variation of $A_2$, which can be easily translated to make similar arguments regarding $A_1$.

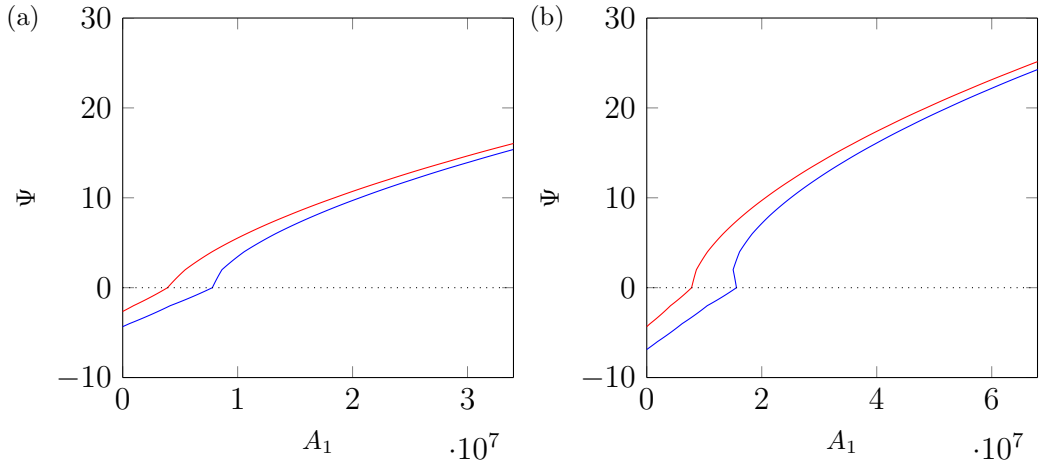


Figure 2.7: Plots showing the effect of varying $A_1$ ($m^3\,s^{-1}$) on the overturning circulation $\Psi$ (Sv) for Earth range salinity, at different values of the reservoir salinities and constant $\gamma$ ($m^3\,s^{-1}$); (a) $\gamma = 5 \times 10^9$, (b) $\gamma = 10^{10}$, $\Delta S^* = 1$ (red), $\Delta S^* = 2$ (blue). The range of $A_1$ is equivalent to varying $\Delta T^*$ between 0 and 40°C.

The behaviour of the solution when varying the salinity forcing (figure 2.8) shows the well established curve with a range of values over which multiple solutions occur (Rahmstorf 1995, Rahmstorf et al. 2005). Negative solutions, indicative of a salinity-driven circulation, occur at larger values of $A_2$ which correspond to greater differences in salinity, and result in a circulation opposite in direction to that observed on Earth. In the oceans on Earth, the most dense water and hence deep water formation occurs where the water is coldest, indicating a temperature-driven circulation; warmer water travels poleward at the surface of the ocean. In the alternative regime the water sinks in the warmest, most saline area of the ocean, filling the deep ocean with warm water which resurfaces in the coldest regions.

On comparing two solutions for different values of $\Delta T^*$, it is seen that in

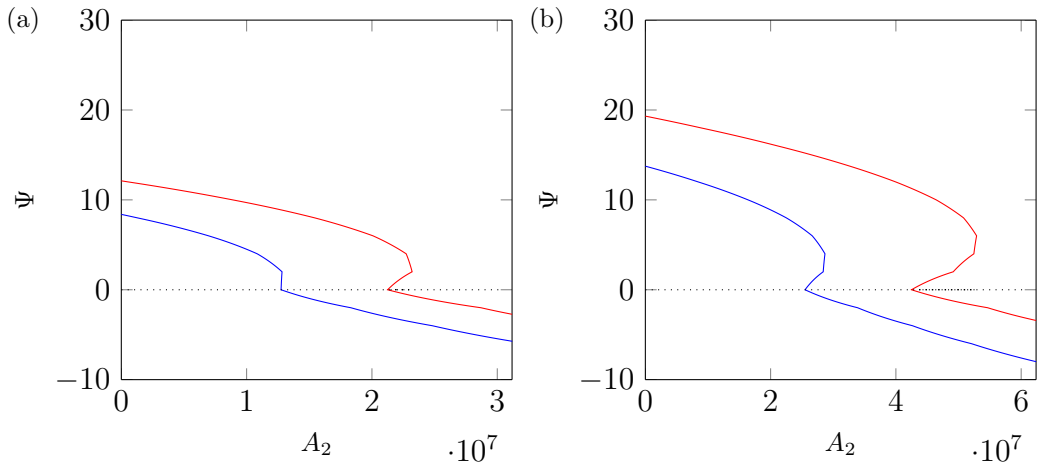


Figure 2.8: Plots showing the effect of varying $A_2$ ($m^3\,s^{-1}$) on the overturning circulation $\Psi$ (Sv) for Earth range salinity, at different values of the reservoir salinities and constant $\gamma$ ($m^3\,s^{-1}$); (a) $\gamma = 5 \times 10^9$, (b) $\gamma = 10^{10}$, $\Delta T^* = 15$ (blue), $\Delta T^* = 25°C$ (red). The range of $A_2$ is equivalent to varying $\Delta S^*$ between 0 and 8.

both cases increasing the value of $A_2$ gives the same pattern of behaviour, but the circulation is temperature-driven up to a larger value of $A_2$ for the greater value of $\Delta T^*$ (figure 2.8). This is physically expected as a larger temperature difference gives a stronger temperature forcing, and hence a larger salinity difference is required to overcome this forcing and reverse the direction of circulation. At this stronger temperature forcing there is also a larger range of values of $A_2$ over which multiple solutions occur.

Comparing the results when varying $A_1$ (figure 2.7) and $A_2$ (figure 2.8) shows that the value of $\gamma$ is also important for the behaviour of the solution. With the larger value of $\gamma$ the magnitudes of $\Psi$ are greater in all cases, which is clearly predicted by (2.20). The parameter $\gamma$ is indicative of the physical constraints of movement of water between the two boxes. Hence, a larger value of $\gamma$ represents more ease of movement between the boxes, which results in a stronger circulation. In addition, for larger $\gamma$, the range of values where multiple solutions exist is extended for larger values of $A_2$. However, the salinity difference at which the circulation reverses is independent of $\gamma$ because $\gamma$ solely influences the magnitude of $\Psi$ and has no effect on the value at which it changes sign.

From varying each of the four parameters $A_1$-$A_4$, it is concluded that the effect of varying the parameters $A_3$ and $A_4$ is small relative to both the

magnitude of $\Psi$, and the dependence of the solutions on $A_1$ and $A_2$. Hence, it is concluded that $A_3$ and $A_4$, which control the timescale for the temperature and salinity forcing, respectively, are not the most crucial parameters in the problem and hence are fixed at their typical values

$$\left.\begin{array}{l} c = \frac{1}{6\times 30\times 86400} \\ d = \frac{1}{18\times 30\times 86400} \\ V = 10^{15} \end{array}\right\} \Longrightarrow \begin{array}{l} A_3 = 6.2\times 10^{-8} \\ A_4 = 1.9\times 10^{-7} \end{array}$$

throughout all following work using the box model.

## 2.4 Stability analysis

When varying the forcing in the model there exist multiple solutions for certain combinations of parameters, this is most clearly seen when investigating the dependence on salinity forcing (figure 2.8). A linear stability analysis of the governing equations (2.15)-(2.17) shows that the middle branch of the solution in these regions is unstable, leaving two stable solutions of opposite sign for a given set of parameters (Dijkstra 2005).

Let

$$\Delta T = \overline{\Delta T} + \widetilde{\Delta T} \tag{2.35}$$

$$\Delta S = \overline{\Delta S} + \widetilde{\Delta S} \tag{2.36}$$

$$\begin{aligned} \Psi &= \overline{\Psi} + \widetilde{\Psi} \\ &= \gamma\Big(\alpha\Big(\overline{\Delta T} + \widetilde{\Delta T}\Big) - \beta\Big(\overline{\Delta S} + \widetilde{\Delta S}\Big)\Big), \end{aligned} \tag{2.37}$$

where an overbar represents a time mean quantity and a tilde the small perturbation from that time mean. Substituting these into (2.16) and (2.17)

gives

$$\frac{\mathrm{d}\Big(\widetilde{\Delta T}\Big)}{\mathrm{d}t} = c\Big(\Delta T^* - \Big(\overline{\Delta T} + \widetilde{\Delta T}\Big)\Big) - \frac{4\gamma}{V}\Big|\alpha\Big(\overline{\Delta T} + \widetilde{\Delta T}\Big) - \beta\Big(\overline{\Delta S} + \widetilde{\Delta S}\Big)\Big|\Big(\overline{\Delta T} + \widetilde{\Delta T}\Big), \tag{2.38}$$

$$\frac{\mathrm{d}\Big(\widetilde{\Delta S}\Big)}{\mathrm{d}t} = d\Big(\Delta S^* - \Big(\overline{\Delta S} + \widetilde{\Delta S}\Big)\Big) - \frac{4\gamma}{V}\Big|\alpha\Big(\overline{\Delta T} + \widetilde{\Delta T}\Big) - \beta\Big(\overline{\Delta S} + \widetilde{\Delta S}\Big)\Big|\Big(\overline{\Delta S} + \widetilde{\Delta S}\Big). \tag{2.39}$$

First assuming $\Psi > 0$, so that $|\Psi| = \Psi$, and neglecting products of the perturbation quantities, gives the linear time evolution equations for the perturbations as

$$\begin{aligned}\frac{\mathrm{d}\widetilde{\Delta T}}{\mathrm{d}t} &= -c\widetilde{\Delta T} - \frac{4\gamma}{V}\Big(\Big(\alpha\widetilde{\Delta T} - \beta\widetilde{\Delta S}\Big)\overline{\Delta T} + \Big(\alpha\overline{\Delta T} - \beta\overline{\Delta S}\Big)\widetilde{\Delta T}\Big)\\ &= \Big(-c - \frac{4\gamma}{V}\Big(2\alpha\overline{\Delta T} - \beta\overline{\Delta S}\Big)\Big)\widetilde{\Delta T} + \Big(\frac{4\gamma}{V}\beta\overline{\Delta T}\Big)\widetilde{\Delta S}, \qquad (2.40)\\ \frac{\mathrm{d}\widetilde{\Delta S}}{\mathrm{d}t} &= -d\widetilde{\Delta S} - \frac{4\gamma}{V}\Big(\Big(\alpha\widetilde{\Delta T} - \beta\widetilde{\Delta S}\Big)\overline{\Delta S} + \Big(\alpha\overline{\Delta T} - \beta\overline{\Delta S}\Big)\widetilde{\Delta S}\Big)\\ &= \Big(-\frac{4\gamma}{V}\alpha\overline{\Delta S}\Big)\widetilde{\Delta T} + \Big(-d - \frac{4\gamma}{V}\Big(2\beta\overline{\Delta S} + \alpha\overline{\Delta T}\Big)\Big)\widetilde{\Delta S}. \qquad (2.41)\end{aligned}$$

These equations have solutions of the form

$$\widetilde{\Delta T} = \widehat{\Delta T}\mathrm{e}^{\lambda t}, \tag{2.42}$$

$$\widetilde{\Delta S} = \widehat{\Delta S}\mathrm{e}^{\lambda t}, \tag{2.43}$$

where $\widehat{\Delta T}$ and $\widehat{\Delta S}$ are constants, and the growth factor $\lambda$ may be complex. The sign of $\mathrm{Re}(\lambda) := \lambda_r$ indicates the stability of the solution. When $\lambda_r > 0$ ($\lambda_r < 0$) the perturbation exhibits exponential growth (decay) in time and hence the solution is unstable (stable).

Substituting (2.42) and (2.43) into (2.40) and (2.41) gives the matrix equation

$$\begin{pmatrix} -c - \frac{4\gamma}{V}(2\alpha\overline{\Delta T} - \beta\overline{\Delta S}) & \frac{4\gamma}{V}\beta\overline{\Delta T} \\ -\frac{4\gamma}{V}\alpha\overline{\Delta S} & -d - \frac{4\gamma}{V}(\alpha\overline{\Delta T} - 2\beta\overline{\Delta S}) \end{pmatrix}\begin{pmatrix}\widehat{\Delta T}\\ \widehat{\Delta S}\end{pmatrix} = \lambda\begin{pmatrix}\widehat{\Delta T}\\ \widehat{\Delta S}\end{pmatrix}; \tag{2.44}$$

an eigenvalue problem requiring

$$\begin{vmatrix} -c - \frac{4\gamma}{V}(2\alpha\overline{\Delta T} - \beta\overline{\Delta S}) - \lambda & \frac{4\gamma}{V}\beta\overline{\Delta T} \\ -\frac{4\gamma}{V}\alpha\overline{\Delta S} & -d - \frac{4\gamma}{V}(\alpha\overline{\Delta T} - 2\beta\overline{\Delta S}) - \lambda \end{vmatrix} = 0 \tag{2.45}$$

for nontrivial solutions to exist. The same approach applied to the case when $\Psi < 0$, so that $|\Psi| = -\Psi$, gives

$$\begin{vmatrix} -c + \frac{4\gamma}{V}(2\alpha\overline{\Delta T} - \beta\overline{\Delta S}) - \lambda & -\frac{4\gamma}{V}\beta\overline{\Delta T} \\ \frac{4\gamma}{V}\alpha\overline{\Delta S} & -d + \frac{4\gamma}{V}(\alpha\overline{\Delta T} - 2\beta\overline{\Delta S}) - \lambda \end{vmatrix} = 0 \tag{2.46}$$

The stability of the solutions presented above for varying $A_2$ is calculated by solving (2.45) and (2.46) with the specific values for each case. These calculations show that there is one unstable solution in the range where multiple solutions exist. This is always the mid-valued solution, which leaves two stable solutions of opposing sign in these regions (figure 2.9).

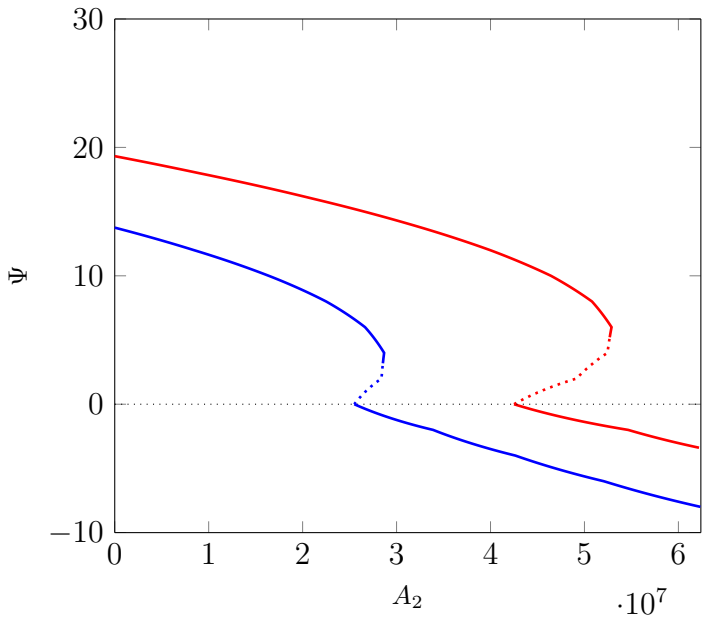


Figure 2.9: The stability of the solutions when varying $A_2$ (figure 2.8(b)); stable solutions are indicated by solid lines, and unstable solutions by dotted lines.

## 2.5 Alternative configurations

The box model may be extended and adapted from the original 2-box configuration (Stommel 1961) to add complexity and increase the applicability for more specific scenarios. For example, three boxes could be used to model interhemispheric circulation; one representing the high northern latitudes, one the equatorial regions, and one the high southern latitudes. An equivalent set of equations to those for the 2-box model may be derived and analysed to find the steady states of such a 3-box system. One of the four possible circulation regimes in this configuration consists of a temperature-driven cell in each hemisphere (figure 2.10), with a second symmetric solution consisting of two salinity-driven circulations and the possibility of stable pole-to-pole circulations of either direction (Vallis 2006, p.645)

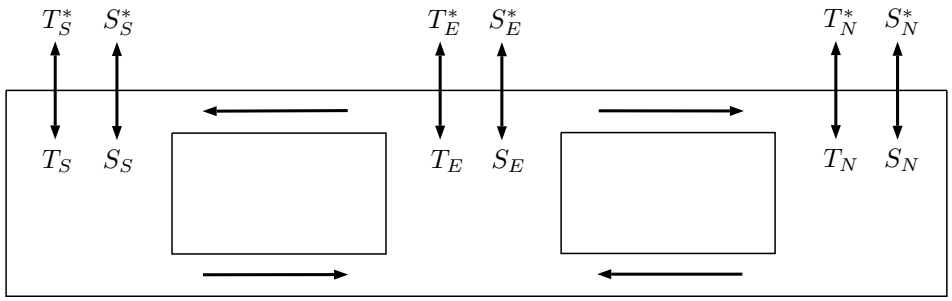


Figure 2.10: Sketch of a 3-box model configuration. Shown with boxes representing high northern latitudes, equatorial regions and high southern latitudes, indicated by $N$, $E$ and $S$, respectively.

A similar three-box configuration has been applied to the Meridional Overturning Circulation (MOC) on Earth (Rooth 1982). In this study the connections are chosen to allow only for a pole-to-pole circulation by limiting the deep connection to a direct link between the two polar boxes, the forcing is chosen to be symmetric about the centre box, and the circulation is controlled by the density difference between the two polar boxes. In this configuration there are only two possible circulation regimes, of opposite direction, similar to the two-box model.

The model may also be extended in alternative configurations, for example using separate boxes for the deep ocean and surface layer in the tropics,

giving four boxes in a 1-2-1 configuration. Again, the possible circulations can be determined by choosing the pattern for the open connections between the boxes, for example restricting any flow between the deep and shallow box in the tropics forces a pole-to-pole circulation. The solutions in this configuration show the same behaviour as seen in the 2-box model; regions with three solutions, two stable and one unstable, with hysteresis (Rahmstorf 1996). Other variations include two levels of boxes at all latitudes, for example in a $2 \times 2$ or $3 \times 2$ configuration. Between these two cases, the increase from four to six boxes introduces an additional four regimes, which are concluded to be less crucial than the two dominant pole-to-pole circulations (Huang et al. 1992).

To further develop an ocean box model it is possible to include additional boxes to represent the atmosphere and hence produce a coupled box model of the atmosphere-ocean system. The simplest such configuration has two ocean boxes and two atmosphere boxes and gives the same physical behaviour as the two-box model (Marotzke & Stone 1995). In a similar way to the ocean-only models, such coupled versions can be advanced by the introduction of further boxes, for example splitting the deep ocean and surface layers and modelling cross-hemispheric flow by using three boxes in latitude (Birchfield 1989, Birchfield et al. 1990).

## 2.6 GCM results

Despite the dramatic advances in computing since the development of the box model, which have allowed for the implementation of general circulation models (GCMs), this simple model is used alongside these modern climate models as a tool in the understanding and analysis of the core behaviour of the MOC. The existence of multiple steady states for a given forcing is a phenomenon which is observed in GCMs, in ocean-only simulations (Bryan 1986, Marotzke & Willebrand 1991) as well as coupled models (Manabe & Stouffer 1988, Hawkins et al. 2011), alongside the same pattern of hysteresis on varying freshwater forcing as in the box model solutions (Rahmstorf 1995).

As in the analysis of the box model, it is found that the salinity forcing is

key in determining the regime of circulation in GCMs. The introduction of salinity perturbations in GCMs can instigate the transition between circulation regimes, for example, a finite-amplitude anomaly transforms a hemispherically symmetric circulation into an asymmetric, pole-to-pole regime (Bryan 1986). With respect to Earth, there is particular interest in the discussion of the potential effects of a significant change in the amount of freshwater discharge in the North Atlantic, where deep water formation primarily occurs, and the resulting impact on the buoyancy-driven ocean circulation (Rahmstorf 1995, Bryden et al. 2005, Rahmstorf et al. 2015).

In terms of the box model an input of freshwater at high latitudes, for example from increased precipitation and the melting of ice sheets, is equivalent to increasing the salinity difference which forces the circulation towards a salinity-driven regime. If this occurs whilst in a temperature-driven regime, which is the state for present day Earth, the system enters the range where unstable solutions exist, resulting in rapid changes in regime. The hysteresis in the system suggests that these changes cannot be reversed by returning to the initial forcing (Rahmstorf et al. 2005). The physical implications of this would present as a sudden shutdown of the thermohaline circulation and, in such a scenario, the need for a significant decrease in salinity forcing, beyond that of the present day, to return the circulation to the initial regime. This phenomenon, predicted by the box model, is observed in the results from a range of GCMs (Rahmstorf 1995, Rahmstorf et al. 2005), including a modern coupled atmosphere-ocean GCM (Hawkins et al. 2011).

The stability of the ocean overturning circulation has a particular sensitivity to freshwater input, through the positive salt-advection feedback in the system (Stommel 1961, Rahmstorf 1996). The mechanism of this feedback is fuelled by an input of freshwater in the high latitudes, discussed above, which has the effect of increasing the salinity difference and slowing the overturning circulation. With a weaker overturning less salt is transported from the saltier low latitude box to the fresher high latitude box and therefore the salinity difference is further increased and the overturning further weakened, creating a positive feedback. Conversely, if the circulation is acting to move salt away from the high latitude box then a weaker circulation increases the salinity of the high latitude box, decreasing the salinity gradient and promoting a recovery of the overturning circulation.

Motivated by the salt-advection feedback, on Earth the transport of freshwater into the Atlantic ocean basin, the primary location of deep water formation, is used as a measure of the stability of the Atlantic meridional overturning circulation. This is analysed by calculating the transport of freshwater across the southern boundary of the Atlantic in GCMs; a negative value is indicative of salt being transported into the Atlantic and therefore a positive feedback occurs, whereas a positive value suggests a recovery of the circulation following a weakening would occur (Hawkins et al. 2011). On making the high latitudes increasingly fresher in a GCM it is found that the sign of the freshwater transport into the Atlantic changes from positive to negative, before a collapse of the circulation occurs, which is indicative of the system becoming unstable (Hawkins et al. 2011).

## 2.7 Summary

A simple two-box model can be employed to make conclusions about the direction and magnitude of the buoyancy-driven component of large-scale ocean circulation. Here, the working and analysis of the well-established solutions for an Earth-like configuration have been presented. The knowledge and computing technology which has developed since the original application of such box models has allowed for huge advances in detailed modelling of ocean circulation, in particular the development of complex general circulation models. However, despite the primitive nature of the box model it is still a useful tool in the understanding and analysis of the fundamental behaviour of buoyancy-driven ocean circulation. Through varying different parameters in the system, the key values are found to be the differences in temperature and salinity forcing and the balance between them; this has the greatest significance in determining both the direction and magnitude of the circulation. On application of the model to an Earth-like scenario, it is shown to produce the fundamental characteristics of the circulation in the oceans on Earth. The simple and accessible nature of the box model makes it particularly useful in the primary investigation of buoyancy-driven ocean circulation in some of the unknown conditions which may occur on exoplanets. For example when the balance between thermal and saline forcing differs from an Earth-like scenario, which will be investigated later.

# Chapter 3

# MOMA

The complexity and applicability of modelling ocean circulation is advanced from a box model by employing numerical methods to solve a more comprehensive system of equations. An ocean general circulation model (OGCM) which solves equations for momentum, temperature and salinity, is employed for this purpose. The model incorporates the key physical processes which drive the large-scale global ocean circulation.

## 3.1 Model description

The OGCM used is the Modular Ocean Model adapted for use with array processors (MOMA) (Bryan 1969, Webb 1996). The model solves the primitive equations (Bryan 1969); the Navier-Stokes equations for momentum, advection-diffusion equations for heat and salt, and an equation of state for density. The model is configured at a relatively coarse resolution, which limits the computational expense of running the model, and hence allows for the execution of a wide range of sensitivity studies of a global ocean. Relatively small scale motion, which cannot be resolved at the coarse resolution of this model, is parameterised using eddy viscosity and eddy diffusivity. Conclusions are made about the ocean circulation and tracer distribution through the computation and subsequent analysis of values of velocity, free surface height, temperature and salinity.

## 3.2 Model equations

The planet is assumed to be spherical with radius $a$ and rotation rate $\Omega$. A spherical coordinate geometry is used; $\lambda$ in the positive eastward direction, $\phi$ in the positive northward direction, and $z$ in the positive vertical direction. Due to the implementation of the thin shell approximation, that is to assume the ocean depth is small relative to the radius of the planet, $z$ is used in place of the conventional $r$ coordinate of spherical geometry. The velocity components in the three directions are denoted $u$, $v$ and $w$, respectively.

There are some approximations made to simplify the model equations, and hence decrease computational expense. These are the incompressibility assumption, the Boussinesq approximation, and hydrostatic balance. Respectively, these mean conservation of mass reduces to conservation of volume, differences in density are negligible everywhere but in the buoyancy term, and vertical velocities are dominated by the balance of gravitational acceleration and pressure gradients.

### 3.2.1 Continuous equations

The incompressibility condition in spherical coordinates with the thin shell approximation is

$$\frac{1}{a\cos\phi}\frac{\partial u}{\partial\lambda}+\frac{1}{a\cos\phi}\frac{\partial v\cos\phi}{\partial\phi}+\frac{\partial w}{\partial z}=0. \tag{3.1}$$

The Laplacian operator in this coordinate system is

$$\nabla^2\phi=\frac{1}{a^2\cos^2\phi}\frac{\partial^2\mu}{\partial\lambda^2}+\frac{1}{a^2\cos\phi}\frac{\partial}{\partial\phi}\left(\cos\phi\frac{\partial\mu}{\partial\phi}\right)+\frac{\partial^2\mu}{\partial z^2}, \tag{3.2}$$

and the material derivative is

$$\frac{\mathrm{D}\mu}{\mathrm{D}t}=\frac{\partial\mu}{\partial t}+\frac{1}{a\cos\phi}\frac{\partial u\mu}{\partial\lambda}+\frac{1}{a\cos\phi}\frac{\partial v\mu\cos\phi}{\partial\phi}+\frac{\partial w\mu}{\partial z}, \tag{3.3}$$

for some scalar $\mu$.

Using these expressions, the horizontal components of the momentum equation are

$$\begin{aligned}\frac{\partial u}{\partial t}+\frac{1}{a\cos\phi}\frac{\partial u^2}{\partial\lambda}+\frac{1}{a\cos\phi}\frac{\partial uv\cos\phi}{\partial\phi}+\frac{\partial uw}{\partial z}-fv=&-\frac{1}{\rho_0 a\cos\phi}\frac{\partial p}{\partial\lambda}+\\&+\frac{A_m}{a^2\cos^2\phi}\frac{\partial^2 u}{\partial\lambda^2}+\frac{A_m}{a^2\cos\phi}\frac{\partial}{\partial\phi}\left(\cos\phi\frac{\partial u}{\partial\phi}\right)+K_m\frac{\partial^2 u}{\partial z^2},\end{aligned} \tag{3.4}$$

$$\begin{aligned}\frac{\partial v}{\partial t}+\frac{1}{a\cos\phi}\frac{\partial uv}{\partial\lambda}+\frac{1}{a\cos\phi}\frac{\partial v^2\cos\phi}{\partial\phi}+\frac{\partial vw}{\partial z}+fu=&-\frac{1}{\rho_0 a}\frac{\partial p}{\partial\phi}+\\&+\frac{A_m}{a^2\cos^2\phi}\frac{\partial^2 v}{\partial\lambda^2}+\frac{A_m}{a^2\cos\phi}\frac{\partial}{\partial\phi}\left(\cos\phi\frac{\partial v}{\partial\phi}\right)+K_m\frac{\partial^2 v}{\partial z^2},\end{aligned} \tag{3.5}$$

where $f=2\Omega\sin\phi$ is the Coriolis parameter, $\rho_0$ is a reference density, $p$ is pressure, and $A_m$ and $K_m$ are the coefficients of horizontal and vertical momentum viscosity, respectively. The metric terms $-(uv\tan\phi)/a$ and $(u^2\tan\phi)/a$ on the left side of (3.4) and (3.5), respectively, are small outside of the very high latitudes and hence are neglected.

With the assumption that the ocean is in hydrostatic balance, the vertical component of the momentum equation simplifies to hydrostatic balance;

$$\frac{\partial p}{\partial z}=-\rho g, \tag{3.6}$$

where $g$ is the gravitational constant and $\rho$ is density. The vertical velocity, $w$, is calculated from the horizontal velocity components, $u$ and $v$, using the incompressibility condition (3.1). The hydrostatic component of pressure, $p$, is calculated by integrating hydrostatic balance (3.6) over depth.

Alongside the momentum equations, there is an advection-diffusion equation for each of the potential temperature, $T$, and salinity, $S$, and an equation of state for density, $\rho$. Respectively, these are

$$\frac{\partial T}{\partial t} + \frac{1}{a\cos\phi}\frac{\partial uT}{\partial \lambda} + \frac{1}{a\cos\phi}\frac{\partial vT\cos\phi}{\partial \phi} + \frac{\partial wT}{\partial z} = \frac{A_h}{a^2\cos^2\phi}\frac{\partial^2 T}{\partial \lambda^2} + \frac{A_h}{a^2\cos\phi}\frac{\partial}{\partial\phi}\left(\cos\phi\frac{\partial T}{\partial\phi}\right) + K_h\frac{\partial^2 T}{\partial z^2}, \quad (3.7)$$

$$\frac{\partial S}{\partial t} + \frac{1}{a\cos\phi}\frac{\partial uS}{\partial \lambda} + \frac{1}{a\cos\phi}\frac{\partial vS\cos\phi}{\partial \phi} + \frac{\partial wS}{\partial z} = \frac{A_h}{a^2\cos^2\phi}\frac{\partial^2 S}{\partial \lambda^2} + \frac{A_h}{a^2\cos\phi}\frac{\partial}{\partial\phi}\left(\cos\phi\frac{\partial S}{\partial\phi}\right) + K_h\frac{\partial^2 S}{\partial z^2}, \quad (3.8)$$

$$\rho = \rho(T, S, z), \quad (3.9)$$

where $A_h$ and $K_h$ are coefficients of horizontal and vertical diffusivity, respectively.

### 3.2.2 Boundary conditions

Boundary conditions for $u$, $v$, $T$ and $S$ are specified at the coasts, ocean floor and surface. The condition on the horizontal velocities at vertical walls is the no-slip condition;

$$(u, v) = (0, 0). \quad (3.10)$$

At the surface, $z = \eta$, a wind stress of magnitude $(\tau_\lambda, \tau_\phi)$ is prescribed, giving the surface condition

$$\rho_0 K_m \frac{\partial(u, v)}{\partial z} = (\tau_\lambda, \tau_\phi) \quad \text{at } z = \eta. \quad (3.11)$$

A bottom stress is specified on the sea floor, $z = -H$, of magnitude $(F_\lambda, F_\phi)$, giving the condition at the sea floor as

$$\rho_0 K_m \frac{\partial(u,v)}{\partial z} = (F_\lambda, F_\phi) \quad \text{at } z = -H, \tag{3.12}$$

where $(F_\lambda, F_\phi) = \rho_0 c_d |(u,v)|(u,v)$, in which $c_d$ is the coefficient of bottom drag. There is also the kinematic boundary condition on the surface;

$$\begin{aligned} &\frac{\mathrm{D}(z-\eta)}{\mathrm{D}t} = 0 \\ \implies \quad &w = \frac{\partial \eta}{\partial t} + \frac{u}{a\cos\phi}\frac{\partial \eta}{\partial \lambda} + \frac{v}{a}\frac{\partial \eta}{\partial \phi} \quad \text{at } z = \eta, \end{aligned} \tag{3.13}$$

and also at the sea floor;

$$\begin{aligned} &\frac{\mathrm{D}(z+H)}{\mathrm{D}t} = 0 \\ \implies \quad &w = -\frac{u}{a\cos\phi}\frac{\partial H}{\partial \lambda} - \frac{v}{a}\frac{\partial H}{\partial \phi} \quad \text{at } z = -H. \end{aligned} \tag{3.14}$$

The condition on temperature and salinity at the vertical walls and on the sea floor is

$$\frac{\partial(T,S)}{\partial n} = 0, \tag{3.15}$$

where $n$ is the normal to the boundary. On the surface a heat, and effective salinity flux $(F_T, F_S)$ is specified, giving the surface condition

$$\rho_0 K_h \frac{\partial(C_p T, S)}{\partial z} = (F_T, F_S) \quad \text{at } z = \eta, \tag{3.16}$$

where $C_p$ is the specific heat capacity.

### 3.2.3 Free surface

The original version of MOMA implemented the rigid-lid approximation; assuming surface height displacement is much smaller than the depth of the ocean and hence neglecting it, this is equivalent to $w = 0$ at $z = 0$. Allowing a free surface means that surface gravity waves can be resolved in the model, however, the speed of these waves restricts the length of the timestep by up

to two orders of magnitude. A free surface may be incorporated into MOMA to give free surface height as an additional prognostic variable when the issue of timestep length is mitigated by splitting the velocity into a baroclinic and barotropic mode (Killworth et al. 1991).

The barotropic mode, $(U, V)$, is the vertically integrated mass flux, using solutions for $(u, v)$ from the momentum equations;

$$U = \int_{-H}^{\eta} u \, dz \quad \text{and} \quad V = \int_{-H}^{\eta} v \, dz, \tag{3.17}$$

where $H$ is the depth of the ocean and $\eta$ is the free surface height. The integral of the baroclinic mode over depth is zero;

$$\int_{-H}^{\eta} u' \, dz = 0 \quad \text{and} \quad \int_{-H}^{\eta} v' \, dz = 0, \tag{3.18}$$

where $(u', v') = (u, v) - (\overline{u}, \overline{v})$, and $(\overline{u}, \overline{v})$ are depth averages of $(u, v)$. The final velocities, redefining $(u, v)$, are the sum of the baroclinic and barotropic modes;

$$u = \frac{U}{H} + u' \quad \text{and} \quad v = \frac{V}{H} + v', \tag{3.19}$$

where it is assumed that $\eta \ll H$.

The equations used to solve for the barotropic mode are the continuity equation, and the $u$ and $v$ momentum equations, all integrated over the depth of the ocean, $-H < z < \eta$. First integrating the continuity equation (3.1) gives

$$\frac{\partial \eta}{\partial t} + \frac{1}{a \cos\phi} \frac{\partial U}{\partial \lambda} + \frac{1}{a \cos\phi} \frac{\partial V \cos\phi}{\partial \phi} = 0, \tag{3.20}$$

where the boundary conditions on $w$ at the surface and ocean floor, (3.13) and (3.14), have been applied. Integrating the $u$ and $v$ momentum equations,

(3.4) and (3.5), over depth gives

$$\frac{\partial U}{\partial t} - fV + \frac{\rho_0 g H}{a\cos\phi}\frac{\partial \eta}{\partial \lambda} = -\frac{1}{a\cos\phi}\frac{\partial}{\partial\lambda}\int_{-H}^{\eta} u^2\,dz + \\ -\frac{1}{a\cos\phi}\frac{\partial}{\partial\phi}\left(\int_{-H}^{\eta} uv\cos\phi\,dz\right) - \frac{g}{a\cos\phi}\int_{-H}^{\eta}\int_{z}^{0}\frac{\partial\rho}{\partial\lambda}\,dz\,dz + \int_{-H}^{\eta}\nabla^2 u\,dz, \tag{3.21}$$

$$\frac{\partial V}{\partial t} + fU + \frac{\rho_0 g H}{a}\frac{\partial \eta}{\partial \phi} = -\frac{1}{a\cos\phi}\frac{\partial}{\partial\lambda}\int_{-H}^{\eta} uv\,dz + \\ -\frac{1}{a\cos\phi}\frac{\partial}{\partial\phi}\left(\int_{-H}^{\eta} v^2\cos\phi\,dz\right) - \frac{g}{a}\int_{-H}^{\eta}\int_{z}^{0}\frac{\partial\rho}{\partial\phi}\,dz\,dz + \int_{-H}^{\eta}\nabla^2 v\,dz, \tag{3.22}$$

where (3.13) and (3.14) have been used as above and

$$p = \rho_0 g\eta + \int_{z}^{0}\rho g\,dz, \tag{3.23}$$

is calculated from integrating (3.6) between the surface and depth $z$.

After calculating the barotropic mode of the velocity field, the final velocity is calculated by a summing the barotropic and baroclinic velocities through (3.19).

## 3.3 Model numerics

Due to their complexity, the nonlinear partial differential equations which govern the system, as detailed in §3.2, are solved using numerical methods. In MOMA, the continuous equations are recast in finite difference form over a discretised domain, and a leapfrog time stepping scheme is implemented to find solutions.

### 3.3.1 Discretisation of the domain

An Arakawa-B grid is used (Mesinger & Arakawa 1976), in which the velocity points are located at the corners of the grid boxes and temperature and salinity at the centres (figure 3.1(a)). The point specifiers used are $i$, $j$ and

$k$, in the $\lambda$-, $\phi$- and $z$-direction, respectively. The grid boxes are of size $\Delta\lambda$ in longitude, $\Delta\phi$ in latitude and $\Delta z_k$ in depth. The values of $\Delta\lambda$ and $\Delta\phi$ are specified in degrees and remain constant throughout the domain, whereas $\Delta z_k$ increases with depth. Bathymetry is defined by specifying each box to be either land or ocean; the number of ocean grid boxes in the vertical in column $(i, j)$ is denoted $K_{i,j}$. In the horizontal, velocity point $(i, j)$ is located at the north-eastern corner of the box which contains tracer point $(i, j)$ at its centre. All of the points at level $k$ are located at the same point in the vertical, which is at the mid-depth of the $k^{th}$ grid box (figure 3.1(b)). The values for the free surface height are located directly above the tracer points. The positioning of variables on this grid allows the use

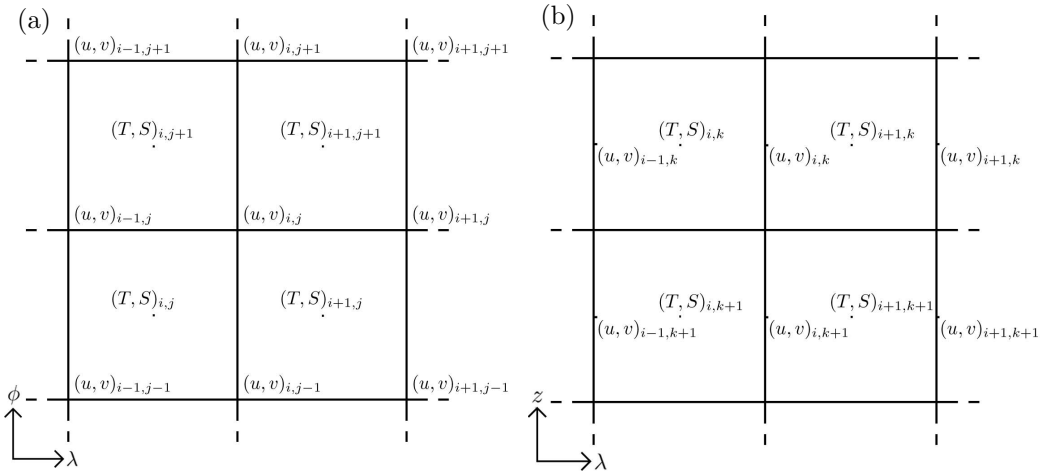


Figure 3.1: Configuration of temperature and salinity, $(T, S)$, and horizontal velocity, $(u, v)$, points on the Arakawa-B grid in the (a) horizontal and (b) vertical plane.

of a semi-implicit Coriolis term; it is calculated through an average of the $n + 1$ and $n - 1$ timestep. This approach decreases computational expense for coarse grid models by allowing the use of a longer timestep because of filtering of inertial and barotropic Rossby waves (Bryan 1969, Semtner 1986*a*). The grid also permits a relatively simple calculation of the advection terms; a single average between two adjacent values for each of the velocity and tracer unites the two quantities at the centre of the grid box faces. The vertical fluxes of momentum and tracers are located at the bottom of the box, directly below the corresponding point. This staggered grid arrangement results in a better representation of Rossby waves when grid boxes are larger than the Rossby radius of the ocean, due to averages being taken over smaller distances (Mesinger & Arakawa 1976, Semtner 1986*b*). In addition, locating velocity points at the edges of the grid boxes allows for

easy application of the no-slip boundary condition at the coasts.

### 3.3.2 Discretisation of the equations

The model employs a central finite differencing scheme in order to solve the equations. Define the difference in the $\lambda$-direction at timestep $n$ of a scalar $\mu$ as

$$\delta_i \mu^n_{i,j,k} = \frac{\mu^n_{i,j,k} - \mu^n_{i-1,j,k}}{\Delta\lambda}, \tag{3.24}$$

with a similar definition for a difference in the $\phi$- and $z$-direction. Note that, due to the arrangement of variables on the grid, this is equivalent to a central difference about the centre of the faces of the grid box, which is where the fluxes are calculated. For consistent index notation with the above definition of $\delta$, the second order central difference in the $\lambda$-direction at grid point $(i, j, k)$ at timestep $n$ of a scaler $\mu$ is

$$\delta^2_i \mu^n_{i+1,j,k} = \frac{\mu^n_{i+1,j,k} - 2\mu^n_{i,j,k} + \mu^n_{i-1,j,k}}{\Delta\lambda^2}, \tag{3.25}$$

with a similar definition in the $\phi$- and $z$-direction. To coincide velocity and tracer points, required for example in the advective terms, averages must be calculated between values at adjacent grid points in each quantity. For this purpose, define the average in the $\lambda$-direction at timestep $n$ of a scalar $\mu$ as

$$\bar{\mu}^n_{i,j,k} = \frac{\mu^n_{i,j,k} + \mu^n_{i+1,j,k}}{2}, \tag{3.26}$$

with a similar definition for an average in the $\phi$- and $z$-direction (figure 3.2(a)).

Definitions (3.24) – (3.26) are used to recast each of the spatial terms of the equations in finite difference form. For the momentum equation the terms of both the $u$ and $v$ components are explicitly included, respectively. The

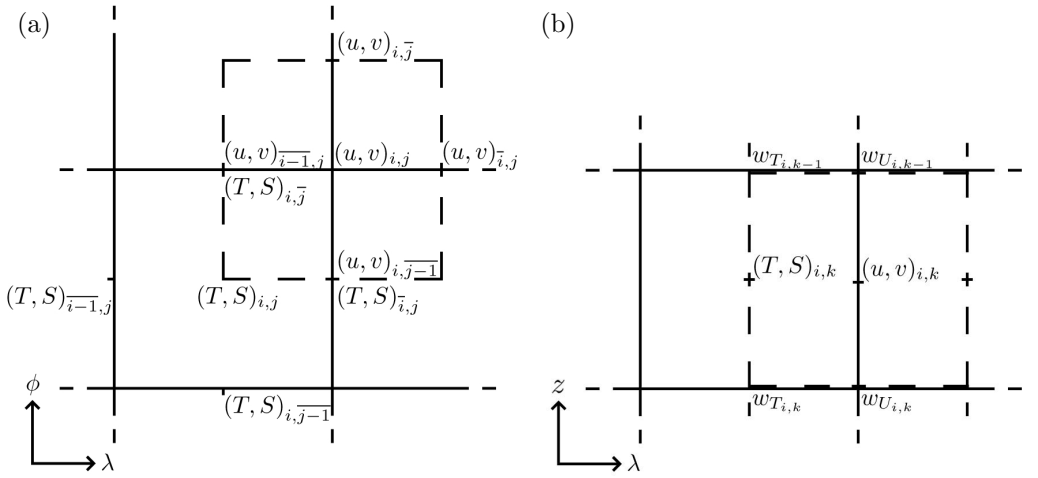


Figure 3.2: (a) Horizontal configuration of averages between adjacent grid points, coinciding velocity and tracer values at the middle of the edges of each box for the calculation of advection. (b) Vertical velocities at the horizontal interfaces between boxes, $w_U$ and $w_T$, vertically aligned with the velocity and tracer points, respectively.

advective terms in the horizontal momentum equations are

$$\frac{1}{a\cos\phi_j}\delta_i\Big(u^n_{\bar{i},j,k}u^n_{\bar{i},\overline{j-1},k}\Big)+\frac{1}{a\cos\phi_j}\delta_j\Big(u^n_{i,\bar{j},k}v^n_{\overline{i-1},\bar{j},k}\cos\phi_j\Big)-\delta_k\Big(u^n_{i,j,\bar{k}}w^n_{Ui,j,k}\Big), \tag{3.27}$$

$$\frac{1}{a\cos\phi_j}\delta_i\Big(v^n_{\bar{i},j,k}u^n_{\bar{i},\overline{j-1},k}\Big)+\frac{1}{a\cos\phi_j}\delta_j\Big(v^n_{i,\bar{j},k}v^n_{\overline{i-1},\bar{j},k}\cos\phi_j\Big)-\delta_k\Big(v^n_{i,j,\bar{k}}w^n_{Ui,j,k}\Big), \tag{3.28}$$

where $\phi_j$ is the latitude at grid point $j$, and $w_{Ui,j,k}$ is the vertical velocity into the grid box directly below the velocity grid point, which is calculated as the average of the vertical velocities below the four surrounding tracer points, $w_{Ti,j,k}$ (Webb 1995)(figure 3.2(b)). The term for advection in the vertical direction is of opposite sign to that in the horizontal as positive flow is taken to be upwards; decreasing $k$. The Coriolis terms, which are treated semi-implicitly to damp inertial oscillations and allow the use of a longer timestep, are

$$-f_j\Big(\alpha v^{n+1}_{i,j,k}+(1-\alpha)v^{n-1}_{i,j,k}\Big), \tag{3.29}$$

$$f_j\Big(\alpha u^{n+1}_{i,j,k}+(1-\alpha)u^{n-1}_{i,j,k}\Big), \tag{3.30}$$

where $f_j$ is the Coriolis parameter at the latitude of grid box $j$, and $0 < \alpha \leqslant 1$ specifies the degree of implicit treatment. When $\alpha = 0$

these terms are instead evaluated at timestep $n$. The pressure gradient terms, calculated by a numerical integration of hydrostatic balance (3.6) with $\rho^n_{i,j,k} = \rho(T^n_{i,j,k}, S^n_{i,j,k}, \Delta z_k)$, are

$$g\delta_i \left( \rho_{i+1,\bar{j},1} \frac{\Delta z_1}{2} + \sum_{m=1}^{k-1} \rho^n_{i+1,\bar{j},\overline{m}} \Delta z_{\overline{m}} \right), \tag{3.31}$$

$$g\delta_j \left( \rho_{\bar{i},j+1,1} \frac{\Delta z_1}{2} + \sum_{m=1}^{k-1} \rho^n_{\bar{i},j+1,\overline{m}} \Delta z_{\overline{m}} \right). \tag{3.32}$$

The diffusive terms are

$$\frac{A_m}{a^2 \cos^2 \phi_j} \delta_i^2 u^{n-1}_{i+1,j,k} + \frac{A_m}{a^2 \cos \phi_j} \delta_j \Big( \cos \phi_j \delta_j u^{n-1}_{i,j+1,k} \Big) + K_m \delta_k^2 u^{n-1}_{i,j,k+1}, \tag{3.33}$$

$$\frac{A_m}{a^2 \cos^2 \phi_j} \delta_i^2 v^{n-1}_{i+1,j,k} + \frac{A_m}{a^2 \cos \phi_j} \delta_j \Big( \cos \phi_j \delta_j v^{n-1}_{i,j+1,k} \Big) + K_m \delta_k^2 v^{n-1}_{i,j,k+1}, \tag{3.34}$$

which are evaluated at timestep $n-1$ for stability in the chosen scheme (O'Brien 1986).

The discretisation of the tracer equations is identical for any tracer, so is only detailed for temperature, $T$, here. The advective terms are

$$\frac{1}{a \cos \phi_j} \delta_i \Big( T^n_{\bar{i},j,k} u^n_{i,\overline{j-1},k} \Big) + \frac{1}{a \cos \phi_j} \delta_j \Big( T^n_{i,\bar{j},k} v^n_{\overline{i-1},j,k} \cos \phi_j \Big) - \delta_k \Big( T^n_{i,j,\bar{k}} w^n_{T_{i,j,k}} \Big), \tag{3.35}$$

where $w_{Ti,j,k}$ is the vertical velocity into grid box $(i, j, k)$ directly below the tracer grid point, and the diffusive terms are

$$\frac{A_h}{a^2 \cos^2 \phi_j} \delta_i^2 T^{n-1}_{i+1,j,k} + \frac{A_h}{a^2 \cos \phi_j} \delta_j \Big( \cos \phi_j \delta_j T^{n-1}_{i,j+1,k} \Big) + K_h \delta_k^2 T^{n-1}_{i,j,k+1}, \tag{3.36}$$

which are again calculated at timestep $n-1$ for stability.

In the model a polynomial approximation of the equation of state is used in place of (3.9), in the case of seawater accurate polynomials have been derived for this purpose (Bryan & Cox 1972, Friedrich & Levitus 1972). Convective adjustment, to address any static instability in the model, is carried out by comparing the density of water in vertically-adjacent grid boxes at each timestep; the water in the boxes is mixed if the deeper density is lower. The number of repetitions of this process in a column at each timestep, $N_c$, is an

option in the model and has a default value of 1.

### 3.3.3 Barotropic mode

The additional computational expense which is required when including a free surface in the model, due to the need for a shorter timestep, is limited by solving for just the barotropic mode of the velocity at the required shorter timestep. This involves time stepping the barotropic mode up to 100 times within each of the longer baroclinic timesteps, and then averaging the values generated by this in time over a single baroclinic timestep to give one value for the barotropic mode of the velocity at each longer baroclinic timestep.

In finite difference form, the spatial terms of the free surface equation (3.20) are

$$\frac{1}{a\cos\phi_j}\delta_i U^{n'}_{i,j-1} + \frac{1}{a\cos\phi_j}\delta_j\Big(V^{n'}_{i-1,j}\cos\phi_j\Big), \tag{3.37}$$

where $n'$ is the shorter barotropic timestep. Note that, by definition, $U$ and $V$ have no variation in the vertical direction and hence no $k$ index.

The finite differencing method which is used can result in a spatial checkerboarding of the solution. Pressure gradients are calculated at each velocity point using the four diagonally surrounding velocity points, in the model this is indirect through the free surface height. This results in two completely independent solutions evolving on two independent subgrids. To solve this issue an additional zero-term is included in (3.20) which links the two subgrids together;

$$c_b\big(\nabla_+\eta - \nabla_\times\eta\big) \equiv 0, \tag{3.38}$$

where $c_b$ is a constant chosen to give the weighting of this additional term, $\nabla_+$ and $\nabla_\times$ are operators involving the vertically and horizontally, and the diagonally adjacent points, respectively. In finite difference form this term is

$$c_b\Big(\nabla_+\eta^{n'-1}_{i,j} + \nabla_\times\eta^{n'-1}_{i,j}\Big), \tag{3.39}$$

where the operators are defined as

$$\nabla_+ \eta_{i,j}^{n'-1} = \eta_{i+1,j}^{n'-1} + \eta_{i,j+1}^{n'-1} - 4\eta_{i,j}^{n'-1} + \eta_{i-1,j}^{n'-1} + \eta_{i,j-1}^{n'-1}, \tag{3.40}$$

$$\nabla_\times \eta_{i,j}^{n'-1} = \eta_{i+1,j+1}^{n'-1} + \eta_{i+1,j-1}^{n'-1} - 4\eta_{i,j}^{n'-1} + \eta_{i-1,j+1}^{n'-1} + \eta_{i-1,j-1}^{n'-1}. \tag{3.41}$$

The terms on the right hand side of (3.21) and (3.22) are calculated only once at each baroclinic timestep, remaining constant for each barotropic timestep within. They are the vertical sum of the corresponding terms from (3.27), (3.28) and (3.31) – (3.34). The remaining terms are timestepped at the shorter barotropic timestep. The Coriolis terms in (3.21) and (3.22) are treated explicitly as $-f_j V_{i,j}^{n'}$ and $f_j U_{i,j}^{n'}$, respectively. The remaining terms of the $U$ and $V$ equations are, respectively,

$$\frac{\rho_0 g H}{a \cos\phi_j} \delta_i \eta_{i+1,\bar{j}}^{n'}, \tag{3.42}$$

$$\frac{\rho_0 g H}{a} \delta_j \eta_{\bar{i},j+1}^{n'}. \tag{3.43}$$

### 3.3.4 Numerical scheme

The equations are timestepped using a leapfrog scheme;

$$\delta_t \mu_{i,j,k}^n = \frac{\mu_{i,j,k}^{n+1} - \mu_{i,j,k}^{n-1}}{2\Delta t}, \tag{3.44}$$

where $\Delta t$ is the timestep associated with the scalar $\mu$. A numerical issue to consider with this scheme is the instability of the diffusive terms, to avoid this instability the diffusive terms must be evaluated at timestep $n-1$ (Richtmyer & Morton 1967), which is equivalent to a forward timestepping scheme for these terms. This combination of leapfrog and forward time differencing schemes provides an efficient method of time integration for the system (O'Brien 1986). However, the leapfrog scheme can lead to a splitting of the odd and even timestep solutions, which is controlled with an occasional Euler backward timestep, usually around every 50 timesteps. A backward, rather than forward, step is preferred as it excites less high-frequency noise (Semtner 1986*a*).

With the leapfrog scheme the equations in finite difference form are

timestepped using

$$\mu^{n+1}_{i,j,k} = \mu^{n-1}_{i,j,k} + 2\Delta t F, \tag{3.45}$$

where $F$ is the sum of the spatial terms in the subject equation, which are detailed in §3.3.2 and §3.3.3.

In the case of the baroclinic velocities, $(u, v)$, the full discretised equations are

$$\frac{u^{n+1}_{i,j,k} - u^{n-1}_{i,j,k}}{2\Delta t_b} - f_j\Big(\alpha v^{n+1}_{i,j,k} + (1-\alpha)v^{n-1}_{i,j,k}\Big) = FU^n_{i,j,k}, \tag{3.46}$$

$$\frac{v^{n+1}_{i,j,k} - v^{n-1}_{i,j,k}}{2\Delta t_b} + f_j\Big(\alpha u^{n+1}_{i,j,k} + (1-\alpha)u^{n-1}_{i,j,k}\Big) = FV^n_{i,j,k}, \tag{3.47}$$

where

$$\begin{aligned}
FU^n_{i,j,k} = &-\frac{1}{a\cos\phi_j}\delta_i\Big(u^n_{\bar{i},j,k}u^n_{\overline{\bar{i},\bar{j-1},k}}\Big) - \frac{1}{a\cos\phi_j}\delta_j\Big(u^n_{i,\bar{j},k}v^n_{\overline{\bar{i-1},\bar{j},k}}\cos\phi_j\Big)\\
&+ \delta_k\Big(u^n_{i,j,\bar{k}}w^n_{Ui,j,k}\Big) - g\delta_i\left(\rho_{i+1,\bar{j},1}\frac{\Delta z_1}{2} + \sum_{m=1}^{k-1}\rho^n_{i+1,\bar{j},\overline{m}}\Delta z_{\overline{m}}\right)\\
&+ \frac{A_m}{a^2\cos^2\phi_j}\delta_i^2 u^{n-1}_{i+1,j,k} + \frac{A_m}{a^2\cos\phi_j}\delta_j\Big(\cos\phi_j\delta_j u^{n-1}_{i,j+1,k}\Big) + K_m\delta_k^2 u^{n-1}_{i,j,k+1},\\
FV^n_{i,j,k} = &-\frac{1}{a\cos\phi_j}\delta_i\Big(v^n_{\bar{i},j,k}u^n_{\overline{\bar{i},\bar{j-1},k}}\Big) - \frac{1}{a\cos\phi_j}\delta_j\Big(v^n_{i,\bar{j},k}v^n_{\overline{\bar{i-1},\bar{j},k}}\cos\phi_j\Big)\\
&+ \delta_k\Big(v^n_{i,j,\bar{k}}w^n_{Ui,j,k}\Big) - g\delta_j\left(\rho_{\bar{i},j+1,1}\frac{\Delta z_1}{2} + \sum_{m=1}^{k-1}\rho^n_{\bar{i},j+1,\overline{m}}\Delta z_{\overline{m}}\right)\\
&+ \frac{A_m}{a^2\cos^2\phi_j}\delta_i^2 v^{n-1}_{i+1,j,k} + \frac{A_m}{a^2\cos\phi_j}\delta_j\Big(\cos\phi_j\delta_j v^{n-1}_{i,j+1,k}\Big) + K_m\delta_k^2 v^{n-1}_{i,j,k+1}.
\end{aligned}$$

For the case $\alpha = 0$ the Coriolis term is evaluated at timestep $n$, and a simple rearrangement of (3.46) and (3.47) gives explicit expressions for $u^{n+1}_{i,j,k}$ and $v^{n+1}_{i,j,k}$. The case presented here is that with a semi-implicit Coriolis term, which means (3.46) and (3.47) must be solved simultaneously through

analytic manipulation to give explicit expressions for $u^{n+1}_{i,j,k}$ and $v^{n+1}_{i,j,k}$;

$$u^{n+1}_{i,j,k} = u^{n-1}_{i,j,k} + 2\Delta t_b \left( \frac{FU^n_{i,j,k} + f_j v^{n-1}_{i,j,k} + 2\Delta t_b \alpha f_j \big(FV^n_{i,j,k} - f_j u^{n-1}_{i,j,k}\big)}{1 + (2\Delta t_b \alpha f_j)^2} \right), \tag{3.48}$$

$$v^{n+1}_{i,j,k} = v^{n-1}_{i,j,k} + 2\Delta t_b \left( \frac{FV^n_{i,j,k} - f_j u^{n-1}_{i,j,k} - 2\Delta t_b \alpha f_j \big(FU^n_{i,j,k} + f_j v^{n-1}_{i,j,k}\big)}{1 + (2\Delta t_b \alpha f_j)^2} \right). \tag{3.49}$$

For tracers $(T, S)$ the equations are identical, and therefore just the discretised equation for $T$ is shown here;

$$\begin{aligned} T^{n+1}_{i,j,k} = T^{n-1}_{i,j,k} + 2\Delta t_T \Bigg( & - \frac{1}{a\cos\phi_j} \delta_i \Big( T^n_{\bar{i},j,k} u^n_{i,\overline{j-1},k} \Big) \\ & - \frac{1}{a\cos\phi_j} \delta_j \Big( T^n_{i,\bar{j},k} v^n_{\overline{i-1},j,k} \cos\phi_j \Big) + \delta_k \Big( T^n_{i,j,\bar{k}} w^n_{T_{i,j,k}} \Big) + \frac{A_h}{a^2 \cos^2\phi_j} \delta_i^2 T^{n-1}_{i+1,j,k} \\ & + \frac{A_h}{a^2 \cos\phi_j} \delta_j \Big( \cos\phi_j \delta_j T^{n-1}_{i,j+1,k} \Big) + K_h \delta_k^2 T^{n-1}_{i,j,k+1} \Bigg). \end{aligned} \tag{3.50}$$

For free surface height, $\eta$, the full discretised equation is

$$\begin{aligned} \eta^{n'+1}_{i,j} = \eta^{n'-1}_{i,j} + 2\Delta t_U \Bigg( & - \frac{1}{a\cos\phi_j} \delta_i U^{n'}_{i,\overline{j-1}} - \frac{1}{a\cos\phi_j} \delta_j \Big( V^{n'}_{\overline{i-1},j} \cos\phi_j \Big) \\ & + c_b \Big( \nabla_+ \eta^{n'-1}_{i,j} + \nabla_\times \eta^{n'-1}_{i,j} \Big) \Bigg), \end{aligned} \tag{3.51}$$

and for the barotropic velocities, $(U, V)$,

$$U^{n'+1}_{i,j} = U^{n'-1}_{i,j} + 2\Delta t_U \left( - \frac{\rho_0 g H}{a\cos\phi_j} \delta_i \eta^{n'}_{i+1,\bar{j}} + f_j V^{n'}_{i,j} + \sum_{k=1}^{K_{i,j}} FU^n_{i,j,k} \Delta z_k \right), \tag{3.52}$$

$$V^{n'+1}_{i,j} = V^{n'-1}_{i,j} + 2\Delta t_U \left( - \frac{\rho_0 g H}{a} \delta_j \eta^{n'}_{\bar{i},j+1} - f_j U^{n'}_{i,j} + \sum_{k=1}^{K_{i,j}} FV^n_{i,j,k} \Delta z_k \right). \tag{3.53}$$

To obtain the final velocity field the baroclinic and barotropic modes are combined. First, the vertical mean is subtracted from the baroclinic mode,

giving

$$(u', v')^n_{i,j,k} = (u, v)^n_{i,j,k} - \frac{1}{K_{i,j}} \sum_{k=1}^{K_{i,j}} (u, v)^n_{i,j,k} \Delta z_k, \tag{3.54}$$

where $(u, v)$ are the velocities calculated using (3.48) and (3.49). Also, the time average of the barotropic mode is calculated as

$$(U, V)^n_{i,j} = \frac{1}{N'} \sum_{n'=1}^{N'} (U, V)^{n'}_{i,j}, \tag{3.55}$$

where $N'$ is the number of barotropic timesteps in one baroclinic timestep. The final value of velocity, redefining $(u, v)$, is the sum of these two quantities using (3.19);

$$(u, v)^n_{i,j,k} = \frac{(U, V)^n_{i,j}}{\sum_{k=1}^{K_{i,j}} \Delta z_k} + (u', v')^n_{i,j,k}. \tag{3.56}$$

## 3.4 Earth-like simulation

The model is run with an Earth-like configuration to give the possibility of comparing the results with observations, and hence assess its ability to model the key large-scale features of the circulation of the oceans on Earth. Modelling this familiar example provides validation of the model, and a foundation from which alterations may be made and results compared.

### 3.4.1 Model configuration

The model is run at a resolution of 4° in the horizontal, both latitudinally and longitudinally, with 15 levels in the vertical (table 3.1). This low resolution gives the possibility of numerous sensitivity studies in later configurations at reasonable computational expense. The land configuration in the model is chosen as an approximate replication of the bathymetry on Earth, with detail to a level which the coarse resolution allows. In the model the ocean depth is set by selecting the number of ocean grid boxes in each column; 15 boxes is the full ocean depth of 5.7 km and 0 boxes is land (figure

| Level index, $k$ | Layer thickness, $\Delta z_k$ (m) | Point depth (m) |
|---|---|---|
| 1 | 30.00 | 15.0 |
| 2 | 46.15 | 53.1 |
| 3 | 68.93 | 110.6 |
| 4 | 99.93 | 195.0 |
| 5 | 140.63 | 315.3 |
| 6 | 192.11 | 481.7 |
| 7 | 254.76 | 705.1 |
| 8 | 327.95 | 996.5 |
| 9 | 409.81 | 1365.4 |
| 10 | 497.11 | 1818.8 |
| 11 | 585.36 | 2360.1 |
| 12 | 669.09 | 2987.3 |
| 13 | 742.41 | 3693.0 |
| 14 | 799.65 | 4464.1 |
| 15 | 836.10 | 5281.9 |
| Total | 5700.00 | |

Table 3.1: Thicknesses, $\Delta z_k$, of the 15 vertical layers, and depth of the associated grid points, where $k = 1$ is the surface box.

3.3).

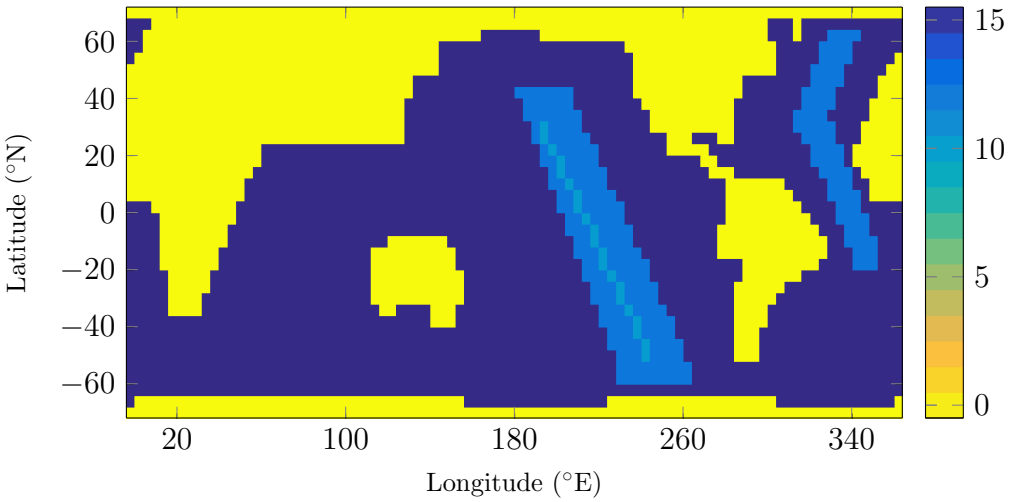


Figure 3.3: Bathymetry of the Earth-like configuration of MOMA, shown in terms of the number of ocean grid boxes in each column.

The ocean surface is forced by temporally constant, zonally-averaged profiles of momentum and tracers, which are derived from climatologies of wind stress (Hellerman & Rosenstein 1983), and temperature and salinity (Levitus 1982). The zonal component of the wind forcing is generally stronger

than the meridional component, and displays the easterly trade winds in the low latitudes and westerlies in the mid-latitudes, reversing at 30°N/S (figure 3.4(a)). The strongest meridional wind forcing is associated with the Trade winds; toward the equator in the low latitudes (figure 3.4(b)). The

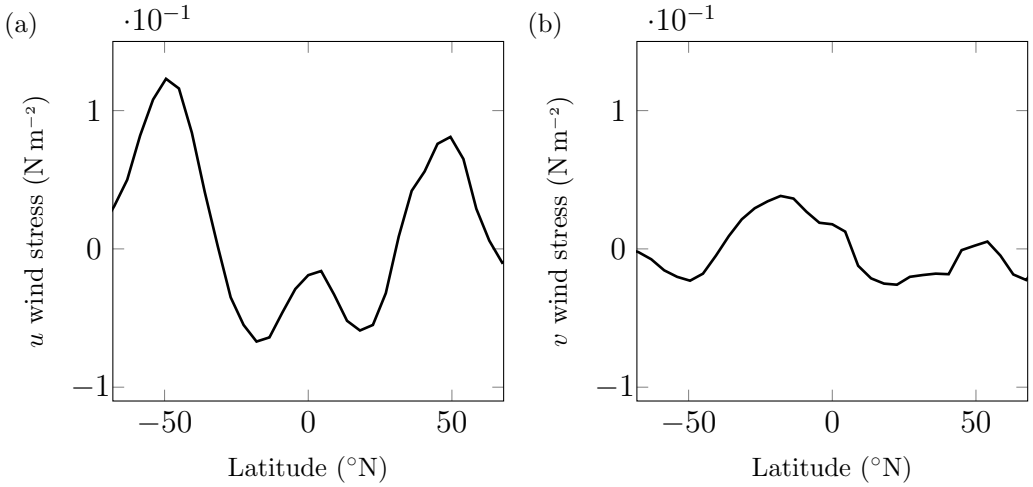


Figure 3.4: Surface wind stress forcing (N m$^{-2}$) in the (a) eastward and (b) northward direction.

temperature forcing is warmest in the tropics, decreasing toward the poles and with a slight dip associated with the intertropical convergence zone at the equator (figure 3.5(a)). The salinity forcing peaks in the tropics as a result of high rates of evaporation there, and also dips at the equator due to the increased rainfall of the intertropical convergence zone (figure 3.5(b)).

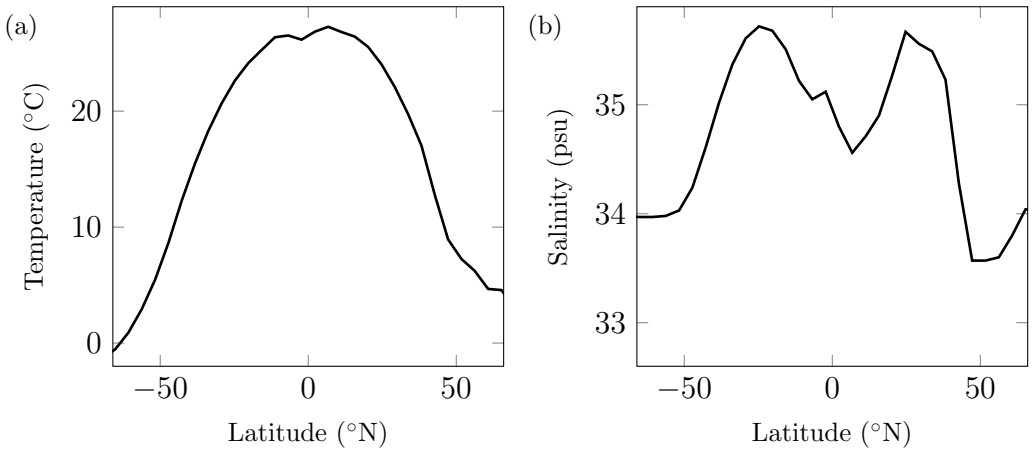


Figure 3.5: Surface tracer forcing for (a) temperature (°C) and (b) salinity (psu).

The default values of the parameters in the model are chosen to be their

typical Earth-like modelling values, and are hence used in all model runs throughout, unless otherwise stated (table 3.2). In some cases these values are constrained by numerical considerations, for example horizontal viscosity which has a lower bound dependent on the horizontal resolution of the numerical grid (Bryan et al. 1975). This restriction is controlled by the thickness of the boundary layer at the coasts which results from the implementation of a no-slip condition. This thickness is $\mathcal{O}(A_m/\beta)^{1/3}$ (Munk 1950), where $\beta = \partial f/\partial\phi$, and so it is required that $A_m > \beta\Delta\lambda^3$. Coarse resolution modelling studies, in the region of $4^\circ$ in the horizontal, therefore set the value of $A_m$ to be at a minimum $\mathcal{O}(10^5)\mathrm{m}^2\,\mathrm{s}^{-1}$ with $A_h$ similarly unrealistically large at $\mathcal{O}(10^3)\,\mathrm{m}^2\,\mathrm{s}^{-1}$, without the same restriction the equivalent parameters in the vertical are much closer to observed values, generally $\mathcal{O}(10^{-4})\,\mathrm{m}^2\,\mathrm{s}^{-1}$ (Bryan et al. 1975, Bryan & Lewis 1979, Bryan 1987).

| Description | Parameter | Value | Unit |
|---|---|---|---|
| Horizontal eddy viscosity | $A_m$ | $1.0 \times 10^5$ | $\mathrm{m}^2\,\mathrm{s}^{-1}$ |
| Horizontal eddy diffusivity | $A_h$ | $2.0 \times 10^3$ | $\mathrm{m}^2\,\mathrm{s}^{-1}$ |
| Vertical viscosity | $K_m$ | $1.0 \times 10^{-4}$ | $\mathrm{m}^2\,\mathrm{s}^{-1}$ |
| Vertical diffusivity | $K_h$ | $1.0 \times 10^{-4}$ | $\mathrm{m}^2\,\mathrm{s}^{-1}$ |
| Tracer relaxation timescale | $\gamma$ | $4.32 \times 10^6$ | s |
| Tracer timestep | $\Delta t_T$ | $7.2 \times 10^3$ | s |
| Barotropic velocity timestep | $\Delta t_U$ | $7.2 \times 10^3$ | s |
| Baroclinic velocity timestep | $\Delta t_b$ | $1.0 \times 10^2$ | s |
| Coefficient of bottom drag | $c_d$ | $1.0 \times 10^{-3}$ | — |
| Weighting of $\nabla^2_+ - \nabla^2_\times$ operator | $c_b$ | 0.1 | — |
| Implicit degree of Coriolis term | $\alpha$ | 0.6 | — |
| Repetitions of convective adjustment | $N_c$ | 1 | — |

Table 3.2: Parameters in MOMA and their default values.

The results presented for all runs are an average of 1000 years in a quasi-steady state; where kinetic energy varies by less than 1%, following a spinup period of up to 7000 years.

### 3.4.2 Results

Sea surface temperature peaks in the region 5-15°N/S, and monotonically decreases from there towards the poles (figure 3.6(a)). There is a slightly cooler band at the equator, associated with the intertropical convergence zone. This surface temperature profile strongly reflects that of the surface forcing in the model (figure 3.5(a)), which is based on observations (figure 3.6(b)), and is hence a reasonably accurate representation of Earth. However, the model is forced with a zonal average of the observations (figure 3.5(a)) which results in the forcing value remaining constant for any given latitude and hence suppresses longitudinal variability, and also results in a smaller range of temperatures in the model results than in the observations; 0 to 27 °C compared to -2 to 30 °C. In particular, the high latitudes are generally warmer than the observations, except the northern North Atlantic which is up to 4.5°C colder, and the low latitudes are generally cooler, particularly at the equator in the Pacific which is over 5°C colder in some regions (figure 3.6(c)). Modelled temperatures in the equatorial regions and the North Atlantic being colder than observations are features which are common to ocean models, the latter due to the greater northward extent of the Gulf Stream in model simulations (Griffies et al. 2009). Higher than observed temperatures in regions off western coasts is consistently observed in model results, and is also a feature of the results here (figure 3.6(c)), which is hypothesised to be a result of poor replication of coastal upwelling in coarse resolution models (Griffies et al. 2009).

At 500 m depth, where surface forcing is not so influential, the model reproduces the temperature distribution observed at this depth in the oceans on Earth (Levitus 1982). At this deeper level, the peaks in temperature are reduced by up to 10 °C from their surface values, and are located in the higher latitudinal range of 20-40°N/S where Ekman pumping causes downwelling of warm surface water (figure 3.7(a)). At this depth there are warmer regions observed at the western side of the basins (figure 3.7(b)) which are relatively well reproduced by the model. The results are almost exclusively warmer at this depth, over 10°C in some coastal regions in the Pacific, with the most notable exception being the mid latitudes of the North Atlantic which reaches a maximum of 4°C colder (figure 3.7(c)). These higher temperatures are related to the approximation of a constant vertical

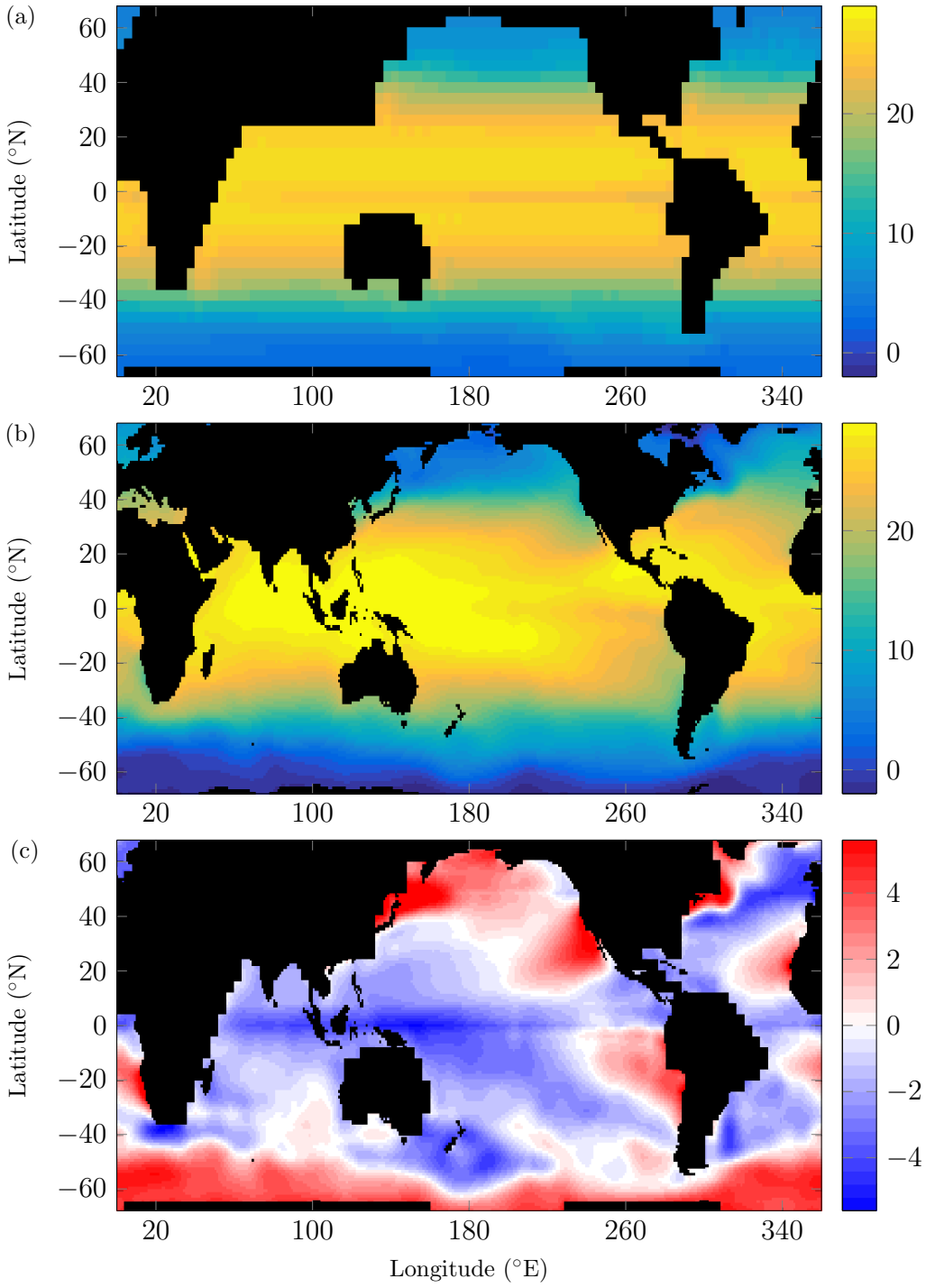


Figure 3.6: Ocean surface temperature (°C) from (a) quasi-steady state model output for an Earth-like configuration, (b) observations of the oceans on Earth (Levitus 1982), and (c) the difference (a)−(b).

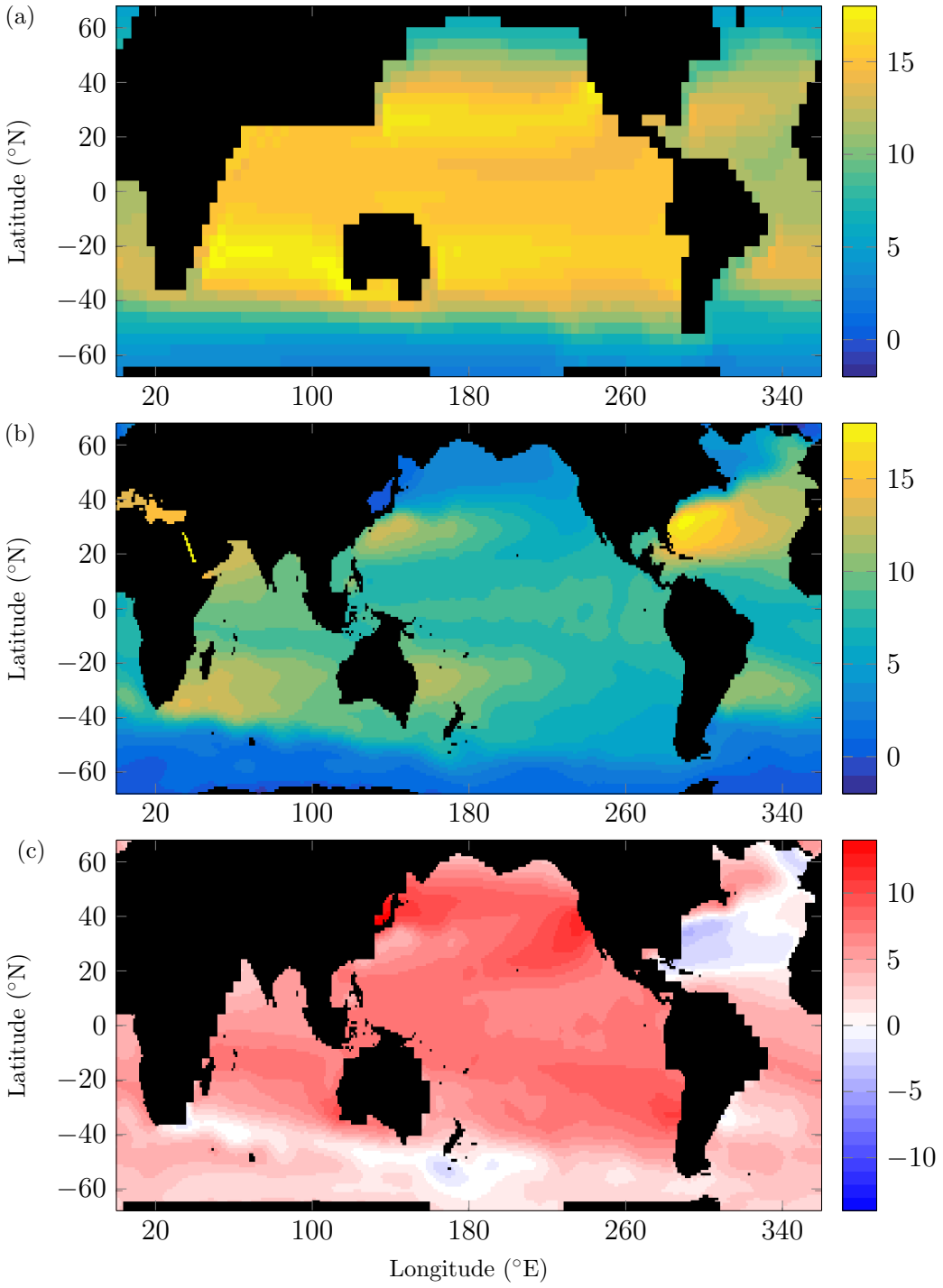


Figure 3.7: Ocean temperature (°C) at 500 m depth from (a) quasi-steady state model output for an Earth-like configuration, (b) observations of the oceans on Earth (Levitus 1982), and (c) the difference (a)−(b).

diffusivity throughout the depth of the ocean, whereas vertical diffusivity actually increases with depth and is therefore high in the upper ocean in the model.

The reduction in temperature with depth seen between the surface and 500 m is consistent with the zonally-averaged temperature distribution (figure 3.8(a)), in which the peak temperature decreases rapidly in the surface 1000 m. Although at a lower gradient, the temperature continues to decrease with depth below this, being consistently less than 10 °C and with most regions cooler than 5 °C. This rapid decrease in the surface layer is limited to the lower latitudes where surface temperatures are greatest; poleward of this region the temperature remains relatively constant at the coldest, deep ocean temperature through the total depth of the ocean. The observations show a similar pattern to the model results (figure 3.8(b)), however the extremes seen in surface temperature and, polar and deep water are not modelled (figure 3.8(b)). Away from the surface, the zonally-averaged temperature is warmer than observations throughout, with the most significant difference of up to 7°C in the low latitudes of the surface 1000 m (figure 3.8(c)); the thermocline in the model results is much deeper than observed.

The peak values in sea surface salinity of 35.7 are in bands in the mid-latitudes, 20-40°N/S, with the freshest regions being in the high northern latitudes (figure 3.9(a)). Salinity is forced in the same way as temperature; with zonally-averaged observed values (figure 3.5(b)), and hence the surface salinity does not display the significant longitudinal variation present in the observations (figure 3.9(b)). This variation is particularly predominant in surface salinity compared to temperature; the Atlantic ocean is significantly more saline, with extensive areas above 37, compared to localised peaks of 36.5 in the Pacific (figure 3.9(b)). Hence, the model results are generally fresher in the Atlantic, up to 2 less than observed values, and more saline in the Pacific, particularly in coastal regions where surface run-off has significant influence (figure 3.9(c)). In addition, the averaging process associated with using zonally-averaged forcing reduces the range of values of sea surface salinity, for example, the peaks in the observations are greater than 37 in contrast to a peak of less than 36 in the model results.

At 500 m depth the latitudes at which the peaks in salinity occur vary very

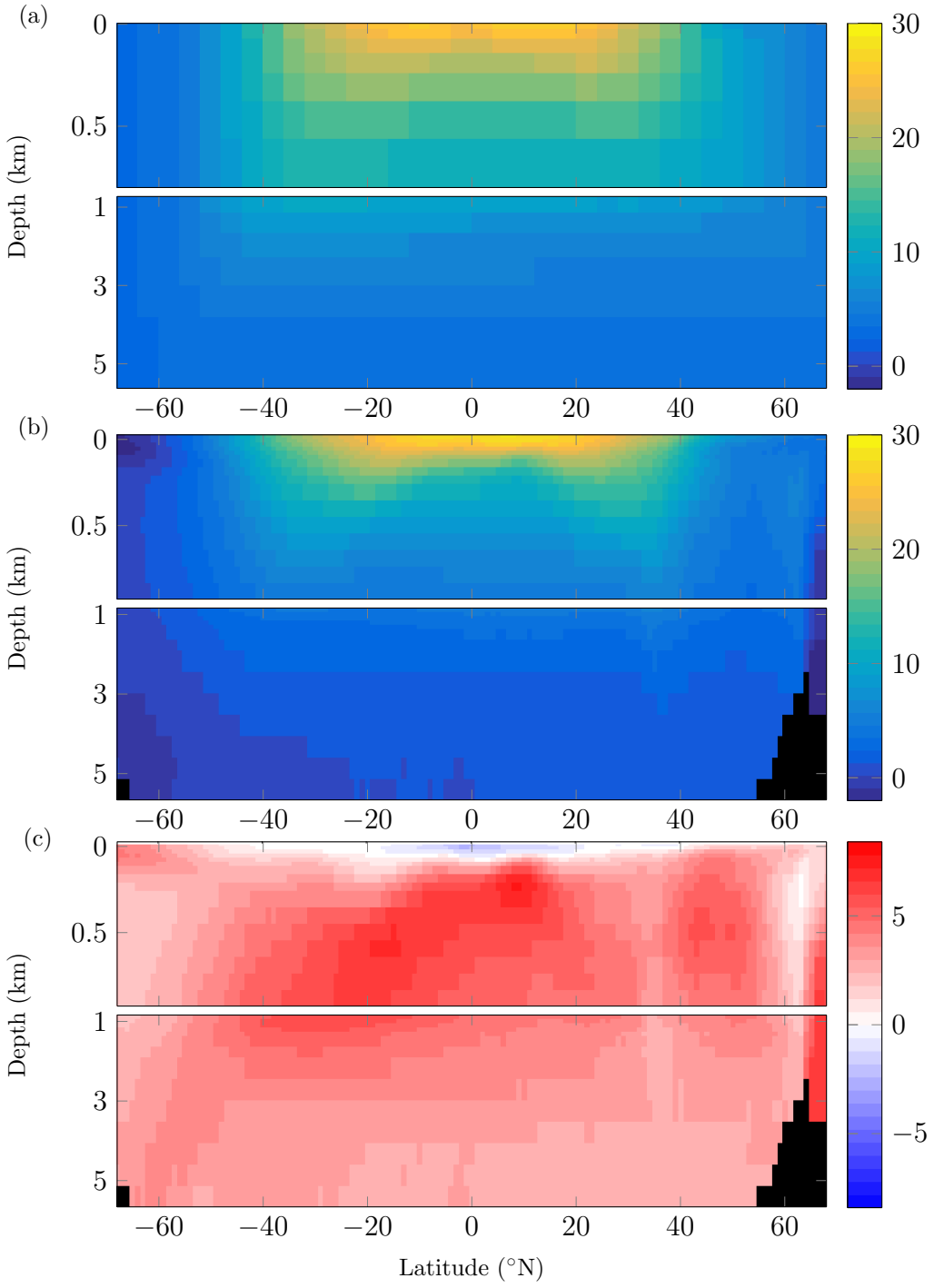


Figure 3.8: Zonally-averaged ocean temperature (°C) from (a) quasi-steady state model output for an Earth-like configuration, (b) observations of the oceans on Earth (Levitus 1982), and (c) the difference (a)−(b). Note the expanded vertical scale in the upper 1 km of the ocean.

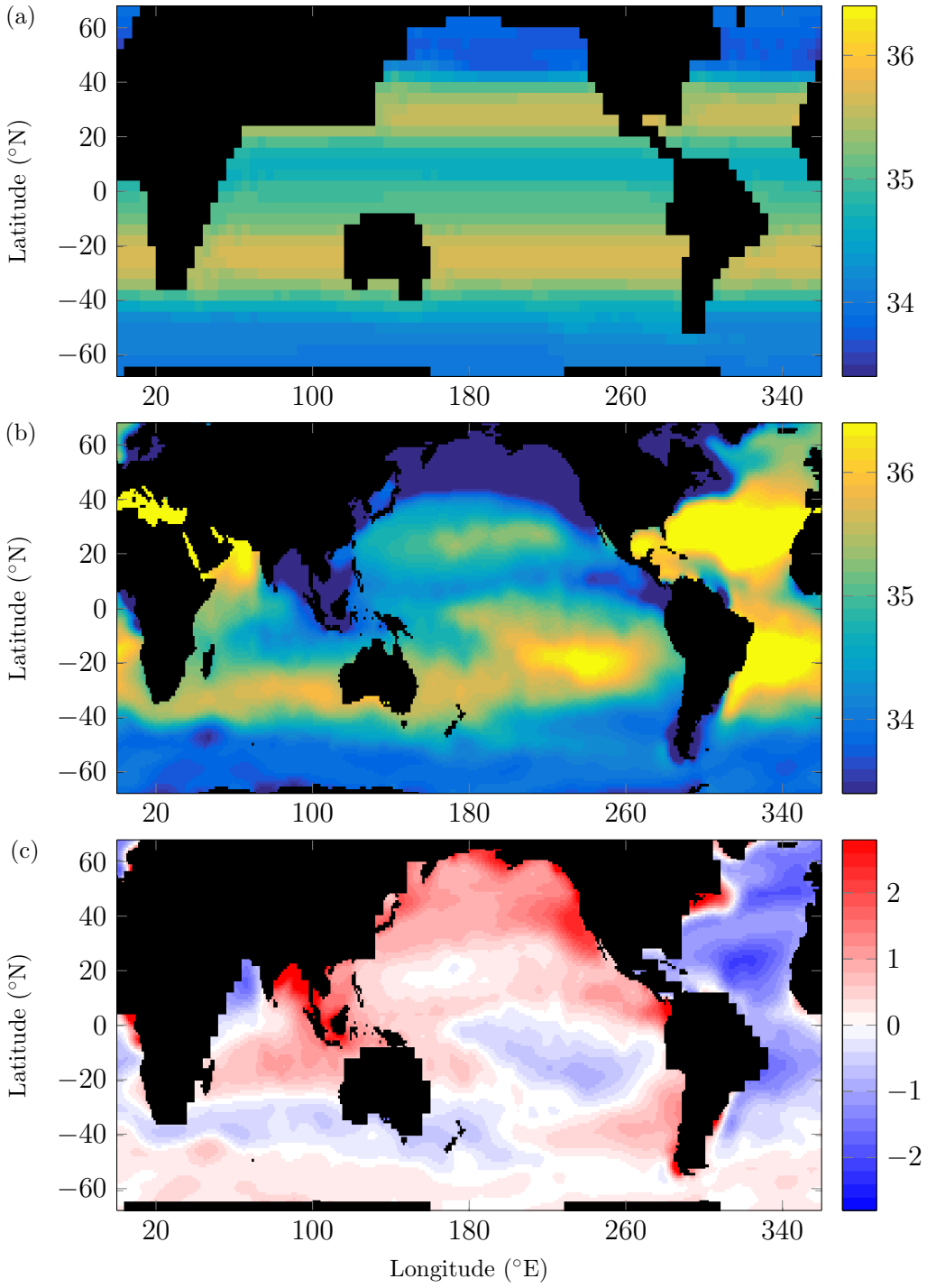


Figure 3.9: Ocean surface salinity (psu) from (a) quasi-steady state model output for an Earth-like configuration, (b) observations of the oceans on Earth (Levitus 1982), note that the colour scale is restricted in the interest of detail, and (c) the difference (a)−(b).

little from the surface (figure 3.10(a)), in contrast to the poleward shift observed in the temperature distribution, such that the latitudes of the peaks in salinity and temperature coincide at this deeper level (figure 3.7(a)). The model results show a decrease in salinity toward the polar regions, which are the freshest areas, however the minima are observed at lower latitudes (figure 3.10(b)). At this depth, as at the surface, the zonal variation in salinity values is not represented; again, the Atlantic is fresher, particularly in the North, and the Pacific generally more saline than the observations (figure 3.10(c)).

The zonally-averaged salinity shows the observed rapid freshening with increasing depth through the surface 500 m, whilst maintaining the latitudes of the peak salinity values at approximately 30°N/S. These distinct peaks in salinity in the surface layers dilute, both latitudinally and vertically away from these regions to concentrations of 34.2 in the deep ocean, which is much fresher than observed values which are closer to 35 (figure 3.11(b)). The most striking difference in structure between the modelled and observed values is a region of particularly saline water extending into the deep ocean in the mid-latitudes of the Northern Hemisphere in the observations (figure 3.11(b)). This is due to the contribution from the Mediterranean Sea which has a particularly high salinity, over 39 in some places, which is not represented in the model land configuration due to the coarse resolution (figure 3.3). In the model results the polar regions are more saline at the surface and fresher at depth than observations, particularly in the regions of deep water formation in the north (figure 3.11(c)). The zonally-averaged salinity in the model is generally fresher than observed, with Antarctic Intermediate Water (AAIW) being the only extensive water mass which is more saline than observations (figure 3.11(c)). Ocean models commonly model AAIW as too saline and, as is also observed in these model results (figure 3.8(c)), too warm (Griffies et al. 2009).

Contours of the free surface height of the ocean offer information about the surface currents; geostrophic balance means these contours are representative of the flow. The strength of the currents is related to the gradient in the free surface height; close contours are indicative of strong currents. The free surface height shows the presence of gyres in the ocean basins, and a strong zonal current in the Southern Hemisphere where there is no meridional boundary (figure 3.12(a)). The strongest gyres in each ocean

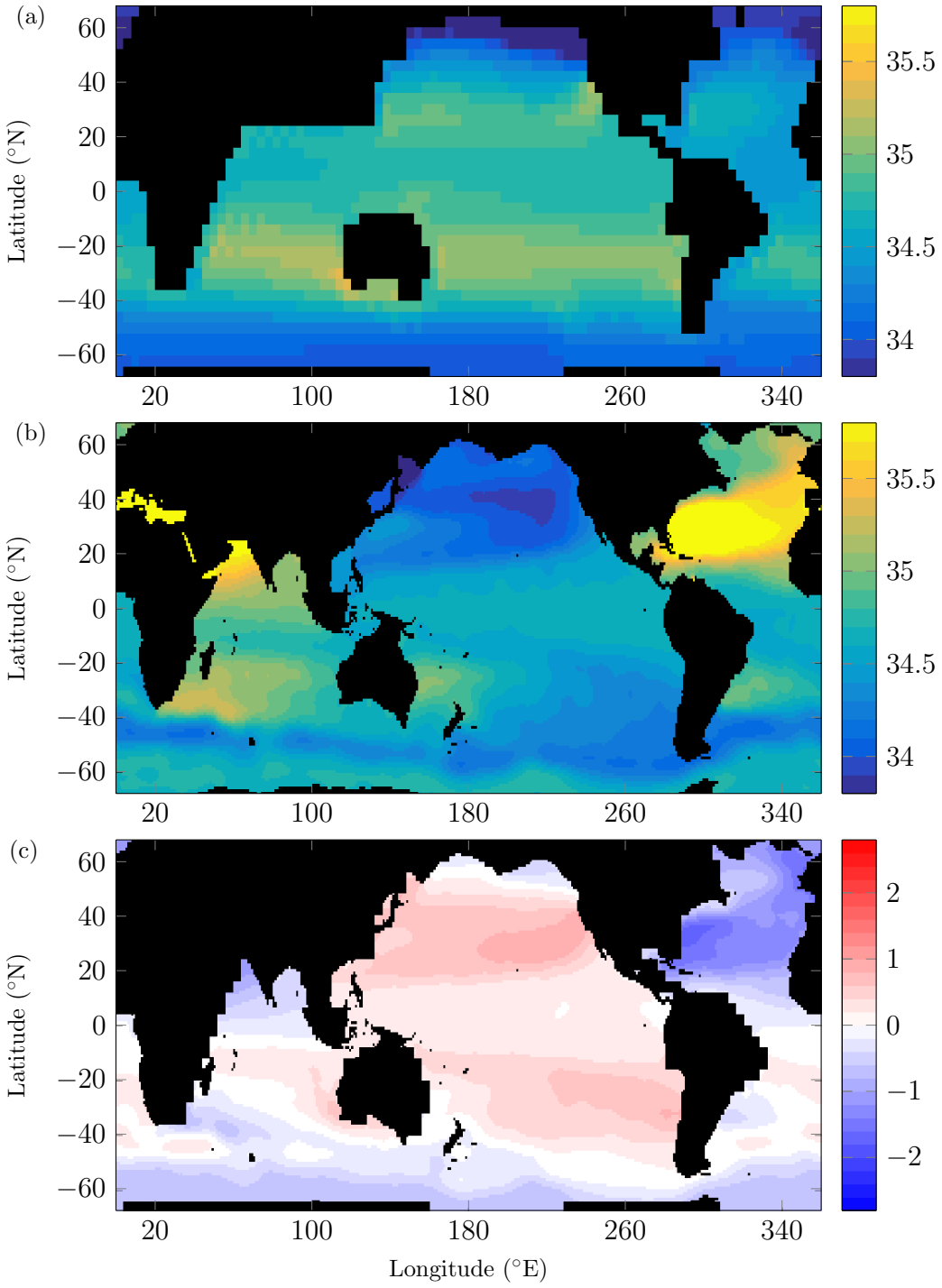


Figure 3.10: Ocean salinity (psu) at 500 m depth from (a) quasi-steady state model output for an Earth-like configuration, (b) observations of the oceans on Earth (Levitus 1982), note that the colour scale is restricted in the interest of detail, and (c) the difference (a)−(b).

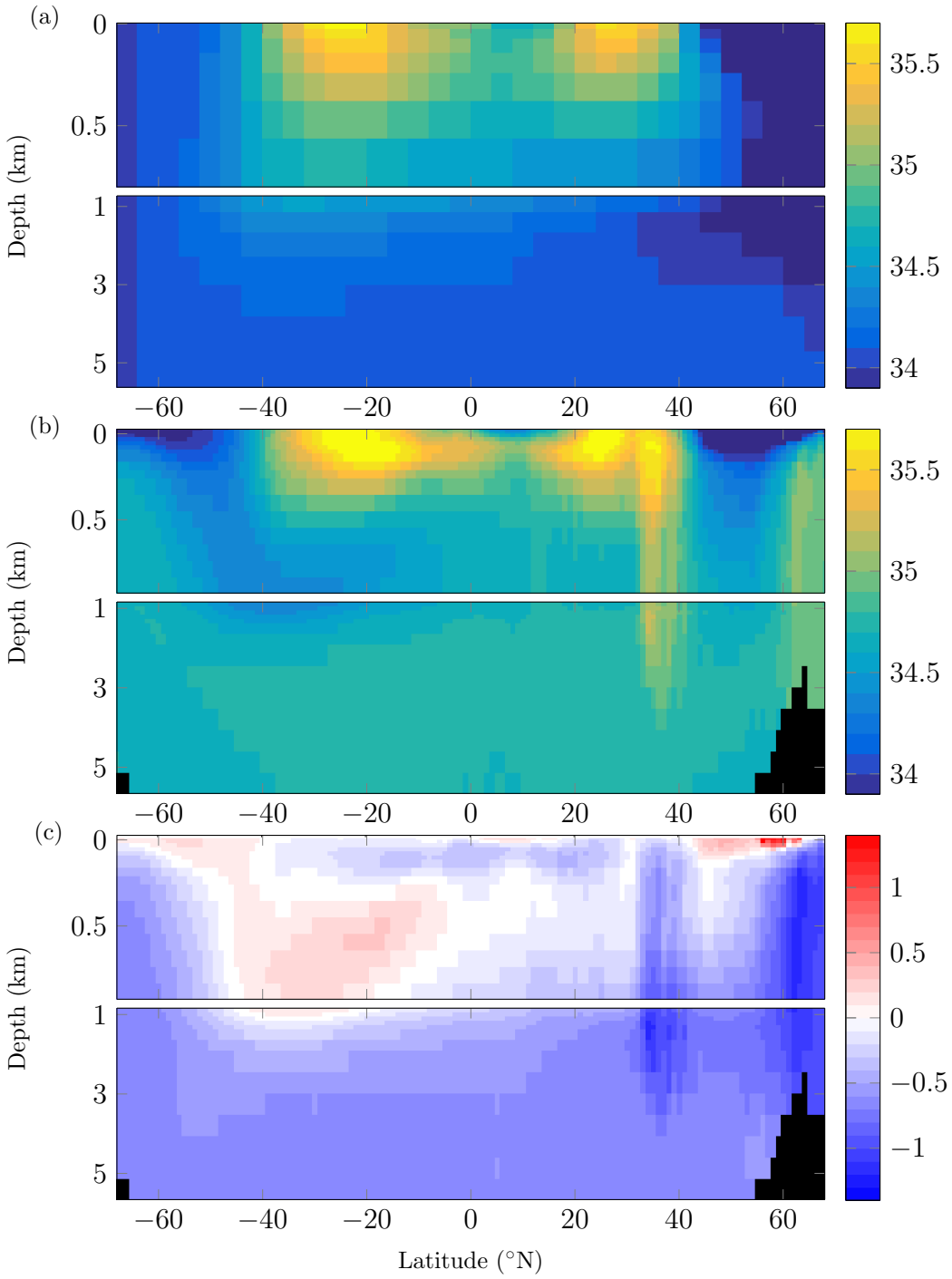


Figure 3.11: Zonally-averaged ocean salinity (psu) from (a) quasi-steady state model output for an Earth-like configuration, (b) observations of the oceans on Earth (Levitus 1982), note that the colour scale is restricted in the interest of detail, and (c) the difference (a)−(b). Note the expanded vertical scale in the upper 1 km of the ocean.

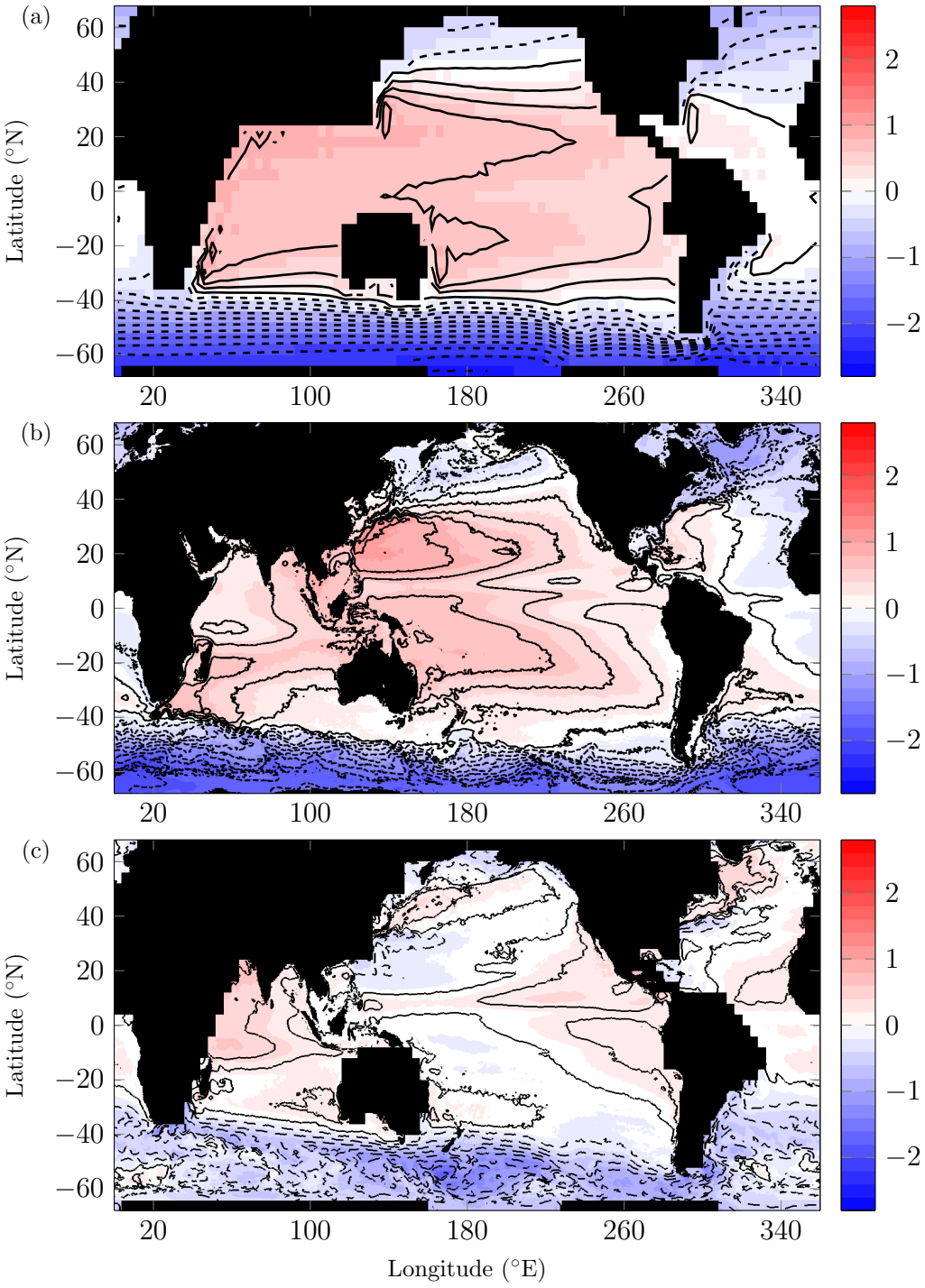


Figure 3.12: Ocean free surface height (m) from (a) quasi-steady state model output for an Earth-like configuration, (b) observations of the oceans on Earth (Maximenko et al. 2009), adjusted such that the mean is zero, and (c) the difference (a)−(b). Contour interval is 0.2 m.

basin are those extending from the equatorial regions to the mid-latitudes. The highest sea surface is found toward the western side of these gyres with a sharp gradient in surface height at the western edge, indicative of a strong poleward-travelling surface current with a weaker equatorward return flow through the rest of the basin. This pattern agrees with the observed currents on Earth, where the subtropical gyres extend from about 10-45°N/S and the velocities at the western edge are at least 10 times the magnitude of the eastern (Pedlosky 1990). The strongest surface current globally is the Antarctic Circumpolar Current (ACC), travelling eastward in the range of latitudes in the Southern Hemisphere where there is no continuous meridional boundary, which allows for a continuous zonal flow to circle the planet. Here, the extreme in sea surface height occurs, lower than 2 m below the mean, in comparison to the peak height in the gyres of less than half that magnitude.

Sea surface height maps calculated from observations of Earth using a combination of satellite and drifting buoy data show this same pattern of gyres, and circumpolar flow in the Southern Hemisphere (figure 3.12(b)). The greatest differences between the gradient in sea surface height, indicative of current strength, between the model results and observations are in regions of western boundary currents and the ACC (figure 3.12(c)). In the north west of both the Pacific and Atlantic there are regions where the surface is higher in the model than observations north of a region which is lower, this is due to the Kuroshio Current and Gulf stream separating from the coast further north than observed. The most extensive difference is in the ACC, which is consistently wider and reaches up to 10° further north in the model compared to observations. The coarse resolution of the model means there are no islands in the region north of Australia to create a boundary between the Indian and Pacific Oceans, resulting in the subtropical gyre in the pacific extending into the northern parts of the Indian ocean and raising the surface higher in the model results than observations.

Contours of the overturning streamfunction show the meridional transport of the deep ocean circulation (figure 3.13), which results in the poleward transport of heat (figure 3.14). The observations show a greater northward heat transport, compared to the model results, at all latitudes outside of the southern ocean. This difference is largely accounted for in the Atlantic ocean, the principal location of deep water formation in the Northern Hemisphere,

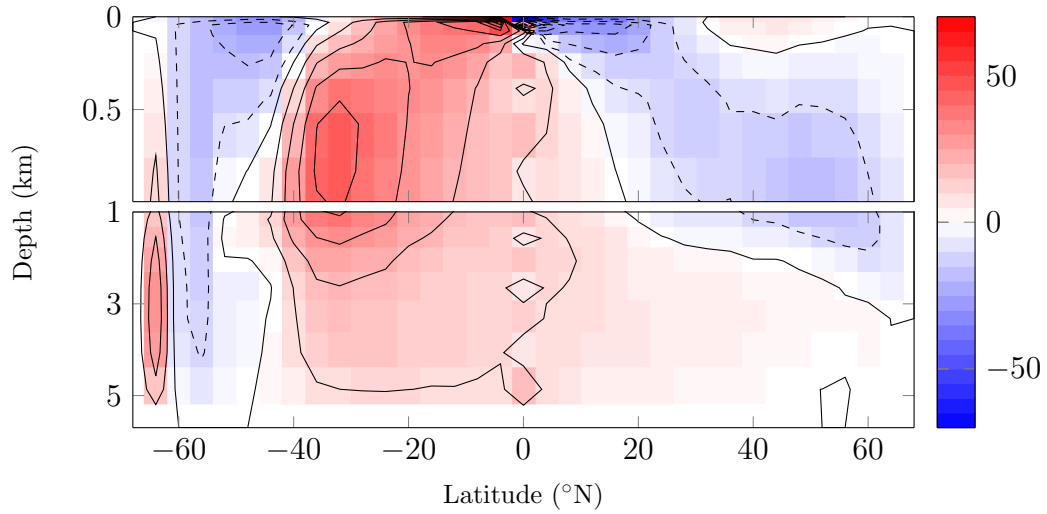


Figure 3.13: Ocean overturning streamfunction (Sv) from quasi-steady state model output for an Earth-like configuration. Contour interval is 10 Sv, positive circulation is anti-clockwise. Note the expanded vertical scale in the upper 1 km of the ocean.

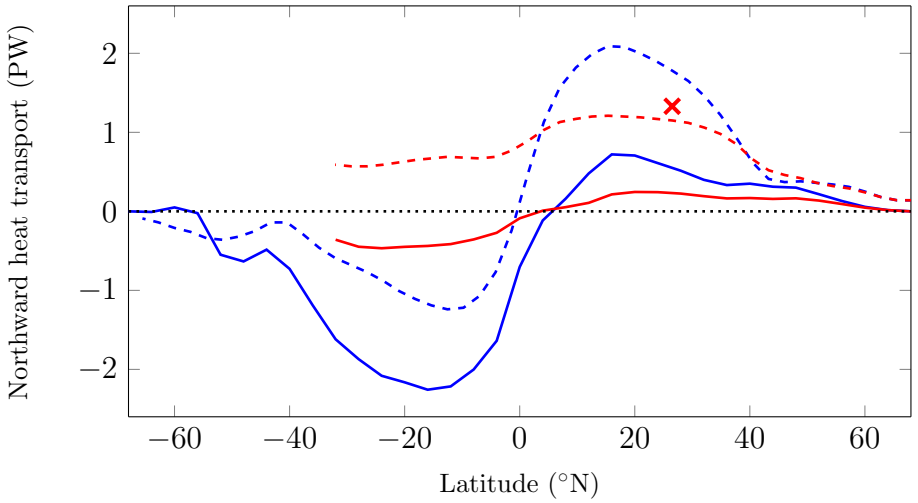


Figure 3.14: (blue) Global and (red) Atlantic basin northward ocean heat transport (PW) from (solid lines) quasi-steady state model output of an Earth-like configuration, and (dashed lines) observations of the oceans on Earth (Trenberth & Caron 2001), (cross) annual mean of observations in the Atlantic at 26.5°N from the Rapid Climate Change–Meridional Overturning Circulation and Heatflux Array (RAPID-MOCHA) (Johns et al. 2011).

where the observed heat transport is northward at all latitudes, whereas the model shows a poleward transport either side of the equatorial region. This difference is due to a weak Atlantic Meridional Ocean Circulation which, at 13 Sv at 30°N, lies comfortably within the predictions from a range of coupled models submitted to the fifth assessment report of the

Intergovernmental Panel on Climate Change (Heuzé et al. 2015), which have a multi-model mean of 18 Sv and range from 10 to 32 Sv. There is also little cross-equatorial flow in the model, with distinct cells bordering at the equator, whereas observations show northward flow in the surface layers throughout both the Atlantic and Pacific basins with southward flow in the layers below this (Ganachaud & Wunsch 2000). The magnitude of this cross-equatorial transport in the Atlantic has been estimated to be 9 Sv (Richardson & Schmitz 1993) but is much weaker at 1 Sv in the model results.

As discussed in reference to the box model (§2.6), the freshwater transport into the Atlantic Ocean basin can be used as a measure of the stability of the overturning circulation through the salt-advection feedback. Calculating the freshwater transport across 34°S in the Atlantic (Hawkins et al. 2011) in the results found using MOMA gives a value of -0.28 Sv. This negative value is indicative of an export of freshwater and therefore an unstable regime, in which a weakening of the circulation results in a freshening of the Atlantic ocean which further decreases the circulation strength. This value lies within the range of values found from various ocean reanalyses and ocean general circulation models, which are generally negative and range from -0.4Sv to +0.1 Sv (Hawkins et al. 2011). The value found also lies between two observational estimates, which also indicate an unstable regime; -0.1 Sv (Huisman et al. 2010) and -0.3 Sv (Weijer et al. 1999).

## 3.5 Coupled modelling

The ocean general circulation model MOMA is coupled to the atmospheric general circulation model IGCM4 (Intermediate Global Circulation Model version 4), using the OASIS (Ocean Atmosphere Sea Ice Soil) coupler, in FORTE (Fast Ocean Rapid Troposphere Experiment). In this coupled configuration MOMA is run at the finer horizontal resolution of 2°, closer to the resolution of the atmospheric component than the coarser 4° resolution, and the Gent-McWilliams parameterisation for ocean eddies is used (Gent & McWilliams 1990).

### 3.5.1 IGCM4

The atmospheric component used in FORTE is IGCM4 (Joshi et al. 2015), which is the latest version of the IGCMs developed at the University of Reading. It is an intermediate model; it solves the baroclinic primitive equations (Hoskins & Simmons 1975) without modelling some more complex features of the climate system. To aid the use of spectral methods and a semi-implicit timestep, the horizontal momentum equations are transformed to equations for the scalars horizontal vorticity and divergence, in addition there is a thermodynamic equation, an equation for surface pressure and an equation for the geopotential.

The model is run with a horizontal resolution of 64 latitudinal and 128 longitudinal grid points, equating to approximately a 2.8° spacing. In the vertical there are 20 layers, with vertical coordinate $\sigma$ = pressure/surface pressure. Spectral methods are used to solve the equations in the horizontal, and finite differences are used in the vertical. A semi-implicit timestep is used to aid stability and allow the use of a longer timestep (Hoskins & Simmons 1975).

To model sea ice there is a linear interpolation of surface properties between -2 and 0°C; roughness, albedo, and heat capacity. This avoids unrealistic dramatic spatial changes in these properties, and accounts for ice melting at warmer temperatures than it freezes; saltwater has lower freezing point than the melting point of ice, which is primarily composed of freshwater. Soil is modelled with a two layer model, with thicknesses of 0.06 m in the upper level and 2.3 m in the lower, with diffusive heat transport between the two levels, and soil moisture is modelled with a simple bucket model (Forster et al. 2000).

The Morcrette radiation scheme is used to model the long and short wave radiative fluxes using temperature, cloud, humidity and trace gases (Zhong & Haigh 1995), which runs once each model day. The cloud scheme (Slingo 1987) has been updated in IGCM4 to better match observed outgoing and surface radiation, as well as to include the implementation of a parameterisation of marine stratocumulus cloud (Kawai & Inoue 2006). The model includes a moist convection scheme which simulates both deep

and shallow convective adjustment (Betts 1986).

### 3.5.2 OASIS

The coupler used in FORTE is OASIS 2.3 (Terray et al. 1999), which is responsible for exchanging fluxes between the atmosphere and ocean components of the model without the need for separate modifications to these. Due to the difference in the numerical grids of the ocean and atmosphere at the ocean surface, interpolation of the fluxes is required to correctly pass them between the two components of the model. This requires an appropriate weighting to be applied to the four surrounding grid points in the interpolation process, in order to represent the proportion of each grid box which overlaps between the ocean and atmosphere. A tiling scheme is employed for coastal points which allows atmosphere grid boxes to be part land and part ocean, and therefore aids precise definition of coasts in the model.

## 3.6 Summary

The OGCM detailed here, MOMA, solves the primitive equations for a global ocean at a relatively coarse resolution, and hence low computational expense. It provides a suitable balance between complexity, adaptability, and computational expense to allow its use in the numerical investigation of a range of sensitivity studies of ocean circulation. It has been verified that, when configured in an Earth-like manner, MOMA reasonably replicates the large scale behaviour of the oceans on Earth. This Earth-like configuration provides a basis from which adaptations can be made for its implementation in the investigation of ocean response to the varying configurations in the following chapters. The model may be coupled to an atmospheric general circulation model to provide the coupled atmosphere-ocean model FORTE.

# Chapter 4

# Land configuration

A particularly Earth-specific element of the configuration presented in chapter 3 is the arrangement of land. Hence, to apply MOMA to an exoplanet, the first adaptation made to the Earth-like setup is to the global configuration of land mass. In this study, when modelling an exoplanet an idealised land configuration is used; a single, vast ocean basin of uniform depth with only limited expanses of land. Such arrangements are chosen as they can be used as simple representations of not only ocean-covered planets but also those with differing land configurations.

## 4.1 Idealised configurations

Despite there being an infinite number of possible land configurations for a terrestrial planet, it is possible to make conclusions about the quantitative behaviour of the circulation resulting from different layouts through investigation of a limited number of simple configurations. Here, the results from two contrasting cases are presented. Both have an island at each pole which extends to 68°N/S, which is necessary to negate numerical instability resulting from grid convergence. The first configuration has no other land, and the second has a single, narrow, full-depth strip of land joining the two polar islands. The two configurations are termed 'waterworld' and 'ridgeworld', respectively (figure 4.1).

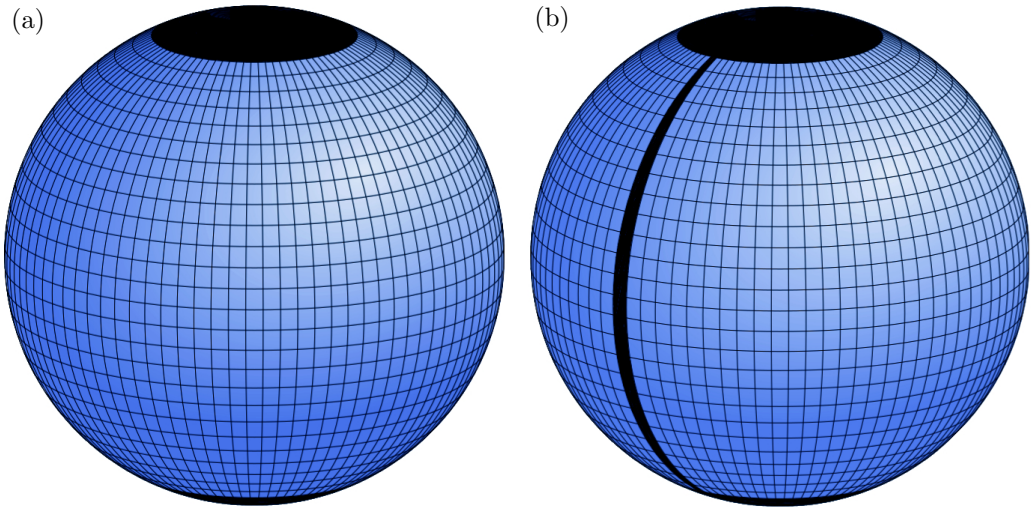


Figure 4.1: (a) Waterworld and (b) Ridgeworld land configuration used in MOMA. The ocean is all full depth; 15 grid boxes, 5.7 km. Land mass is shown in black; the polar islands, required for numerical stability reasons, extend to 68°N/S .

The built in surface forcing profiles in MOMA are based on Earth climatologies, and hence reflect the hemispheric asymmetry of the land mass on Earth. Hence, when making the land hemispherically symmetric in these aquaplanet configurations, the original forcing of the southern hemisphere, where there is a significantly lower proportion of land on Earth, is reflected in the northern to give symmetric forcing profiles.

### 4.1.1 Waterworld

With the absence of a barrier to the zonal flow there is no time mean pressure gradient in the $\lambda$-direction, and hence geostrophic balance predicts the absence of time mean flow in the $\phi$-direction;

$$-f\bar{v} = \frac{1}{\rho}\frac{\partial \bar{p}}{\partial \lambda} \equiv 0 \quad \Longrightarrow \quad \bar{v} \equiv 0, \tag{4.1}$$

where an overbar represents a time mean quantity. Without poleward geostrophic flow there are strong zonal currents circling the planet at all latitudes, the strength of which is bounded primarily by bottom friction. The currents travel westward at low latitudes, with a maximum velocity of $1.76\,\mathrm{m\,s^{-1}}$ at the equator, and eastward at high latitudes, peaking in strength at $0.38\,\mathrm{m\,s^{-1}}$ (figure 4.2). This is in contrast to the maximum strength of $0.1\,\mathrm{m\,s^{-1}}$ in the poleward flow just north and south of the equator, an order of magnitude weaker than in the zonal direction (figure 4.3). Despite the poleward geostrophic flow being zero, this strength of poleward flow results from Ekman currents which are forced by the surface wind stress.

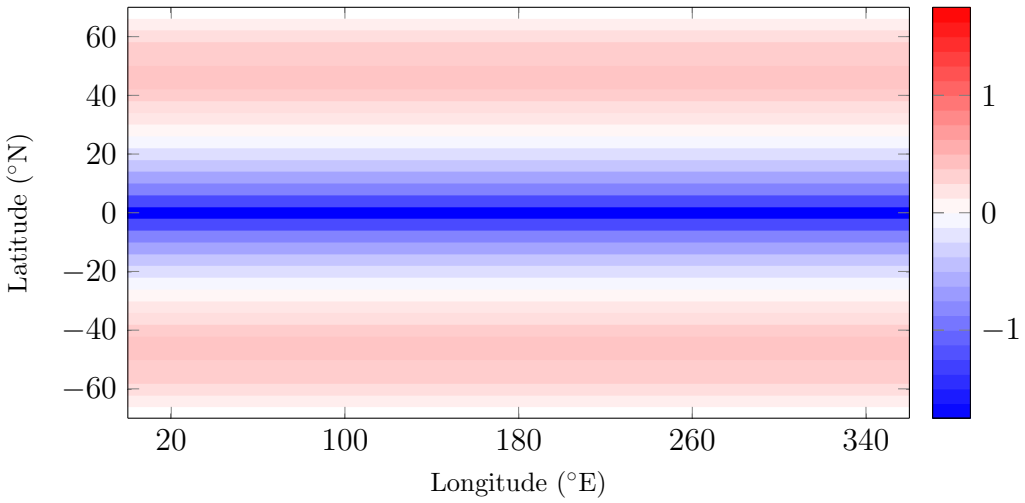


Figure 4.2: Quasi-steady state eastward ocean surface velocity ($\mathrm{m\,s^{-1}}$) for a waterworld configuration.

The free surface height reflects the zonal nature of the surface currents (figure 4.4). The maxima in the free surface height of 3.2 m occur in the region of convergence in each hemisphere; at 30°N/S where the direction of the zonal current reverses. The free surface is below the reference height poleward of 40°N/S, where the flow is westward, and reaches a minimum of 8.9 m below

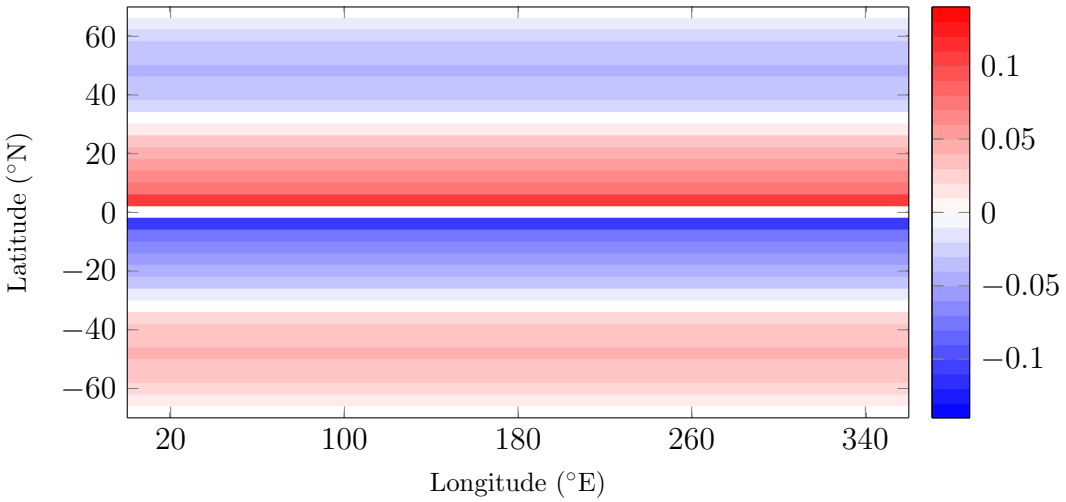


Figure 4.3: Quasi-steady state northward ocean surface velocity ($\mathrm{m\,s^{-1}}$) for a waterworld configuration. Note the different scale to the zonal velocity (figure 4.2).

at the coast of each polar island.

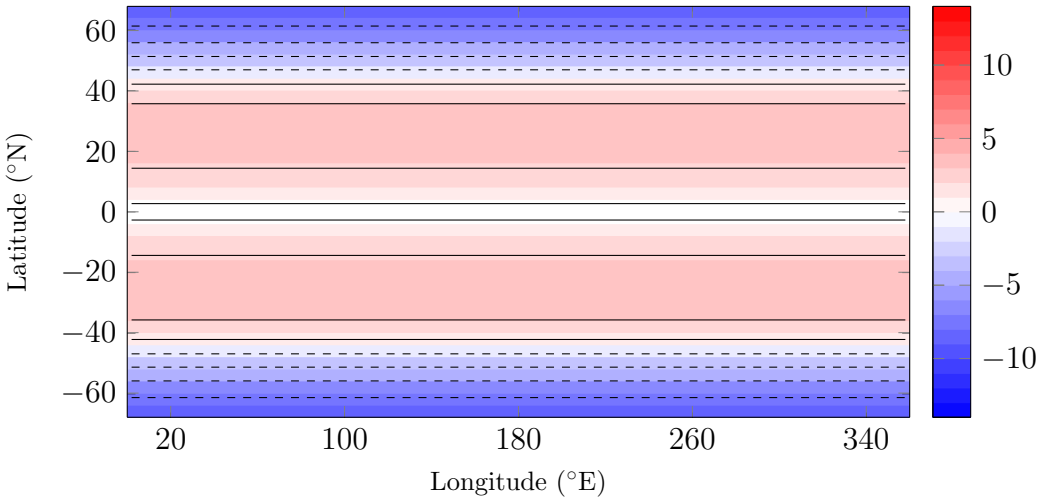


Figure 4.4: Quasi-steady state ocean free surface height (m) for a waterworld configuration. Contour interval is 2 m.

The overturning streamfunction shows a series of deep overturning cells which extend from the surface to the sea floor (figure 4.5). These cells are driven by surface wind forcing which, through Ekman transport, creates a region of convergence in the mid-latitudes and divergence at the equator and high latitudes, resulting in downwelling and upwelling of water, respectively. Without geostrophy driving flow poleward these wind-driven cells carry water to the deep ocean. The wind-forcing is balanced by the horizontal

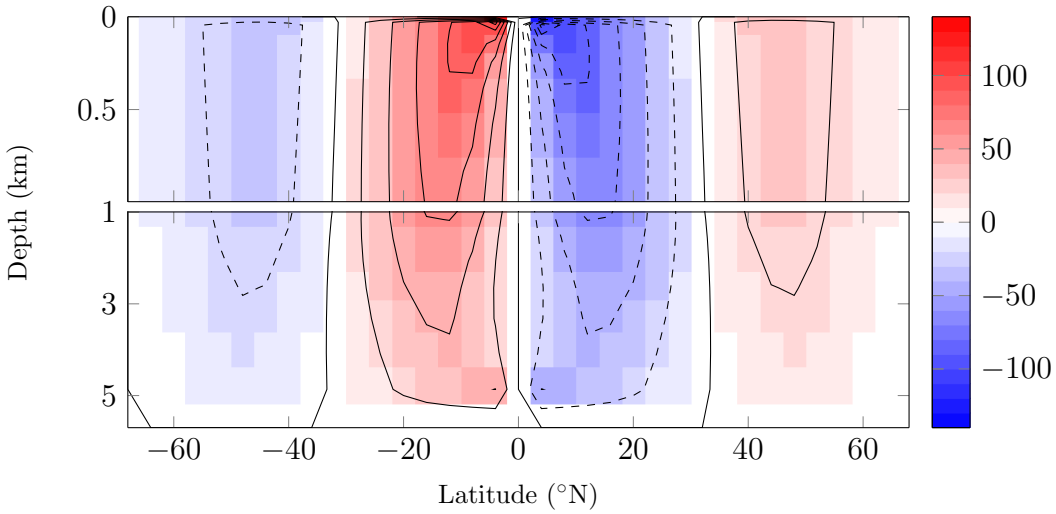


Figure 4.5: Quasi-steady state ocean overturning streamfunction (Sv) for a waterworld configuration. Contour interval is 20 Sv, positive circulation is anti-clockwise. Note the expanded vertical scale in the upper 1 km of the ocean.

momentum viscosity, which is used as a parameterisation for eddies in MOMA, and bottom friction. This deep circulation pattern is reflected in the zonally-averaged temperature; deep advection of warm surface water by Ekman pumping in the mid-latitudes, and Ekman upwelling of cooler water at the equator and high latitudes (figure 4.6).

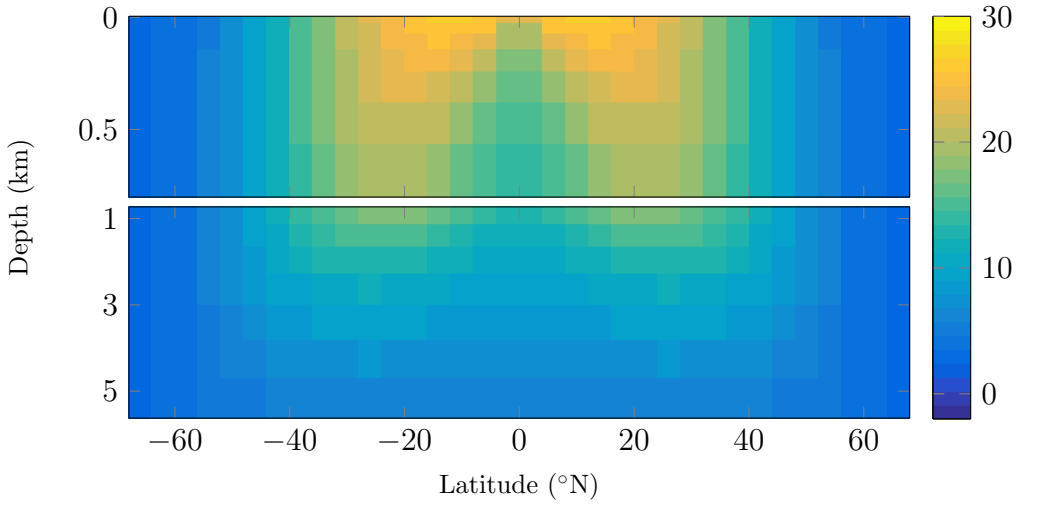


Figure 4.6: Quasi-steady state zonally-averaged ocean temperature (°C) for a waterworld configuration. Note the expanded vertical scale in the upper 1 km of the ocean.

Other modelling studies of the waterworld aquaplanet configuration have

been carried out using a coupled atmosphere-ocean general circulation model (AOGCM); the Fast Ocean, Rapid Troposphere Experiment model (FORTE), in which MOMA is coupled with the Reading Intermediate General Circulation Model (IGCM3) (Smith et al. 2006), and the Massachusetts Institute of Technology general circulation model (MITgcm) (Marshall et al. 2007). On comparing the results from MOMA to those from these two AOGCMs for similar waterworld configurations, the structure of the resulting circulation is found to be in agreement across models. There are strong zonal currents which agree in their pattern of direction and relative strength, and the overturning cells have the same deep structure with the locations of deep water formation in the mid-latitudes of each of the models all lying within $10^\circ$ of $30^\circ$N/S. In the case of the MITgcm it is possible to completely remove all land as a cubed sphere is used for the grid, which avoids issues with convergence of the grid lines at the poles and allows the modelling of a waterworld configuration without polar islands. The similarity of the results from the MITgcm and MOMA shows that the presence of land covering the poles does not qualitatively change the ocean circulation.

When there is no geostrophy to drive meridional currents eddies are a critical process in the poleward transport, in an analogous way to the Antarctic Circumpolar Current (ACC) on Earth (Hallberg & Gnanadesikan 2006). In this scenario the primary forces in balance are the surface wind forcing and friction, both at the bottom, and internally which results in return flow at all depths (Smith et al. 2006). An idealised study of the ACC concludes that the current is predominantly driven by wind forcing when there is no barrier, and even a partial barrier has significant implications for the flow; introducing a half depth barrier, and hence a zonal pressure gradient, increases the transport in the ACC by a factor of three (Gill & Bryan 1971). When investigating the impact of wind forcing on eddy transport in the ACC it is shown that it is a key influencing factor, and hence highlights the associated issues with parameterising eddies in OGCMs (Hallberg & Gnanadesikan 2006).

An alternative to the diffusive representation of eddies which is used here, and an intermediate step to the expensive full resolution of eddies, is the Gent-McWilliams (GM) parameterisation (Gent & McWilliams 1990). The GM parameterisation involves mixing along isopycnals and eddy-induced

advection of tracers, in comparison to the simpler cartesian diffusion of an eddy viscosity approach. By modelling a waterworld configuration with these two parameterisations, eddy viscosity and GM, in the same coarse resolution coupled model in turn, it is shown that the former produces acceptably similar results to the latter (Smith et al. 2006). However, this is only shown in a single model set up and cannot be assumed to be a reasonable approximation in all configurations, where other influencing parameters may be varied. For example, more specific investigation of the ACC shows the lack of ability of parameterisations to accurately react to changes in wind forcing (Hallberg & Gnanadesikan 2006).

Parameterising eddies through diffusive processes is a crude approximation which has been derived and verified for an Earth-like scenario. This restricts its validity in different scenarios, which is important to remember when considering modelling with this parameterisation in alternative configurations. Due to this unreliability, the unknown response of eddies to changing ocean and planetary properties, and the lack of feasibility of running an eddy-resolving model for global sensitivity studies, this land configuration will not be used any further in this study due to its inherent high dependence on eddy transport.

### 4.1.2 Ridgeworld

In contrast to waterworld, a meridional barrier at all latitudes means geostrophic currents dominate the poleward flow in the ridgeworld configuration. This makes the ocean dynamics for a ridgeworld configuration closer to those in an ocean basin on Earth than for a waterworld configuration, despite the continental configuration for a ridgeworld configuration being more geographically similar to waterworld than Earth. The free surface height clearly shows the familiar gyres in each hemisphere with strong, poleward-flowing western boundary currents in the mid-latitudes (figure 4.7). The similarity is also clear in the comparison of the zonally-averaged temperature distribution (figure 4.8); there is a much shallower thermocline than that seen for a waterworld configuration, and it is notably similar to that of the Earth-like configuration (figure 3.8). Hence, ridgeworld may be considered as a general scenario for a planet with oceans

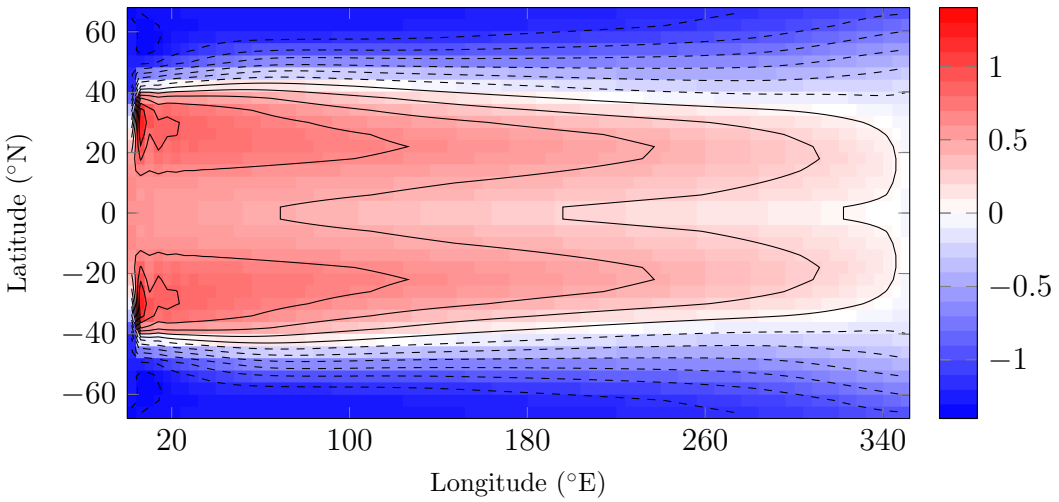


Figure 4.7: Quasi-steady state ocean free surface height (m) for a ridgeworld configuration. Contour interval is 0.2 m

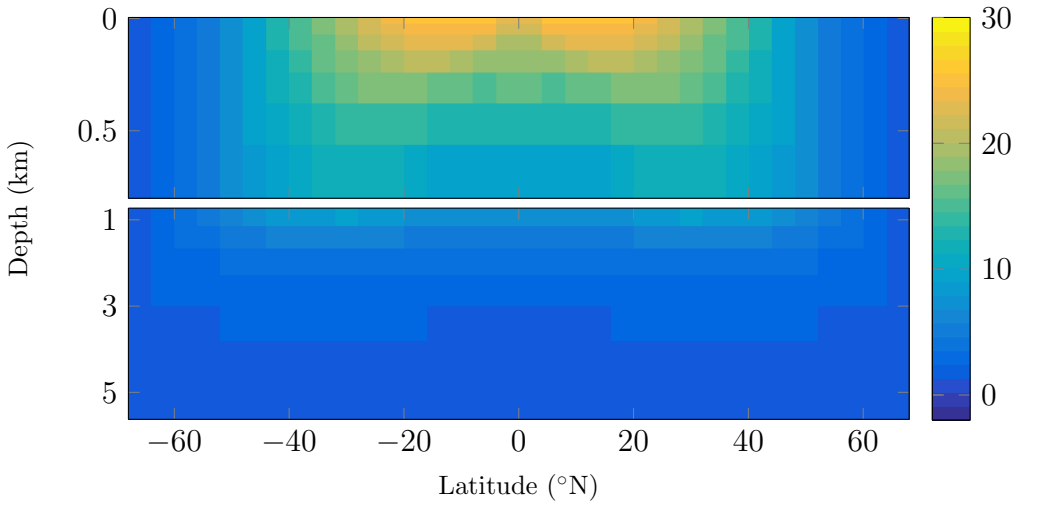


Figure 4.8: Quasi-steady state zonally-averaged ocean temperature (°C) for a ridgeworld configuration. Note the expanded vertical scale in the upper 1 km of the ocean.

and significant latitudinal land coverage, and is used here as the idealised configuration in MOMA throughout. The similarity of the circulation for a ridgeworld configuration to that of an Earth-like configuration, as well as the large contrast to a waterworld configuration, is a result which has been demonstrated using coupled AOGCMs; both with polar islands (Smith et al. 2006) and without (Enderton & Marshall 2009). A ridgeworld configuration is therefore used as a control run (§4.2).

### 4.1.3 Further possibilities

Many studies have investigated the influence of land configuration on ocean circulation with differing applications. Most commonly the purpose is to deepen the understanding of the ocean circulation on present day Earth, but there have also been efforts to understand the climate of the early Earth, and more recently exoplanetary applications have emerged.

A similar configuration to ridgeworld with a significantly wider land mass connecting two polar islands, and hence a narrower ocean basin, results in the same qualitative circulation as ridgeworld; gyres in each hemisphere with strong western boundary currents, and a thermally-driven, hemispherically-symmetric overturning circulation with deep water formation at the poles (Smith & Dubois 2004) (figure 4.9). The deep overturning cells in this scenario are stronger than those of ridgeworld, and hence a smaller meridional temperature gradient is sustained. Most deep water formation occurs in the high latitudes, which have warmer surface waters than ridgeworld, and hence the deep ocean is much warmer at over 8°C in the deepest parts. The smaller difference in the temperature between water at the surface and in the deep ocean which results means that, despite the stronger overturning circulation, the total poleward heat transport is less than for a ridgeworld configuration.

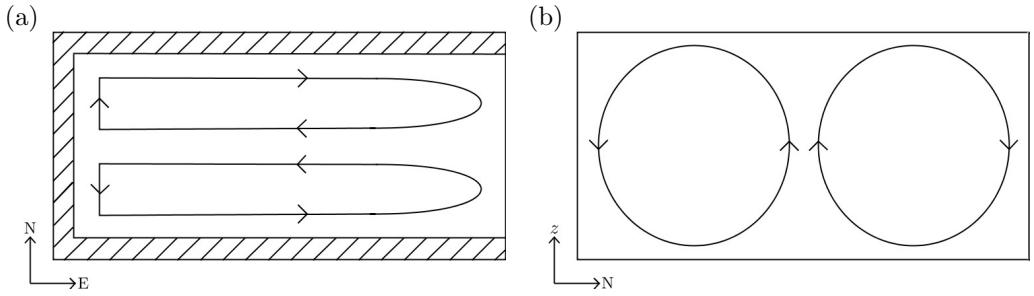


Figure 4.9: Schematics for a ridgeworld-like land configuration showing (a) land configuration (hatched area) and horizontal circulation in the surface layer, and (b) meridional overturning circulation.

A variant which is dynamically closer to waterworld is a scenario where the ocean is of variable and random depth, up to a maximum of 4000 m, with 1-5% land coverage (Kiernet et al. 2013). Including some experimentation with locating archipelagos, it is found that this range of topographical

scenarios has little impact on the circulation; all configurations result in the zonal currents and deep, wind-driven overturning cells seen for a waterworld configuration (figure 4.10).

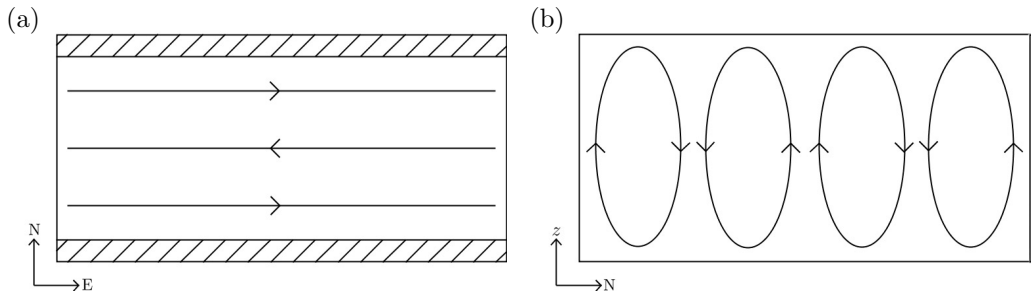


Figure 4.10: Schematics for a waterworld-like land configuration showing (a) land configuration (hatched area) and horizontal circulation in the surface layer, and (b) meridional overturning circulation.

Many studies have analysed the impact of the presence of a gap in the high southern latitudes of a meridional barrier due to its similarity to Drake Passage on Earth, as well as to investigate a simple combination of a waterworld and ridgeworld configuration. The general behaviour which results from this configuration is hemispherically asymmetric, with a waterworld-like structure in the latitudes of the gap and a ridgeworld-like structure elsewhere (figure 4.11), a contrast which is due to the lack of a zonal pressure gradient in the range of latitudes with no land (Smith et al. 2006). Deep water formation primarily occurs in the high northern latitudes, increasing by about 50% compared to that with a complete barrier (Bjornsson & Toggweiler 2001). Deep water travels southward at depth and, in contrast to the symmetric cases discussed, continues across the equator to a region of upwelling at the southern limit of the barrier, poleward of which diffusive processes dominate the transport. The same circulation is found when modelling with a similar configuration but without polar islands, which is consistent with the concluded limited influence of polar islands, identified in the equivalent waterworld and ridgeworld model comparisons (Enderton & Marshall 2009).

The investigation of the influence of a gap in the meridional barrier is furthered by varying the depth to which the gap extends. Due to the induced zonal pressure gradient across the barrier, reducing the depth of the gap from full depth to half depth increases the transport of the circumpolar current by a factor of three (Gill & Bryan 1971). Adding a distribution of subsurface

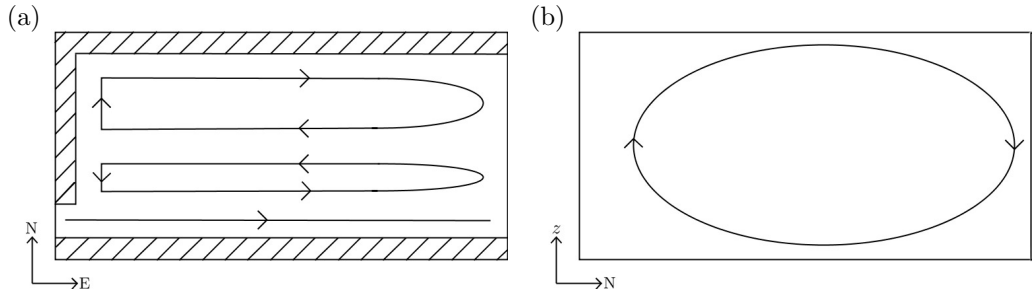


Figure 4.11: Schematics for a ridgeworld-like land configuration with an opening similar to Drake Passage showing (a) land configuration (hatched area) and horizontal circulation in the surface layer, and (b) meridional overturning circulation.

ridges throughout the ocean is found to enhance the effect of introducing the break in the meridional barrier (Bjornsson & Toggweiler 2001); the circulation from northern deep water formation is strengthened and the increase (decrease) of temperature and salinity in the northern (southern) hemisphere is greater.

As expected, maintaining a hemispherically-symmetric land configuration is reflected in the symmetry of the results. With a gap in a meridional barrier which is centred about the equator there is a similar combination of waterworld and ridgeworld features as in the case when a similar gap is off centre; a strong zonal current over the latitudes of the gap and surface gyres poleward on each side. However, a crucial difference is the lack of cross-equatorial flow, deep water is formed at each pole and upwells in the mid-low latitudes of the same hemisphere (Enderton & Marshall 2009).

A configuration with a representation of Drake Passage can be advanced toward an Earth-like configuration by modelling with multiple ocean basins, whilst maintaining a circumpolar gap. With two identical basins the meridional circulation has a similar structure to having just one, however, the northern deep water formation is isolated to just one of the basins and hence there is a dramatically different overturning circulation in each (Marotzke & Willebrand 1991). Changing the width of each basin can influence which of them hosts the deep water formation (Nilsson et al. 2013). Alternatively, breaking the symmetry by altering the southern extent of each barrier independently, and hence introducing a range of latitudes where there is a single meridional barrier, can allow a gyre to extend from one barrier beyond the other and for greater interaction between the water masses in

each of the two basins (Nilsson et al. 2013).

## 4.2 Control run

An aquaplanet with a ridgeworld land configuration, with all other properties unchanged from their default Earth-like values, is used as a control case for the runs throughout the following chapters. Comparison to the results presented here allows the isolation of, and strongest conclusions regarding the effects of changing different planetary and oceanic properties on ocean state.

### 4.2.1 Circulation

The meridional overturning circulation is dominated by a single, buoyancy-driven cell in each hemisphere, which consists of relatively intense deep water formation at the highest latitudes and upwelling in the equatorial region (figure 4.12). The peak in strength in these cells is 58 Sv at 40°N/S

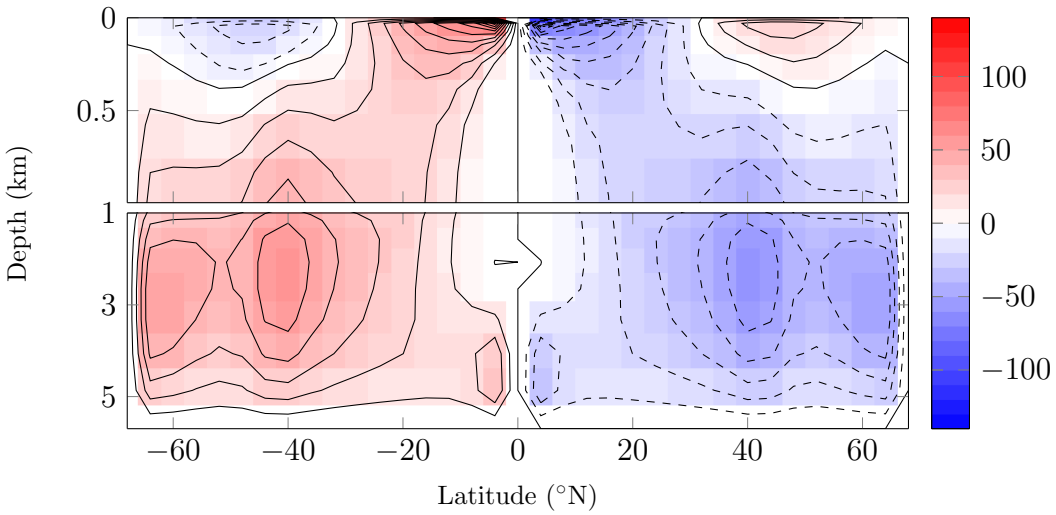


Figure 4.12: Quasi-steady state ocean overturning Circulation (Sv) for a ridgeworld configuration. Contour interval is 10 Sv, positive circulation is anti-clockwise. Note the expanded vertical scale in the upper 1 km of the ocean.

and 3000 m depth. An appropriate application of the two-box model

(chapter 2) to this configuration would consist of two connected boxes in each hemisphere, without a connection between the two since there is negligible cross-equatorial flow in the results. In each hemisphere there is a temperature-driven circulation with sinking in the high latitude box and poleward travelling surface water; a positive circulation in terms of the box model. As discussed above, calculating the freshwater transport in the cells allows conclusions about the stability of the circulation due to the salt-advection feedback (§2.6). In this configuration the freshwater transport is -0.16 Sv at 30°N, which is indicative of an unstable circulation, with the same conclusion for the southern hemisphere circulation due to the symmetry in the configuration.

There are also a series of shallow cells in the surface 500 m, two in each hemisphere which converge in the mid-latitudes, and are strongly concentrated toward the surface. This strong surface component of the circulation is wind-driven; Ekman transport in the meridional direction resulting from the primarily zonal prevailing winds causes convergence, and hence downwelling of water in the mid-latitudes (Price et al. 1987), creating a peak in the overturning circulation away from the primary location of deep water formation in the high latitudes. The overall maximum overturning strength of 105 Sv is located near the surface adjacent to the equator. FORTE (a coupled model with a similar ocean component) gives a slightly stronger deep overturning to MOMA, but with peaks near the poles and in the deep equatorial region rather than the mid-latitudes, however, the wind-driven circulation is weaker, and peaks in the same surface region as in MOMA (Smith et al. 2006). The cells either side of the equator in the deep ocean are a result of low vertical resolution in the model (Miller 2007, p.116).

The behaviour of the near-surface currents is observed from the contours of free surface height (figure 4.7), but may also be concluded from separately analysing the two horizontal components of the velocity field. The most striking features in the surface velocity are a strong, westward current flowing along the equator, peaking at $0.66\,\mathrm{m\,s^{-1}}$ (figure 4.13), and intense poleward-travelling boundary currents at the western edge of the basin of strength $0.47\,\mathrm{m\,s^{-1}}$ (figure 4.14). In contrast to the strong western boundary currents, the equatorward return flow throughout the interior and at the eastern side of the gyre is an order of magnitude weaker than the poleward

velocities; a ratio which is observed in the comparable gyres on Earth (Pedlosky 1990). Overall, there is westward (eastward) flow in the low (high)

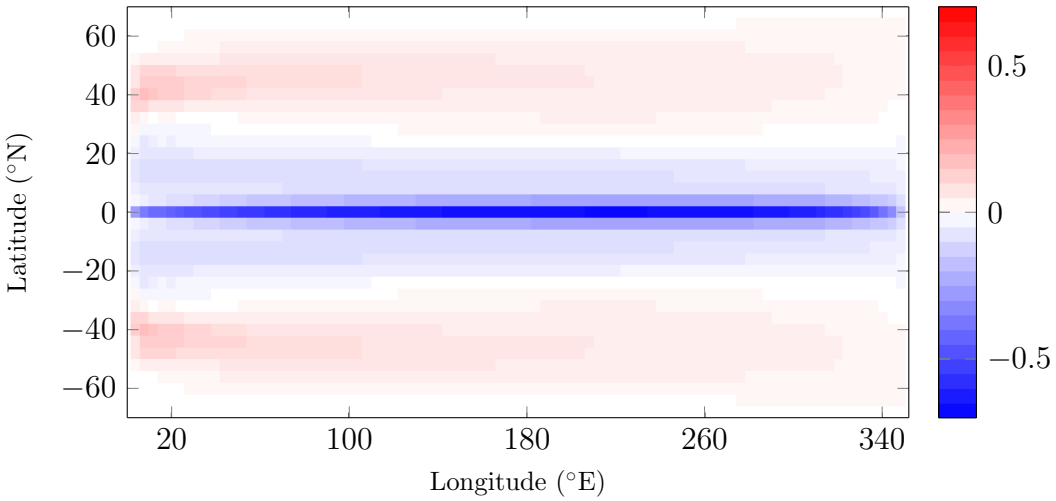


Figure 4.13: Quasi-steady state eastward ocean surface velocity ($\mathrm{m\,s^{-1}}$) for a ridgeworld configuration.

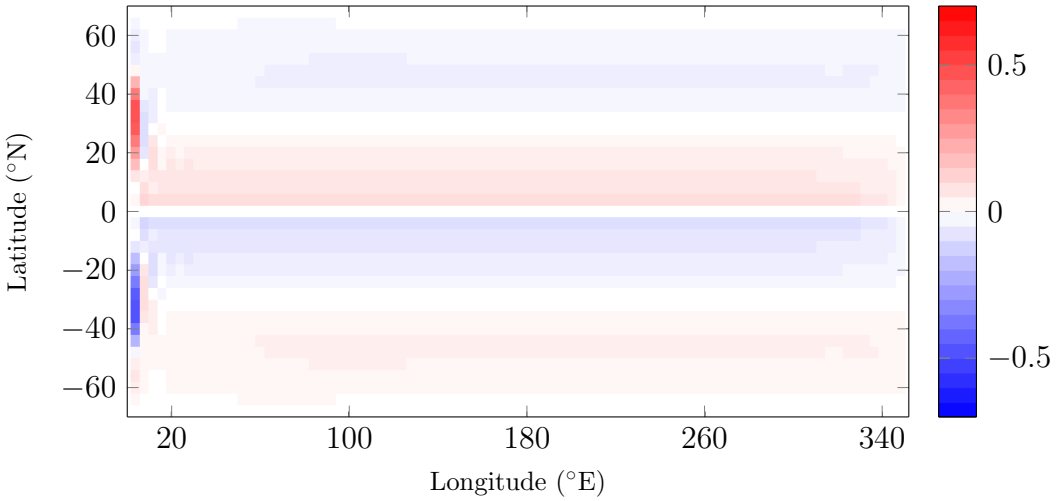


Figure 4.14: Quasi-steady state northward ocean surface velocity ($\mathrm{m\,s^{-1}}$) for a ridgeworld configuration.

latitudes of each hemisphere and, away from the western boundary current, a poleward (equatorward) flow in the low (high) latitudes. This culminates in a single gyre in each hemisphere with a strong western boundary current, which is clear from the contours of free surface height, in particular, the strong gradient at the western edge (figure 4.7).

### 4.2.2 Tracers

The surface temperature of the ocean peaks at just above 26°C at 10°N/S. This latitude corresponds to the maxima in the profile of the surface temperature forcing, which reflects the cooler climate at the equator on Earth. The distribution of heat clearly reflects the movement in the surface gyres; the peak temperatures occur toward the western side of the basin due to the strong equatorial current, and the temperature at the western boundary is greater than other longitudes at any given latitude because of the poleward-travelling western boundary currents found there (figure 4.15). The gradients in surface temperature are less away from these regions where

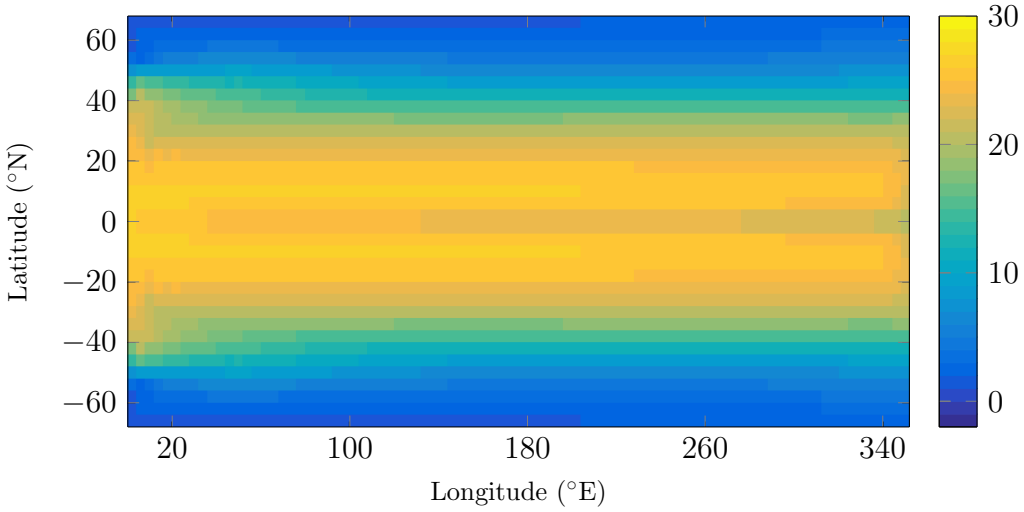


Figure 4.15: Quasi-steady state ocean surface temperature (°C) for a ridgeworld configuration.

the strongest currents occur, with temperatures consistently in the region of 2°C in the highest latitudes and a steady increase from there toward the peaks either side of the equator. At 500 m depth the warmest regions are more extensive; they occur at the western side of the basin in the range of 20-40°N/S and extend 60° longitude into the basin from the coast. Despite being the warmest regions at this depth, they are considerably cooler than the surface, at just 17.5°C, unlike the coldest regions which are similar in structure and temperature at 500 m and the surface (figure 4.16). The poleward shift in the latitude of the peak temperature between the surface and 500 m below is seen as a general trend through the surface layers in the zonally-averaged temperature (figure 4.8). This measure also shows a continuous cooling with depth, which is more dramatic in the upper 1 km,

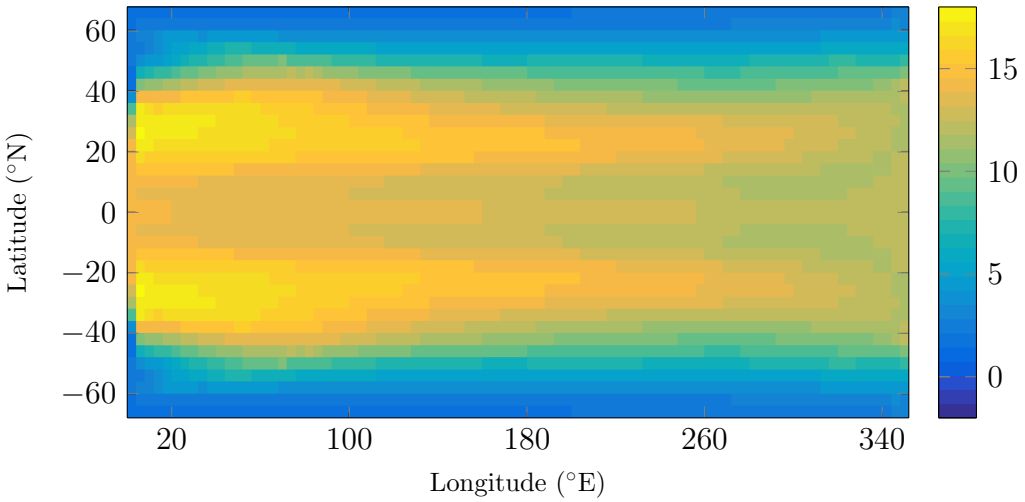


Figure 4.16: Quasi-steady state ocean temperature (°C) at 500 m depth for a ridgeworld configuration.

with temperatures consistently cooler than 5°C below 2500 m.

The surface salinity displays a more zonal pattern than the temperature, but the presence of the surface gyres, in particular the western boundary currents, is again clear (figure 4.17). The peak value of 35.7 occurs in the

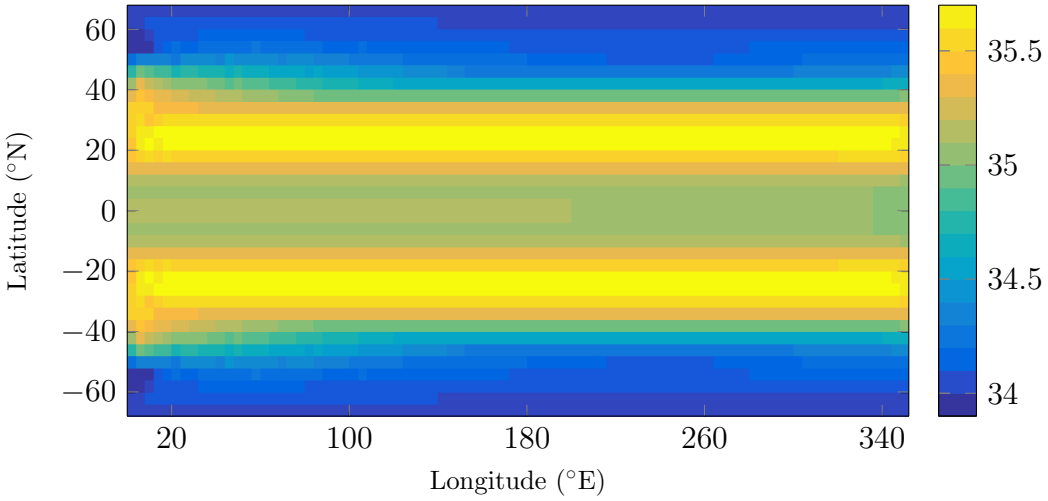


Figure 4.17: Quasi-steady state ocean surface salinity (psu) for a ridgeworld configuration.

region of 20-30°N/S, with a fresher band in between in the low latitudes, and the freshest regions of 34 in the highest latitudes. The surface density has minima of 1023 $\mathrm{kg\,m^{-3}}$ just north and south of the equator, which relate to the warmest regions, and maxima of 1027 $\mathrm{kg\,m^{-3}}$ in the highest latitudes, where the coldest regions occur. This relation of the surface temperature

and density distribution highlights the dominance of the temperature in controlling density, and suggests a thermally-driven buoyancy circulation in the ocean (figure 4.18).

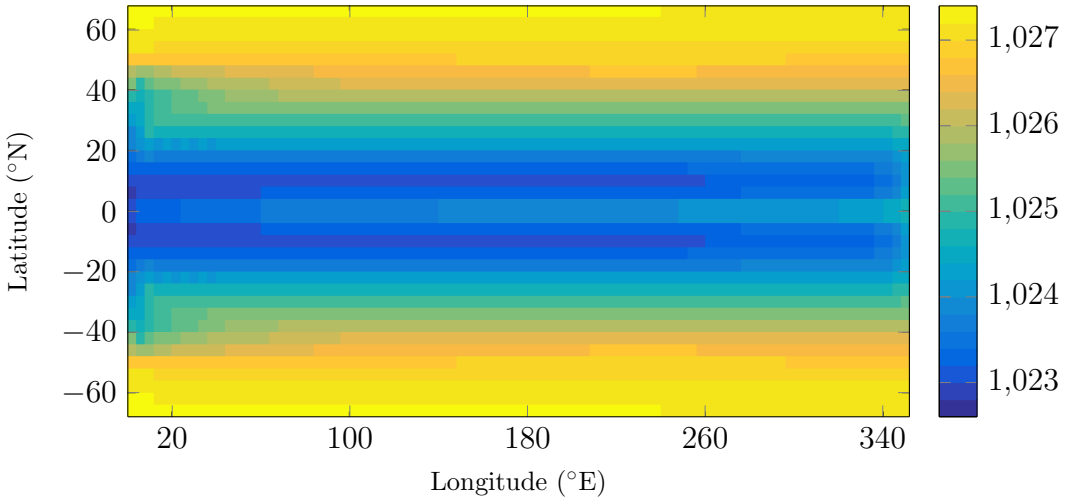


Figure 4.18: Quasi-steady state ocean surface density ($\mathrm{kg\,m^{-3}}$) for a ridgeworld configuration.

At 500 m depth the salinity distribution is very similar to that of the temperature at that depth, in comparison to the notable difference between the two tracers at the surface, with peak value 35.2 (figure 4.19). The

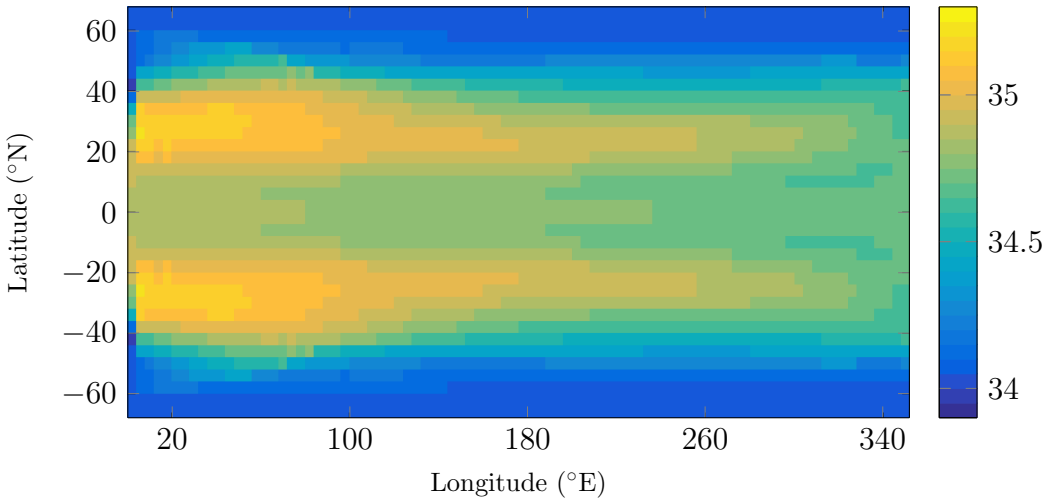


Figure 4.19: Quasi-steady state ocean salinity (psu) at 500 m depth for a ridgeworld configuration.

zonally-averaged salinity differs from that of temperature in having a weaker stratification of the surface layers and a smaller change in the latitude of the peak value with depth (figure 4.20). Similar to the surface, the density at

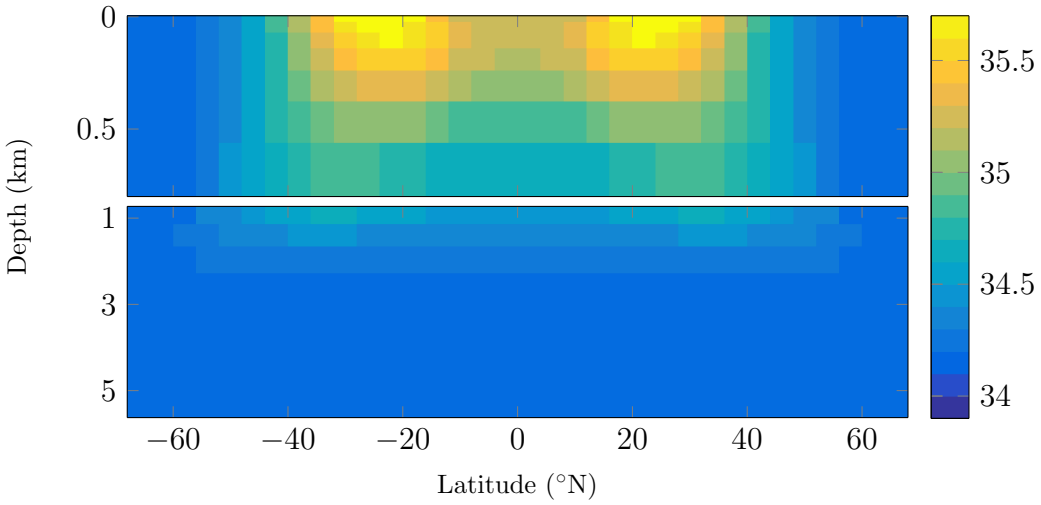


Figure 4.20: Quasi-steady state zonally-averaged ocean salinity (psu) for a ridgeworld configuration. Note the expanded vertical scale in the upper 1 km of the ocean.

500 m depth is again dominated by the temperature; the densest regions are of similar value to that at the surface at the highest latitudes and the lightest are significantly denser at 1026 $\mathrm{kg\,m^{-3}}$ (figure 4.21). Again,

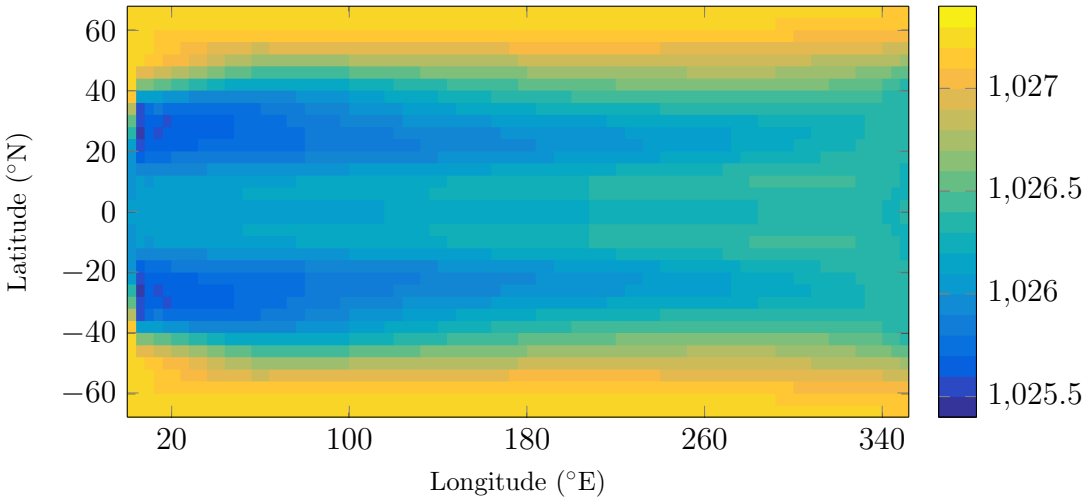


Figure 4.21: Quasi-steady state ocean density ($\mathrm{kg\,m^{-3}}$) at 500 m depth for a ridgeworld configuration.

the zonally-averaged density profile is closer in structure to that of the temperature than salinity, which is most clearly seen in the sharper gradient in the upper ocean and minima in the low latitudes where the warmest regions occur (figure 4.22).

The results from AOGCMs for this configuration, in which the key difference

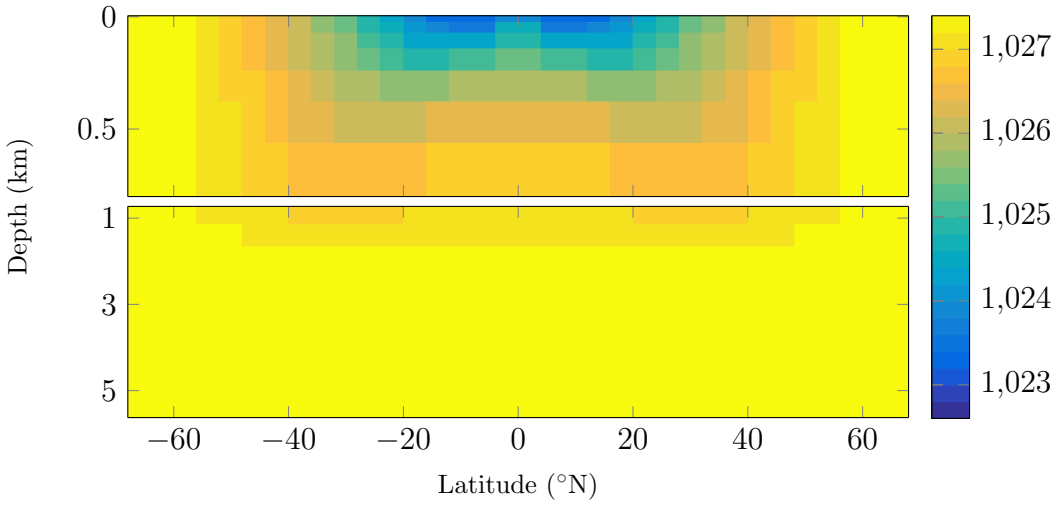


Figure 4.22: Quasi-steady state zonally-averaged ocean density ($\mathrm{kg\,m^{-3}}$) for a ridgeworld configuration. Note the expanded vertical scale in the upper 1 km of the ocean.

is that the surface forcing is not fixed as it is in this study, show similar spatial distributions of tracer quantities. However, there is a notable difference in the range of values; peaks in temperature are at similar latitudes but are greater than 30°C at the surface (Smith et al. 2006, Enderton & Marshall 2009), compared to 26°C here, and 20°C at 500 m (Smith et al. 2006), compared to 17.5°C here. Similarly, salinity values are found to have a much greater range; over 36.5 in the mid latitudes at the surface to a minimum of 33 at the poles (Enderton & Marshall 2009), compared to the much narrower range of between 34 and 35.7 found here. These smaller ranges observed in the results presented here, compared to the coupled model, occur due to the narrower range of forcing values, which is a feature of the zonally-constant forcing profiles that are calculated as averages of observed values.

### 4.2.3 Heat transport

The poleward heat transport peaks at 2.8 PW at 16°N/S, and displays a steady decrease from there toward the poles (figure 4.23). Two coupled modelling studies agree with each other in finding a much smaller magnitude of poleward heat transport, peaking at nearly half the value found here at 1.5 PW (Smith et al. 2006, Enderton & Marshall 2009), however the

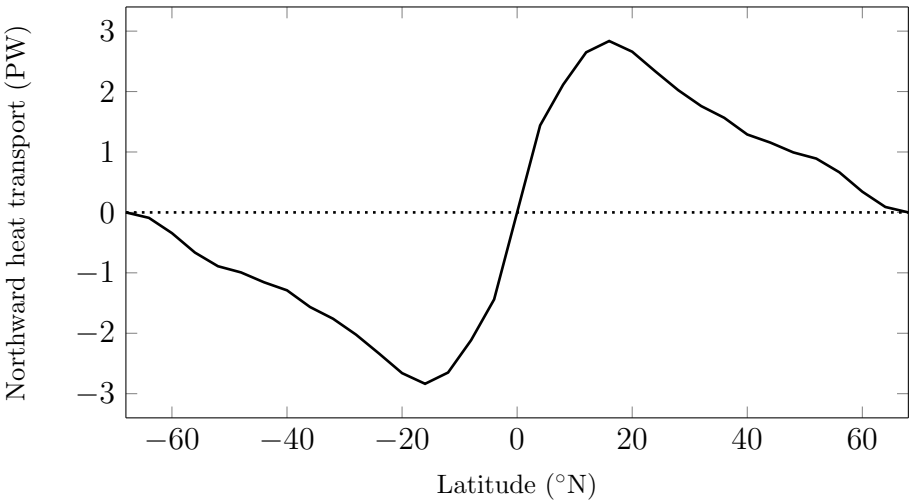


Figure 4.23: Quasi-steady state northward ocean heat transport (PW) for a ridgeworld configuration.

latitudinal structure of the heat transport differs between these studies; both a similar pattern to that found in this study, with the latitudes of the peak value at 18°N/S (Enderton & Marshall 2009), and a peak considerably further poleward at 40°N/S (Smith et al. 2006), are independently found. The corresponding surface heat flux is into the ocean equatorward of 16°N/S and to the atmosphere poleward of that, with peak magnitude $83\,\mathrm{W\,m^{-2}}$ at the equator and $35\,\mathrm{W\,m^{-2}}$ in the high latitudes, respectively (figure 4.24).

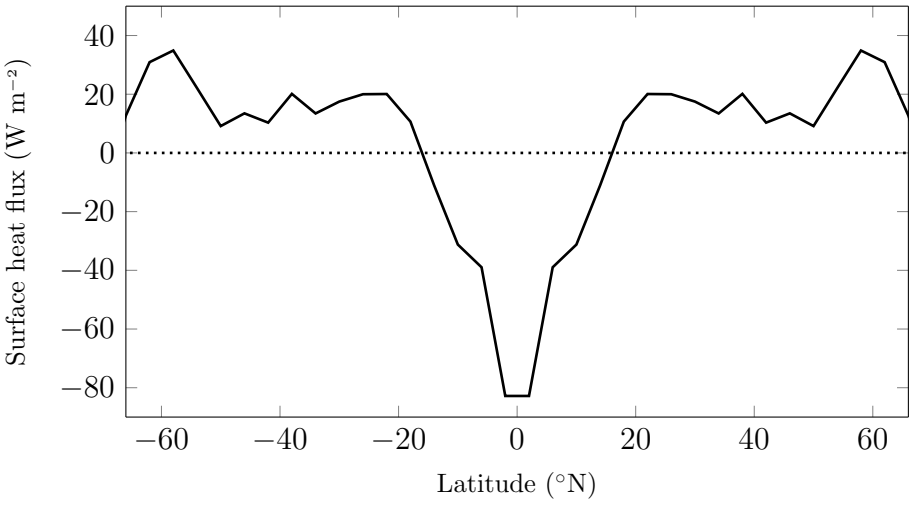


Figure 4.24: Quasi-steady state ocean surface heat flux ($\mathrm{W\,m^{-2}}$) for a ridgeworld configuration. Positive values are from ocean to atmosphere.

## 4.3 Removing wind forcing

Removing wind forcing of the surface of the ocean allows conclusions to be made about the dominant contributions from the wind and buoyancy forcing to the overturning circulation, and their influence on tracer distribution.

### 4.3.1 Circulation

Without wind forcing the overturning circulation does not comprise of any shallow cells, which is expected as these surface cells are primarily wind-driven. Alongside this, there are also significant differences in the deep circulation. As in the wind-driven case, there is a cell in each hemisphere with deep water formation in the high latitudes and upwelling at the equator, but without wind forcing the strength of this overturning is weaker and concentrated further poleward, with a peak of 44 Sv located at mid-depth in the high latitudes (figure 4.25). This is in contrast to the peak of 58 Sv

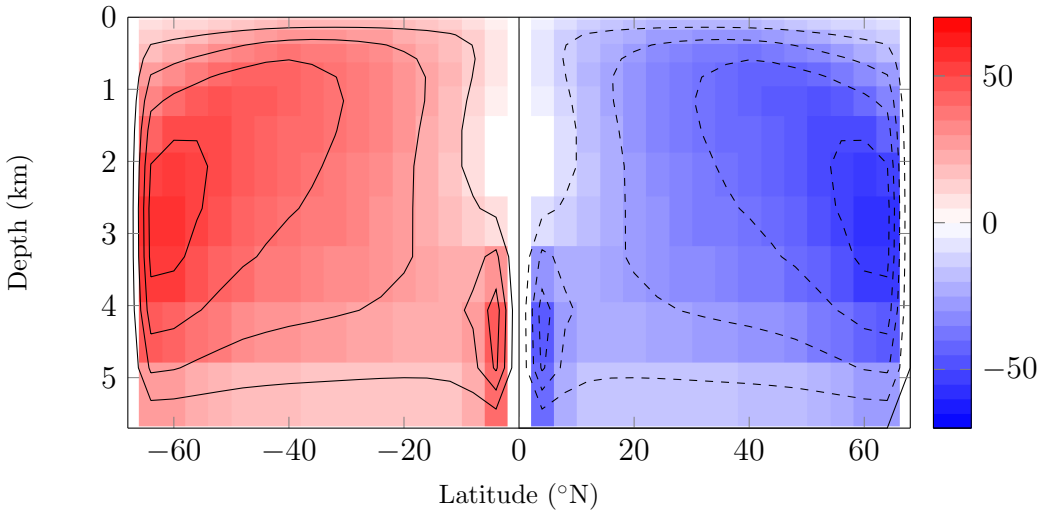


Figure 4.25: Quasi-steady state ocean overturning circulation (Sv) for a ridgeworld configuration without wind forcing. Contour interval is 10 Sv, positive circulation is anti-clockwise.

being located in the mid latitudes in the wind-driven case (figure 4.12), where Ekman pumping at the centre of the gyres adds an additional driver to the deep circulation (Pedlosky 1990). This process is demonstrated when comparing the structure of the circulation with and without wind forcing

here with that of coupled studies; in the coupled AOGCMs, despite the presence of wind forcing at the surface, the circulation is more similar to that of the non-wind-driven case here, which is consistent with the weaker wind-forced overturning in the coupled AOGCM results than in MOMA (Smith et al. 2006, Enderton & Marshall 2009). The box model can be used as a conceptual representation of this configuration in the same arrangement as for the case with wind forcing. Here the salt-advection feedback also suggests an unstable circulation with a freshwater transport of -0.14 Sv at 30°N.

Due to the direct impact of wind forcing on the surface velocities of the ocean it would be expected, and is found, that these are significantly reduced when wind forcing is removed. The greatest difference is the much weaker westward-flowing equatorial current (figure 4.26); $0.08\,\mathrm{m\,s^{-1}}$ compared to

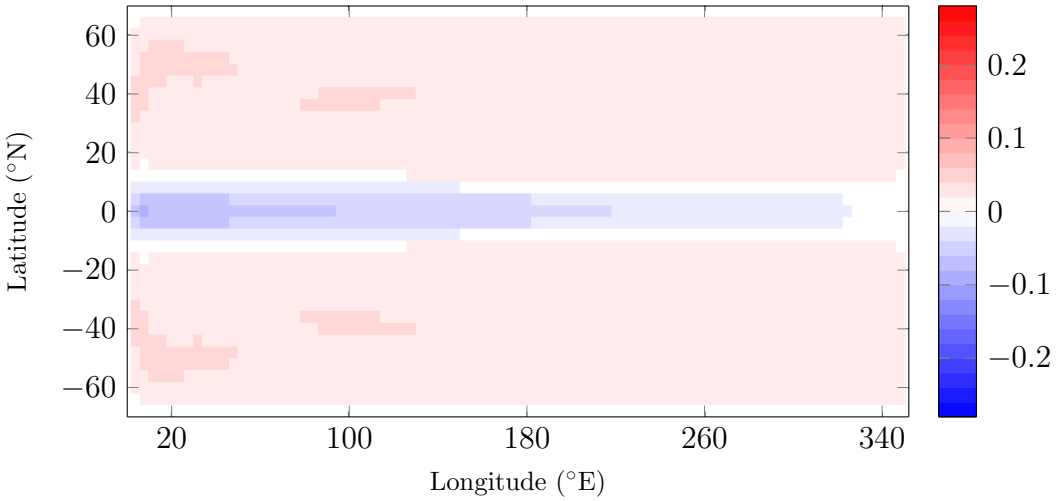


Figure 4.26: Quasi-steady state eastward ocean surface velocity ($\mathrm{m\,s^{-1}}$) for a ridgeworld configuration without wind forcing.

$0.66\,\mathrm{m\,s^{-1}}$ in the wind-driven case (figure 4.13). The poleward surface velocity is negligible away from the poleward-travelling western boundary currents, which are approximately half the strength of those found in the wind-driven case (figure 4.27). Together, the components of the surface velocity field are indicative of the same gyre structure as seen with wind forcing although it is much weaker, which is also clear from mapping the free surface height (figure 4.28). There are steeper gradients in surface height in the wind-driven case, particularly in the regions of intense currents at the western boundary, with a larger variation of 2.7 m compared to 1.6 m without wind forcing. The minima occur in the same location; the high latitudes at

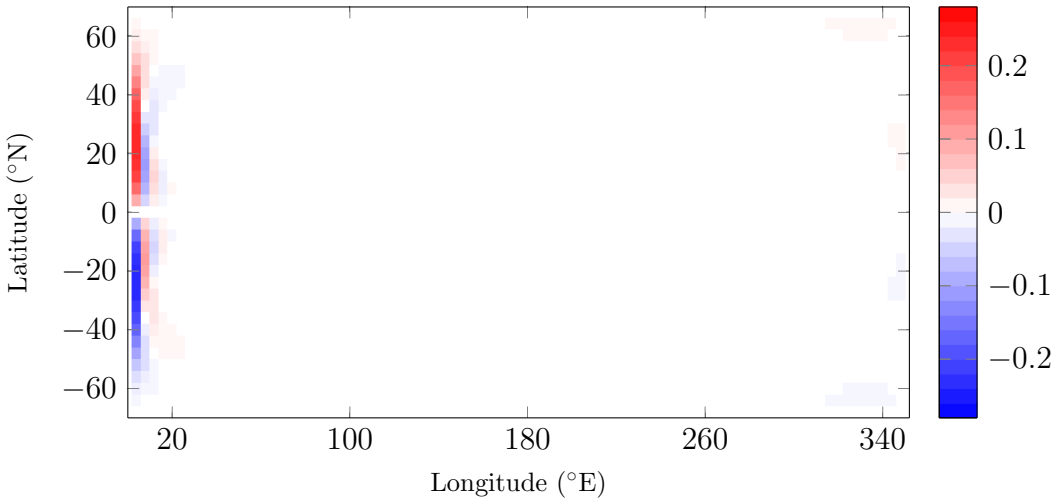


Figure 4.27: Quasi-steady state northward ocean surface velocity ($\mathrm{m\,s^{-1}}$) for a ridgeworld configuration without wind forcing.

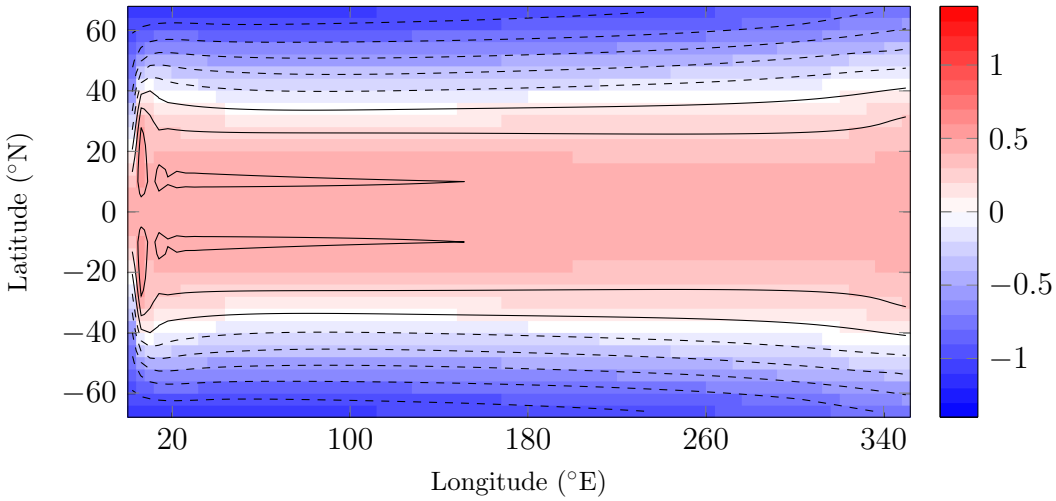


Figure 4.28: Quasi-steady state ocean free surface height (m) for a ridgeworld configuration without wind forcing. Contour interval is 0.2 m.

the western boundary, whereas the maxima are located 20° further poleward, at 30°N/S, in the case with wind forcing.

### 4.3.2 Tracers

Consistent with the impact of wind forcing on the circulation, the greatest differences in the tracer distributions from removing wind forcing are in the surface layers. Without the strong wind-driven current flowing along the equator there is less advection of heat toward the western edge of the

basin, and also a limited upwelling of cooler deep water to the surface in the equatorial regions. The weaker circulation results in a much smaller decline in surface temperature between the peaks in the tropics, of just 0.2°C, which are slightly cooler than in the wind-driven case. There is much less longitudinal variation; the warmest region covers approximately 30° latitude centred about the equator, with a maximum temperature of 25.8°C, and extends across the entire width of the basin (figure 4.29). The

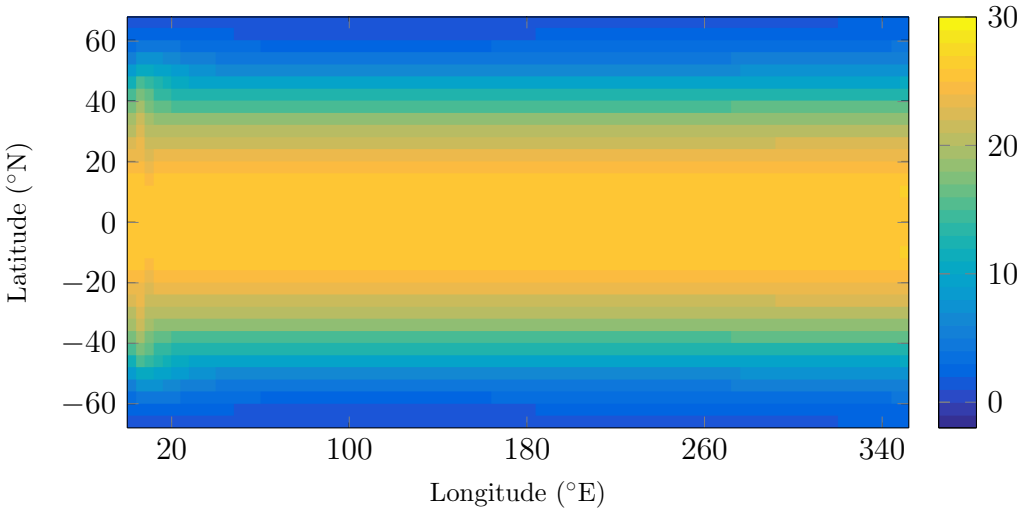


Figure 4.29: Quasi-steady state ocean surface temperature (°C) for a ridgeworld configuration without wind forcing.

surface also shows a more zonal pattern in salinity (figure 4.30) and, more notably, in the density distribution (figure 4.31). There are also smaller

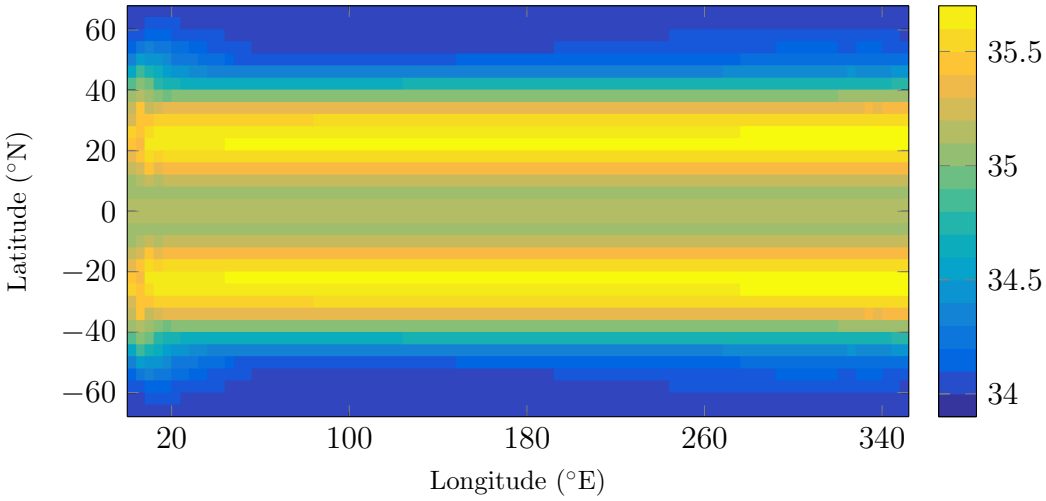


Figure 4.30: Quasi-steady state ocean surface salinity (psu) for a ridgeworld configuration without wind forcing.

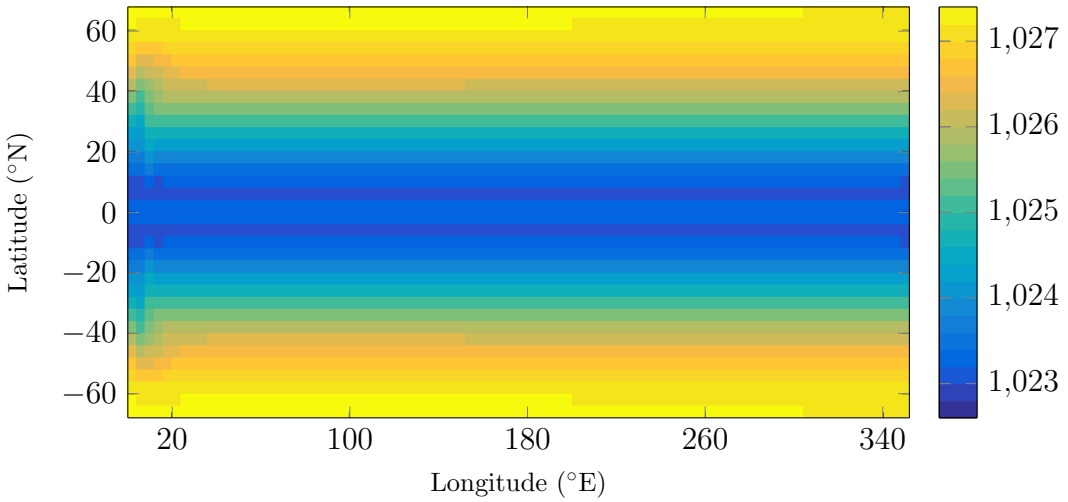


Figure 4.31: Quasi-steady state ocean surface density ($\mathrm{kg\,m^{-3}}$) for a ridgeworld configuration without wind forcing.

meridional gradients in the surface tracers without wind forcing.

With the absence of wind-driven mixing and Ekman pumping in the upper ocean, warmer surface water does not penetrate as deeply and hence the thermocline is shallower without wind forcing (figure 4.32). This result

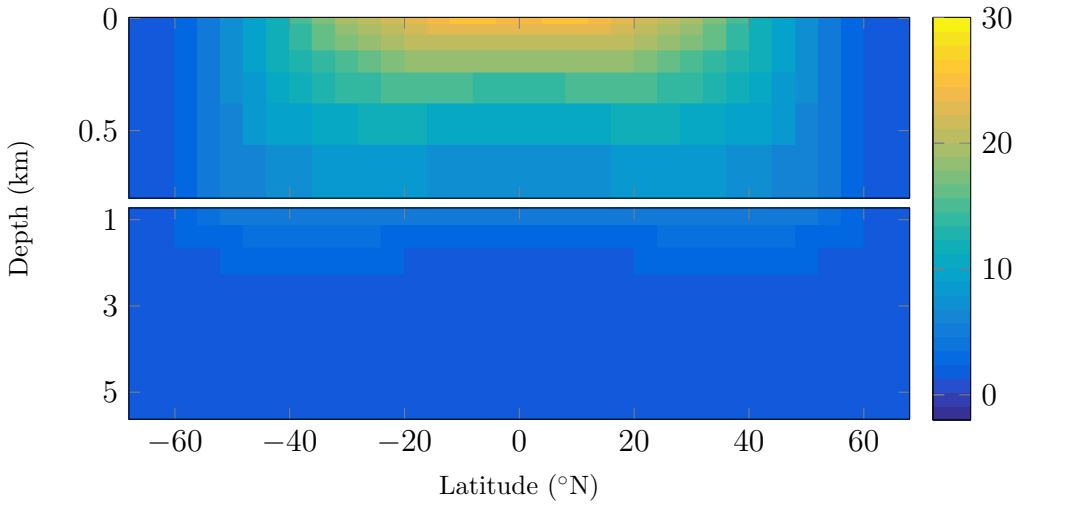


Figure 4.32: Quasi-steady state zonally-averaged ocean temperature (°C) for a ridgeworld configuration without wind forcing. Note the expanded vertical scale in the upper 1 km of the ocean.

has been shown generally in an Earth-like configuration using a version of MOM with wind strengths from 1/2 to 4 times the strength of the Earth climatology (Vallis 2000), where the scaling (thermocline depth) $\sim$ (wind strength)$^{1/2}$ derived previously (Welander 1971) is demonstrated.

With this particularly sharp gradient in temperature in the upper ocean, at 500 m depth the temperature is consistently below 15°C (figure 4.33), which is cooler than in the wind-driven case where downwelling from Ekman

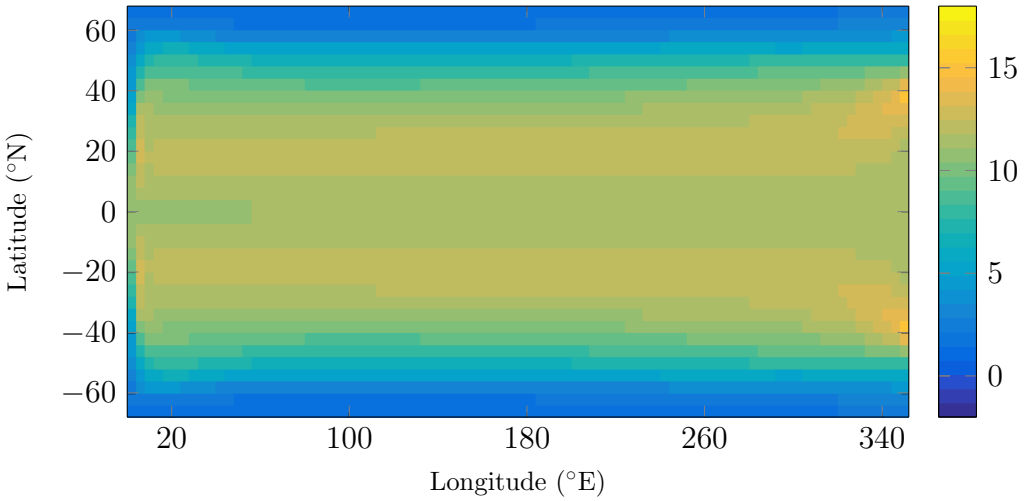


Figure 4.33: Quasi-steady state ocean temperature (°C) at 500 m depth for a ridgeworld configuration without wind forcing.

pumping in the centre of the gyres results in warmer regions at depth (figure 4.16). For the same reason, at 500 m depth the water in the mid-latitudes is considerably fresher (figure 4.34) and denser (figure 4.35) than in the wind-driven case.

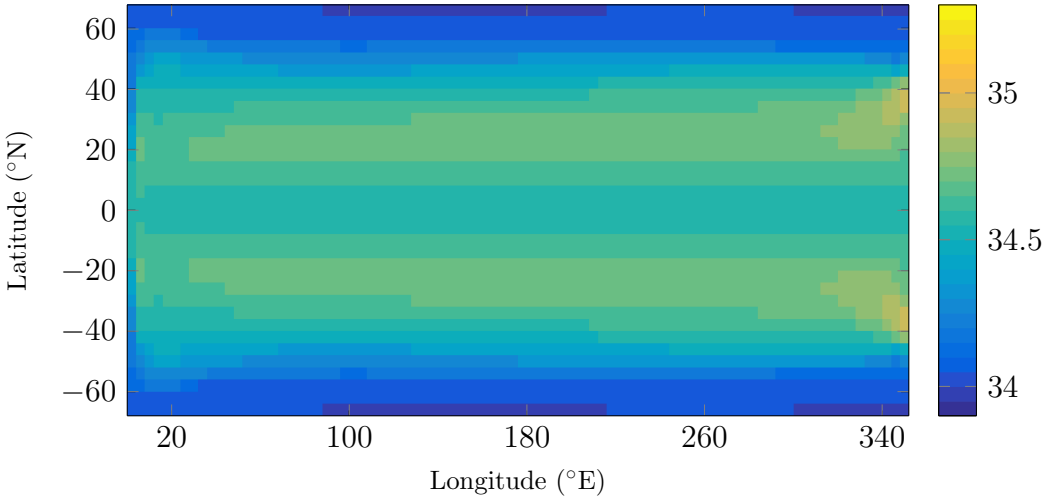


Figure 4.34: Quasi-steady state ocean salinity (psu) at 500 m depth for a ridgeworld configuration without wind forcing.

The zonally-averaged tracer distributions show smaller gradients between the surface and deep ocean, which is warmer (figure 4.32), more saline (figure

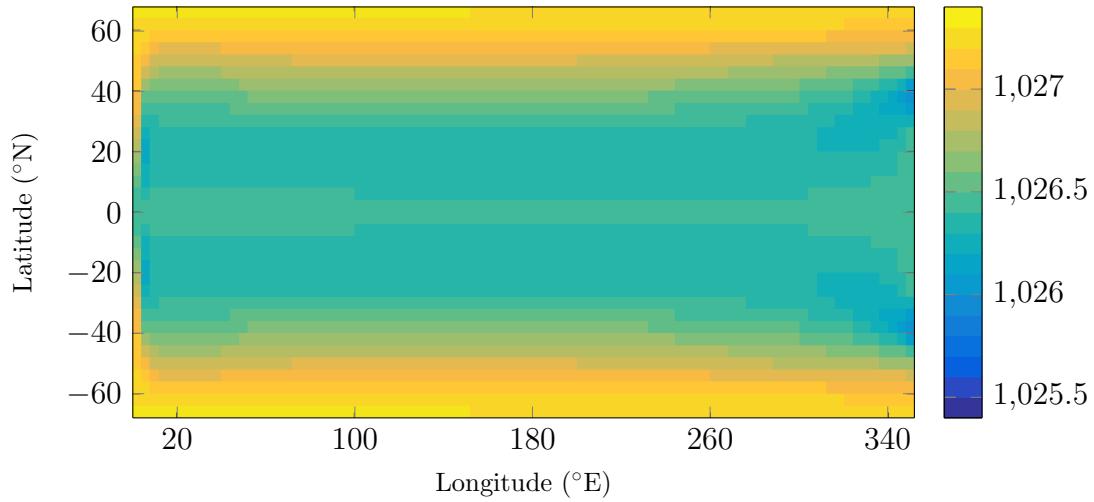


Figure 4.35: Quasi-steady state ocean density ($\mathrm{kg\,m^{-3}}$) at 500 m depth for a ridgeworld configuration without wind forcing.

4.36), and slightly less dense (figure 4.37) than in the wind-driven case. This occurs due to the smaller meridional gradients at the surface, and hence the deep water formed in the high latitudes has these different properties.

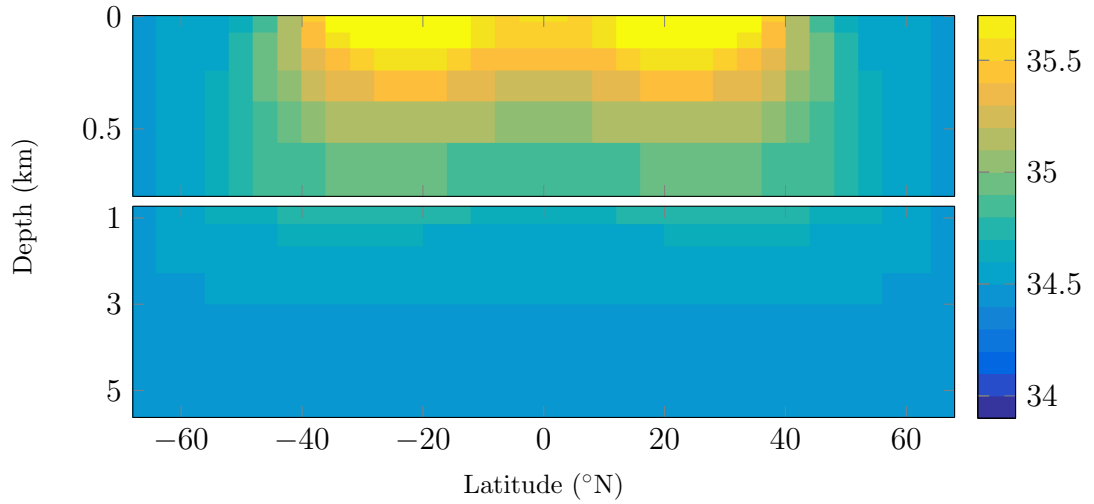


Figure 4.36: Quasi-steady state zonally-averaged ocean salinity (psu) for a ridgeworld configuration without wind forcing. Note the expanded vertical scale in the upper 1 km of the ocean.

### 4.3.3 Heat transport

Wind-forcing enhances the poleward heat transport predominantly in the lower latitudes, below 40°N/S, it lowers the latitude and almost doubles

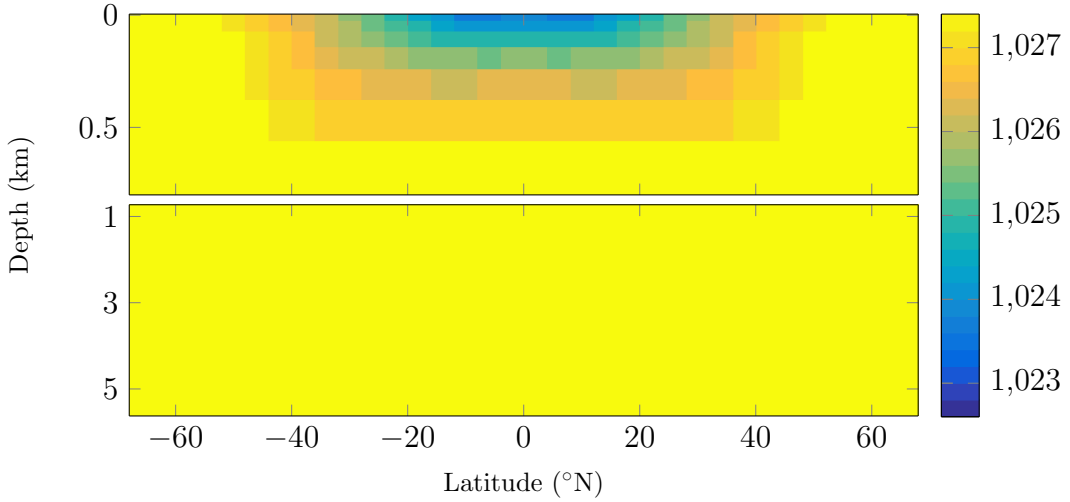


Figure 4.37: Quasi-steady state zonally-averaged ocean density ($\mathrm{kg\,m^{-3}}$) for a ridgeworld configuration without wind forcing. Note the expanded vertical scale in the upper 1 km of the ocean.

the magnitude of the peak value of heat transport from 1.5 PW at 30°N/S without, to 2.8 PW at 15°N/S with wind forcing (figure 4.38). This results in

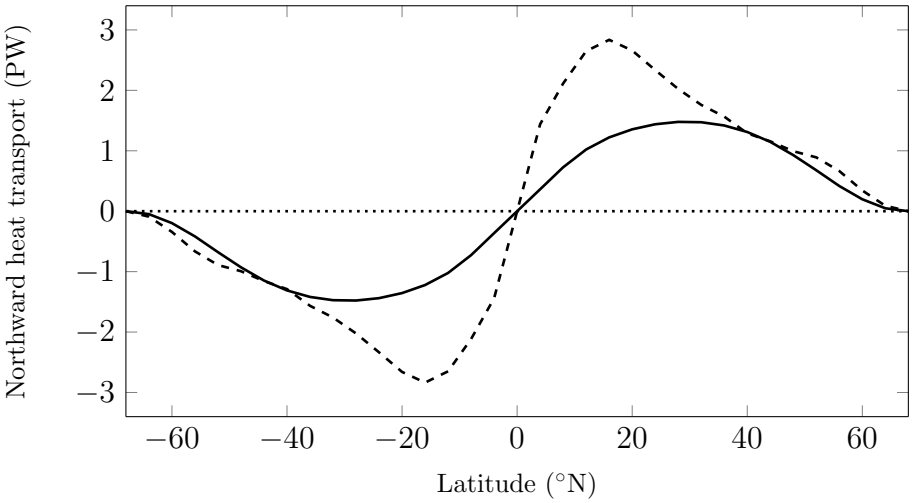


Figure 4.38: Quasi-steady state northward ocean heat transport (PW) for a ridgeworld configuration (solid line) without, and (dashed line) with wind forcing.

a surface heat flux of similar magnitude in the high latitudes in both cases, where the ocean warms the climate, however there is much less warming in the mid latitudes without wind forcing (figure 4.39). Heat is absorbed into the ocean over a much more extensive area in the low latitudes, between 30°N/S, but at a significantly weaker rate than in the wind-driven case, peaking at just $21\,\mathrm{W\,m^{-2}}$ at the equator opposed to $83\,\mathrm{W\,m^{-2}}$ with the

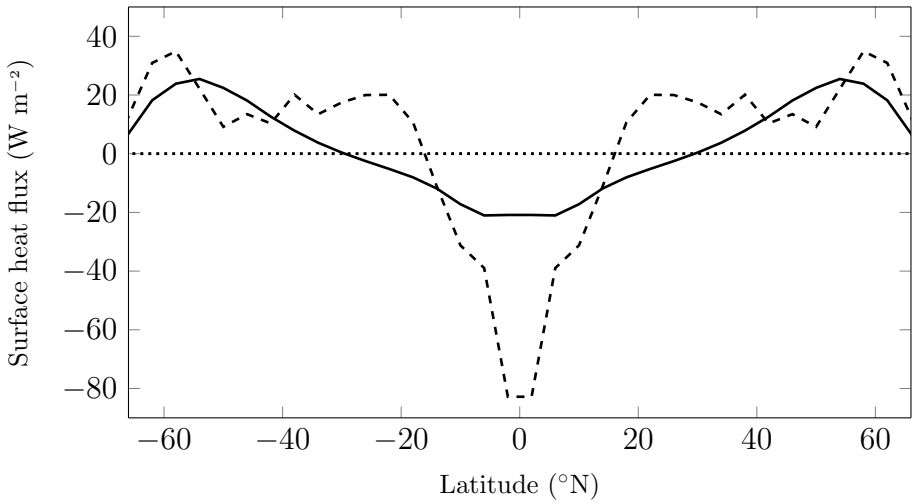


Figure 4.39: Quasi-steady state ocean surface heat flux ($\mathrm{W\,m^{-2}}$) for a ridgeworld configuration (solid line) without, and (dashed line) with wind forcing. Positive values are from ocean to atmosphere.

enhanced surface mixing in the wind-driven case.

## 4.4 Summary

The crucial consideration in the alteration of land configuration is the presence of a meridional barrier in the ocean, a feature which has significant implications for the resulting circulation and tracer distribution. Without any land mass interrupting the zonal flow, geostrophic balance does not govern the dynamics and instead eddy transport becomes the dominant process in the poleward transport, in an analogous way to the Antarctic Circumpolar Current on Earth. Since the eddy parameterisation used in MOMA does not respond to changing oceanic and planetary properties, a land configuration where eddy processes are not dominant is selected to investigate different configurations.

With this conclusion, and also noting that a single full depth barrier is the most general representation of a collection of land masses, the ridgeworld configuration presented here will be used as the default land configuration throughout the following work. In simulations using the coupled model, a single cell barrier is also used but the barrier extends to one grid box below the ocean surface to remove the direct effect of the land on the atmosphere

and give the clearest conclusions about the atmospheric behaviour. The results from the ocean model when run with the ridgeworld configuration and all other properties in their Earth-like state, are used for comparison to those obtained when varying other factors in the following chapters, in order to make conclusions about their impact on ocean circulation. The results obtained in the ridgeworld configuration of MOMA show the same behaviour of circulation and tracer distribution as those obtained from similar configurations using coupled atmosphere-ocean models.

Conclusions about the buoyancy- and wind-driven components of the overturning circulation can be made by running the model in an identical configuration with and without wind forcing and comparing the results. Making this comparison with results from the ridgeworld configuration shows that wind forcing not only strengthens the surface currents and produces additional strong and shallow overturning cells, with the associated deeper mixing of tracers, but also enhances the deep ocean circulation. This approach allows for separation of the dominant wind- and buoyancy-driven components of the circulation without conclusions about the interactions between the two components.

# Chapter 5

# Ocean salinity

The concentration of salt in an exoplanetary ocean is not necessarily the same as that of the oceans on Earth, and hence the impact of varying the salinity in the ocean is investigated. A general relationship between the mean salinity and salinity gradients is derived, which has significant implications for the circulation at different mean salinities. The importance of ocean salinity is shown through modelling, with the box model and MOMA, of cases ranging in salinity from freshwater to that of the Dead Sea on Earth.

Some of the work in this chapter is published in
Cullum, J., Stevens, D.P. & Joshi, M.M. (2016) 'Importance of Ocean Salinity for Climate and Habitability', *Proc. Nat. Acad. Sci.* 113(16), 4278-4283.

## 5.1 Salinity range

The salinity of any oceans on a terrestrial planet is controlled by the quantity of water and the quantity of dissolved salt which the seawater on the planet is composed of. There is some uncertainty around the method of delivery of water to a planet, with more recent studies suggesting it is largely determined during planetary formation with later delivery from comets being responsible for only a limited amount of the water on Earth (Morbidelli et al. 2000, Raymond et al. 2007, Fischer-Gödde & Kleine 2017). The dissolved salt is determined primarily by delivery from rivers and groundwater; for example weathering processes extract sodium from rocks which combines with chlorine released from volcanic activity to give sodium chloride, and extraction occurs through salt deposits on the sea floor and as evaporites, as well as brine in the pores of sedimentary rock (Knauth 1998, Hay et al. 2006). Variability in these factors gives a large range of possibilities for ocean salinity.

There is evidence that the mean salinity of the oceans on Earth has decreased from up to double the present day level since the Archean, 2500 million year ago (Knauth 1998), and from above $50\,\mathrm{g\,kg^{-1}}$ from the start of the phanerozoic, 540 million years ago (Hay et al. 2006). These changes over geological timescales are caused by a lack of instantaneous balance in the delivery and extraction of salt to the ocean, as well as changes in the volume of ice sheets. Climate modelling of Earth with double the present day salinity finds a reduction in strength of the overturning circulation in the North Atlantic of 20%, as well as responses in the global mean sea surface temperature (Williams et al. 2010).

Modelling of water delivery during planetary formation concludes that there could be an extensive range of possible ocean masses; planets in the habitable zone may have a small fraction to hundreds of times the volume of water in the oceans on Earth (Raymond et al. 2004, 2007). Ocean salinity can also be influenced by ocean extent, for example the immense pressures at the floor of a very deep global ocean, which may occur on a super earth with a similar water mass fraction to Earth (0.02-0.05%), could maintain a layer of ice at the bottom of the ocean (Kaltenegger et al. 2013) and limit any effect of geological processes on salinity, giving the possibility of a low

salinity ocean.

## 5.2 Relating mean salinity and salinity gradients

Using the concept of the box model (chapter 2), a relationship between the mean salinity and salinity gradient is derived. The mean salinity $\overline{S}$ is such that the two connected boxes have salinity $\overline{S} + s'$ and $\overline{S} - s'$, where $s'$ is the salinity anomaly, and so the salinity difference $\Delta S = 2s'$. Equating the change in salinity in one of the boxes, here chosen to be the low latitude box, to the sum of the inward and outward flow gives

$$\frac{\mathrm{d}\big(\overline{S} + s'\big)}{\mathrm{d}t} = \frac{1}{V}\Big(\big(\overline{S} - s'\big)\Psi - \big(\overline{S} + s'\big)\big(\Psi - Q\big)\Big). \tag{5.1}$$

where $\Psi$ is the overturning circulation, and $Q$ is the atmospheric freshwater transport (figure 5.1). Taking the steady state gives

$$\begin{aligned} & \big(\overline{S} - s'\big)\Psi = \big(\overline{S} + s'\big)\big(\Psi - Q\big) \\ \Longrightarrow\ & \Big(\Psi - \frac{Q}{2}\Big)\Delta S = Q\overline{S}, \\ \Longrightarrow\ & \Delta S \propto \overline{S}, \end{aligned} \tag{5.2}$$

for given $\Psi$ and $Q$. This shows the direct proportionality which exists between the mean salinity and the salinity gradients which are sustained in the ocean, a relationship which is shown for the first time in this work.

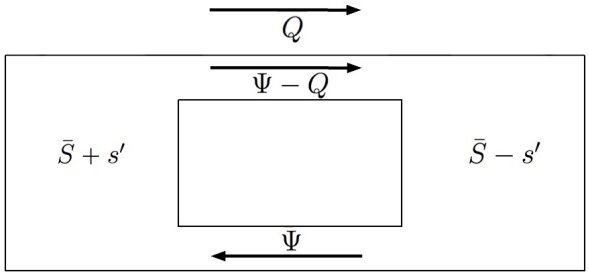


Figure 5.1: The Stommel box model with mean salinity $\bar{S}$, salinity difference $2s'$, circulation $\Psi$, and freshwater transport $Q$.

## 5.3 Equation of state

The equation of state is an empirical relationship determining how the density depends on temperature and salinity. It is derived for a given water mass from fitting an equation to observations, and hence the work here is limited to using equations of state which have been derived for water masses found on Earth. In particular, freshwater, oceans on Earth, and the Dead Sea, hereafter referred to as low-, mid-, and high-range salinity, respectively. Approximations are made to the equation of state in each case to allow analytic solutions to the box model.

### 5.3.1 Low-range salinity

When considering an ocean of freshwater, or that with a low salinity, the maximum density is not at the coldest temperature; for freshwater it occurs at 4°C. With increasing salinity the temperature of the maximum density decreases until it is equal to the freezing point (figure 5.2).

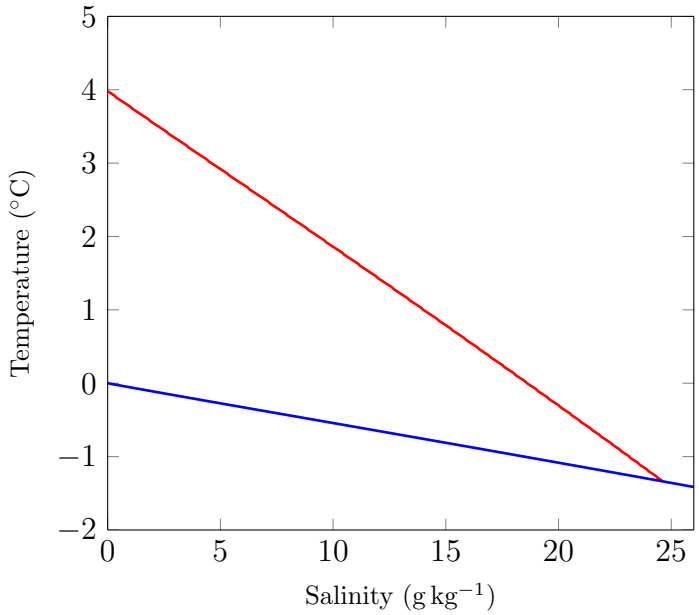


Figure 5.2: Red line is the relation between salinity and the temperature of the maximum density (°C). This decreases linearly with increasing salinity. The blue line is the freezing point of sea water as a function of salinity (Gill 1982, p.602). The temperature of the maximum density equals the freezing point at a salinity of approximately 24.5 g kg$^{-1}$.

The freshwater case is considered here, as this simplifies the problem by removing salinity. The temperature range investigated is between 0°C and 8°C, in which the equation of state can be approximated with the quadratic relation

$$\rho = \rho_0\big(1 - \alpha^2(T - T_m)^2\big), \tag{5.3}$$

where $T_m = 4\,^\circ\mathrm{C}$ is the temperature of the maximum density, $\rho_0 = 1000\,\mathrm{kg\,m^{-3}}$ is a reference density, and $\alpha = 2.6 \times 10^{-3}\,^\circ\mathrm{C}^{-1}$ (Farrow 2012).

### 5.3.2 Mid-range salinity

The mid-range salinity is the case discussed for the Earth-like solutions to the box model (chapter 2). A linearised equation of state is used;

$$\rho = \rho_0(1 - \alpha T + \beta S), \tag{5.4}$$

where $\alpha = 1.7 \times 10^{-4}\,^\circ\mathrm{C}^{-1}$ and $\beta = 7.8 \times 10^{-4}\,\mathrm{kg\,g^{-1}}$. The linearity of this form of the equation of state means equations for the differences in temperature and salinity between the boxes may be solved analytically.

### 5.3.3 High-range salinity

A study of water in the Dead Sea finds the equation of state using samples with salinity in the region of $260\,\mathrm{g\,kg^{-1}}$, which is approximately 7.5 times greater than that found in the deep oceans on Earth, as

$$\begin{aligned}\rho = \rho_w + (&1.153480 - 1.920077 \times 10^{-3}T \\ &+ 1.717675 \times 10^{-5}T^2)S + 1.133635 \times 10^{-2}S^{3/2},\end{aligned} \tag{5.5}$$

where

$$\begin{aligned}\rho_w =&999.8395 + 6.7914 \times 10^{-2}T - 9.0894 \times 10^{-3}T^2 + 1.0171 \times 10^{-4}T^3 - \\ &- 1.2846 \times 10^{-6}T^4 + 1.1592 \times 10^{-8}T^5 - 5.0125 \times 10^{-11}T^6,\end{aligned} \tag{5.6}$$

(Krumgalz & Millero 1982). In a similar way to the mid-range case, a linearisation is made to this equation of state to give an equation of the form (5.4). In the high case the coefficient of thermal expansion is $\alpha = 5.0 \times 10^{-4}\,^{\circ}\mathrm{C}^{-1}$ and the coefficient of haline contraction is $\beta = 14 \times 10^{-4}\,\mathrm{kg\,g}^{-1}$. This linearisation is a reasonable approximation to make, which is clear from plotting contours of the full and linearised equations (figure 5.3); the maximum percentage error of this linearisation within the ranges of temperature and salinity shown is 1.1%.

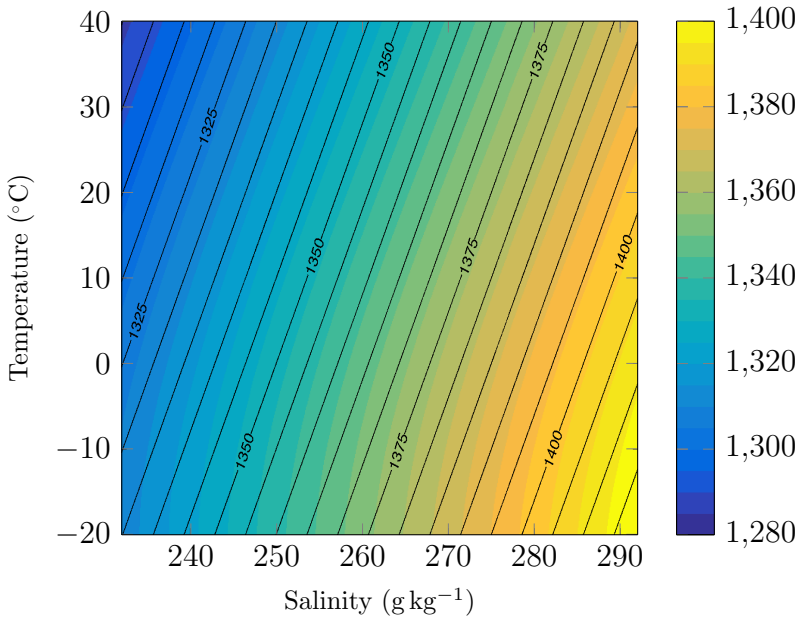


Figure 5.3: Contour plot of the density of water in the Dead Sea ($\mathrm{kg\,m}^{-3}$) as a function of temperature and salinity. Shading is the full equation of state (5.5), and the overlaid black contours are the linearised approximation.

## 5.4 Box model solutions

The box model is used to investigate the possible directions and strengths of the ocean circulation at different concentrations of salt.

### 5.4.1 Model configuration

The two-box model configuration is used (chapter 2) with the default parameters (table 2.1), except those dependent on salinity; $\alpha$, $\beta$, and $\Delta S^*$. In each salinity range investigated the equation of state in the model is changed, and the appropriate parameter ranges are considered, in particular those for temperature, and salinity forcing consistent with the derived relationship (§5.2).

### 5.4.2 Low-range salinity

The nonlinear behaviour of the equation of state for this case requires the equations for temperature and salinity in each box to be considered (2.8)-(2.13), rather than the equations for the the differences in temperature and salinity between the boxes (2.18)-(2.20). However, the freshwater case is chosen since there is no salt to consider; $S \equiv 0$, which reduces the set of equations by removing those for the salinity in each box. The equations to be solved are then

$$c(T_1^* - T_1) - \frac{2}{V}|\Psi|(T_1 - T_2) = 0, \tag{5.7}$$

$$c(T_2^* - T_2) - \frac{2}{V}|\Psi|(T_2 - T_1) = 0, \tag{5.8}$$

$$\Psi = A(\rho_1 - \rho_2). \tag{5.9}$$

Substituting for $\rho_1$ and $\rho_2$ in (5.9) using (5.3) gives

$$\Psi = A\rho_0\alpha^2\big(2T_m(T_1 - T_2) - (T_1^2 - T_2^2)\big). \tag{5.10}$$

Equations (5.7) and (5.8) with (5.10) are solved using the computer algebra system *Maple* to give $\Psi$ in terms of $T_1^*$ and $T_2^*$. The solution is plotted for $0 \leqslant T_1^* \leqslant T_2^* \leqslant 8^\circ$C (figure 5.4).

The strongest circulations are found when $T_1^* = 0^\circ$C and $T_2^* = 4^\circ$C, and when $T_1^* = 4^\circ$C and $T_2^* = 8^\circ$C, as these give the greatest density differences between the boxes. The density gradient is the same in each case but the densest water is in a different box, hence these two cases have circulation of

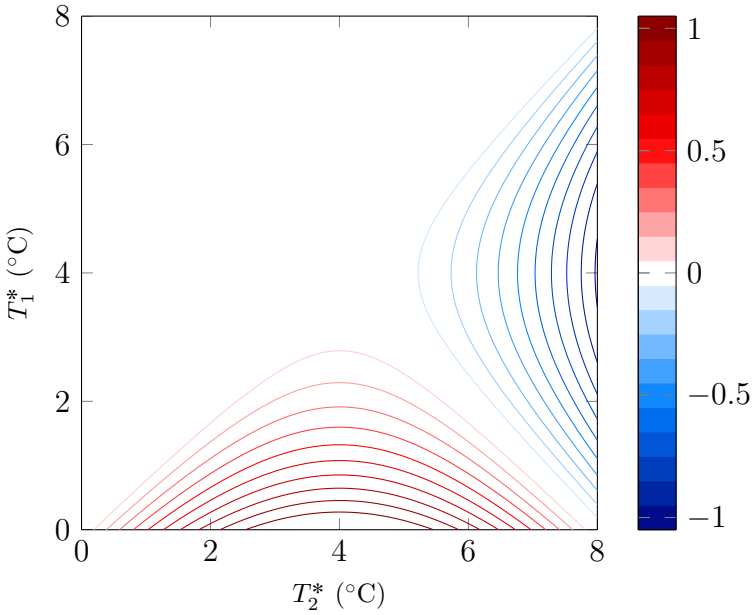


Figure 5.4: Box model solution for the magnitude and direction of the overturning circulation $\Psi$ (Sv) for the low-range salinity case, as a function of temperature forcing $T_1^*$ and $T_2^*$ (°C) ($T_1^* \leqslant T_2^*$). The contour interval is 0.1 Sv.

equal magnitude but opposite direction; sinking in either warmer or cooler regions. There is no circulation when $T_1^* + T_2^* = 8$ and when $T_1^* = T_2^*$ as the densities of the two boxes are equal when either of these conditions are true. The magnitude of the circulations considered are relatively small compared to the other salinity cases, this is due to the narrow temperature range considered. However, with larger ranges of temperature this behaviour would still influence the circulation wherever temperatures vary across 4°C in a freshwater ocean, for example multiple overturning cells with deep water formation where water has a temperature of 4°C (figure 5.5). In freshwater lakes the 4°C isotherm creates a boundary layer between regions of different mixing conditions, and downwelling of water at this temperature creates a two-cell circulation (Farrow 2012) in a similar sense to those proposed here for ocean circulation (figure 5.5).

As salinity increases from the completely freshwater case a similar behaviour of the density, as a function of temperature at fixed salinity, is observed to that of freshwater; the maximum density is above the freezing point. This is true for salinities up to approximately 24.5 g kg$^{-1}$ (figure 5.2). However, as the salinity increases, the temperature of the maximum density decreases and becomes closer to that of the freezing point. Hence, the range of

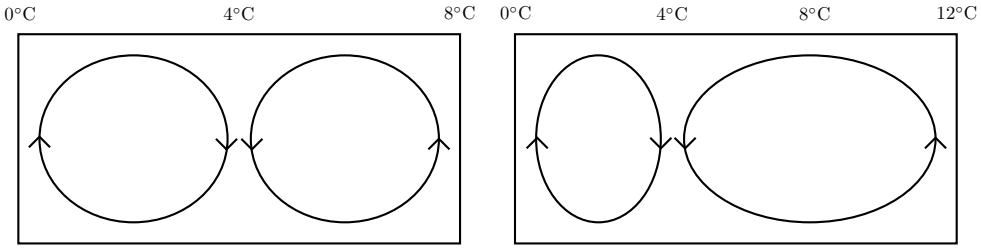


Figure 5.5: Schematics showing theoretical circulations for a freshwater ocean over different temperature ranges. The densest water occurs at 4°C, and hence deep water formation would be expected to occur at this temperature.

temperatures for which similar behaviour to that in the freshwater case would be observed decreases, resulting in this behaviour being negligible for the higher values of salinity in the range $0 - 24.5\,\mathrm{g\,kg^{-1}}$.

### 5.4.3 Mid-range and high-range salinity

The method of solution is the same for both the mid- and high-range salinity cases; equations for the differences in temperature and salinity between the boxes are solved. The mid-range salinity case is exactly the Earth-like solution to the box model (Chapter 2, §2.3), and the high-range case is solved in an identical way with the appropriate values of $\alpha$ and $\beta$.

The key difference which needs to be considered when changing the mean salinity of the water mass, is that the salinity difference which can be maintained between the boxes is proportional to the mean salinity of the water; $\Delta S \propto \overline{S}$, and hence for realistic results the forcing must be scaled using this relationship. This means the range of salinity forcing corresponding to, for example, $0 - 5\,\mathrm{g\,kg^{-1}}$ for mid-range salinity is $0 - 38\,\mathrm{g\,kg^{-1}}$ for high-range salinity, which is an increase by the same factor as that of the increase in the mean salinity which is 7.5 between the mid- and high-range salinity cases. Hence for comparison the results are plotted varying $\Delta S^*/\overline{S}$, at a constant temperature forcing (figure 5.6).

The results show a positive circulation with a low gradient in salinity forcing, multiple solutions with a moderate gradient, and a reversal of the circulation

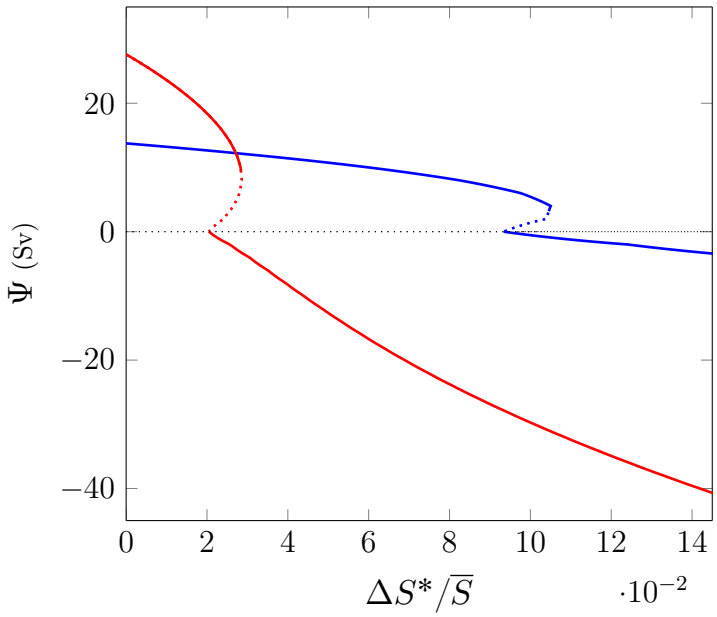


Figure 5.6: Box model solutions for the magnitude of the overturning circulation $\Psi$ (Sv) for the (blue) mid-range, and (red) high-range salinity scenarios, dotted lines indicate unstable solutions, $\Delta S^*$ is the gradient in salinity forcing and $\overline{S}$ is the mean salinity. The scaling $\Delta S \propto \overline{S}$ means direct comparison is possible when $\Delta S^*/\overline{S}$ is varied. The range presented is equivalent to 0–5 g kg$^{-1}$ and 0–38 g kg$^{-1}$ for $\Delta S^*$ in the mid- and high-range salinity cases, respectively. A salinity-driven circulation occurs when $\Delta S^*/\overline{S} > 0.105$ and 0.03, respectively.

to a negative, salinity-driven regime at higher salinity gradients. Outside of the multiple solution range, the model results show that a gradient in the salinity forcing of 3.5 g kg$^{-1}$ and 8 g kg$^{-1}$ in the mid- and high-range salinity case, respectively, results in a salinity-driven circulation. Note that, although larger in absolute value, the value of salinity forcing in the high-range salinity case is relatively weaker due to the proportionality between the mean salinity and the salinity gradient. Thus in the high range salinity scenario it is more likely that a negative circulation occurs, with sinking in warmer regions, and warm water travelling polewards at depth: opposite to what is seen on Earth. This would result in the upwelling of warm water in the high latitudes, which would warm the climate in these regions by a greater amount than with a circulation of the opposite direction.

## 5.5 Numerical simulations

Numerical modelling of the ocean at different salinities using MOMA provides a more complete picture of ocean circulation in the different salinity ranges considered, and provides a comparison to the results found using the box model.

### 5.5.1 Model configuration

The default ridgeworld land configuration is used (figure 4.1(b)) with the default parameters (table 3.2), excluding the horizontal eddy diffusivity which is changed to $5 \times 10^3\,\mathrm{m^2\,s^{-1}}$ for stability reasons, and wind forcing is included. The appropriate equation of state is selected in each case for the salinity range being investigated (§5.3), note that the results for the mid-range salinity scenario vary slightly from those for the control run (§4.2) due to the different form of the equation of state; here a linearisation of the polynomial equation of state employed earlier is used. The surface forcing is adapted to correspond to the appropriate range of salinity and temperature in that scenario; in the mid-range case the values remain unchanged from the Earth observations, in the low-range case the temperature values are scaled to be in the range 0-8°C and salinity is removed, and in the high-range case the salinity values are scaled to be in the range 240-268 $\mathrm{g\,kg^{-1}}$ in accordance with the scaling $\Delta S \propto \overline{S}$. In the high salinity case the ocean is initialised at 21°C, instead of the standard value 0°C, as this is closer to the final steady state of the deep ocean, and therefore negates an initial long period of vertical heat diffusion into the deep ocean, significantly reducing the spin-up period.

### 5.5.2 Circulation

The numerical results for the circulation confirm the prediction of the box model; extensive buoyancy-driven circulation cells of direction opposite to the Earth-like sense occur in both the low- and high-range salinity scenarios (figure 5.7(a,c)). Whereas the mid-range salinity scenario shows an

Earth-like circulation; a single deep overturning cell in each hemisphere with deep water formation in the high latitudes (figure 5.7(b)). This is the same configuration as the control run (§4.2), with the only difference being the linearised equation of state, and a similar value for the freshwater transport at 30°N of -0.14 Sv is again indicative of an unstable circulation.

The low-range salinity scenario exhibits deep water formation in the region of 30°N/S, with upwelling at the equator and in the high latitudes (figure 5.7(a)). This forms two overturning cells in each hemisphere of opposite direction, which both descend into the deep ocean and have similar latitudinal extent but different strengths; the peak in strength in the high latitude cell of 30 Sv is less than a quarter of that in the low latitudes. With two overturning cells in each hemisphere a two-box model would not accurately model this scenario, as sinking occurs at the latitude forced to 4°C at the surface which creates the two overturning cells. The strengths of the high and low latitude circulation cells are not equal due to the decrease in ocean volume with latitude. Note that the absence of salt in this configuration means that the salt-advection feedback is not present; deep water formation will always occur where surface water is at 4°C.

The circulation in the high-range salinity scenario is similar to that found in the low-range case; there are two cells in each hemisphere with deep water formation between them (figure 5.7(c)). However, in this case the low latitude cell is shallower and the cells have more comparable strength with peaks of 95 Sv and 47 Sv in the low and high latitudes, respectively. With a similar configuration of cells to that in the freshwater case, a box model would again not be suitable to simulate this circulation. The strong overturning cells in the deep equatorial region, similar to the weaker pattern acknowledged in the control run (§4.2), are again likely to be a result of the low vertical resolution in the model (Miller 2007, p.116). Calculating the freshwater transport in each of the cells suggests an unstable circulation regime in this configuration; -0.27 Sv in the high latitude cell at 50°N and +0.032 Sv in the low latitude cell at 16°N. The positive value in the low latitude cell is still indicative of an instability since the cell has a negative circulation direction.

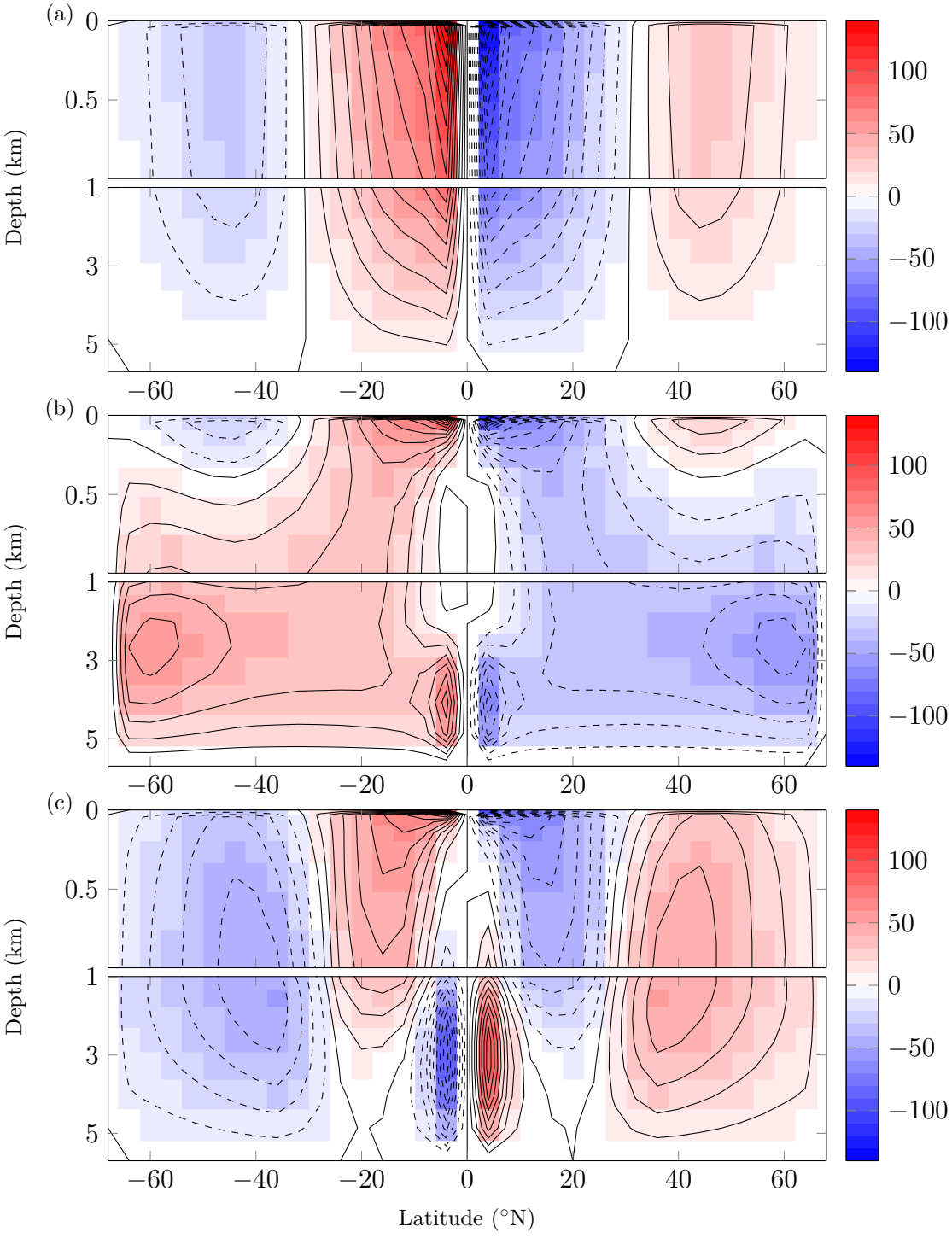


Figure 5.7: Quasi-steady state overturning streamfunction (Sv) for a ridgeworld configuration with (a) low-range, (b) mid-range, and (c) high-range salinity. Contour interval is 10Sv, positive circulation is anti-clockwise. Note the expanded vertical scale in the upper 1 km of the ocean.

### 5.5.3 Tracers

The values of density vary greatly between the different salinity scenarios due to the different concentrations of salt, however the significant factor is the distribution of density, which is found to have marked differences between the three cases. In particular, the peaks in surface density vary in latitude between the three salinity ranges and, as expected since the densest water forms into deep water, are found to correspond to the location of deep water formation. This is just poleward of 30°N/S in the low-range (figure 5.8(a)), in the highest latitudes in the mid-range (figure 5.8(b)), and in the region of 30°N/S for the high-range salinity scenario (figure 5.8(c)).

The relative temperature and salinity of the deep water vary considerably between each of the salinity ranges, which is a consequence of the different locations at which it is formed. The locations of deep water formation are also clear in the zonally-averaged temperature and salinity; they are identified as the latitudes where there is a lack of stratification of the water column due to the deep convection of surface waters. The properties of the surface at these locations then extend into and throughout the deep ocean.

In the low-range salinity case the densest water is 4°C, and hence the deep ocean is at this temperature (figure 5.9(a)), which is in the middle of the full temperature range of that case. In the mid-range salinity scenario the deep water is the coldest (figure 5.9(b)) and freshest (figure 5.10(a)) in the zonally-averaged distributions, with values of 3°C and $34.2\,\mathrm{g\,kg^{-1}}$. This is in large contrast to the high-range salinity scenario in which the deep water is relatively warm (figure 5.9(c)) and the most saline (figure 5.10(b)) with values of 22°C and $267\,\mathrm{g\,kg^{-1}}$.

### 5.5.4 Heat transport

The structure and magnitude of the poleward heat transport shows the clear relation to the structure and strength of the overturning circulation (figure 5.11). In the low-range salinity case the heat transport peaks either side of the equator at 1.2 PW, which corresponds to the latitudes of the strongest circulation, and is very small in the mid- and high latitudes where

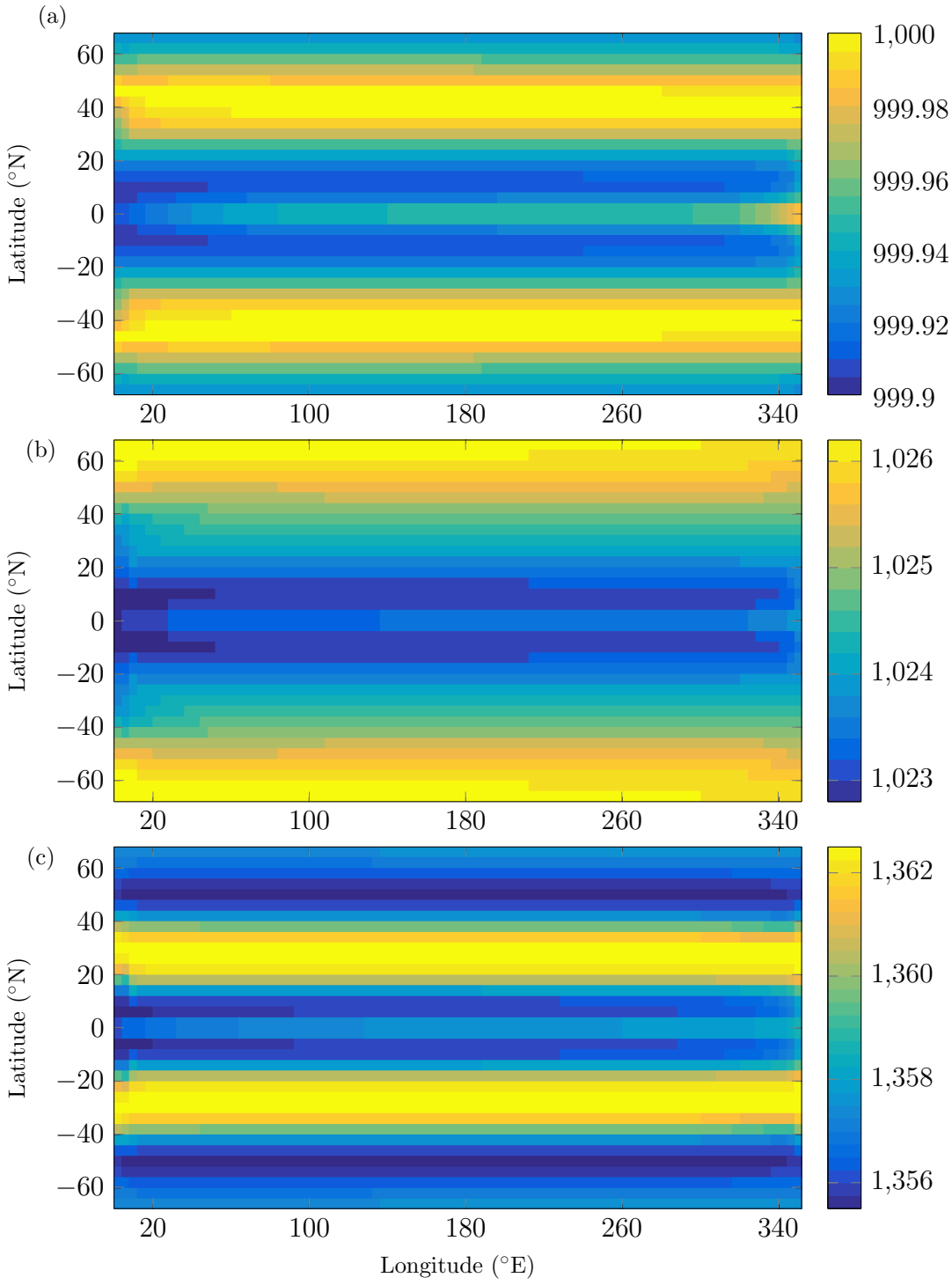


Figure 5.8: Quasi-steady state surface density ($\mathrm{kg\,m^{-3}}$) for a ridgeworld configuration with (a) low-range, (b) mid-range, and (c) high-range salinity.

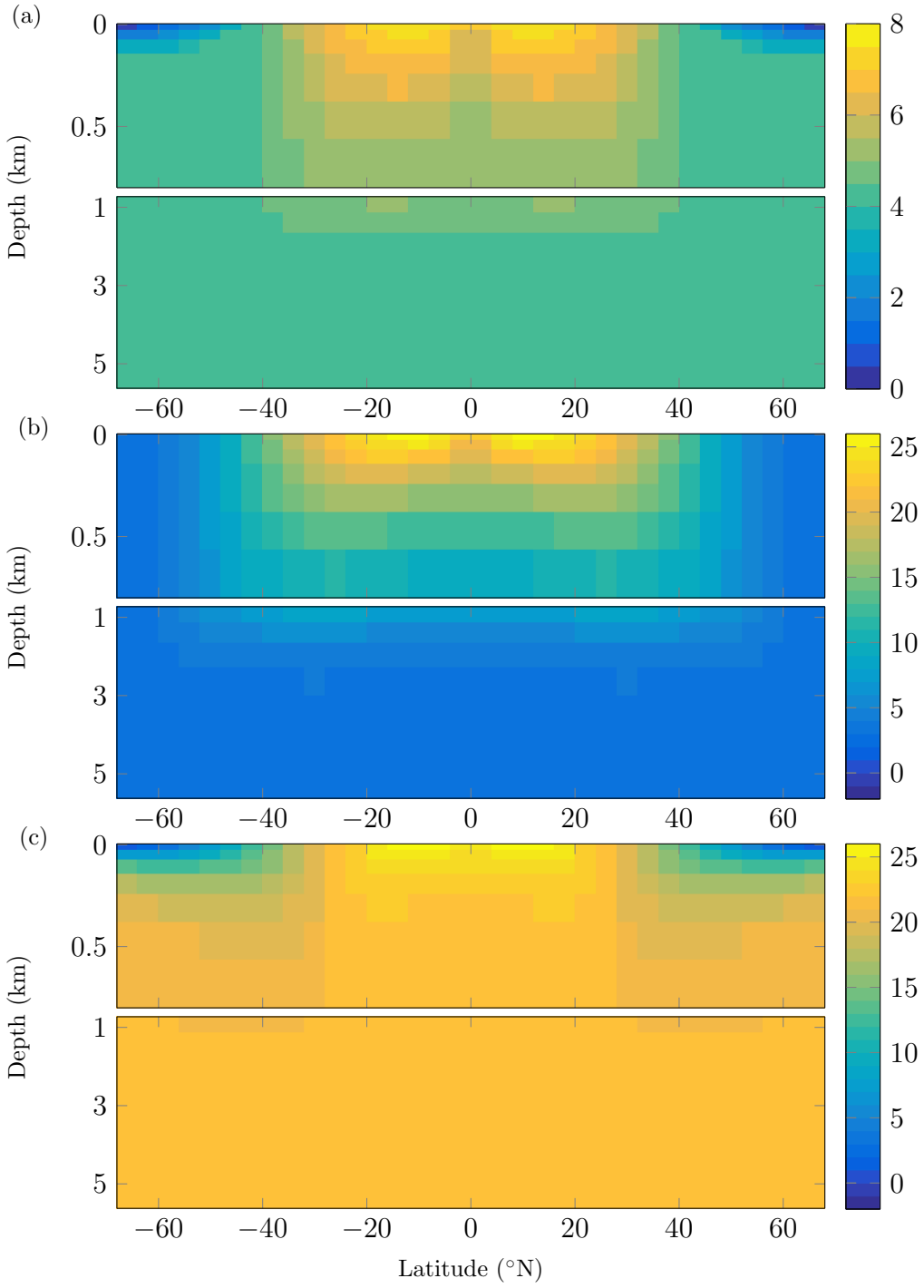


Figure 5.9: Quasi-steady state zonally-averaged ocean temperature (°C) for a ridgeworld configuration with (a) low-range, (b) mid-range, and (c) high-range salinity. Note the expanded vertical scale in the upper 1 km of the ocean.

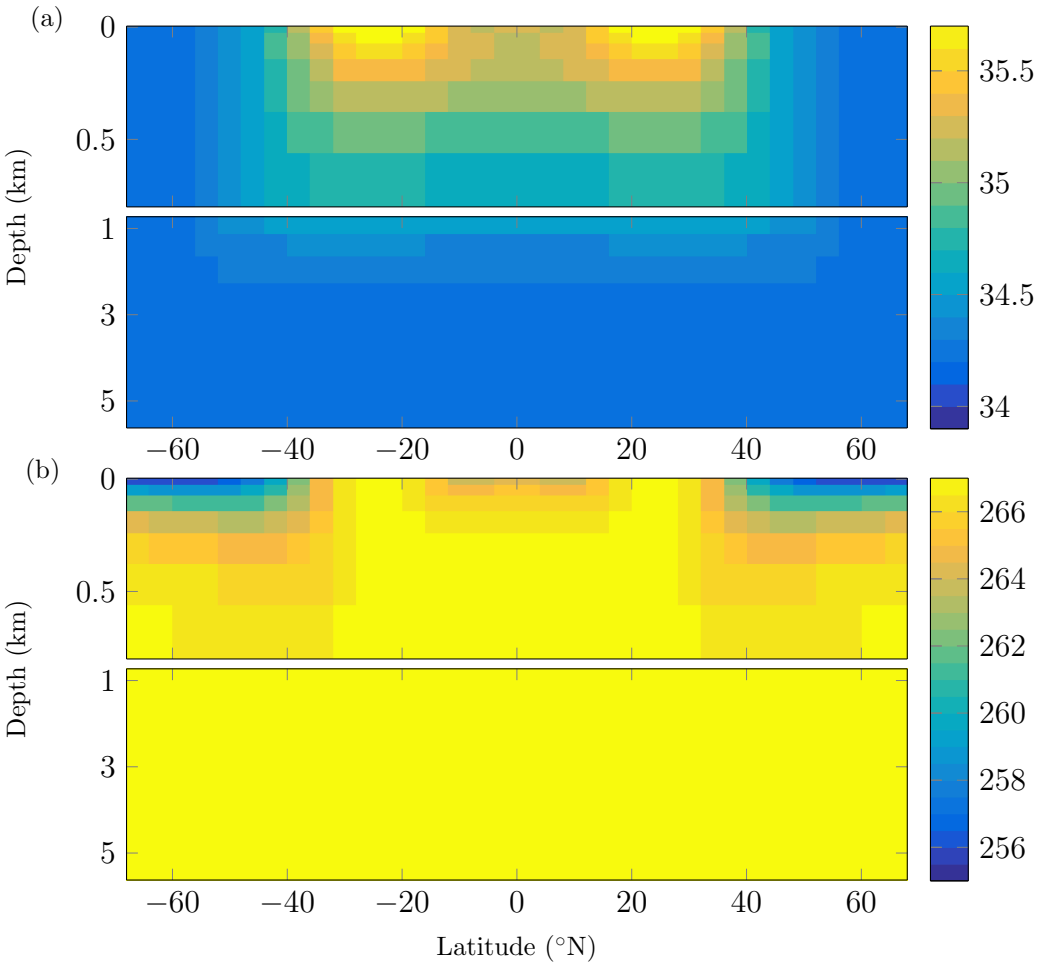


Figure 5.10: Quasi-steady state zonally-averaged ocean salinity ($\mathrm{g\,kg^{-1}}$) for a ridgeworld configuration with (a) mid-range, and (b) high-range salinity. Note the expanded vertical scale in the upper 1 km of the ocean.

the circulation is much weaker. The largest peak in heat transport of the three cases occurs in the mid-range salinity scenario, in the low latitudes with a value of 3.6 PW. The peak in heat transport for the high-range salinity case occurs in the mid-latitudes at 1.8 PW.

The latitudinal pattern of the heat transport reflects the structure of the overturning circulation. In particular, the poleward heat transport is very small at latitudes of deep water formation where overturning cells meet and there is little transport between them. This is particularly clear in the high-range salinity scenario in which there are two clear peaks in the heat transport in each hemisphere, which correspond to the two overturning cells, with negligible transport where the cells meet just below 30°N/S.

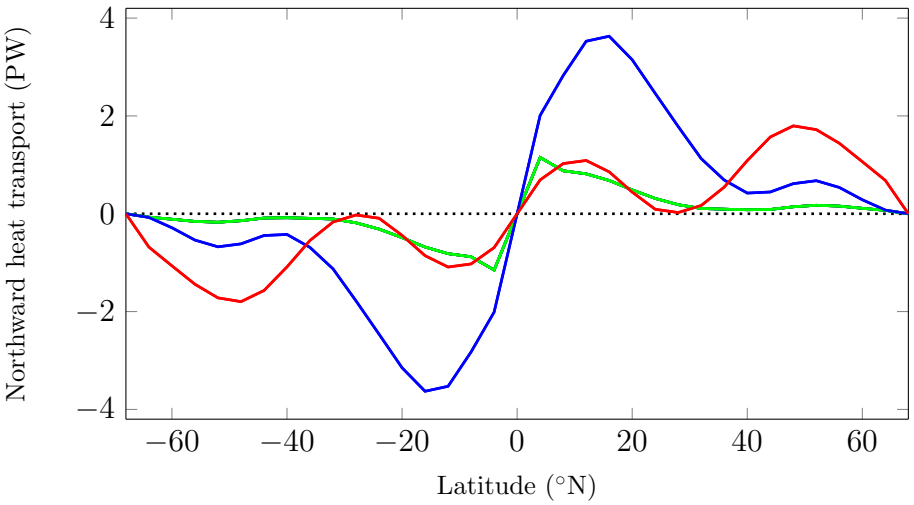


Figure 5.11: Quasi-steady state northward ocean heat transport (PW) for a ridgeworld configuration with (green) low-range, (blue) mid-range, and (red) high-range salinity.

In the low-range salinity case the surface heat flux to the atmosphere peaks at $16\,\mathrm{W\,m^{-2}}$ in the low latitudes, which is associated with the strongest region of circulation moving warm water poleward at the surface of the ocean which is warming the atmosphere away from the equatorial region (figure 5.12). In the mid-range case the peak of $44\,\mathrm{W\,m^{-2}}$ is in the region of 20-30°N/S, which is again associated with warm poleward travelling surface water. The high-range case shows the largest peaks of all three cases at $96\,\mathrm{W\,m^{-2}}$, and are located in the highest latitudes, this is a result of the upwelling of particularly warm deep water in the cold high latitudes. In the mid-range case there is warm water travelling poleward at the surface over a much larger range of latitudes compared to the other cases due to the existence of a single overturning cell in each hemisphere, this has an associated heat flux to the atmosphere over a larger region. This is in largest contrast to the high-range salinity scenario in which there is a limited region in the low latitudes over which warm water is travelling poleward at the surface and warming the atmosphere and significant regions where the warmest water is travelling poleward in the deep ocean, where it maintains its temperature, and upwells at the highest latitudes at which it warms the atmosphere.

The greatest heat flux into the ocean occurs in the low latitudes in all three cases, however the magnitude varies; $66\,\mathrm{W\,m^{-2}}$, $116\,\mathrm{W\,m^{-2}}$ and $40\,\mathrm{W\,m^{-2}}$ in the low-, mid-, and high-range salinity scenarios, respectively. This change

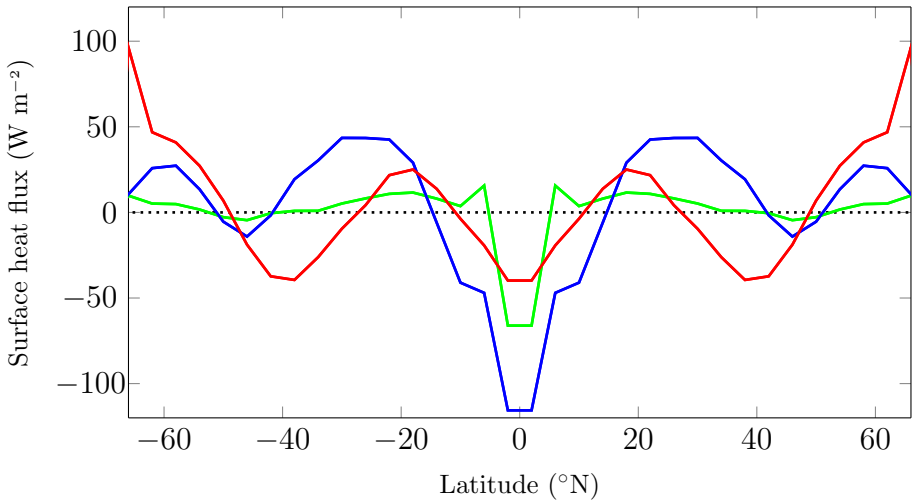


Figure 5.12: Quasi-steady state surface heat flux ($\mathrm{W\,m^{-2}}$) for a ridgeworld configuration with (green) low-range, (blue) mid-range, and (red) high-range salinity.

in heat flux is related to the temperature of the upwelling water at the equator; the largest flux occurs in the mid-range salinity case as this has the coldest deep water. In the high-range salinity case there are peaks of the same magnitude in the mid-latitudes which occur due to the equatorward flow of cold water at the surface, which is associated with the overturning cells poleward of 30°N/S. This phenomenon also occurs in the other two cases, however it is much lower due to the weaker associated circulation.

## 5.6 Summary

With different possibilities for the quantity of water and salt in exoplanetary oceans there is no reason to limit the possible ocean salinities to the ranges found in the oceans on Earth. Modelling ocean circulation with the two-box model at different salinities shows an increased likelihood of meridional overturning circulations with opposite direction to those of the oceans on Earth, for salinity both higher and lower than Earth ocean concentrations. The results from the box model above can be concisely summarised using a regime diagram to illustrate circulation direction as a function of three variables: mean temperature, equator-pole temperature gradient, and equator-pole salinity gradient (figure 5.13). The proportionality between the salinity gradient forcing $\Delta S^*$ and $\overline{S}$ means the two values do not need

separate consideration, whereas $\Delta T^*$ and $\overline{T}$ can be varied independently.

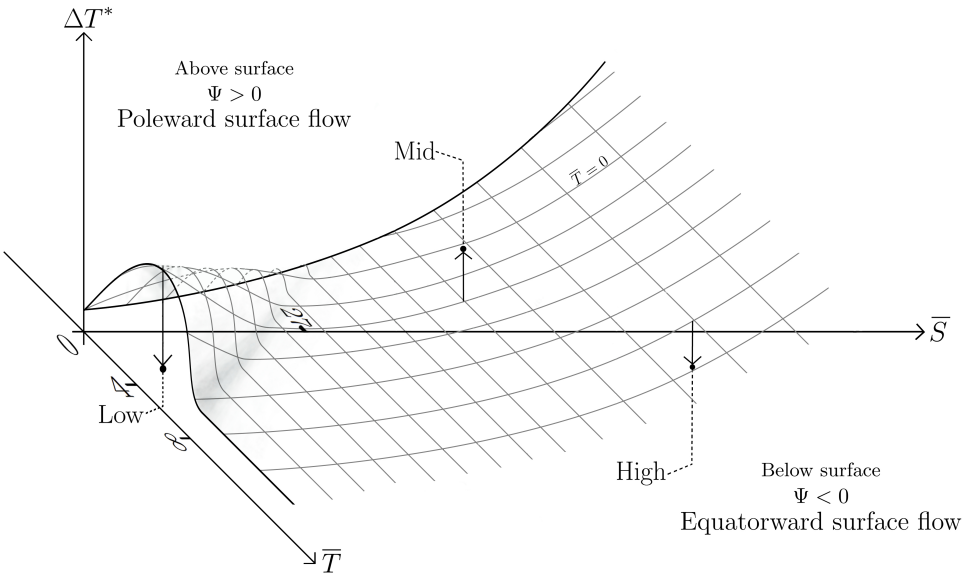


Figure 5.13: A schematic illustrating the direction and magnitude of the overturning circulation, $\Psi$, from the box model solutions. The behaviour depends on the values of temperature gradient forcing $\Delta T^*$, the mean temperature $\overline{T}$ and mean salinity $\overline{S}$. The locations of the low-, mid- and high-range salinities considered are indicated in reference to the surface.

The gridded surface represents the values where there is no circulation, above the surface there is a positive circulation (poleward flowing surface water), and below it there is a negative circulation (equatorward flowing surface water). The magnitude of the circulation is strengthened as the distance (and hence density difference between the boxes) from the surface increases. The figure illustrates how a negative circulation becomes increasingly likely as the mean salinity increases, indicated by the surface tilting upwards with an increasing salinity gradient.

The simplifications in the box model limit the applicability of the conclusions which may be drawn, however it does provide a useful summary of the general behaviour of the system. A more complete picture is found from numerical modelling using MOMA with different salinity ranges, which supports the conclusions found using the box model.

An ocean where the temperature gradient is the dominating driver of circulation typically exhibits sinking at the poles, however, in a scenario

such as the high-range salinity case presented here, the circulation is driven primarily by the gradient in salinity and deep water formation occurs at lower latitudes. The result of this is the formation of warm and saline deep water which fills the deep ocean, and upwelling of this water in the high latitudes warms the polar regions. In the low-salinity case, here modelled with a freshwater ocean, the nonlinear nature of the equation of state gives a similar circulation pattern to the high-range salinity case.

# Chapter 6

# Planetary rotation period

Here it is shown that ocean dynamics have a strong dependence on planetary rotation period, for which there is a wide range of possibilities. This dependence includes the poleward ocean heat transport, velocities and thermal structure of the ocean, the response of which is predicted by both a scale analysis of the governing equations, and shown through numerical modelling with MOMA.

Some of the work in this chapter is published in
Cullum, J., Stevens, D. & Joshi, M. (2014) 'The Importance of Planetary Rotation Period for Ocean Heat Transport', *Astrobiology* 14(8).

## 6.1 Atmospheric response

Existing studies have investigated the dependence of atmospheric dynamics on the planetary rotation period, with and without a dynamic ocean component. When modelling the atmospheric component of the system, it is found that the peak in poleward energy transport by the meridional circulation has no discernible trend as the rotation period is lengthened up to 64 days (Del Genio & Suozzo 1987). A similar conclusion is made when modelling with a coupled atmosphere-ocean model; for rotation periods longer than a day the atmospheric heat transport is found to be approximately constant (Vallis & Farneti 2009).

The latitudinal extent and strength of the Hadley cell responds to changes in rotation period; the strength increases and the descending branch moves poleward as the rotation period is lengthened. The Hadley cell extent increases from 30°N to 60°N when lengthening the rotation period from 1 day to 8 days, and extends to the pole at 64 days (Del Genio & Suozzo 1987, Williams 1988, Kaspi & Showman 2015). As the Hadley cell extends in this way it replaces eddies as the primary process of poleward heat transport, at a rotation period of 5 days (Kaspi & Showman 2015), and acts to decrease the meridional temperature gradient (Del Genio & Suozzo 1987, Hunt 1979). This change in circulation is reflected in the structure of the mean meridional energy transport, in particular an increase in transport at the high latitudes (Del Genio & Suozzo 1987, Kaspi & Showman 2015).

The global mean temperature is found to be cooler at longer rotation periods, toward being tidally locked, due to two responses affecting the planetary albedo; an increase in cloud albedo results from stronger convergence at low-levels (Yang et al. 2014a), and an increase in global sea-ice fraction, particularly at low latitudes in areas emerging from the night side, assuming Earth-like radiation (Salameh et al. 2018).

The horizontal velocities are found to increase for rotation periods from 1 up to 8 days, at which point a regime change occurs due to an increase in the Rossby number and consequent breakdown of geostrophic dynamics (Del Genio & Suozzo 1987, Williams 1988). This change in dynamics occurs at a much shorter rotation period for the atmosphere compared to the ocean

as the Rossby number is an order of magnitude smaller for the ocean (Vallis 2006, p.85), and therefore more extensive trends in dynamics are expected to be found in the ocean response to lengthening rotation period.

## 6.2 Scale analysis

The impact of planetary rotation period on the ocean circulation, structure, and heat transport may be predicted with a scale analysis of the governing equations (Bryan & Cox 1967, Graham 2008). First, a scale for the horizontal velocities may be derived from equating the vertical derivative of geostrophic balance with the horizontal derivative of hydrostatic balance;

$$\begin{aligned} \frac{\partial(\rho_0 f v)}{\partial z} &= -\frac{\partial^2 p}{\partial x \partial z} = \frac{\partial(\rho g)}{\partial x}, \\ \implies \rho_0 f \frac{\partial v}{\partial z} &= g \frac{\partial \rho}{\partial x}, \\ \implies \frac{\rho_0 f U}{d} &= \frac{g \rho_0 \alpha \Delta T}{L}, \\ \implies U &= \frac{g \alpha \Delta T d}{f L}, \end{aligned} \tag{6.1}$$

using the scales $x, y \sim L$, $z \sim d$, $u, v \sim U$, and $\rho \sim \rho_0 \alpha T$. Second, an alternative scale is found for the horizontal velocities using the vertical advection-diffusion balance (Munk 1966);

$$\begin{aligned} w \frac{\partial T}{\partial z} &= K_h \frac{\partial^2 T}{\partial z^2}, \\ \implies \frac{W}{d} &= \frac{K_h}{d^2}, \\ \implies U &= \frac{K_h L}{d^2}, \end{aligned} \tag{6.2}$$

with the additional scaling of the vertical velocity $w \sim W$, and utilising the scaling of mass continuity; $W/d = U/L$. Equating (6.1) and (6.2) gives the scale for the thermocline depth, $d$;

$$\begin{aligned} \frac{g \alpha \Delta T d}{f L} &= \frac{K_h L}{d^2}, \\ \implies d &= \left( \frac{K_h f L^2}{g \alpha \Delta T} \right)^{1/3}. \end{aligned} \tag{6.3}$$

Substituting (6.3) into (6.1) gives the scale for the horizontal velocities as

$$U = \left( \frac{K_h (g\alpha\Delta T)^2}{f^2 L} \right)^{1/3}. \tag{6.4}$$

A scale for the overturning streamfunction $\psi \sim \Psi$ is calculated using (6.3) and (6.4) as

$$\begin{aligned} \Psi &= ULd, \\ &= \left( \frac{K_h (g\alpha\Delta T)^2}{f^2 L} \right)^{1/3} L \left( \frac{K_h f L^2}{g\alpha\Delta T} \right)^{1/3}, \\ &= \left( \frac{K_h^2 g\alpha\Delta T L^4}{f} \right)^{1/3}. \end{aligned} \tag{6.5}$$

Finally, a scale for the poleward heat transport is calculated using (6.5) as

$$\begin{aligned} Q &= \rho_0 C_p \Delta T \Psi, \\ &= \rho_0 C_p \Delta T \left( \frac{K_h^2 g\alpha\Delta T L^4}{f} \right)^{1/3}, \\ &= \rho_0 C_p \left( \frac{K_h^2 g\alpha\Delta T^4 L^4}{f} \right)^{1/3}. \end{aligned} \tag{6.6}$$

From the relations (6.3) – (6.6) the impact of varying the rotation rate $\Omega \sim f$ on the thermocline depth, horizontal velocities, overturning circulation, and heat transport, respectively, is concluded to be

$$d \sim \Omega^{1/3}, \tag{6.7}$$

$$U \sim \Omega^{-2/3}, \tag{6.8}$$

$$\Psi \sim \Omega^{-1/3}, \tag{6.9}$$

$$Q \sim \Omega^{-1/3}. \tag{6.10}$$

Hence, the conclusion of this scale analysis is that a longer rotation period would result in a shallower thermocline, larger horizontal velocities, a stronger overturning circulation, and a greater poleward heat transport.

## 6.3 Numerical simulations

Numerical modelling of the ocean circulation and tracer distribution using MOMA provides a verification of the relations found from the scale analysis (§6.2). An existing study of ocean modelling at different planetary rotation periods confirms the predicted increase in poleward heat transport with longer rotation periods; mid-latitude ocean energy transport increases from approximately 0.5 PW to almost 0.8 PW when lengthening the rotation period from 1 to 4 days (Vallis & Farneti 2009), which quantitatively agrees with the scaling derived here (6.10). Here, a more detailed analysis of the ocean circulation and structure at different rotation periods adds to this conclusion.

### 6.3.1 Model configuration

The default ridgeworld land configuration is used (figure 4.1(b)), with the default parameters (table 3.2). The rotation period is either 1, 3, or 10 Earth days, where an Earth year is approximated to 360 days, which corresponds to rotation rates of $\Omega_1 = \pi/43200\,\mathrm{rad\,s^{-1}}$, $\Omega_3 = \pi/129600\,\mathrm{rad\,s^{-1}}$, and $\Omega_{10} = \pi/432000\,\mathrm{rad\,s^{-1}}$, respectively. The range of rotation periods used corresponds to realistic exoplanet rotation periods; for very small M-dwarfs the rotation periods of tidally locked planets are less than 10 days, which is inferred from the stellar mass and orbital radius (Heath et al. 1999). In order to achieve meaningful results when lengthening the rotation period the wind forcing is removed, as it is known that the winds are sensitive to rotation period (Del Genio & Suozzo 1987, Williams 1988).

### 6.3.2 Circulation

As the scale (6.8) predicts, the horizontal velocities are stronger at longer rotation periods. The greatest response is in the magnitude of the eastward surface velocity component in the western high latitudes; the maximum is $0.05\,\mathrm{m\,s^{-1}}$ at 1 day compared to $0.10\,\mathrm{m\,s^{-1}}$ at 3 day, and $0.26\,\mathrm{m\,s^{-1}}$ at a 10 day rotation period. The equatorial current more than doubles when

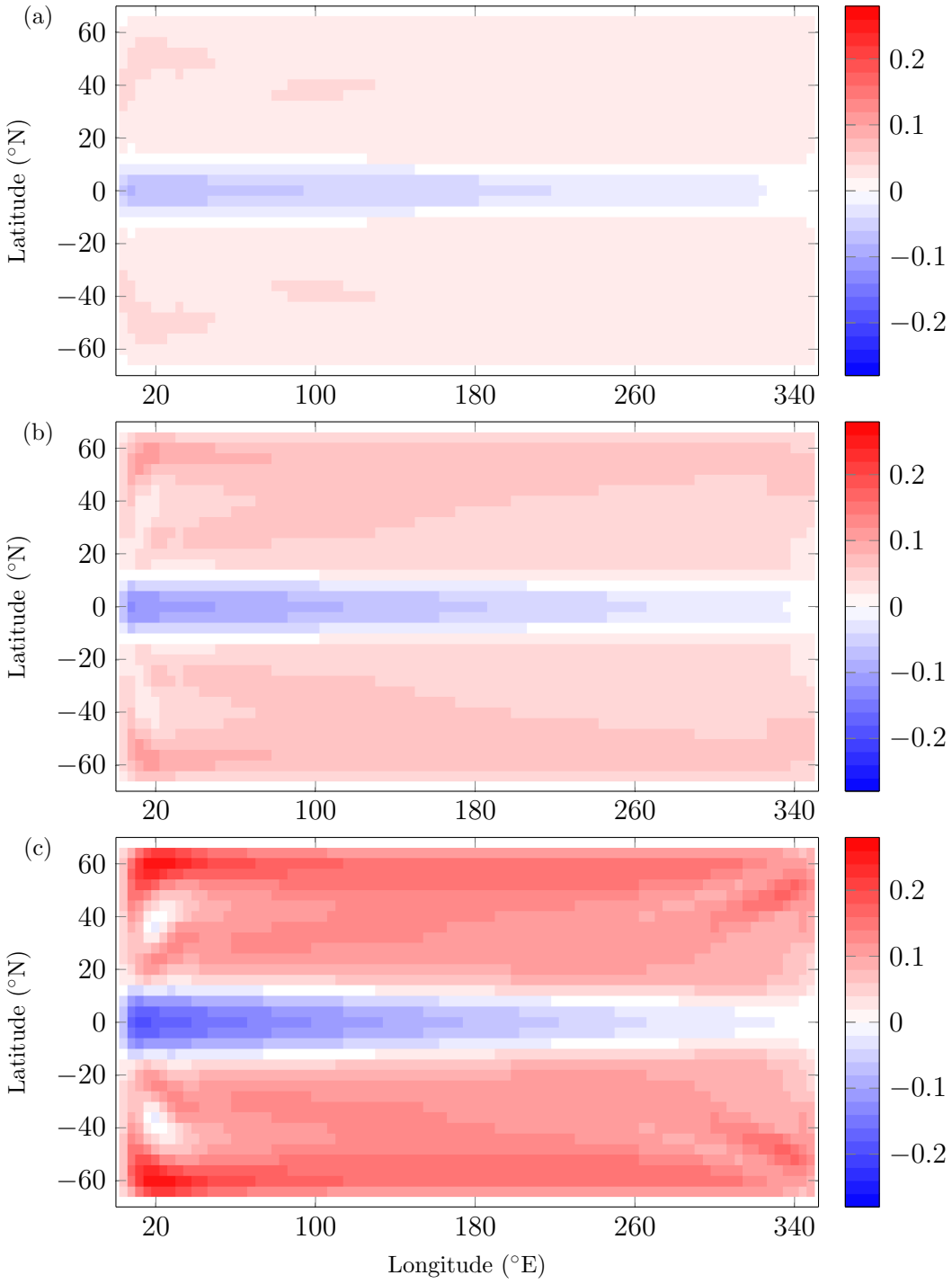


Figure 6.1: Quasi-steady state eastward ocean surface velocity ($\mathrm{m\,s^{-1}}$) for a ridgeworld configuration with (a) 1 day rotation period, (b) 3 day rotation period, and (c) 10 day rotation period.

lengthening the rotation period from 1 to 10 days; with an increase in the peak magnitude from $0.08\,\mathrm{m\,s^{-1}}$ to $0.19\,\mathrm{m\,s^{-1}}$ (figure 6.1). The magnitude of the zonal surface velocity is stronger throughout the vast majority of the ocean, which is seen by inspection of the surface values, as well as the zonally-averaged profiles. These confirm the conclusion that the largest response to lengthening the rotation period occurs in the high latitudes (figure 6.2), where the change in $f$ with rotation period is greatest.

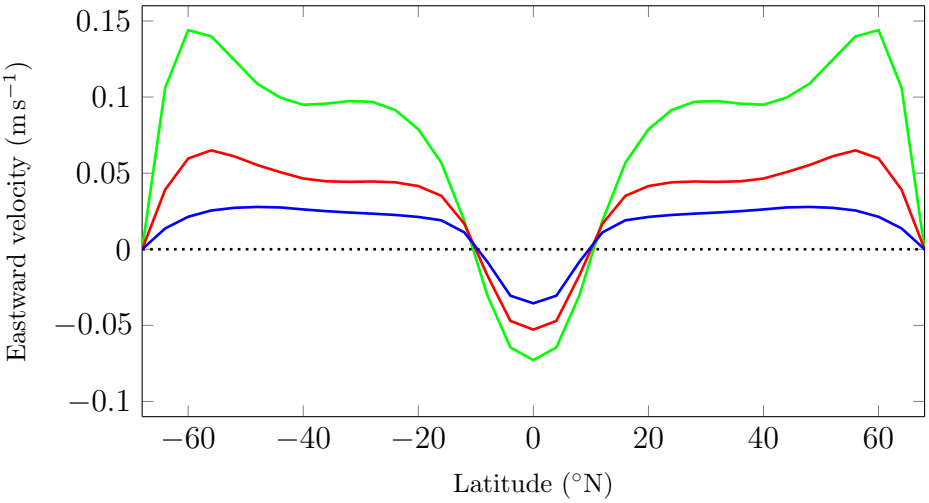


Figure 6.2: Quasi-steady state zonally-averaged surface eastward velocity ($\mathrm{m\,s^{-1}}$) for a ridgeworld configuration with (blue) 1 day rotation period, (red) 3 day rotation period, and (green) 10 day rotation period.

The northward surface velocity field is dominated by the western boundary current which, as well as its counter current, is stronger at longer rotation periods. In particular, at 30°N the peak northward velocity more than doubles from $0.22\,\mathrm{m\,s^{-1}}$ at a 1 day to $0.54\,\mathrm{m\,s^{-1}}$ at a 10 day rotation period (figure 6.3). Inspection of this cross section also shows that the western boundary current is wider at longer rotation periods; this is in qualitative agreement with the theory, in which the boundary layer thickness scales with $\beta^{-1/3}$ (Munk 1950), where $\beta$ is the gradient of the Coriolis parameter $f$.

The overturning circulation is stronger at longer rotation periods; the peak value is 45 Sv at a 1 day, 58 Sv at a 3 day, and 104 Sv at a 10 day rotation period, which occurs in the high latitudes (figure 6.4). The structure of the circulation is similar at a 1 and 3 day rotation period, however there is a qualitative difference in the 10 day case. At a 10 day rotation period the circulation is much shallower and there exist weak overturning cells in the

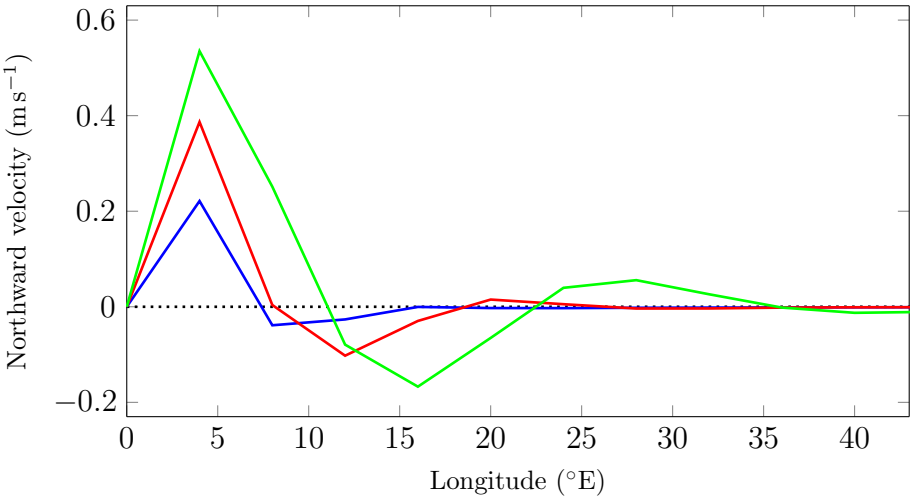


Figure 6.3: Quasi-steady state northward ocean surface velocity (m s$^{-1}$) for a ridgeworld configuration at the western side of the basin at 30°N, with (blue) 1 day rotation period, (red) 3 day rotation period, and (green) 10 day rotation period.

low latitudes at depth, which have opposite orientation to the primary cells, whereas in the 1 and 3 day cases there is a single overturning cell in each hemisphere. This difference can also be seen by considering how the peak value changes with depth (figure 6.5), which shows a much weaker (stronger) circulation in the lower (upper) half of the ocean for a 10 day rotation period, compared to 1 and 3 days. In general, the peak value occurs at shallower depth at longer rotation periods.

The overturning circulation in all 3 cases could be modelled using the box model with two boxes in each hemisphere, as for the control case (§4.2), with sinking in the high latitude box and upwelling in the low latitudes. However, the box model does not include any rotational effects and therefore could not be used to model the change with rotation period explored here. The stability of the circulation found using MOMA can be considered in terms of the salt advection feedback; the freshwater transport at 30°N is -0.14 Sv at a 1 day, -0.20 Sv at a 3 day, and -0.30 Sv at a 10 day rotation period. These all indicate an unstable circulation and, since the values scale with the strength of the overturning circulation, it is concluded that the rotation period does not impact on the stability of the circulation.

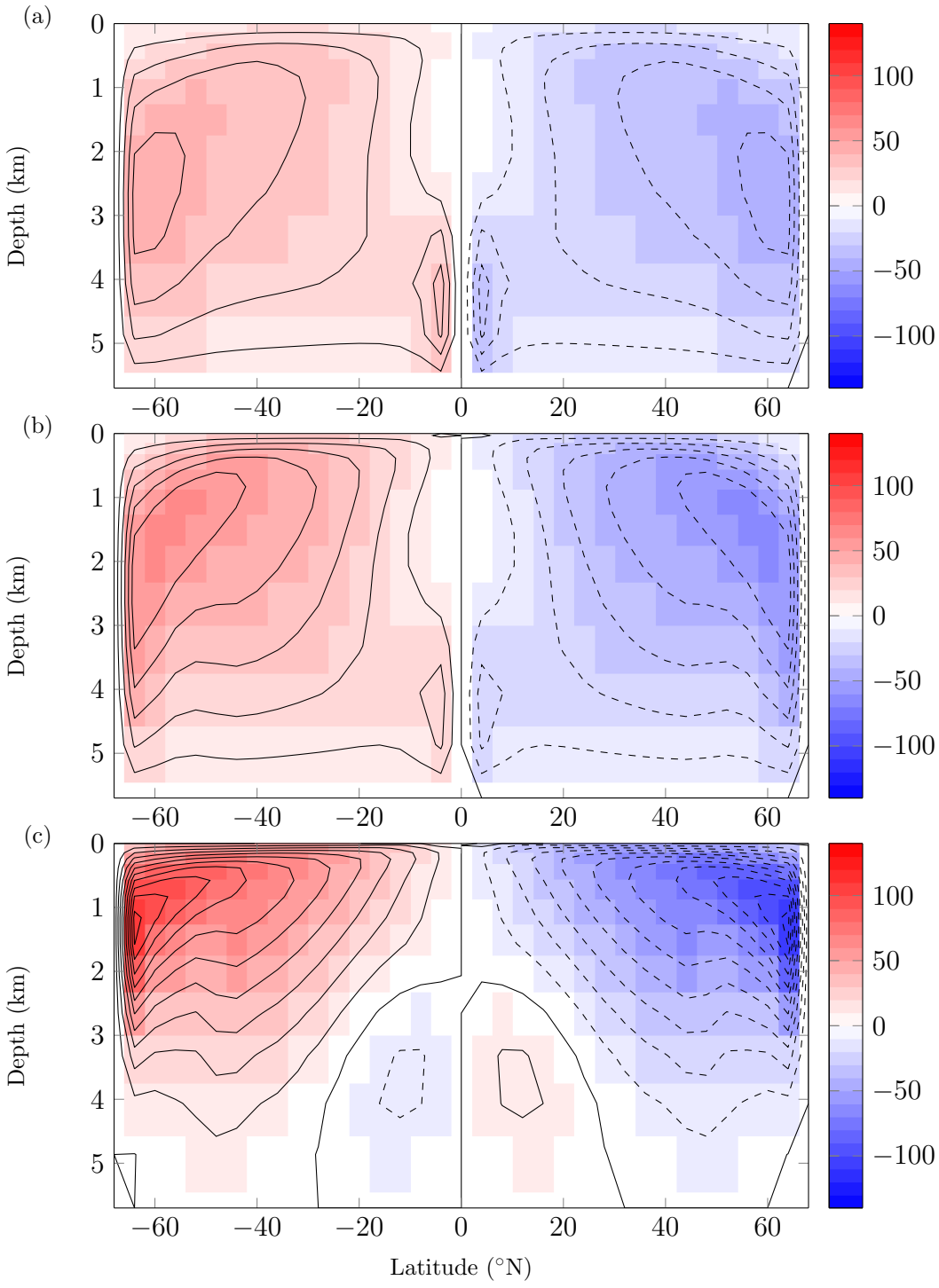


Figure 6.4: Quasi-steady state overturning streamfunction (Sv) for a ridgeworld configuration with (a) 1 day rotation period, (b) 3 day rotation period, and (c) 10 day rotation period. Contour interval is 10Sv, positive circulation is anti-clockwise.

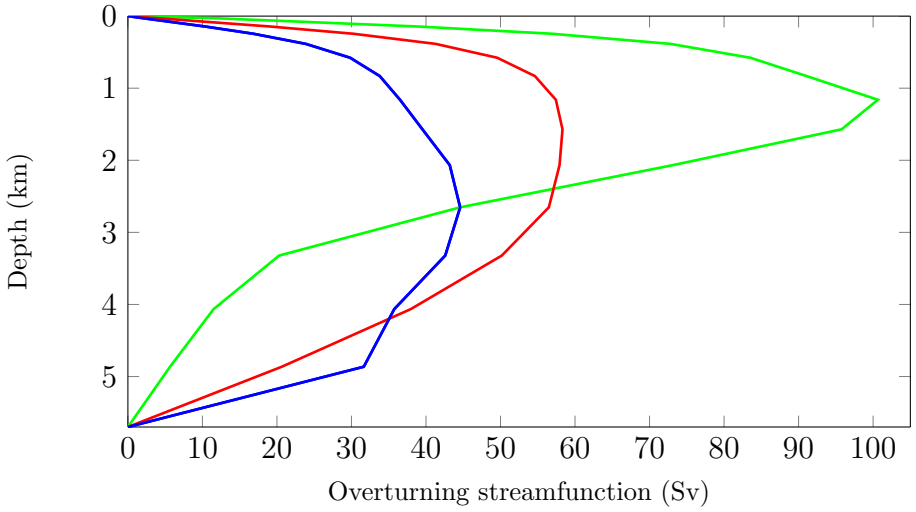


Figure 6.5: Quasi-steady state peak overturning streamfunction (Sv) with depth for a ridgeworld configuration with (blue) 1 day rotation period, (red) 3 day rotation period, and (green) 10 day rotation period.

### 6.3.3 Tracers

As the rotation period is lengthened, cooling is observed throughout the majority of the ocean, including the deep ocean (figure 6.6). This drop in temperature peaks in the surface 1000 m of the equatorial regions. The only area of warming is near the surface at high latitudes. The maximum cooling is 3°C and 6.2°C at a 3 and 10 day rotation period, respectively. The warming observed is smaller in magnitude with values 0.6°C and 1.6°C, respectively.

The warmer water in high latitudes, which is observed in the zonally-averaged temperature when increasing the rotation period, corresponds to the regions of greatest warming of water at the surface (figure 6.7). The greatest difference in surface temperature when lengthening the rotation period is a warming of 7.5°C in the high latitudes at the western side of the basin, with the majority of other areas displaying a significantly smaller response as the rotation period is lengthened. The wider and stronger western boundary current, which occurs at longer rotation periods (figure 6.3), results in a wider warm region at the surface near the western boundary. The stronger counter current which occurs adjacent to this is seen as cooler regions in the cases with the a longer rotation period.

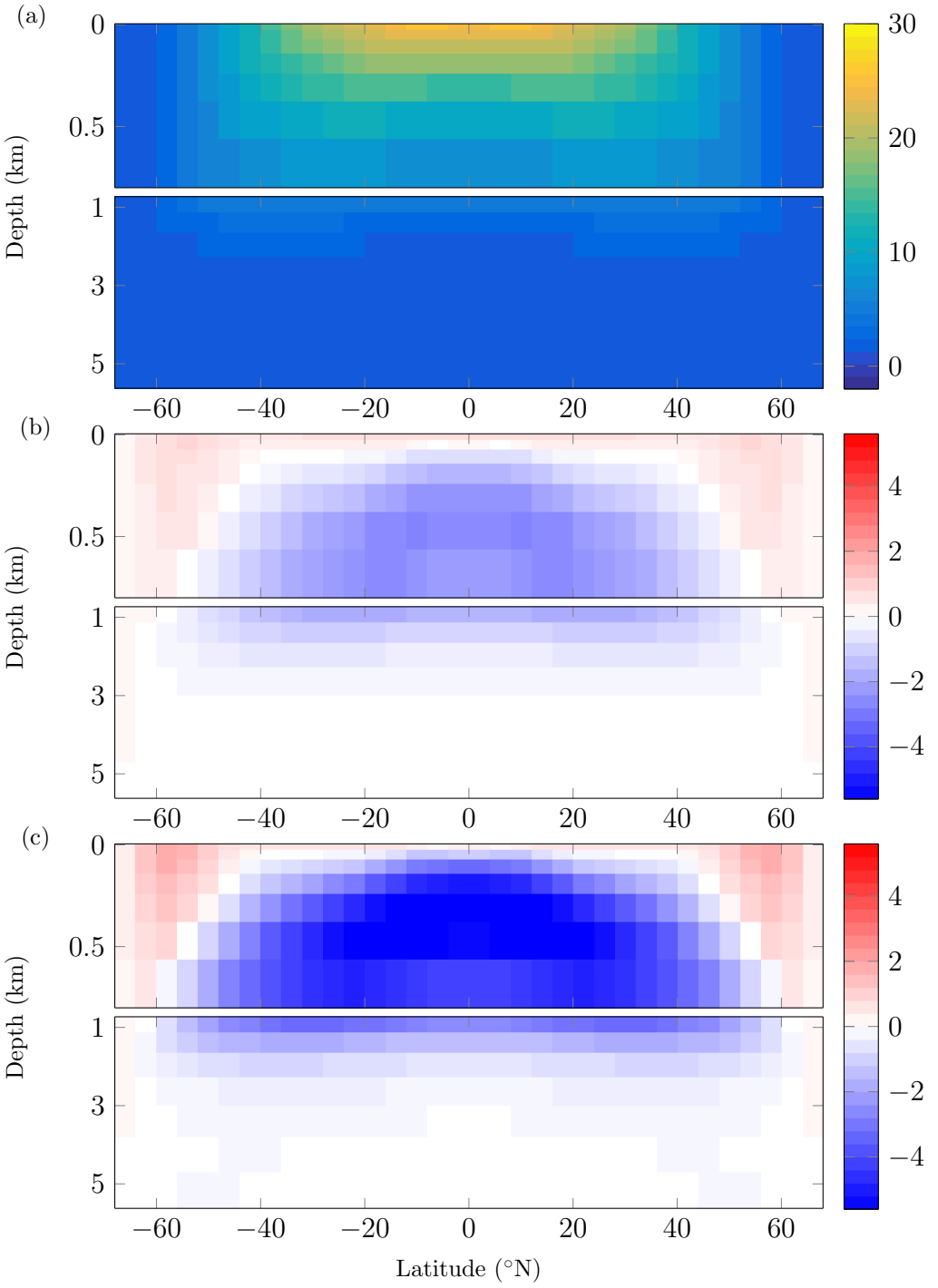


Figure 6.6: Quasi-steady state zonally-averaged ocean temperature (°C) for a ridgeworld configuration with (a) 1 day rotation period, (b) the difference 3 day - 1 day rotation period, and (c) the difference 10 day - 1 day rotation period. Note the expanded vertical scale in the upper 1 km of the ocean.

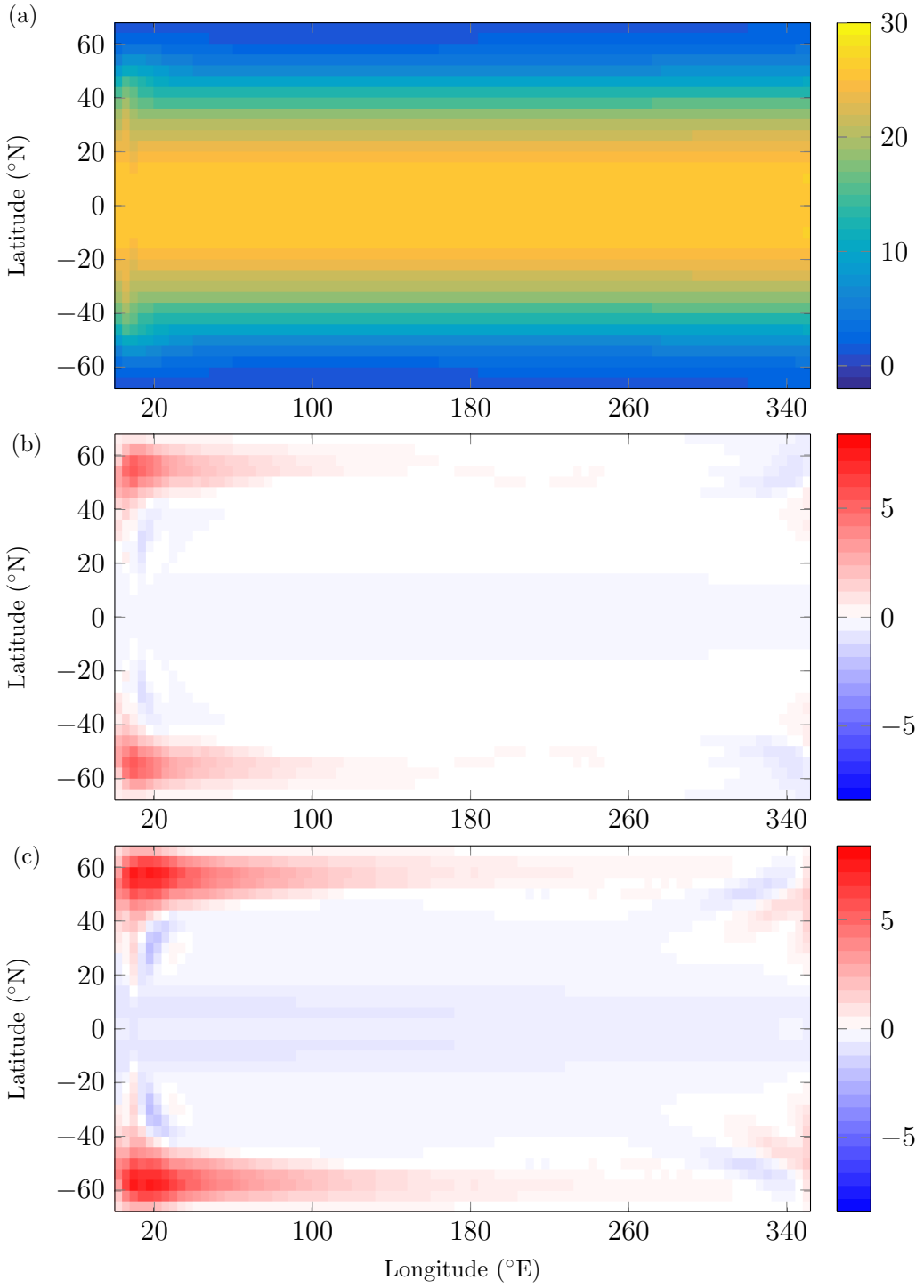


Figure 6.7: Quasi-steady state ocean surface temperature (°C) for a ridgeworld configuration with (a) 1 day rotation period, (b) the difference 3 day - 1 day rotation period, and (c) the difference 10 day - 1 day rotation period.

Since deep water formation occurs in the high latitudes (figure 6.4), the warmer water at the surface there is convected downwards and creates the warmer regions seen in the zonally-averaged temperature (figure 6.6). This is also seen in the temperature at 500 m depth (figure 6.8), where the vast majority of the ocean is cooler when the rotation period is longer, with only small areas of warmer water in the high latitudes. The coolest regions are found at the eastern boundary where there is greater upwelling of cold bottom water, which is associated with the stronger overturning circulation at longer rotation periods.

The thermocline depth is calculated from the temperature using

$$d = \frac{\int_{-H}^{0} \big(T - T(z=-H)\big) z \, dz}{\int_{-H}^{0} \big(T - T(z=-H)\big) \, dz}, \tag{6.11}$$

where $H$ is the depth of the ocean (Park & Bryan 2000). The differences in the ocean temperature when varying the rotation period, described above, correspond to a shallower thermocline depth at longer rotation periods (figure 6.9), as predicted by the scaling (6.7). This is true in most regions, however, in the low latitudes the thermocline is deeper for the 10 day case than in the 3 day case. This can be explained by a qualitative difference in the overturning circulation in the 10 day case, in which the upwelling in the low latitudes does not extend from the equatorial deep ocean as it does in the 1 and 3 day cases (figure 6.4).

### 6.3.4 Heat transport

The peak heat transport more than doubles from 1.5 PW to 3.2 PW with an increase in the rotation period from 1 day to 10 days (figure 6.10). This increase in strength is consistent with the associated scale (6.10). On increasing the rotation period from 1 day to 4 days in an Earth-like configuration the mean ocean heat transport between 20°N and 60°N increases from 0.5 PW to 0.8 PW (Vallis & Farneti 2009). The equivalent value here is an increase from 1.1 PW to 1.7 PW when increasing the rotation period from 1 day to 3 days. Despite the larger change in rotation period in the Earth-like case to the ridgeworld configuration, the values increase by approximately the same factor, with the difference lying in the inclusion of

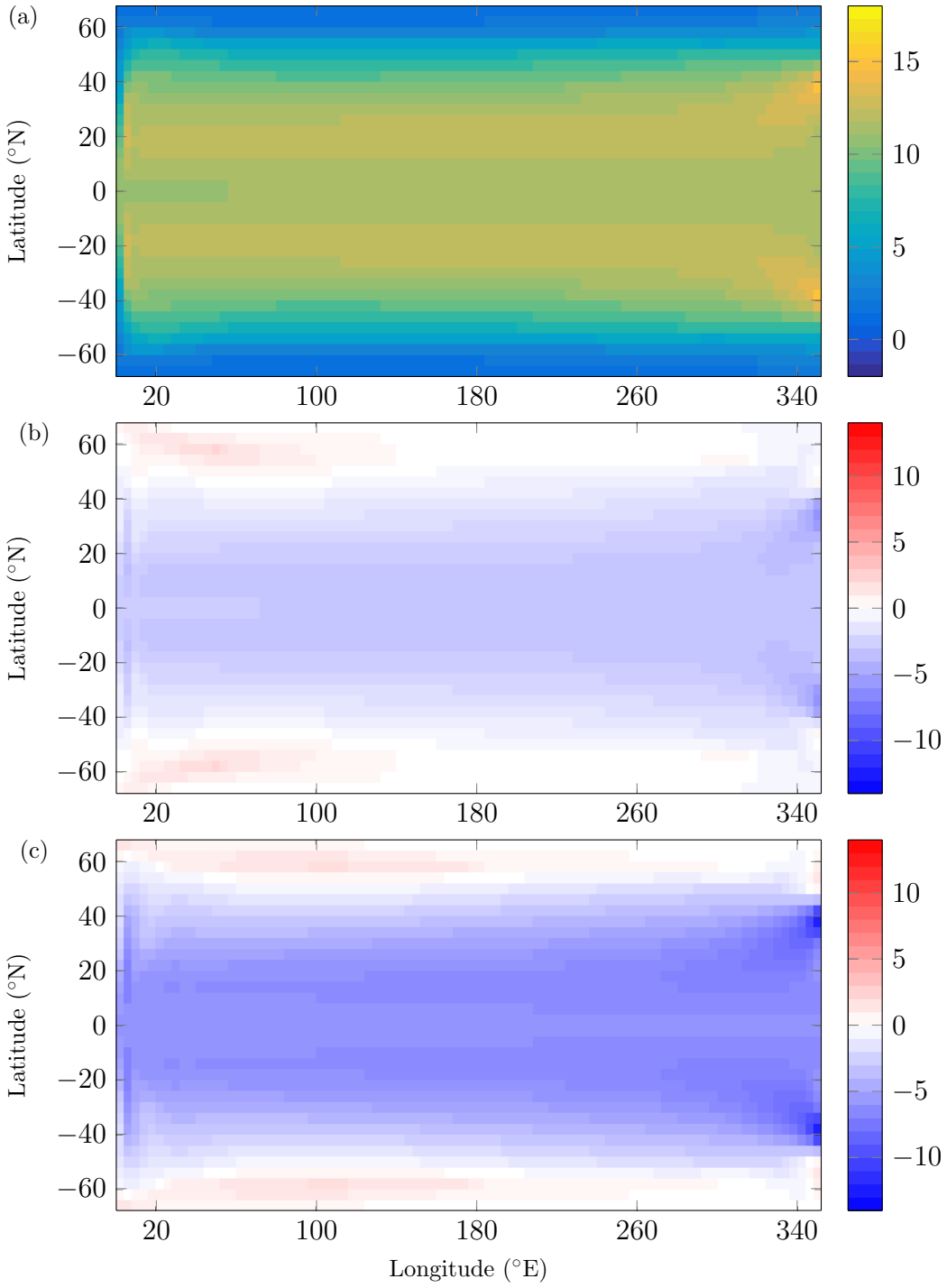


Figure 6.8: Quasi-steady state ocean temperature (°C) at 500 m depth for a ridgeworld configuration with (a) 1 day rotation period, (b) the difference 3 day - 1day rotation period, and (c) the difference 10 day - 1day rotation period.

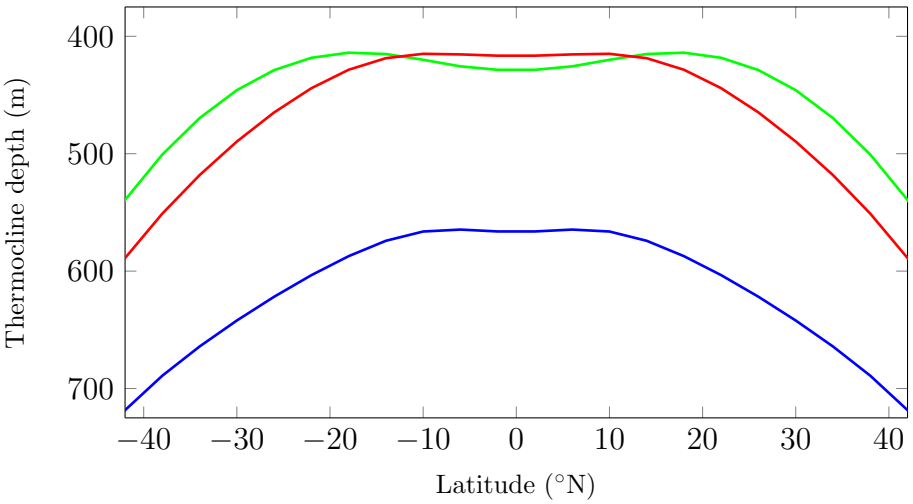


Figure 6.9: Quasi-steady state zonally-averaged thermocline depth (m) for a ridgeworld configuration with (blue) 1 day rotation period, (red) 3 day rotation period, and (green) 10 day rotation period.

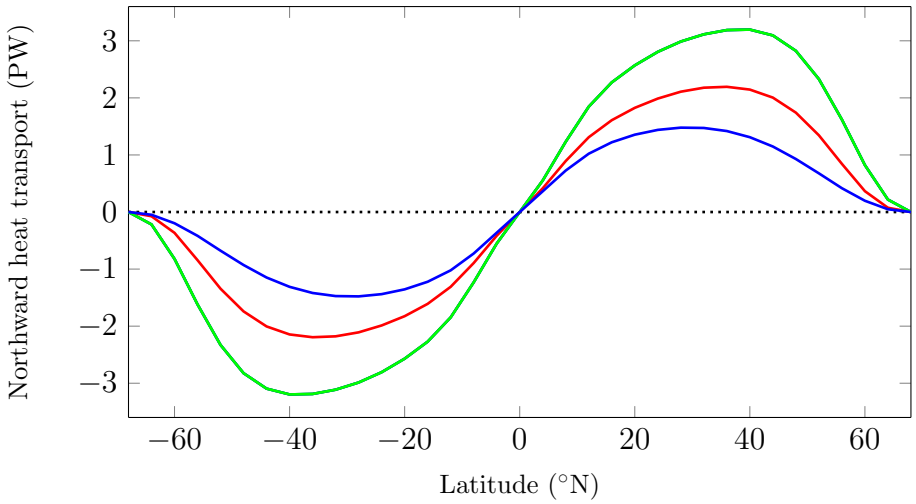


Figure 6.10: Quasi-steady state northward ocean heat transport (PW) for a ridgeworld configuration with (blue) 1 day rotation period, (red) 3 day rotation period, and (green) 10 day rotation period.

wind forcing and coupled modelling.

Due to the constraint of fixed surface forcing in the model the magnitude of the changes in surface temperature with rotation period are limited. Consequently, a better measure of the potential impact of rotation period on the surface temperatures is the surface heat flux (figure 6.11). As the rotation is slowed there is an increase in the heat flux from the ocean to the atmosphere in the high latitudes. There is also an increase in the heat flux into the ocean, which occurs over a larger area, in the equatorial regions.

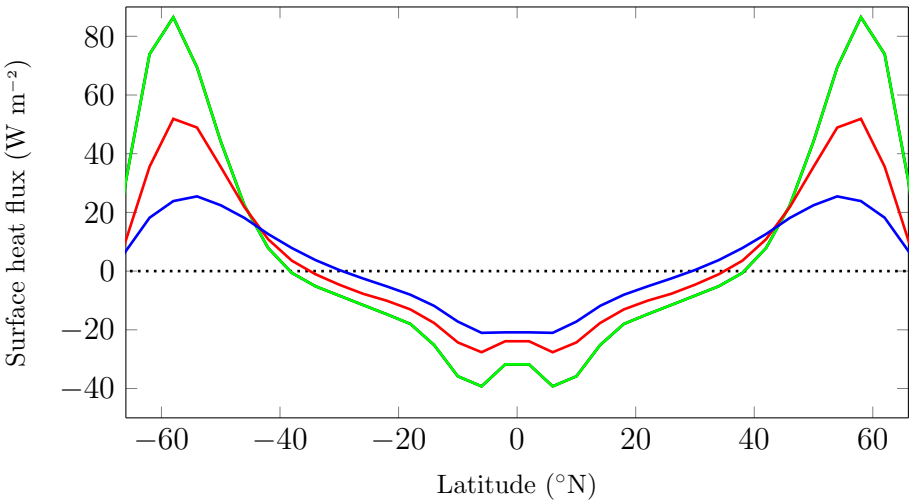


Figure 6.11: Quasi-steady state surface heat flux ($\mathrm{W\,m^{-2}}$) for a ridgeworld configuration with (blue) 1 day rotation period, (red) 3 day rotation period, and (green) 10 day rotation period. Positive values are from the ocean to the atmosphere.

The peak heat flux to the atmosphere increases by more than a factor of 3, from $25\,\mathrm{W\,m^{-2}}$ to $86\,\mathrm{W\,m^{-2}}$, when the rotation period is increased from 1 day to 10 days. This would result in warmer high latitudes and cooler low latitudes, which equates to a decreases in the meridional temperature gradient at the surface.

## 6.4 Comparison of scale analysis and model

The results obtained from the model may be compared to the values predicted by the scalings, where the thermocline depth in the model is calculated using (6.11) and the zonally-averaged value at 30°N is used (Park & Bryan 2000). From the calculated values (table 6.1) and inspection of logarithmic plots relating each of the quantities to the rotation rate (figure 6.12), it is seen that the relations (6.7) – (6.10) obtained from the scale analysis agree with the behaviour determined numerically using MOMA.

The scaling and model values are not as close for the thermocline depth as for the other measures due to the uncertainty of approximating a single thermocline depth in a continuous profile, and taking an average of a measure with high spatial variability. Despite this the prediction of the

| Rotation period | $d$ (m) | | $U$ ($\mathrm{m\,s^{-1}}$) | | $\Psi$ (Sv) | | $Q$ (PW) | |
|---|---|---|---|---|---|---|---|---|
| | Model | Scale | Model | Scale | Model | Scale | Model | Scale |
| 1 day | 640 | 640 | 0.0235 | 0.0235 | 44.6 | 44.6 | 1.478 | 1.478 |
| 3 days | 488 | 443 | 0.0450 | 0.0489 | 58.3 | 64.3 | 2.192 | 2.132 |
| 10 days | 446 | 297 | 0.0889 | 0.1091 | 100.6 | 96.1 | 3.178 | 3.184 |

Table 6.1: Comparison of quasi-steady state values from the model to those predicted by the scalings (6.7) – (6.10) for mean thermocline depth $d$ (m) at 30°N/S, mean magnitude of horizontal surface velocity $U$ ($\mathrm{m\,s^{-1}}$), peak overturning streamfunction $\Psi$ (Sv), and peak ocean heat transport $Q$ (PW). Scaling values are calculated using the model value at 1 day rotation period.

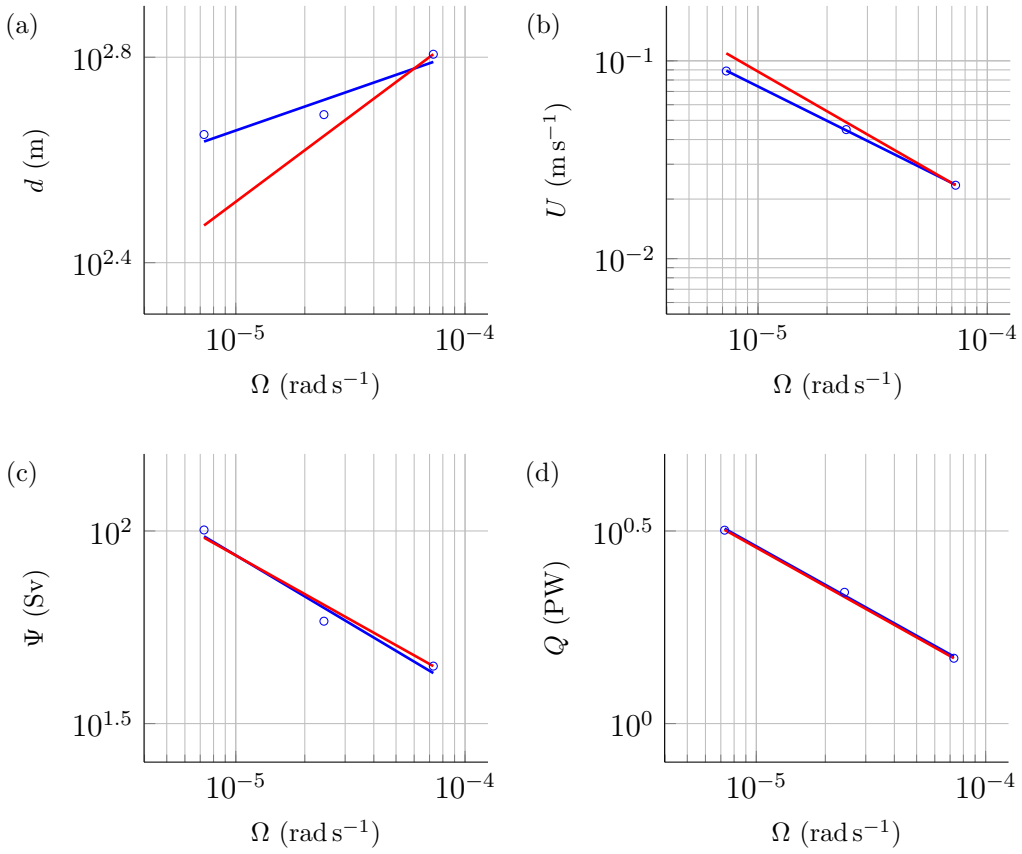


Figure 6.12: Plots with logarithmic scale axes showing (blue circles) the values predicted by the model, with (blue line) the associated line of best fit, and (red line) the relationship predicted by the scale analysis (6.7) – (6.10), for (a) mean thermocline depth $d$ (m) at 30°N/S, (b) mean magnitude of horizontal surface velocity $U$ ($\mathrm{m\,s^{-1}}$), (c) peak overturning streamfunction $\Psi$ (Sv), and (d) peak ocean heat transport $Q$ (PW).

general behaviour from the scale analysis is observed in the model results (figure 6.12(a)); as the rotation period is lengthened the thermocline depth

becomes shallower. There is good agreement between the values predicted by the scale analysis and found in the model for the horizontal velocities (figure 6.12(b)), and for the overturning circulation (figure 6.12(c)), and the scaling for the ocean heat transport predicts the model values with surprising accuracy (figure 6.12(d)) given the approximations in the scale analysis. To quantify the accuracy of the predictions from the scale analysis, the power relationships between each of these quantities and the rotation rate, from the scale analysis and model results, are compared (table 6.2); this is the comparison of the gradient of the lines in each of the plots (figure 6.12).

| Quantity | Power relation $m$ | |
|---|---|---|
| | Scale | Model |
| $d$ | 1/3 | 0.16 |
| $U$ | -2/3 | -0.58 |
| $\Psi$ | -1/3 | -0.36 |
| $Q$ | -1/3 | -0.33 |

Table 6.2: Comparison of the power relationship between each quantity and the rotation rate $\Omega$ (Quantity $\sim \Omega^m$) from the scale analysis and model results.

## 6.5 Summary

The impact of varying the rotation period of a planet on the ocean may be predicted by a scale analysis of the dominant balances in the ocean, and also shown using a numerical model. In both cases, it is found that lengthening the rotation period of a planet makes the thermocline depth shallower, horizontal velocities greater, the overturning circulation stronger, and the poleward ocean heat transport greater. Overall, the impact of a longer rotation period is to decrease the equator-pole temperature gradient, however more detailed conclusions are not possible here due to the fixed surface forcing employed by MOMA.

# Chapter 7

# Tidal locking

A tidally locked configuration, where one side of the planet always faces its star, is a likely scenario for planets orbiting smaller stars in the habitable zone (figure 1.2(a)). In such a situation large thermal gradients potentially exist between the light and dark side, with the ocean and atmosphere acting to smooth this contrast. Smaller stars, such as red dwarfs constitute 70% of the stars in our galaxy and hence this is expected to be a common orbital configuration for planets in the habitable zone. The ocean state in such scenarios is investigated using the coupled atmosphere-ocean general circulation model FORTE.

## 7.1 Atmospheric modelling

The vast majority of climate modelling studies of tidally locked planets focus on the atmospheric component of the climate system. Model complexity ranges from an idealised two-column model (Yang & Abbot 2014), to atmospheric general circulation models (Joshi et al. 1997, Joshi 2003, Merlis & Schneider 2010, Edson et al. 2011, Leconte et al. 2013), and coupled atmosphere-ocean general circulation models (Yang et al. 2013).

The atmospheric circulation is found to consist of a thermally direct cell, with ascending flow at the substellar point and descending flow elsewhere (Merlis & Schneider 2010, Edson et al. 2011, Leconte et al. 2013) and low level flow from dark to light side through the polar regions (Joshi et al. 1997). Equatorial superrotation; an eastward jet above the equator with greater velocity than the surface, is also a feature of the atmospheric circulation on tidally locked planets (Joshi et al. 1997, Merlis & Schneider 2010, Edson et al. 2011, Leconte et al. 2013), and is driven by the equatorward movement of eastward momentum by planetary scale Rossby waves, which result from the large longitudinal temperature contrasts (Showman & Polvani 2011). Due to this driving factor, the existence and strength of superrotation depends on the rotation period of the planet; in particular the Rossby radius of deformation, which scales inversely with the Coriolis parameter. Superrotation is a dominant factor when the Rossby radius of deformation is of planetary scale.

The zonally-averaged meridional circulation is also found to have dependence on the planetary rotation period; at a rotation period of 365 days a Hadley cell type circulation is found, which is approximately three times the strength of that on Earth and extends to the high latitudes, and at the more rapid rotation rate of Earth a reversal of this circulation occurs with descending flow at the equator and ascending flow in the region of 15°N/S (Merlis & Schneider 2010).

Despite different circulation patterns at different rotation periods, the temperature contrast between the light and dark side is similar (Merlis & Schneider 2010). A more crucial factor for temperature is the inclusion of an ocean which reduces the temperature gradient between the light and dark

side, as well as smoothing the sharp temperature gradient at the terminator, which it does through the heat transport in the ocean and latent heat flux in the atmosphere (Joshi 2003, Edson et al. 2011). The inclusion of a hydrological cycle also increases the global mean temperature, by over 35°C at the rotation period of Earth, through the greenhouse effect (Edson et al. 2011).

At the inner edge of the habitable zone cloud feedback effects are identified as an important factor in the stability of atmospheres of tidally locked planets; high level cloud on the light side, which results from convection at the substellar point, increases the albedo and acts to cool the planet (Yang et al. 2013, Yang & Abbot 2014). This is a negative feedback on the system as warmer temperatures increase convective cloud cover, further lowering the albedo and cooling the climate. Infrared radiation to space on the dark side of the planet is also identified as an important process in cooling the climate of planets at the inner edge of the habitable zone (Yang & Abbot 2014).

The main conclusion which is gained from modelling the atmosphere of tidally locked planets is that warm enough dark side temperatures can be maintained to sustain a global atmosphere, and hence the potential for stable liquid surface water (Joshi et al. 1997, Joshi 2003, Edson et al. 2011, Yang et al. 2013).

## 7.2 Numerical simulations

The coupled atmosphere-ocean general circulation model FORTE is used to model climate, with the focus of the analysis on the ocean, in a tidally-locked configuration. Existing studies have found the ocean plays an important role in global heat transport; modelling an aquaplanet shows easterly currents along the equator substantially extend the region of open water, from the 'eyeball' state found with a slab ocean model, into the dark side and dramatically limits ice thickness (Hu & Yang 2014, Yang et al. 2014b). The heat transport from light to dark side is found to be greater with increasing ocean depth, and a limited exploration of the location of barriers concludes a barrier at the western terminator has little impact on ice thickness, in

contrast to a barrier at both terminators which results in significantly thicker ice on the dark side (Yang et al. 2014b). Here, the ocean dynamics are investigated when the longitude, relative to the substellar point, of a single meridional barrier in the ocean is varied.

### 7.2.1 Model configuration

A ridgeworld-type land configuration is used; a subsurface barrier extends from the sea floor to 30 m below the surface (one ocean grid box). The location of the star is fixed relative to the planet to provide a tidally-locked scenario, with the substellar point chosen to be at 180°E, whilst an Earth-like rotation rate is maintained. Four simulations are performed with the barrier located at a different longitude in each; 0°E, 90°E, 180°E, and 270°E, which correspond to the antistellar point, the terminator 90°W of the substellar point, the substellar point, and the terminator 90°E of the substellar point, respectively.

Some of the parameters in the finer resolution configuration of MOMA used in the coupled model vary from those used in the ocean only runs, and in addition there are parameters associated with the Gent-McWilliams scheme (table 7.1). With the implementation of isopycnal diffusivity the horizontal eddy diffusivity is zero everywhere except the surface layer. In the surface layer it provides a parameterisation of waves in the equatorial region, and hence varies with latitude, $\phi$, with the profile $A_h\big(2 + 38\exp\big(-(\phi/0.07)^4\big)\big)$, where $A_h = 1.0 \times 10^3\,\mathrm{m^2\,s^{-1}}$. The vertical diffusion is chosen to increase linearly with depth with the profile $K_h(1 - 9z/H)$, where $K_h = 1.0 \times 10^{-4}$. The results presented are an average of the last 100 years of quasi-steady state model output of a 1200 year run.

### 7.2.2 Surface properties

For each of the barrier locations the peaks in the surface temperature of 34-35°C occur in the mid latitudes north and south of the substellar point. These peaks occur away from the substellar point due to the strong eastward surface current at the equator as well as cloud cover at the substellar point,

| Description | Parameter | Value | Unit |
|---|---|---|---|
| Horizontal eddy viscosity | $A_m$ | $1.0 \times 10^4$ | $m^2\,s^{-1}$ |
| Horizontal eddy diffusivity | $A_h$ | see text | $m^2\,s^{-1}$ |
| Vertical viscosity | $K_m$ | $2.0 \times 10^{-4}$ | $m^2\,s^{-1}$ |
| Vertical diffusivity | $K_h$ | see text | $m^2\,s^{-1}$ |
| Isopycnal tracer diffusivity | *ahisop* | $2.5 \times 10^3$ | $m^2\,s^{-1}$ |
| Steep slope horizontal diffusivity | *ahsteep* | $3.0 \times 10^3$ | $m^2\,s^{-1}$ |
| Isopycnal thickness diffusivity | *athkdf* | $3.0 \times 10^3$ | $m^2\,s^{-1}$ |
| Tracer timestep | $\Delta t_T$ | $2.7 \times 10^3$ | s |
| Barotropic velocity timestep | $\Delta t_U$ | $2.7 \times 10^3$ | s |
| Baroclinic velocity timestep | $\Delta t_b$ | $4.5 \times 10^1$ | s |

Table 7.1: Parameters in MOMA when used in coupled modelling which differ from those in the ocean only model (table 3.2).

and are found in a similar location when modelling without a meridional barrier (Hu & Yang 2014). The minima of cooler than -42°C are found in the high latitudes (figure 7.1). More detail of the impact of the barrier on surface temperature is discussed in terms of the difference from the mean of the four different cases (figure 7.2).

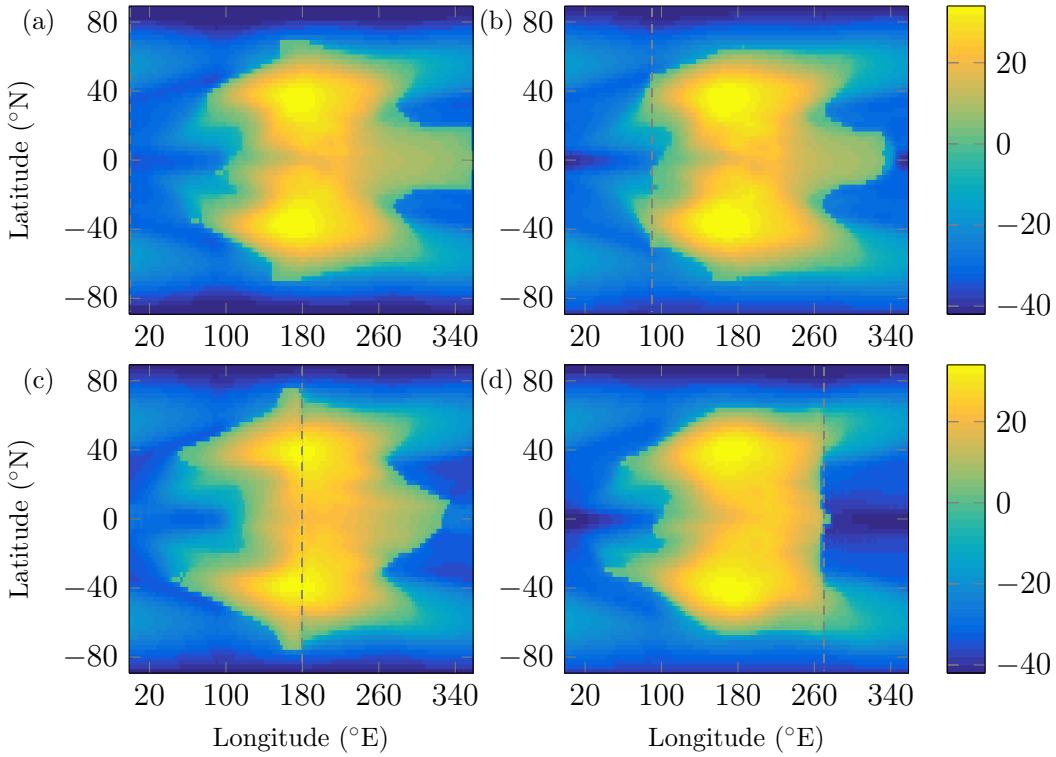


Figure 7.1: Quasi-steady state surface temperature (°C) for a tidally locked ridgeworld configuration with the substellar point at 180°E and the subsurface barrier at (a) 0°E, (b) 90°E, (c) 180°E, and (d) 270°E.

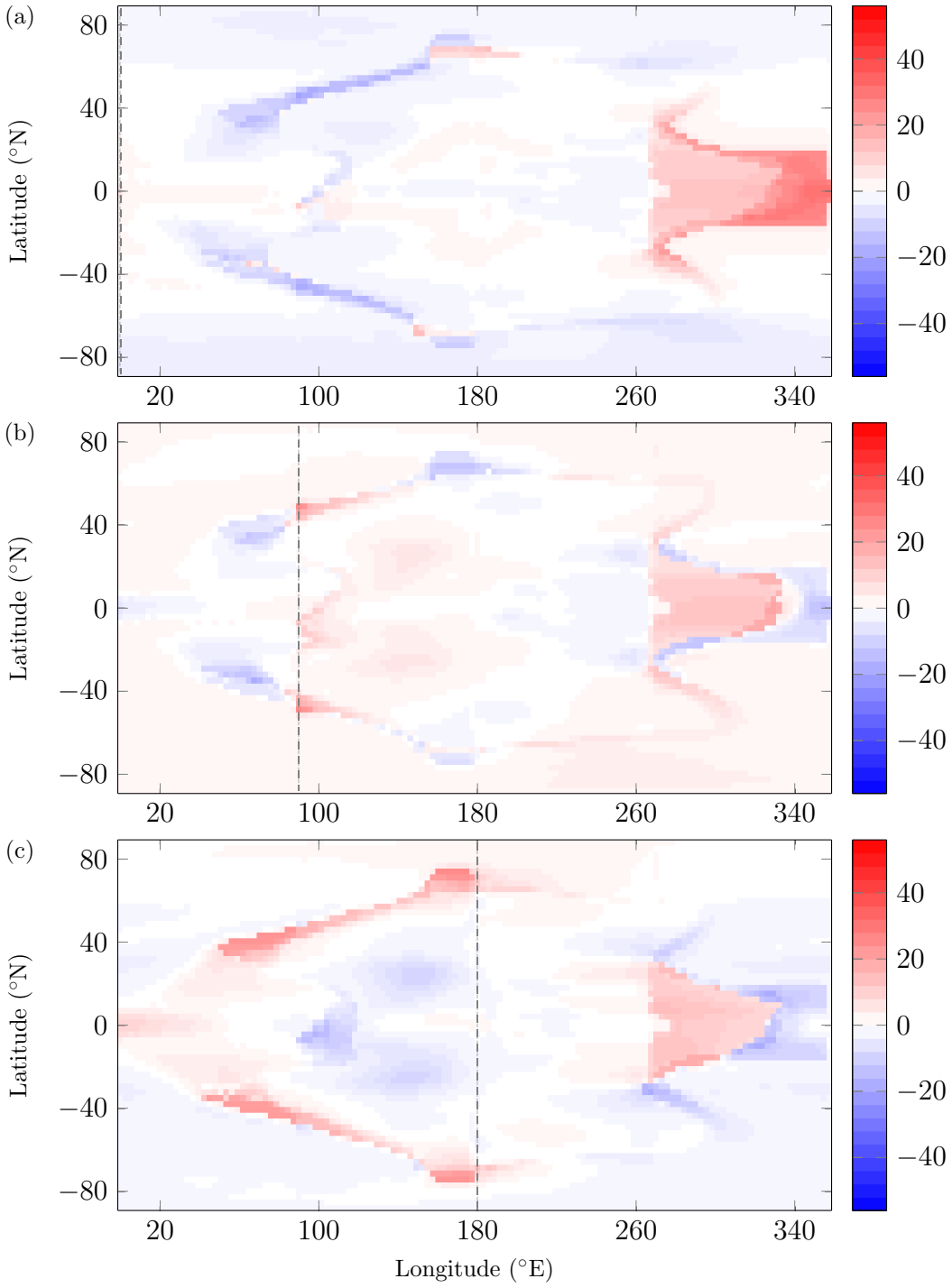


Figure 7.2: Quasi-steady state surface temperature difference (°C) for a tidally locked ridgeworld configuration with the substellar point at 180°E and the subsurface barrier at (a) 0°E, (b) 90°E, (c) 180°E, and (d) 270°E from (e) the mean of the four cases.

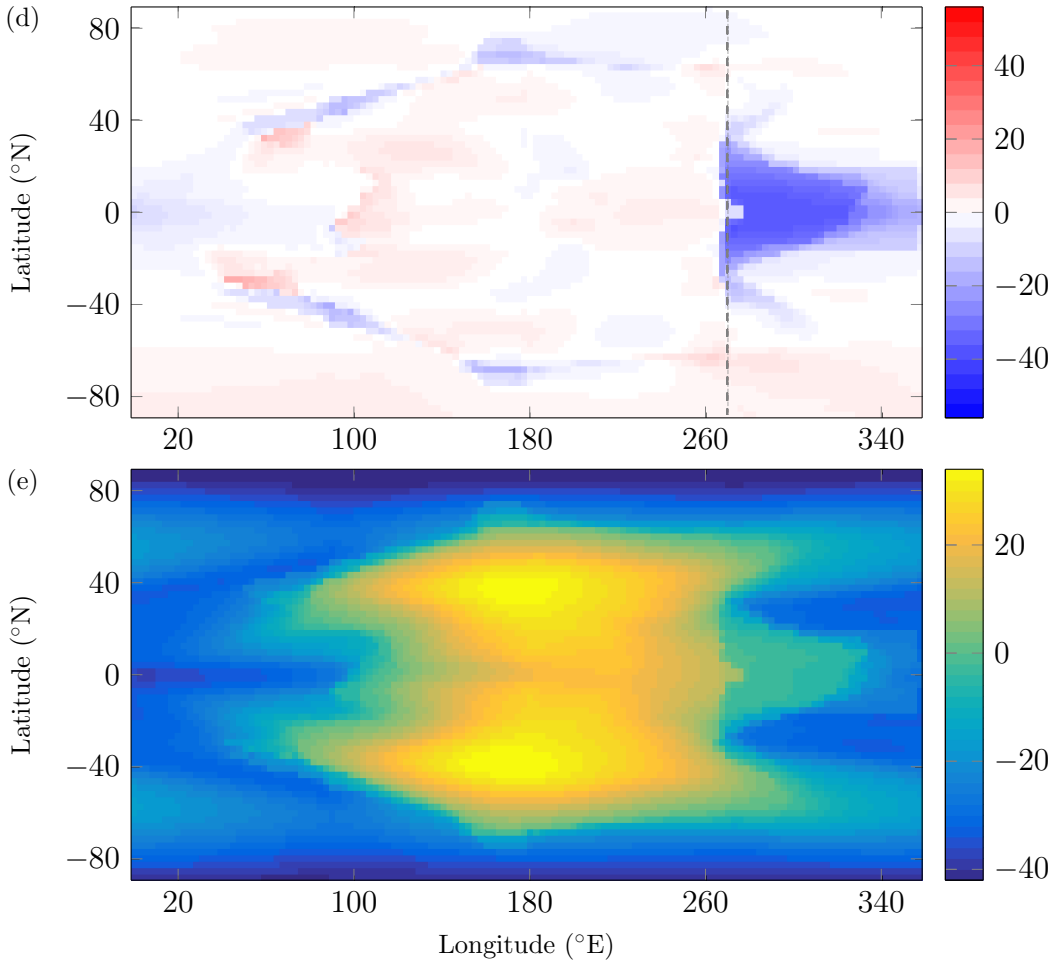


Figure 7.2: Quasi-steady state surface temperature difference (°C) for a tidally locked ridgeworld configuration with the substellar point at 180°E and the subsurface barrier at (a) 0°E, (b) 90°E, (c) 180°E, and (d) 270°E from (e) the mean of the four cases.

The most noticeable differences from the mean of the four cases occurs on the dark side in the low latitudes between 270 and 0°E when the barrier is located at either edge of this region. When the barrier is located at 0°E the surface between 270°E and the barrier is up to 31°C warmer than the mean (figure 7.2(a)), and corresponds to an ice-free region extending up to the barrier (figure 7.3(a)). In the case with the barrier at 270°E the surface temperature east of the barrier is considerably colder than the mean by up to 37°C (figure 7.2(d)) and is associated with a region of thick ice cover (figure 7.3(d)) due to the barrier blocking the eastward flow at the equator.

The ice extent has a strong relation to the surface air temperature, which is evident at the western edge of the area of open ocean, between 40 and 80°N/S in the western hemisphere, where there are significant variations in

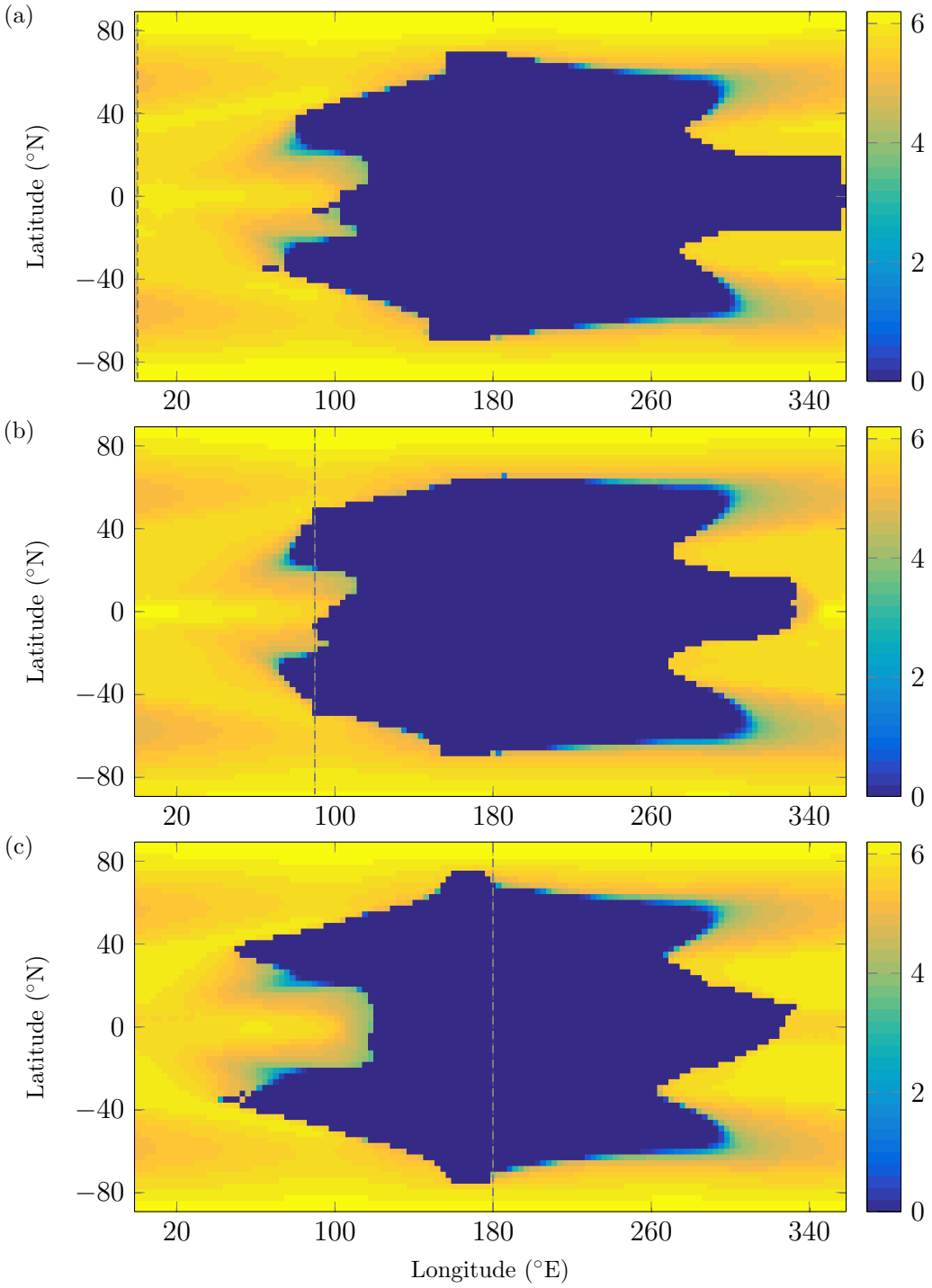


Figure 7.3: Quasi-steady state ice thickness (m) for a tidally locked ridgeworld configuration with the substellar point at 180°E and the subsurface barrier at (a) 0°E, (b) 90°E, (c) 180°E, and (d) 270°E.

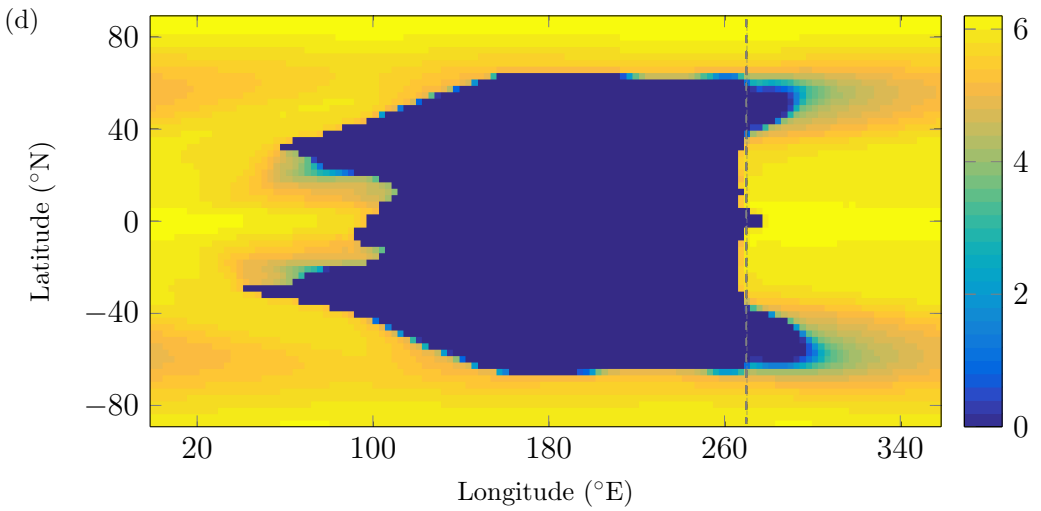


Figure 7.3: Quasi-steady state ice thickness (m) for a tidally locked ridgeworld configuration with the substellar point at 180°E and the subsurface barrier at (a) 0°E, (b) 90°E, (c) 180°E, and (d) 270°E.

the ice extent. With the barrier at 0°E the ice extends further equatorward in this region (figure 7.3(a)) giving bands of temperatures colder than the mean (figure 7.2(a)). The opposite, more open ocean (figure 7.3(c)) and warmer temperatures in the western hemisphere (figure 7.2(c)), occurs when the barrier is located at 180°E.

A combination of warmer and cooler regions is found when the barrier is located at 90°E. West of the barrier there are cooler regions where the barrier blocks flow from the warm light side. East of the barrier western boundary currents warm the surface further poleward (figure 7.2(b)). This keeps a greater amount of the ocean ice-free on the eastern side of the barrier compared to the western side (figure 7.3(b)).

### 7.2.3 Surface fluxes

The surface heat flux is into the ocean in the region surrounding the substellar point, between 40°N/S, where the planet receives the most stellar radiation (figure 7.4). The strongest such flux occurs just east of the substellar point when the barrier is located at 0 and 90°E, with peak magnitudes of 557 and 579 $\mathrm{W\,m^{-2}}$, respectively (figure 7.4(a,b)). Surrounding this area are regions of heat flux from the ocean to the

atmosphere which cover a lot of the light, as well as the dark side. There is an extremely strong flux to the atmosphere, peaking at over 900 W m$^{-2}$, in the low latitudes immediately west of the barrier when it is located at 270°E (figure 7.4(d)). There is a very small heat flux in regions where there is ice cover since the layer of ice acts to insulate the surface of the ocean. This results in extensive areas of approximately zero heat flux in the high latitudes and on the dark side of the planet. In addition to the two-dimensional fields, considering zonally- and meridionally-averaged profiles of surface heat flux allows for a clearer comparison between the four cases.

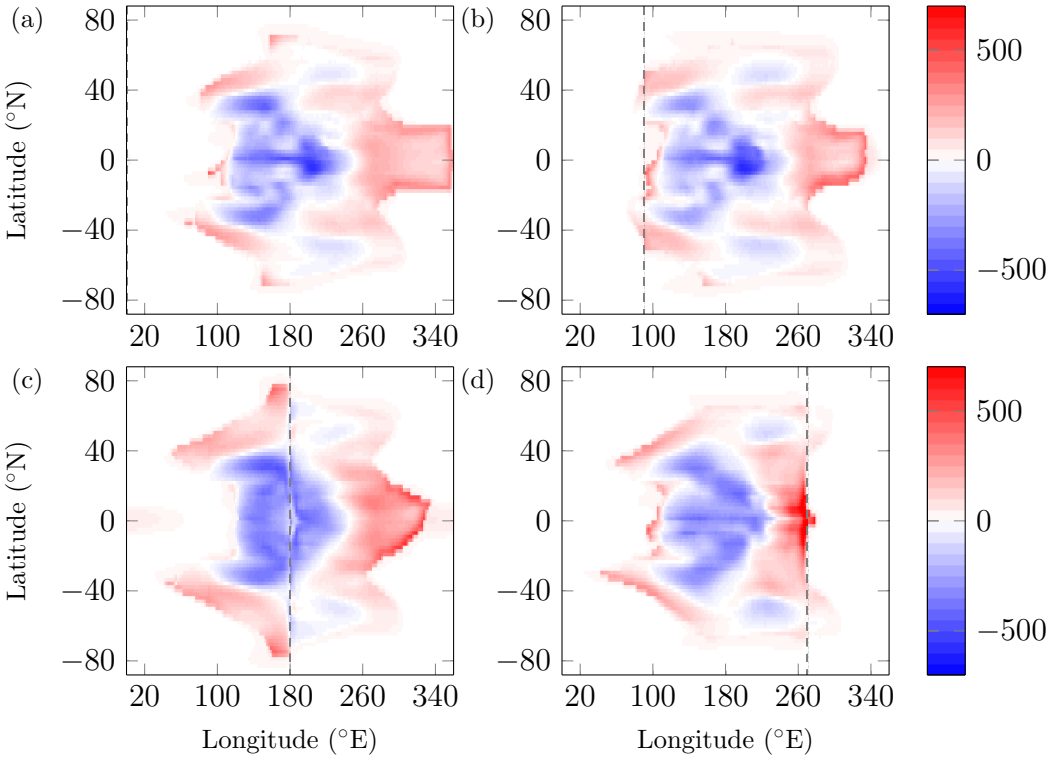


Figure 7.4: Quasi-steady state surface heat flux (W m$^{-2}$) for a tidally locked ridgeworld configuration with the substellar point at 180°E and the subsurface barrier at (a) 0°E, (b) 90°E, (c) 180°E, and (d) 270°E. Positive values are from the ocean to the atmosphere.

The zonally-averaged profile shows the strongest heat flux into the ocean in the low latitudes when the barrier is located at 0 and 90°E of magnitude 83 and 81 W m$^{-2}$, respectively (figure 7.5), which agrees with the conclusion from analysis of the two-dimensional fields above. These two cases also show a relatively strong flux to the atmosphere in the region of 15°N/S which is not seen in the other cases; this positive flux of up to 30 W m$^{-2}$ is related to the region of heat flux to the atmosphere between 260 and 360°E which

has peaks at the ice edges at these latitudes (figure 7.4(a,b)). However, the largest peaks in the zonally-averaged heat flux to the atmosphere occur at 40°N/S in all cases, with the strongest occurring when the barrier is located at 180°E of 66 W m$^{-2}$.

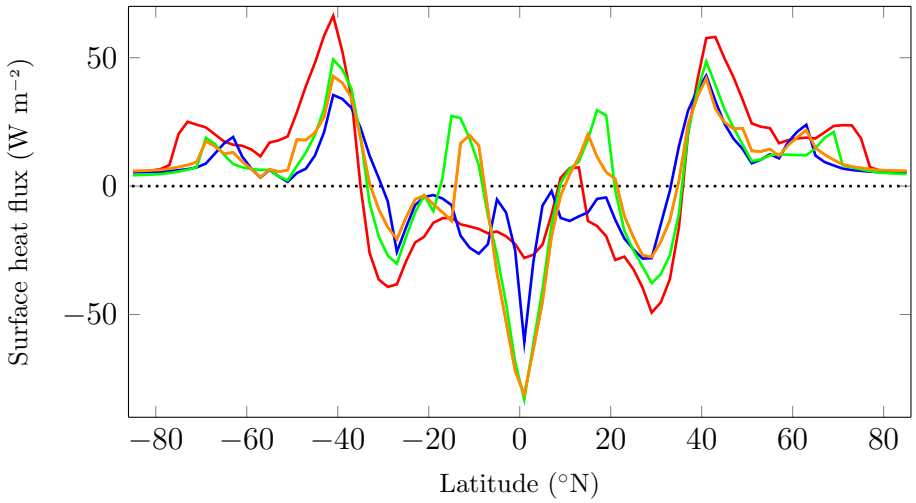


Figure 7.5: Quasi-steady state zonally-averaged surface heat flux (W m$^{-2}$) for a tidally locked ridgeworld configuration with the substellar point at 180°E and the subsurface barrier at (green) 0°E, (orange) 90°E, (red) 180°E, and (blue) 270°E. Positive values are from the ocean to the atmosphere.

The meridionally-averaged profile shows the heat flux is into the ocean between approximately 110 and 220-240°E, and is from the ocean at all other longitudes in all cases (figure 7.6). The most marked difference is when the barrier is located at 270°E in which there is a spike in heat flux to the atmosphere of 343 W m$^{-2}$ just west of the barrier, which corresponds to the region of greatest heat flux in the two-dimensional fields (figure 7.4(b)), and east of this shows the lowest heat flux in this region of the four cases due to the most extensive ice coverage there. Of the other cases, the greatest heat flux both to and from the ocean occurs in the case where the barrier is located at 180°E; the flux into the ocean peaks at 177 W m$^{-2}$ at 150°E and from the ocean peaks at 157 W m$^{-2}$ just east of 270°E.

### 7.2.4 Circulation

In the tidally locked case the most significant overturning circulation, and that which shows the largest dependence on barrier location, is in the

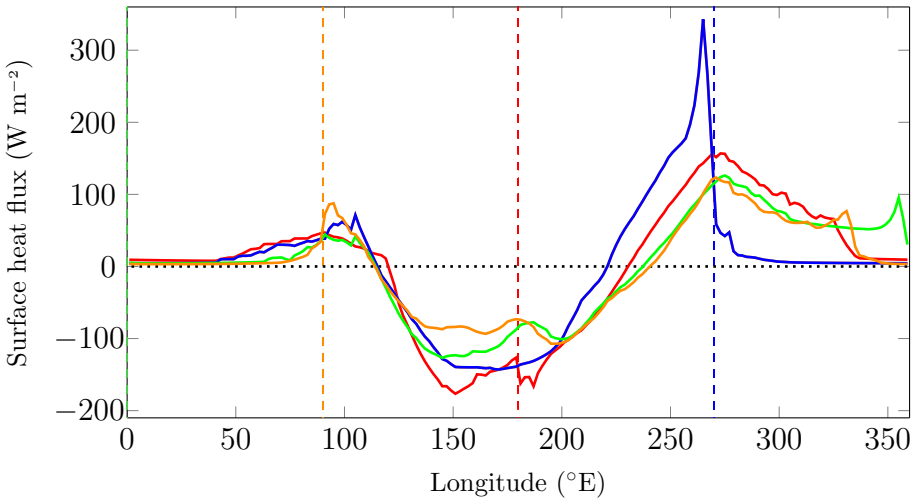


Figure 7.6: Quasi-steady state meridionally-averaged surface heat flux ($\mathrm{W\,m^{-2}}$) for a tidally locked ridgeworld configuration with the substellar point at 180°E and the subsurface barrier at (green) 0°E, (orange) 90°E, (red) 180°E, and (blue) 270°E. Positive values are from the ocean to the atmosphere.

zonal direction. The zonal overturning circulation shows a similar structure when the barrier is located at 0°E and 90°E, whereas the other cases show significantly different patterns (figure 7.7). With the barrier at 0°E there is a negative circulation cell, with eastward flowing surface water, which is predominantly in the upper 1 km of the ocean and extends into the deep ocean west of 120°E. The cell consists of deep water formation at the western side of the barrier which coincides with the ice edge in the low latitudes, and upwelling from the deep ocean in the region of 110°E. Below this circulation, in the deep ocean there is a cell of opposite direction and weaker magnitude, peaking at less than half the strength at 120 Sv, extending longitudinally from 130°E to the barrier at 360°E.

As mentioned, a similar pattern of circulation is observed when the barrier is located at 90°E, with the primary difference being that the deep cell extends to the surface on the dark side, east of the location of deep water formation which is slightly further west and again coincides with the ice edge there (figure 7.7(b)). In this case the two cells are of more equal strength; both peaking in the region of 200 Sv. The circulation is in general weaker when the barrier is located at 180°E, peaking at 135 Sv at mid-depth 40° west of the barrier (figure 7.7(c)). There is a negative circulation cell through the depth of the ocean either side of the barrier, which extends through the deep ocean on the dark side beneath a positive circulation cell in the upper

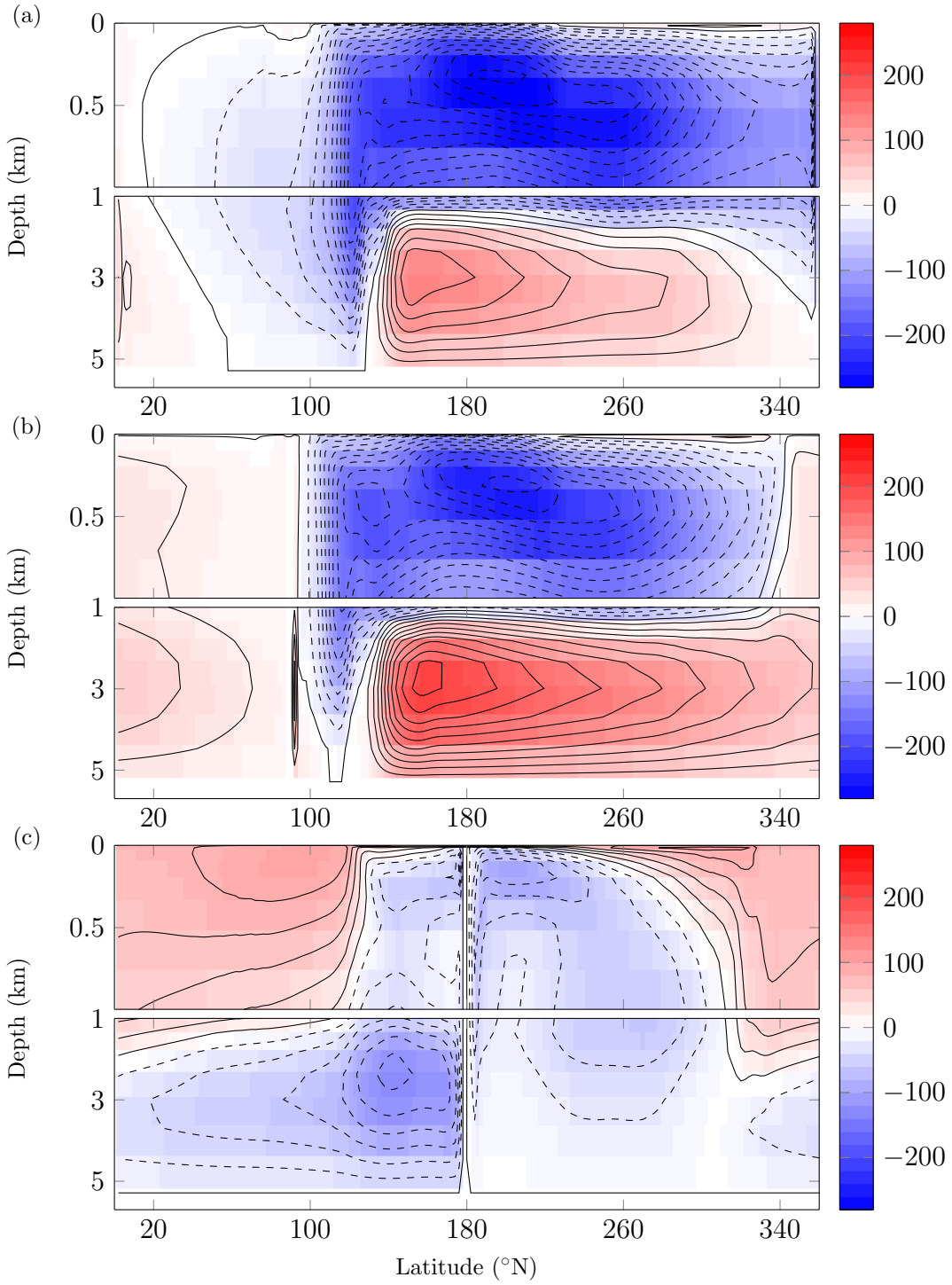


Figure 7.7: Quasi-steady state zonal overturning circulation (Sv) for a tidally locked ridgeworld configuration with the substellar point at 180°E and the subsurface barrier at (a) 0°E, (b) 90°E, (c) 180°E, and (d) 270°E. Contour interval is 20 Sv, positive circulation is anti-clockwise. Note the expanded vertical scale in the upper 1 km of the ocean.

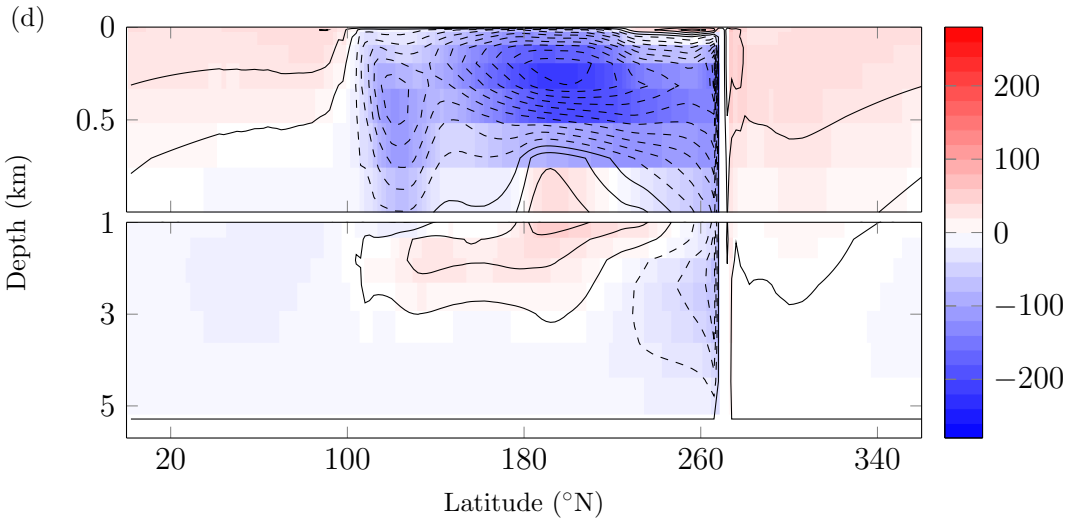


Figure 7.7: Quasi-steady state zonal overturning circulation (Sv) for a tidally locked ridgeworld configuration with the substellar point at 180°E and the subsurface barrier at (a) 0°E, (b) 90°E, (c) 180°E, and (d) 270°E. Contour interval is 20 Sv, positive circulation is anti-clockwise. Note the expanded vertical scale in the upper 1 km of the ocean.

layers. With the barrier at 270°E the circulation is dominated by a negative cell on the light side in the upper 1 km of ocean, with deep water formation occurring adjacent to the barrier (figure 7.7(d)). The strength of this cell peaks at over 200 Sv, with relatively weak circulation elsewhere which is again positive in the surface layers of the dark side.

These patterns of circulation are also reflected in the meridionally-averaged temperature (figure 7.8), particularly in the upper 1 km of the ocean. In all four of the barrier locations the circulation from the light to dark side warms the ocean on the dark side of the planet to a temperature above the surface temperature. This results in the warmest regions of the ocean on the dark side occurring below the surface layers, which are cooled from above, and are approximately 2°C warmer than the surface. In the cases where the barrier is located at 0°E and 90°E the downwelling of warm surface water at the ice edge correlates with these warmer regions below the surface layer in the upper 1 km of the ocean (figure 7.8(a,b)). When the barrier is located at 90°E, there is a clear temperature difference across the barrier of 1.7°C at 500 m depth, which is associated with the stronger circulation east of the barrier transporting heat from the surface into the interior of the ocean (figure 7.8(b)).

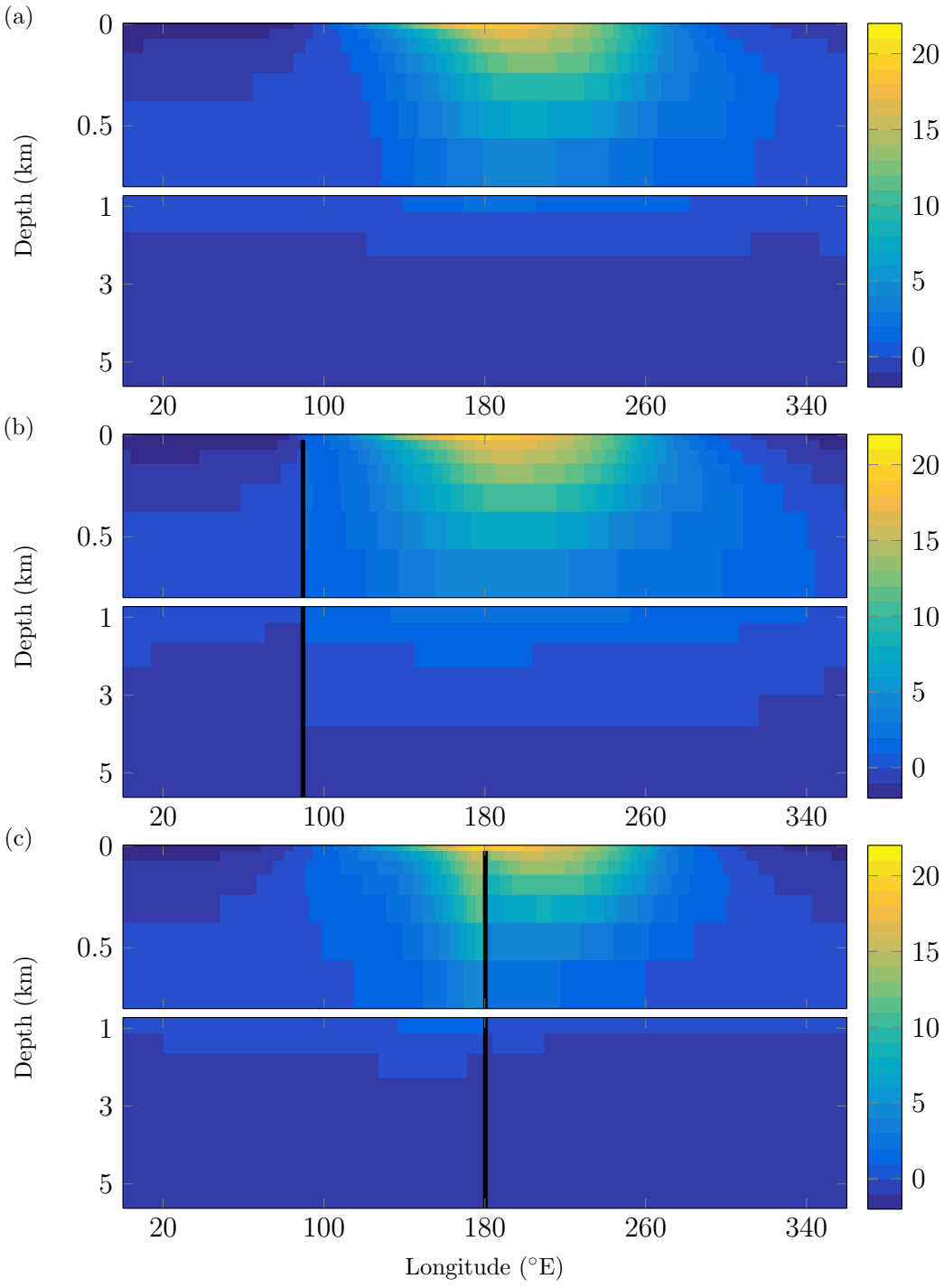


Figure 7.8: Quasi-steady state meridionally-averaged temperature (°C) for a tidally locked ridgeworld configuration with the substellar point at 180°E and the subsurface barrier at (a) 0°E, (b) 90°E, (c) 180°E, and (d) 270°E. Note the expanded vertical scale in the upper 1 km of the ocean.

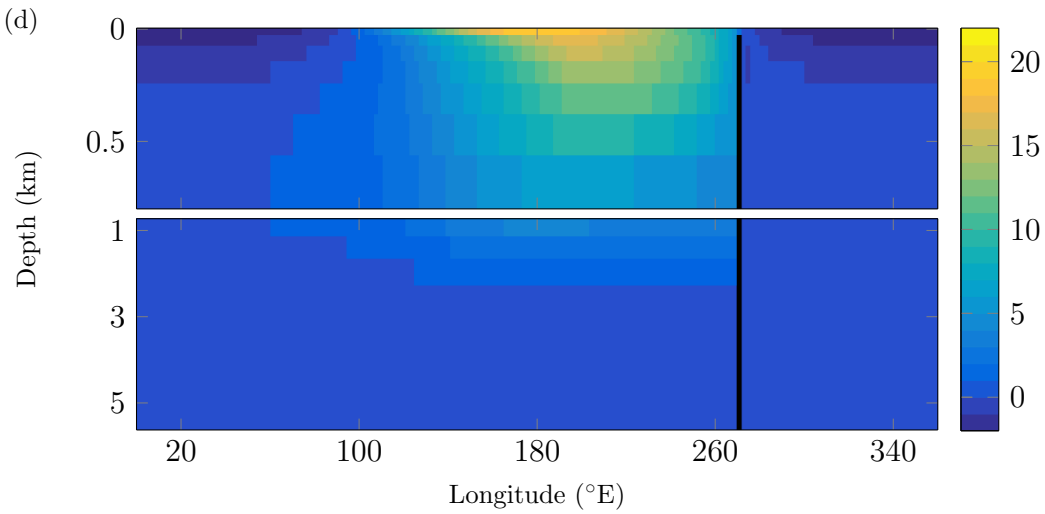


Figure 7.8: Quasi-steady state meridionally-averaged temperature (°C) for a tidally locked ridgeworld configuration with the substellar point at 180°E and the subsurface barrier at (a) 0°E, (b) 90°E, (c) 180°E, and (d) 270°E. Note the expanded vertical scale in the upper 1 km of the ocean.

With the barrier located at 180°E there is a significant temperature difference across the barrier of 4.4°C at 500 m depth, in this case intense downwelling of warm water from the surface on the western side of the barrier creates a region of relatively warm water through the surface 1 km of the ocean (figure 7.8(c)). On the eastern side there is an upwelling of water which is therefore cooler than the western side, however, this circulation cell is relatively shallow (figure 7.7(c)), and hence this area of water is still significantly warmer than the deep ocean. A similar downwelling of water west of the barrier when located at 270°E creates the largest temperature difference across the barrier of all four cases of 4.9°C at 500 m depth (figure 7.8(d)). In this case the downwelling is the most intense of the four cases, and extends into the deep ocean, which also creates the warmest deep ocean temperature of the four cases at consistently above 0°C compared to negative temperatures of up to -1°C in the other cases.

### 7.2.5 Heat transport

Outside of the low latitudes the meridional ocean heat transport is generally from equator to pole and is small, less than 1 PW, poleward of 50°N/S (figure 7.9). The heat transport peaks in magnitude at values between 4 and 6 PW

in each of the cases, however the latitude of these peaks varies depending on the barrier location. All cases show peaks in the low latitudes, which are the greatest globally when the barrier is located at 0°E and 90°E, however, with the barrier at 180°E and 270°E there are peaks further poleward at 35°N/S and 20°N/S, respectively. This peak occurs furthest poleward when the barrier is at 180°E because the barrier is in an ice free area of ocean in this case which means there are strong western boundary currents along the barrier carrying heat poleward. In contrast, the case with the barrier at 270°E has the strongest and deepest meridional overturning circulation outside of the low latitudes of all the cases, which is responsible for the peak in meridional heat transport at 20°N/S in this case.

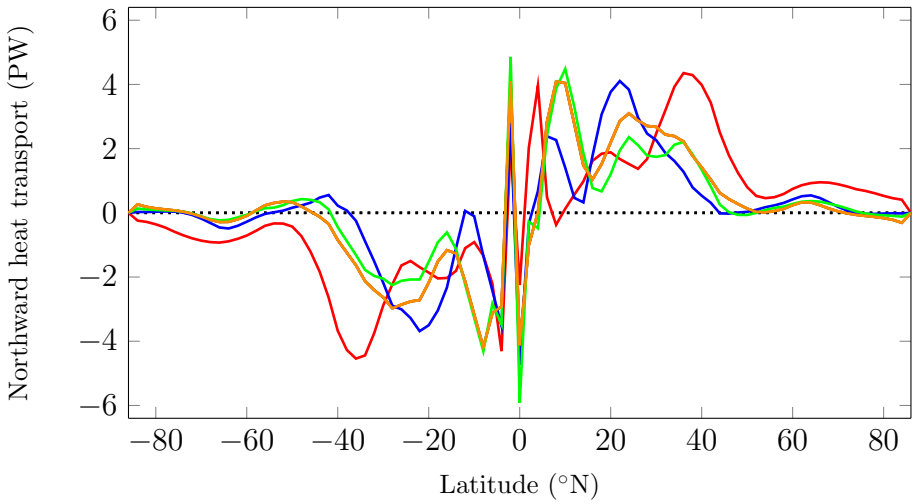


Figure 7.9: Quasi-steady state northward ocean heat transport (PW) for a tidally locked ridgeworld configuration with the substellar point at 180°E and the subsurface barrier at (green) 0°E, (orange) 90°E, (red) 180°E, and (blue) 270°E.

Computation of the zonal heat transport is nontrivial as there is a large net volume flux, and hence an arbitrary offset in the computed value. Here, the problem is overcome by computing the heat transport due to the deviation from the spatial mean of the zonal flow. The zonal heat transport is predominantly eastward, with a region of relatively weak westward transport which is in general between approximately 0 and 140°E (figure 7.10). The most extensive region of westward transport occurs when the barrier is at 270°E; it occurs between 320 and 150°E and peaks at 3.5 PW. The heat transport in the zonal direction shows significantly larger magnitudes than that in the meridional direction, with peak values of up to 13.0 PW in the

eastward direction. In all cases the peak occurs between 180 and 270°E, with the largest peak in the case with the barrier located at 180°E, and a peak of 11.6, 9.7 and 9.6 PW when the barrier is located at 0, 270 and 90°E, respectively.

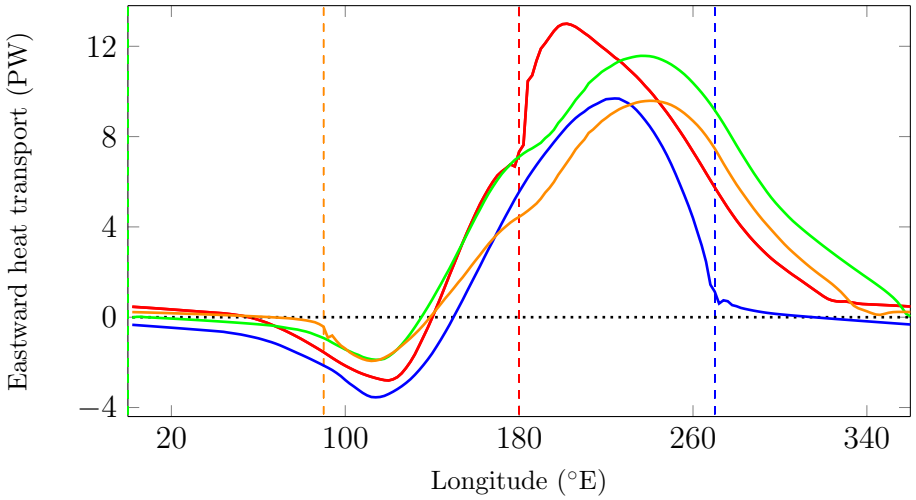


Figure 7.10: Quasi-steady state eastward ocean heat transport (PW) for a tidally locked ridgeworld configuration with the substellar point at 180°E and the subsurface barrier at (green) 0°E, (orange) 90°E, (red) 180°E, and (blue) 270°E.

All cases display a similar pattern with longitude, with the most noticeable deviations being in the cases where the barrier is located at 180°E; where the peak is the largest and occurs furthest west which is associated with stronger gyres resulting from the barrier being in the ice free area of ocean, and when the barrier is located at 270°E; where there is a smaller heat transport east of the peak which becomes very small east of 270°E where the barrier restricts the heat transport from the light to dark side.

Similar issues arise in the computation of the eastward atmospheric heat transport to that in the ocean; it is calculated to within an arbitrary constant. Given the atmospheric heat transport is computed using a different method to the ocean, using energy fluxes rather than temperature and velocity, the same approach is not used, instead the atmospheric heat transport is presented such that the transport is zero at 0°E and is therefore discussed in terms of divergence. The atmosphere does not correctly conserve energy due to the use of a spectral scheme (Holden et al. 2016) giving the top-of-atmosphere energy balance as 5.2, 5.1, 4.9 and 5.2 $\mathrm{W\,m^{-2}}$

with the barrier at 0, 90, 180 and 270°E, respectively, which is accounted for in the computation of the atmospheric heat transport.

The influence of the position of the barrier in the ocean has less impact on the atmospheric than the ocean zonal heat transport, however there is still a difference between the four cases (figure 7.11). The greatest differences occur in the region of the eastern terminator, with the most noticeable occurring when the barrier is located at 270°E. In this case there is the largest divergence away from the substellar point and the sharpest peak, this correlates to the smallest heat transport at this longitude in the ocean which also displays a rapid change in profile (figure 7.10). This suggests there is a compensation between the atmospheric and oceanic heat transport, bearing comparison to Bjerknes compensation on Earth (Bjerknes 1964). This is supported by the case with the barrier at 180°E, which has the largest heat transport in the ocean and smallest divergence of heat transport in the atmosphere.

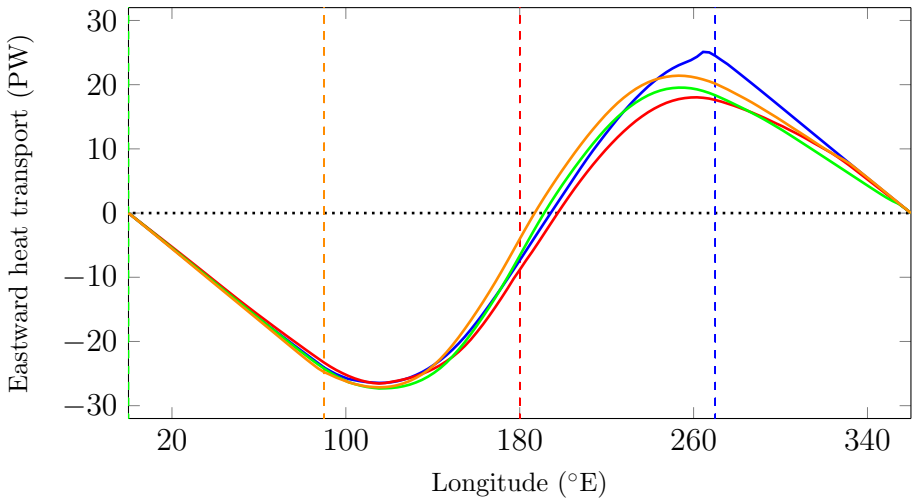


Figure 7.11: Quasi-steady state eastward atmospheric heat transport (PW) for a tidally locked ridgeworld configuration with the substellar point at 180°E and the subsurface barrier at (green) 0°E, (orange) 90°E, (red) 180°E, and (blue) 270°E.

The compensation between the atmospheric and oceanic heat transport is considered further by comparison of the peak divergence in the atmosphere, ocean and the total (table 7.2), which shows a smaller variability in the total than the individual components. The total is surprisingly close in three of the cases; with the barrier at 0, 90 and 180°E, again highlighting the strong

impact of the barrier being located at the eastern terminator.

| Barrier location (°E) | Peak divergence (PW) | | |
|---|---|---|---|
| | Ocean | Atmosphere | Total |
| 0 | 13.4 | 46.9 | 60.3 |
| 90 | 11.5 | 48.5 | 60.0 |
| 180 | 15.8 | 44.6 | 60.4 |
| 270 | 13.2 | 51.6 | 64.8 |

Table 7.2: Peak divergence in zonal heat transport in the ocean, atmosphere and the total for a tidally locked ridgeworld configuration with different barrier locations.

The transport of heat from the light to dark side can also be compared by analysing the distribution of surface air temperature on the light and dark side using probability density functions (figure 7.12). The light side temperatures show a similar distribution in all of the cases, with a peak in the region of 20-25°C, and limited areas below 0°C which are primarily associated with the polar regions. This similarity between the light side in each of the cases is also seen in the mean surface temperature of the light side, which have a relatively small range with values from 9.6 to 11.9°C, this minimum and maximum corresponds to the barrier being located at 0°E and 90°E, respectively. The probability density functions show limited areas with temperatures between 0 and -10°C, this is due to the ice albedo feedback which acts to further cool the surface air temperature when ice forms (Ebert & Curry 1993), and the insulating effect it has which restricts the warming effect of the ocean on the surface temperature due to the larger heat capacity of the ocean.

The surface temperatures on the dark side show a greater dependence on the location of the barrier than those of the light side; the distribution of surface air temperatures either side of the freezing point varies more considerably between the four cases, also, a significantly larger range of almost 7.5°C is seen in the mean dark side temperatures. The greatest similarity is between the cases where the barrier is located at 0°E and 90°E (figure 7.12(a,b)), these both show a sharp peak in dark side temperatures in the region of -30°C, a similar extent of positive temperatures up to 15°C, and the warmest dark side mean temperatures of -17.5 and -18.9°C, respectively. These

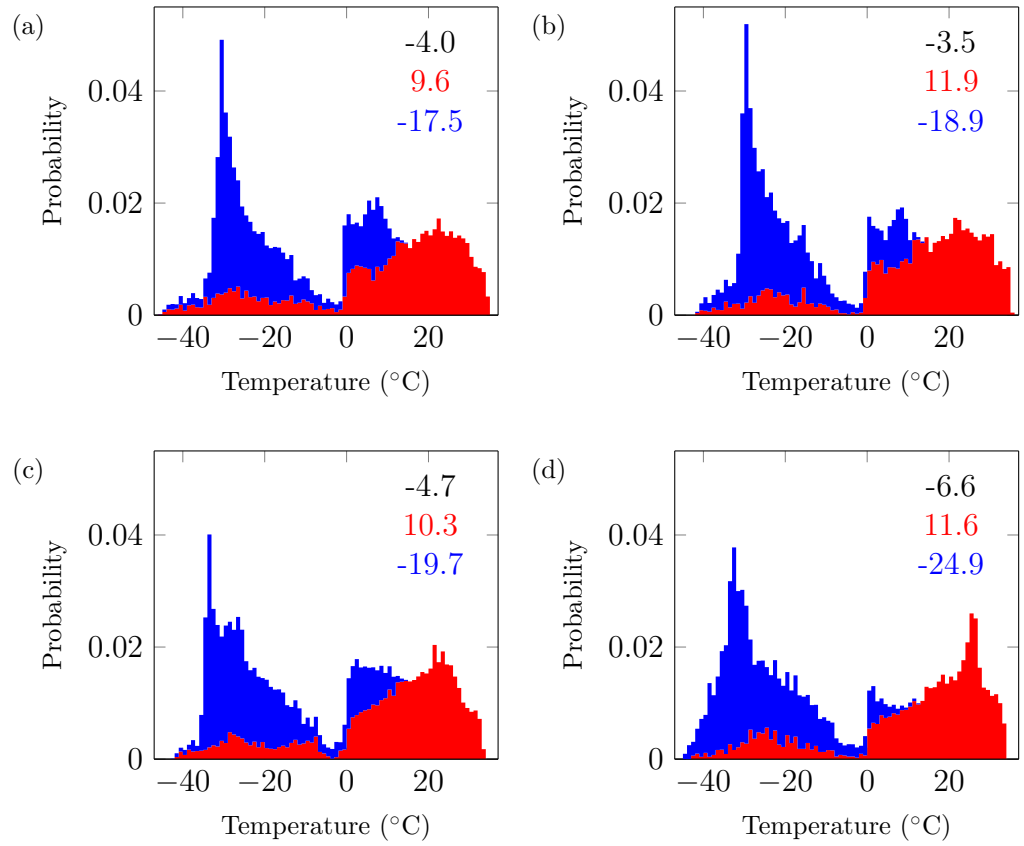


Figure 7.12: Quasi-steady state surface air temperature (°C) probability density functions for the (red) light and (blue) dark side of a tidally locked ridgeworld configuration with the substellar point at 180°E and the subsurface barrier at (a) 0°E, (b) 90°E, (c) 180°E, and (d) 270°E. Values are the (black) global, (red) light, and (blue) dark side mean temperature.

warmest dark side temperatures are associated with circulation patterns with single overturning cells extending throughout the light and dark side, which more efficiently transport heat from the warmer to cooler regions (figure 7.7(a,b)).

Comparison of the mean temperatures with maps of the surface air temperature shows the region in the low latitudes between 270 and 360°E is key; this is warmer than average when the barrier is located at 0°E and colder than average when located at 270°E (figure 7.2(a,d)), which correspond to the warmest and coldest dark side mean temperatures of -17.5 and -24.9°C, respectively. The coldest of these, with the barrier at 270°E, has a high mean temperature on the light side of 11.6°C which, along with the coldest dark side, is indicative of a relatively small heat transport from light to dark side, which is observed in the zonal heat transport (figure 7.10). This is

due to the location of the barrier restricting the eastward heat transport from the light side, and corresponds to the greatest ice coverage of the four cases (figure 7.3(d)). This case also corresponds to the coldest global mean temperature of -6.6°C, with the warmest being when the barrier is located at 90°E with a value of -3.5°C.

## 7.3 Summary

Here the impact of placing a meridional barrier at different longitudes in the ocean of a tidally locked planet has been analysed, and it is found that the zonal heat transport varies with its positioning. The cases with a barrier through the antistellar point and at the terminator east of it show similar circulation patterns, which extend eastward from the light side into the dark side and correspond to the largest heat transports across the eastern terminator. In contrast, a barrier through the substellar point or at the terminator east of it restricts the heat transport from light to dark side, this effect is particularly strong in the second of these cases which has the coldest dark side, and coldest global mean temperature.

# Chapter 8

# Conclusions

Modelling potential exoplanetary ocean configurations has given rise to conclusions about the climates of exoplanets and potential implications for the habitable zone width (§1.3). In particular, investigations have been made into the impacts of varying ocean salinity, planetary rotation period, and the influence of tidal locking on the ocean temperature and salinity distribution, circulation and heat transport.

## 8.1 Ocean salinity

For the first time the effect of both increasing and decreasing ocean salinity from the current Earth value has been investigated and shown to give ocean circulations which are reversed in direction to the Earth-like sense. In particular, the novel proportionality between the mean salinity and the gradients in salinity which can be maintained in the ocean is derived and employed. Ocean salinity may be related to the proportion of land and ocean coverage on a planet; with less land the limited available area for weathering would limit the salt input into the ocean and could result in a low salinity. With smaller areas of ocean and a large availability of land to facilitate weathering processes the opposite situation, with a high salinity ocean, may arise.

The key factor is the balance between the temperature and salinity forcing, since they act in opposing directions. For example, a negative salinity-driven circulation occurs at a mid range salinity if the temperature gradients are sufficiently small. An example of this occurring could be on a planet whose atmosphere is considerably denser than that of Earth, which results in a significantly smaller equator-pole temperature gradient (Joshi et al. 1997, Kliore & Patel 1982).

As ocean salinity increases the density responds far more strongly to differences in precipitation and evaporation, and hence the circulation has much stronger dependence on the salinity forcing. The evaporation and precipitation and hence profile of salinity forcing varies significantly with the degree of obliquity, and consequently the circulation also exhibits this strong dependence. For instance, the model used here is forced by annual mean zonally-averaged temperature and salinity profiles derived from observations on Earth, which includes the effects of the seasonally varying intertropical convergence zone (ITCZ). The greatest salinity forcing is at the edges of the ITCZ at approximately 20°N/S, which defines this as the latitude of deep water formation in the high salinity case. However, no such effect is seen in the mid range salinity scenario. Our results therefore suggest that the extent of the effect of orbital obliquity on planetary ocean circulation also depends on ocean salinity.

As the salinity of water increases the freezing point decreases, meaning that an ocean of higher salinity has less potential to form sea ice and so remains ice free at much lower temperatures. As well as having direct impacts on the ocean circulation, this also results in less global ice coverage, lowering the planetary albedo, consequently warming the climate (Budyko 1969) and directly changing the width of the habitable zone.

The implications of the value of ocean salinity on climate have been shown to have great significance for the entire structure of the large scale ocean circulation, and the resulting ocean heat transport. Indeed, the mean salinity of the ocean might be considered to be key in determining ocean thermal structure in an analogous manner to atmospheric pressure.

## 8.2 Planetary rotation period

It has been shown that lengthening the planetary rotation period increases the meridional heat transport; when increasing the rotation period from 1 to 10 days the heat transport is found to more than double. This dependence of ocean heat transport on rotation period has been concluded previously in the context of deepening the understanding of the ocean circulation on Earth, where comparable quantitative results are found with a coupled atmosphere-ocean model when lengthening the rotation period from 1 to 4 days (Vallis & Farneti 2009). Here, the additional conclusions that a longer rotation period increases the magnitude of the overturning circulation, shallows the thermocline depth, and increases the horizontal velocities is presented for the first time, as well as the application to the oceans of exoplanets.

Although only a restricted number of rotation periods have been investigated with numerical modelling here, the scale analysis extends the presented argument to a much larger range of rotation periods. Since the Rossby number ($\mathrm{Ro} = U/fL$) is an order of magnitude smaller in the ocean compared to the atmosphere, 0.01 in the ocean and 0.1 in the atmosphere in mid-latitudes at 1 day rotation period (Vallis 2006, p.85), the corresponding change in regime observed in the atmosphere at approximately 10 days would be expected to occur in the ocean at a much longer rotation

period, approximately 100 days. Numerical modelling at longer rotation periods would require a higher resolution model since the Rossby radius of deformation, which has $1/f$ dependence and a typical value of $\mathcal{O}(10\,\mathrm{km})$ at 1 day rotation period (Gill 1982, p.207), becomes larger at longer rotation periods, and therefore eddies become the scale of a grid box. At this size they are no longer represented by the parameterisation but are also not properly resolved in the model.

The results regarding rotation period have been shown by modelling the buoyancy-driven component of the ocean circulation in isolation. However, with longer planetary rotation periods the Ekman mass transport increases due to its $1/f$ dependence (Vallis 2006, p.107) and, furthermore, atmospheric wind velocities increase as the rotation period is lengthened over the range of rotation periods investigated here (Del Genio & Suozzo 1987, Williams 1988). Combined these would increase the poleward heat transport in the ocean when lengthening the rotation period and, hence, it would be expected that the component of the heat transport resulting from direct wind forcing would also increase with an increased rotation period, enhancing the increase shown by the results presented.

## 8.3 Tidal locking

The modelling of the ocean in a tidally locked configuration is furthered here from existing work (Hu & Yang 2014) by the inclusion of a meridional barrier in the ocean located at different longitudes. It is concluded that the location of this land mass has significant implications for the zonal heat transport. This has shown that even very small areas of land which block the zonal flow can have large implications for the circulation patterns in the ocean, and the transport of heat from the light to dark side. In a comparable way to simulations without a meridional barrier (Hu & Yang 2014), a strong eastward surface current is found which extends the ice free area eastward from the region of the substellar point, beyond the terminator and into the dark side when not restricted by a barrier.

The location of the barrier has been shown to affect the mean temperature of the light and dark side, as well as the global mean, which has implications for

the habitability of tidally locked planets. A greater dependence of the dark side temperature, compared to the light side, on the positioning of land is identified, which suggests the location of land mass on a tidally locked planet would have a greater significance for the distance of the outer boundary of the habitable zone compared to the inner boundary.

Modelling with a dynamic atmosphere allows for a comparison between the heat transport of the atmosphere and ocean components of the system, which has shown that the ocean provides an important proportion of the zonal heat transport. In addition, the interaction between the two components shows an element of compensation between the two, which is represented as a smaller range in the total atmosphere-ocean heat transport, compared to the ocean and atmosphere heat transports alone, between the configurations with different locations of the land barrier.

## 8.4 Significance of results

The impact on ocean heat transport, and resulting climatic temperatures, of each of the investigations presented here has significance for the habitable zone. For example, in an ocean with a high mean salinity, warm water fills the deep ocean and upwells in the cold high latitudes, which warms these coldest regions and therefore extends the outer limit of the habitable zone. Increasing salinity has little effect on the temperatures in the warmest regions in the low latitudes and therefore would not be expected to have a significant impact on the location of the inner edge of the habitable zone. There is also the effect of increasing salinity on sea ice formation, with higher salinity lowering the freezing point of seawater, which reduces the potential for permanent runaway glaciation, which also has the effect of extending the outer limit of the habitable zone. Overall, the impact of significantly increasing the salinity is to widen the habitable zone.

Lengthening the rotation period increases the heat transported by the ocean from the low to high latitudes, this has the effect of warming the cold, high latitudes and cooling the warm, low latitudes. Overall, this has the effect of smoothing temperature gradients on the planet. Without such large extremes in temperature the habitable zone is widened by both moving the

outer limit further away from the star and moving the inner limit closer to the star, making a planet with a longer rotation period generally more likely to be habitable than one with a shorter period.

When introducing a barrier to a tidally locked configuration it is shown that the largest implication for mean temperatures is in the mean dark side temperature, which has greatest significance for the outer edge of the habitable zone. The mean dark side temperature decreases as the barrier is moved east from the antistellar point, which moves the outer boundary of the habitable zone increasingly closer to the star, narrowing the habitable zone due to the increased potential for condensation of $CO_2$ and runaway glaciation.

The investigations presented here show the importance of any oceans in the modelling of exoplanetary climate, alongside the established significance of the atmospheric component (Joshi et al. 1997, Merlis & Schneider 2010, Edson et al. 2011), due to the implications for factors such as temperature distribution and ice extent. It cannot be assumed that any exoplanetary oceans behave in a similar manner to that on Earth. In particular, differences in the ocean salinity can give qualitatively different circulation patterns, and changes in the rotation period has significant implications for the poleward heat transport. In a tidally locked configuration, not only the significance of ocean heat transport has been highlighted, but also the impact of even small areas of land for the heat transport from the light to dark side has been shown. All of these effects have significance for the habitable zone, as described here, and it is therefore important to consider these factors when making conclusions about the climate and habitability of exoplanets, including in the study of specific discovered planets (Del Genio et al. 2017).

## 8.5 Future work

One of the ways in which the investigations presented here could be further explored is with the application of a higher resolution eddy resolving ocean general circulation model, due to the limitation of the parameterisations used in the modelling here. This is of particular interest in the case of changing the planetary rotation period, due to the strong dependence of the

Rossby radius on planetary rotation. This would also open the possibility of investigating the case without a meridional barrier in the ocean, in which eddies are the dominant process in the poleward heat transport.

An additional way of furthering the studies presented using an ocean only model is in the use of a coupled atmosphere-ocean general circulation model. This is of particular interest when changing the ocean salinity since the key difference in the ocean arises from difference in the impact of precipitation and evaporation on the changes in salinity in the ocean. In the case of changing the rotation period, a particular area of investigation with a coupled model would be the impact of the changes in the wind-driven component of the ocean heat transport. In general, modelling the coupled system allows for more complete conclusions to be made about the climate system, with the ability to model the response of the atmosphere, as well as the ocean, to the changing conditions, and the feedbacks between the two components.

The tidally locked configuration could be furthered by simulating more realistic physical aspects of a planet orbiting a small star in the habitable zone. For example, such a planet would be expected to have a longer rotation period than 1 Earth day, which is used here; a planet with this rotation period would be orbiting a 0.01 solar-mass star, which is smaller than the limit for hydrogen burning (Edson et al. 2011). In addition, the spectrum of stellar radiation could be modified to that of a red dwarf star; a smaller star emits light at longer wavelengths, which has implications for the ice-albedo feedback (Joshi & Haberle 2012).

In this work, a change in each of the three factors investigated is explored in isolation, however, on a given exoplanet any combination of these factors is possible. Therefore, the modelling of combinations of variations in these parameters is an area for future work. Based on the conclusions presented here it is only possible to speculate on the possible impacts of certain combinations on ocean circulation. For example, a high salinity ocean in a tidally locked configuration with the barrier at the antistellar point or the terminator east of it, may result in the downwelling of warm surface water on the light side which would warm the deep ocean and upwell in the region of the antistellar point. This would be expected to increase the warming effect by the ocean on the dark side of the planet, extending the outer limit of

the habitable zone. However, solid conclusions may only be made following modelling of potential scenarios, which is an area for future investigation.

In addition to the factors explored here, on any given exoplanet there are many other properties which are likely to differ from their Earth-like values, some of which may also have significant influence on ocean circulation. Examples include ocean bathymetry and depth (Yang et al. 2014b), obliquity (Ferreira et al. 2014), and continental configuration (Smith et al. 2006, Enderton & Marshall 2009, Nilsson et al. 2013). The combined effect of changes in these parameters on any oceans is an area for future investigation.

# Bibliography


Armstrong, J., Barnes, R., Domagal-Goldman, S., Breiner, J., Quinn, T. & Meadows, V. (2014), 'Effects of extreme obliquity variations on the habitability of exoplanets', *Astrobiology* **14**(4), 277–291.

Betts, A. K. (1986), 'A new convective adjustment scheme. Part I: Observational and theoretical basis', *Quarterly Journal of the Royal Meteorological Society* **112**, 677–691.

Birchfield, G. E. (1989), 'A coupled ocean-atmosphere climate model: temperature versus salinity effects on the thermohaline circulation', *Climate Dynamics* **4**, 57–71.

Birchfield, G. E., Wyant, M. & Wang, H. (1990), 'A coupled ocean-atmosphere box model of the Atlantic ocean: a bimodal climate response', *Journal of Marine Systems* **1**, 197–208.

Bjerknes, J. (1964), 'Atlantic air-sea interaction', *Advances in Geophysics* **10**, 1–82.

Bjornsson, H. & Toggweiler, J. R. (2001), The climatic influence of Drake Passage, *in* B. J. H. D. Seidov & M. Maslin, eds, 'The Oceans and Rapid Climate Change: Past, Present, and Future', American Geophysical Union, pp. 243–259.

Bryan, F. (1986), 'High-latitude salinity effects and interhemispheric thermohaline circulations', *Nature* **323**, 301–304.

Bryan, F. (1987), 'Parameter sensitivity of primitive equation ocean general circulation models', *Journal of Physical Oceanography* **17**, 970–985.

Bryan, K. (1969), 'A numerical method for the study of the circulation of the world ocean', *Journal of computational physics* **4**, 347–376.

Bryan, K. & Cox, M. D. (1967), 'A numerical investigation of the oceanic general circulation', *Tellus* **19**(1), 54–80.

Bryan, K. & Cox, M. D. (1972), 'An approximate equation of state for numerical models of ocean circulation', *Journal of Physical Oceanography* **2**, 510–514.

Bryan, K. & Lewis, L. J. (1979), 'A water mass model of the world ocean', *Journal of Geophysical Research* **84**, 2503–2517.

Bryan, K., Manabe, S. & Pacanowski, R. C. (1975), 'A global ocean-atmosphere climate model. Part II. The oceanic circulation', *Journal of Physical Oceanography* **5**, 30–46.

Bryden, H. L., Longworth, H. R. & Cunningham, S. A. (2005), 'Slowing of the Atlantic meridional overturning circulation at 25°n', *Nature* **438**, 655–657.

Budyko, M. I. (1969), 'The effect of solar radiation variations on the climate of the Earth', *Tellus* **21**, 611–619.

Del Genio, A. D. & Suozzo, R. J. (1987), 'A comparative study of rapidly and slowly rotating dynamical regimes in a terrestrial general circulation model', *Journal of Atmospheric Sciences* **44**, 973–986.

Del Genio, A. D., Way, M. J., Amundsen, D. S., Aleinov, I., Kelley, M., Kiang, N. Y. & Clune, T. L. (2017), Habitable climate scenarios for Proxima Centauri b with a dynamic ocean. arXiv:1709.02051 [astro-ph.EP].

Dijkstra, H. A. (2005), *Nonlinear Physical Oceanography: A Dynamical Systems Approach to the Large Scale Ocean Circulation and El Niño*, Springer Science & Business Media.

Dole, S. H. (1964), *Habitable Planets for Man*, Blaisdell, New York.

Ebert, E. E. & Curry, J. A. (1993), 'An intermediate one-dimensional thermodynamic sea ice model for investigating ice-atmosphere interactions', *Journal of Geophysical Research* **98**, 10085–10109.

Edson, A., Lee, S., Bannon, P., Kasting, J. F. & Pollard, D. (2011), 'Atmospheric circulations of terrestrial planets orbiting low-mass stars', *Icarus* **212**, 1–13.

Enderton, D. & Marshall, J. (2009), 'Explorations of atmosphere–ocean–ice climates on an aquaplanet and their meridional energy transports', *Journal of Atmospheric Sciences* **66**, 1593–1611.

Farrow, D. (2012), 'A model for the evolution of the thermal bar system', *European Journal of Applied Mathematics* **24**, 161–177.

Ferreira, D., Marshall, J., O'Gorman, P. A. & Seager, S. (2014), 'Climate at high-obliquity', *Icarus* **243**, 236–248.

Fischer-Gödde, M. & Kleine, T. (2017), 'Ruthenium isotopic evidence for an inner Solar System origin of the late veneer', *Nature* **541**, 525–527.

Forster, P., Blackburn, M., Glover, R. & Shine, K. P. (2000), 'An examination of climate sensitivity for idealised climate change experiments in an intermediate general circulation model', *Climate Dynamics* **16**, 833–849.

Fowler, A. (2011), *Mathematical Geoscience*, Vol. 36 of *Interdisciplinary Applied Mathematics*, Springer-Verlag London.

Friedrich, H. & Levitus, S. (1972), 'An approximation to the equation of state for sea water, suitable for numerical ocean models', *Journal of Physical Oceanography* **2**, 514–517.

Ganachaud, A. & Wunsch, C. (2000), 'Improved estimates of global ocean circulation, heat transport and mixing from hydrographic data', *Nature* **408**, 453–457.

Gent, P. R. & McWilliams, J. C. (1990), 'Isopycnal mixing in ocean circulation models', *Journal of Physical Oceanography* **20**, 150–155.

Gill, A. (1982), *Atmosphere-Ocean Dynamics*, Vol. 30 of *International Geophysics Series*, Academic Press, California.

Gill, A. E. & Bryan, K. (1971), 'Effects of geometry on the circulation of a three-dimensional southern-hemisphere ocean model', *Deep-Sea Research* **18**(685-721).

Graham, T. (2008), Sensitivity of the Global Climate to Vertical Ocean Diffusivity and other Parameters in Coupled Climate Models, PhD thesis, University of East Anglia.

Griffies, S. M., Biastoch, A., Böning, C., Bryan, F., Danabasoglu, G., Chassignet, E. P., England, M. H., Gerdes, R., Haak, H., Hallberg, R. W., Hazeleger, W., Jungclaus, J., Large, W. G., Madec, G., Pirani, A., Samuels, B. L., Scheinert, M., Gupta, A. S., Severijns, C. A., Simmons, H. L., Treguier, A. M., Winton, M., Yeager, S. & Yin, J. (2009), 'Coordinated ocean-ice reference experiments (COREs)', *Ocean Modelling* **26**, 1–46.

Hallberg, R. & Gnanadesikan, A. (2006), 'The role of eddies in determining the structure and response of the wind-driven Southern Hemisphere overturning: results from the modeling eddies in the Southern Ocean (MESO) project', *Journal of Physical Oceanography* **36**, 2232–2252.

Hart, M. E. (1979), 'Habitable zones about main sequence stars', *Icarus* **37**, 351–357.

Hawkins, E., Smith, R. S., Allison, L. C., Gregory, J. M., Woollings, T. J., Pohlmann, H. & de Cuevas, B. (2011), 'Bistability of the Atlantic overturning circulation in a global climate model and links to ocean freshwater transport', *Geophysical Research Letters* **38**(L10605).

Hay, W. W., Migdisov, A., Balukhovsky, A. N., Wold, C. N., Flögel, S. & Söding, E. (2006), 'Evaporites and the salinity of the ocean during the Phanerozoic: Implications for climate, ocean circulation and life', *Palaeogeography, Palaeoclimatology, Palaeoecology* **240**, 3–46.

Heath, M. J., Doyle, L. R., Joshi, M. M. & Haberle, R. M. (1999), 'Habitability of planets around red dwarf stars', *Origins of Life and Evolution of the Biosphere* **29**, 405–424.

Hellerman, S. & Rosenstein, M. (1983), 'Normal monthly wind stress over the world ocean with error estimates', *Journal of Physical Oceanography* **13**, 1093–1104.

Heuzé, C., Heywood, K. J., Stevens, D. P. & Ridley, J. K. (2015), 'Changes in global ocean bottom properties and volume transports in CMIP5 models under climate change scenarios', *Journal Of Climate* **28**(2917-2944).

Holden, P. B., Edwards, N. R., Fraedrich, K., Kirk, E., Lunkeit, F. & Zhu, X. (2016), 'PLASIM–GENIE v1.0: a new intermediate complexity AOGCM', *Geoscientific Model Development* **9**, 3347–3361.

Hoskins, B. J. & Simmons, A. J. (1975), 'A multi-layer spectral model and the semi-implicit method', *Quarterly Journal of the Royal Meteorological Society* **101**, 637–655.

Hu, Y. & Yang, J. (2014), 'Role of ocean heat transport in climates of tidally locked exoplanets around M dwarf stars', *Proceedings of the National Academy of Sciences* **111**(2).

Huang, R. X., Luyten, J. R. & Stommel, H. M. (1992), 'Multiple equilibrium states in combined thermal and saline circulartion', *Journal of Physical Oceanography* **22**, 231–246.

Huisman, S. E., den Toom, M., Dijkstra, H. A. & Drijfhout, S. (2010), 'An indicator of the multiple equilibria regime of the Atlantic meridional overturning circulation', *Journal of Physical Oceanography* **40**, 551–567.

Hunt, B. G. (1979), 'The influence of the Earth's rotation rate on the general circulation of the atmosphere', *Journal of the Atmospheric Sciences* **36**, 1392–1408.

Johns, W. E., Baringer, M. O., Beal, L. M., Cunningham, S. A., Kanzow, T., Bryden, H. L., Hirschi, J. J. M., Marotzke, J., Meinen, C. S., Shaw, B. & Curry, R. (2011), 'Continuous, array-based estimates of Atlantic ocean heat transport at 26.58N', *Journal of Climate* **24**, 2429–2449.

Joshi, M. M. (2003), 'Climate model studies of synchronously rotating planets', *Astrobiology* **3**(2).

Joshi, M. M. & Haberle, R. M. (2012), 'Suppression of the water ice and snow albedo feedback on planets orbiting red dwarf stars and the subsequent widening of the habitable zone', *Astrobiology* **12**(1), 3–8.

Joshi, M. M., Haberle, R. M. & Reynolds, R. T. (1997), 'Simulations of the atmospheres of synchronously rotating terrestrial planets orbiting M dwarfs: conditions for atmospheric collapse and the implications for habitability', *Icarus* **129**, 450–465.

Joshi, M., Stringer, M., van der Wiel, K., O'Callaghan, A. & Fueglistaler, S. (2015), 'IGCM4: a fast, parallel and flexible intermediate climate model', *Geoscientific Model Development* **8**, 1157–1167.

Kaltenegger, L., Sasselov, D. & Rugheimer, S. (2013), 'Water-planets in the habitable zone: atmospheric chemistry, observable features, and the case of Kepler-62e and -62f', *The Astrophysical Journal Letters* **775**(L47).

Kaspi, Y. & Showman, A. P. (2015), 'Atmospheric dynamics of terrestrial exoplanets over a wide range of orbital and atmospheric parameters', *The Astrophysical Journal* **804**(60).

Kasting, J. F. (1988), 'Runaway and moist greenhouse atmospheres and the evolution of Earth and Venus', *Icarus* **74**, 472–494.

Kasting, J. F., Whitmire, D. P. & Reynolds, R. T. (1993), 'Habitable zones around main sequence stars', *Icarus* **101**, 108–128.

Kawai, H. & Inoue, T. (2006), 'A simple parameterization scheme for subtropical marine stratocumulus', *Scientific Online Letters on the Atmosphere* **2**, 17–20.

Kiernet, H., Feulner, G. & Petoukhov, V. (2013), 'Albedo and heat transport in 3-d model simulations of the early Archeon climate', *Climate of the Past* **9**, 1841–1862.

Killworth, P. D., Stainforth, D., Webb, D. J. & Peterson, S. M. (1991), 'The development of a free-surface Bryan-Cox-Semtner ocean model', *Journal of Physical Oceanography* **21**, 1333–1348.

Kliore, A. J. & Patel, I. R. (1982), 'Thermal structure of the atmosphere of Venus from Pioneer Venus radio occultations', *Icarus* **52**, 320–334.

Knauth, L. P. (1998), 'Salinity history of the Earth's early ocean', *Nature* **395**, 554–555.

Krumgalz, B. & Millero, F. (1982), 'Physico-chemical study of Dead Sea waters', *Marine Chemistry* **11**, 477–492.

Leconte, J., Forget, F., Charnay, B., Wordsworth, R., Selsis, F., Millour, E. & Spiga, A. (2013), '3D climate modeling of close-in land planets: circulation patterns, climate moist bistability, and habitability', *Astonomy and Astrophysics* **554**(A69).

Levitus, S. (1982), *Climatological Atlas of the World Ocean*, NOAA professional paper, U.S. Department of Commerce, National Oceanic and Atmospheric Administration.

Manabe, S. & Stouffer, R. (1988), 'Two stable equilibria of a coupled ocean-atmosphere model', *Journal of Climate* **1**, 841–866.

Manabe, S. & Strickler, R. F. (1964), 'Thermal equilibrium of the atmosphere with a convective adjustment', *Journal of The Atmospheric Sciences* **21**, 361–385.

Marotzke, J. & Stone, P. H. (1995), 'Atmospheric transports, the thermohaline circulation, and flux adjustments in a simple coupled model', *Journal of Physical Oceanography* **25**, 1350–1364.

Marotzke, J. & Willebrand, J. (1991), 'Multiple equilibria of the global thermohaline circulation', *Journal of Physical Oceanography* **21**, 1372–1385.

Marshall, J., Ferreira, D., Campin, J. M. & Enderton, D. (2007), 'Mean climate and variability of the atmosphere and ocean on an aquaplanet', *Journal Of The Atmospheric Sciences* **64**, 4270–4286.

Maximenko, N., Niiler, P., Rio, M.-H., Melnichenko, O., Centurioni, L., Chambers, D., Zlotnicki, V. & Galperin, B. (2009), 'Mean dynamic topography of the ocean derived from satellite and drifting buoy data using three different techniques', *Journal Of Atmospheric And Oceanic Technology* **26**, 1910–1919.

Mayor, M. & Queloz, D. (1995), 'A Jupiter-mass companion to a solar-type star', *Nature* **378**, 355–359.

Merlis, T. M. & Schneider, T. (2010), 'Atmospheric dynamics of Earth-like tidally locked aquaplanets', *Journal of Advances in Modeling Earth Systems* **2**(13).

Mesinger, F. & Arakawa, A. (1976), *Numerical methods used in atmospheric models*, Vol. 1 of *GARP publications series*, Global Atmospheric Research Programme, GARP.

Miller, R. N. (2007), *Numerical modelling of ocean circulation*, Cambridge University Press.

Morbidelli, A., Chambersz, J., Lunine, J. I., Petit, J. M., Robert, F., Valsecch, G. B. & Cyr, K. E. (2000), 'Source regions and timescales for the delivery of water to the Earth', *Meteoritics & Planetary Science* **35**, 1309–1320.

Munk, W. H. (1950), 'On the wind-driven ocean circulation', *Journal of Meteorology* **7**, 79–93.

Munk, W. H. (1966), 'Abyssal recipes', *Deep-Sea Research* **13**, 707–730.

NASA (2017*a*), 'NASA'.
**URL:** *https://www.nasa.gov*

NASA (2017*b*), 'NASA Exoplanet Archive'.
**URL:** *https://exoplanetarchive.ipac.caltech.edu*

Nilsson, J., Langen, P. L., Ferreira, D. & Marshall, J. (2013), 'Ocean basin geometry and the salinification of the Atlantic ocean', *Journal of Climate* **26**, 6163–6184.

O'Brien, J. J. (1986), *The Diffusive Problem*, Springer Netherlands, Dordrecht, pp. 127–144.

Park, Y.-G. & Bryan, K. (2000), 'Comparison of thermally driven circulations from a depth-coordinate model and an isopycnal-layer model. Part I: scaling-law sensitivity to vertical diffusivity', *Journal of Physical Oceanography* **30**, 590–605.

Pedlosky, J. (1990), 'The dynamics of the oceanic subtropical gyres', *Science* **248**, 316–322.

Pierrehumbert, R. & Gaidos, E. (2011), 'Hydrogen greenhouse planets beyond the habitable zone', *The Astrophysical Journal Letters* **734**(L13).

Price, J. F., Weller, R. A. & Schudlich, R. R. (1987), 'Wind-driven ocean currents and Ekman transport', *Science* **238**, 1534–1538.

Quintana, E. V., Barclay, T., Raymond, S. N., Rowe, J. F., Bolmont, E., Caldwell, D. A., Howell, S. B., Kane, S. R., Huber, D., Crepp, J. R., Lissauer, J. J., Ciardi, D. R., Coughlin, J. L., Everett, M. E., Henze, C. E., Horch, E., Isaacson, H., Ford, E. B., Adams, F. C., Still, M., Hunter, R. C., Quarles, B. & Selsis, F. (2014), 'An Earth-sized planet in the habitable zone of a cool star', *Science* **344**(6181), 277–280.

Rahmstorf, S. (1995), 'Bifurcations of the Atlantic thermohaline circulation in response to changes in the hydrological cycle', *Nature* **378**, 145–149.

Rahmstorf, S. (1996), 'On the freshwater forcing and transport of the Atlantic thermohaline circulation', *Climate Dynamics* **12**, 799–811.

Rahmstorf, S., Box, J. E., Feulner, G., Mann, M. E., Robinson, A., Rutherford, S. & ernicht, E. J. S. (2015), 'Exceptional twentieth-century slowdown in Atlantic Ocean overturning circulation', *Nature Climate Change* **5**, 475–480.

Rahmstorf, S., Crucifix, M., Ganopolski, A., Goosse, H., Kamenkovich, I., Knutti, R., Lohmann, G., Marsh, R., Mysak, L. A., Wang, Z. & Weaver, A. J. (2005), 'Thermohaline circulation hysteresis: A model intercomparison', *Geophysical Research Letters* **32**(L23605).

Raymond, S. N., Quinn, T. & Lunine, J. I. (2004), 'Making other Earths: dynamical simulations of terrestrial planet formation and water delivery', *Icarus* **168**, 1–17.

Raymond, S. N., Quinn, T. & Lunine, J. I. (2007), 'High-resolution simulations of the final assembly of Earth-like planets. 2. Water delivery and planetary habitability', *Astrobiology* **7**, 66–84.

Richardson, P. L. & Schmitz, W. J. (1993), 'Deep cross-equatorial flow in the Atlantic measured with SOFAR floats', *Journal of Geophysical Research* **98**, 8371–8387.

Richtmyer, R. D. & Morton, K. (1967), *Difference methods for initial-value problems*, 2nd edn, Interscience, New York.

Rivera, E. J., Lissauer, J. J., Butler, R. P., Marcy, G. W., Vogt, S. S., Fischer, D. A., Brown, T. M., Laughlin, G. & Henry, G. W. (2005), 'A $\sim$7.5 $M_\oplus$ planet orbiting the nearby star, GJ 8761', *The Astrophysical Journal* **634**, 625–640.

Rooth, C. (1982), 'Hydrology and ocean circulation', *Progress in Oceanography* **11**, 131–149.

Roquet, F., Madec, G., Brodeau, L. & Nycander, J. (2015), 'Defining a simplified yet "realistic" equation of state for seawater', *Journal of Physical Oceanography* **45**, 2564–2579.

Rushby, A. J., Claire, M. W., Osborn, H. & Watson, A. J. (2013), 'Habitable zone lifetimes of exoplanets around main sequence stars', *Astrobiology* **13**(9).

Salameh, J., Popp, M. & Marotzke, J. (2018), 'The role of sea-ice albedo in the climate of slowly rotating aquaplanets', *Climate Dynamics* **50**, 2395–2410.

Sanchis-Ojeda, R., Rappaport, S., Winn, J. N., Levine, A., Kotson, M. C., Latham, D. W. & Buchhave, L. A. (2013), 'Transits and occultations of an Earth-sized planet in an 8.5 hr orbit', *The Astrophysical Journal* **774**(54).

Semtner, A. J. (1986*a*), *Finite-Difference Formulation of a World Ocean Model*, Springer Netherlands, Dordrecht, pp. 187–202.

Semtner, A. J. (1986*b*), *History and Methodology of Modelling the Circulation of the World Ocean*, Springer Netherlands, Dordrecht, pp. 23–32.

Showman, A. P. & Polvani, L. M. (2011), 'Equatorial superrotation on tidally locked exoplanets', *The Astrophysical Journal* **738**(71).

Slingo, J. M. (1987), 'The development and verification of a cloud prediction scheme for the ECMWF model', *Quarterly Journal of the Royal Meteorological Society* **113**, 899–927.

Smith, R. & Dubois, C. (2004), 'Ocean circulation and climate in an idealised Pangean OAGCM', *Geophysical Research Letters* **31**(L18207).

Smith, R. S., Dubois, C. & Marotzke, J. (2006), 'Global climate and ocean circulation on an aquaplanet ocean-atmosphere general circulation model', *Journal of Climate* **19**, 4719–4737.

Stommel, H. (1961), 'Thermohaline convection with two stable regimes of flow', *Tellus* **13**, 224–230.

Terray, L., Valcke, S. & Piacentini, A. (1999), The OASIS coupler user guide version 2.3, Technical Report TR/CMGC/99-37, CERFACS.

Thorpe, R. B., Gregory, J. M., Johns, T. C., Wood, R. A. & Mitchell, J. F. B. (2001), 'Mechanisms determining the Atlantic thermohaline circulation response to greenhouse gas forcing in a non-flux-adjusted coupled climate model', *Journal of Climate* **14**, 3102–3116.

Trenberth, K. E. & Caron, J. M. (2001), 'Estimates of meridional atmosphere and ocean heat transports', *Journal of Climate* **14**, 3433–3443.

Vallis, G. K. (2000), 'Large-scale circulation and production of stratification: effects of wind, geometry, and diffusion', *Journal of Physical Oceanography* **30**, 933–954.

Vallis, G. K. (2006), *Atmospheric and Oceanic Fluid Dynamics*, Cambridge University Press, Cambridge, U.K.

Vallis, G. K. & Farneti, R. (2009), 'Meridional energy transport in the coupled atmospere-ocean system: scaling and numerical experiments', *Quarterly Journal of the Royal Meteorological Society* **135**, 1643–1660.

Webb, D. J. (1995), 'The vertical advection of momentum in Bryan-Cox-Semtner ocean general circulation models', *Journal of Physical Oceanography* **25**, 3186–3195.

Webb, D. J. (1996), 'An ocean model code for array processor computers', *Computers and Geosciences* **22**, 569–578.

Weijer, W., de Ruijter, W. P. M., Dijkstra, H. A. & van Leeuwen, P. J. (1999), 'Impact of interbasin exchange on the Atlantic overturning circulation', *Journal of Physical Oceanography* **29**, 2266–2284.

Welander, P. (1971), 'The thermocline problem', *Philosophical Transactions of the Royal Society of London* **270**, 415–421.

Williams, D. M. & Kasting, J. F. (1997), 'Habitable planets with high obliquities', *Icarus* **129**, 254–267.

Williams, G. P. (1988), 'The dynamical range of global circulations - I', *Climate Dynamics* **2**, 205–260.

Williams, P. D., Guilyardi, E., Madec, G., Gualdi, S. & Scoccimarro, E. (2010), 'The role of mean ocean salinity in climate', *Dynamics of Atmospheres and Oceans* **49**, 108–123.

Wolszczan, A. & Frail, D. A. (1992), 'A planetary system around the millisecond pulsar PSR1257 + 12', *Nature* **355**(6356), 145–147.

Yang, J. & Abbot, D. S. (2014), 'A low-order model of water vapor, clouds, and thermal emission for tidally locked terrestrial planets', *The Astrophysical Journal* **784**(155).

Yang, J., Cowan, N. B. & Abbot, D. S. (2013), 'Stabilizing cloud feedback dramatically expands the habitable zone of tidally locked planets', *The Astrophysical Journal Letters* **771**(L45).

Zhong, W. & Haigh, J. D. (1995), 'Improved broadband emissivity parameterization for water vapor cooling rate calculations', *Journal of Atmospheric Sciences* **52**, 124–138.